

FRIEDRICH-SCHILLER-UNIVERSITÄT JENA
Fakultät für Sozial- und Verhaltenswissenschaften
Institut für Sportwissenschaft

Intersection of Ground Reaction Force Vectors During Human Locomotion

Schnittpunkt der Bodenreaktionskräfte
bei der menschlichen Fortbewegung

Dissertation

zur Erlangung des akademischen Grades

doctor philosophiae (Dr. phil.)

vorgelegt dem Rat der Fakultät für Sozial- und Verhaltenswissenschaften
der Friedrich-Schiller-Universität Jena
von M.A. Johanna Vielemeyer
geboren am 14. März 1992 in Jena

Gutachter

1. PD Dr. Roy Müller (Bayreuth)
2. Prof. Dr. Reinhard Blickhan (Jena)

Tag der mündlichen Prüfung: 03. Februar 2022

Acknowledgments

First and foremost, I would like to express my sincere gratitude to my supervisor PD Dr. Roy Müller for his continuous support of my dissertation, enthusiasm, and immense knowledge. He always took time to answer and discuss my questions, be it content or organization, and under his guidance I was able to work purposefully all the time. Furthermore, I would like to express my gratitude for him having initiated the project and for his trust that I could collaborate. I could not have imagined having a better advisor and mentor for my dissertation.

Besides, a very special word of thanks goes to my second supervisor Prof. Dr. Reinhard Blickhan for the insightful comments, the copious and profound answers to my questions, and productive discussions. I thank both supervisors for supporting and inspiring my enthusiasm for research, especially in biomechanics, from the very beginning.

My sincere thanks also go to Eric Griebach who participated in the project during the first year. In addition to our cooperation in development and execution of the measurements, I would like to honor his contribution in developing the software and writing the paper. Furthermore, I appreciate our advantageous and interesting discussions, his immense knowledge, outstanding intelligence, and willingness to patiently answer my questions even after participating in the project.

I am grateful, too, to my colleagues Nora-Sophie Staufenberg, Dr.-Ing. Daniel Renjewski and Prof. Dr. ir. Daniel Rixen, from the Technical University of Munich, Özge Drama and Alexander Badri-Sprowitz from the Max Planck Institute for Intelligent Systems in Stuttgart, and Soran AminiAghdam for the good collaborations.

I would also like to extend my thanks to the subjects who willingly made themselves available for research.

My thanks are also due to the proofreaders Christian Rimpau for the linguistic improvement of this work and Sebastian Riese for the very helpful suggestions for content and linguistic improvement.

Special thanks go to my friends who patiently listened to my enthusiastic explanations of the experiments and research results and with whom I was able to have one or the other scientific argument; especially Anne Weber and Hannes Zöllner, who patiently answered my technical and physical questions.

My loving thanks go to my child for holding out in my belly long enough for me to finish this work.

Zusammenfassung

Der menschliche Gang und dessen Stabilisierung ist eine komplexe Aufgabe, auch wenn er im Alltag allgegenwärtig ist und von den meisten Menschen nicht bewusst kontrolliert wird. Das bedeutet, dass grundlegende Stabilisierungsmechanismen verwendet werden. Frühere Untersuchungen legen nahe, dass möglicherweise das *virtual-pendulum*-Konzept beim Gehen über einen ebenen Untergrund diese Aufgabe übernimmt und den Körper wie ein physikalisches Pendel stabilisiert. Hierbei schneiden sich die Bodenreaktionskräfte in einem Punkt oberhalb des Körperschwerpunkts, dem *virtual pivot point*. Es ist jedoch unklar, ob das virtual-pendulum-Konzept auch bei Störungen wie dem Gehen über unebenen Untergrund oder dem Gehen mit veränderter Körperhaltung angewendet wird. Darüber hinaus fehlt in bisherigen Studien die exakte Unterscheidung in einfach und doppelt unterstützte Standphase des Gehens. Außerdem beschäftigt sich die Literatur fast ausschließlich mit dem virtual pivot point beim Gehen, wobei das Laufen kaum Beachtung findet.

Daher wurden für diese Arbeit verschiedene Experimente durchgeführt, um die genannten Unklarheiten zu beseitigen. In **Kapitel 2** wurde untersucht, ob der virtual pivot point bei extrinsischen Störungen des menschlichen Gehens, speziell dem Gehen über sichtbare und verdeckte Stufen, zur Kontrolle der dynamischen Stabilität genutzt wird. Dabei gingen die Probanden mit zwei verschiedenen Geschwindigkeiten über einen Laufweg, welcher in der Mitte eine Absenkung beinhaltete. Diese war zunächst sichtbar und hatte eine Höhe von 0, 10 bzw. 20 cm. Anschließend wurde sie verdeckt, sodass für den Probanden unklar war, ob die Höhe 0 oder 10 cm beträgt. Es konnte beobachtet werden, dass die Bodenreaktionskräfte bei allen Bedingungen überwiegend über den Körperschwerpunkt in die Nähe eines Punktes zeigten. Die Abweichungen von diesem Punkt waren gering, weshalb vermutet wird, dass bei diesen extrinsischen Störungen das virtual-pendulum-Konzept zur Stabilisierung des Körpers genutzt wird.

Kapitel 3 beschäftigte sich mit der Frage, ob der virtual pivot point in der doppelt unterstützten Phase des Gehens beobachtet werden kann. Dazu gingen die Probanden mit einer selbstgewählten Geschwindigkeit über einen ebenen Laufweg. Es konnte herausgefunden werden, dass die Bodenreaktionskräfte, im Gegensatz zur einfach unterstützten Phase, mit geringer Streuung in den Körperschwerpunkt zeigten.

In **Kapitel 4** wurde schließlich das Laufen untersucht. Es fanden Experimente statt, bei denen die Probanden sowohl über einen ebenen Laufweg als auch über ein 10 cm tiefes Loch laufen sollten. Zusätzlich wurde das menschliche Laufen numerisch mithilfe

einer Simulation untersucht, wofür das Masse-Feder-Modell mit Rumpf genutzt wurde. Es konnte beobachtet werden, dass die Bodenreaktionskräfte mit geringer Streuung unter den Körperschwerpunkt zeigten. Die Implementierung der experimentellen Ergebnisse in der Simulation ergab ein stabiles System, sowohl für das ebene Laufen, als auch für das Hinablaufen einer Stufe.

Die wichtigsten Ergebnisse der vorherigen Kapitel bezüglich des virtual pivot point wurden in **Kapitel 5** zusammengefasst. Außerdem wurden die Ergebnisse verglichen und untersucht, welchen Einfluss die Eingangsvariablen auf die Position und die Streuung des virtual pivot points haben. Dazu wurden auch sowohl methodische Unterschiede in der Datenerhebung und -auswertung, als auch Messungenauigkeiten betrachtet und deren Auswirkungen auf die Ergebnisse analysiert. Schließlich wurden Grenzen und Möglichkeiten zur Weiterentwicklung des virtual-pendulum-Konzepts aufgeführt.

Abstract

Human gait and its stabilization is a complex task, even though it is ubiquitous in everyday life and not consciously controlled by most people. Thus, basic stabilization mechanisms are used. Previous research suggests that the *virtual pendulum* concept maintains the upright position when walking over a level surface, stabilizing the body like a physical pendulum. The concept assumes that the ground reaction forces intersect at a point above the body's center of mass, the *virtual pivot point*. However, it is unclear whether the virtual pendulum concept is also used for perturbations such as walking over uneven ground or walking with altered posture. Furthermore, previous studies lack the exact distinction between single and double supported stance phases of walking. Additionally, the literature considers almost exclusively the virtual pivot point during walking, and not during running.

Therefore, several experiments were conducted for this thesis to address the aforementioned ambiguities. **Chapter 2** investigated whether the virtual pivot point is used to control dynamic stability in extrinsic perturbations of human walking, concretely walking over visible and camouflaged curbs. For this purpose, the subjects walked with two different speeds over a walkway, which included a curb in the middle. This was initially visible and had a height of 0, 10 or 20 cm. Afterwards the curb was camouflaged, so that it was unclear to the subject whether the height was 0 or 10 cm. It was observed that in all conditions the ground reaction forces pointed predominantly to the vicinity of a point above the center of mass. The deviations from the point were small. Thus, it is suspected that the virtual pendulum concept is used to stabilize the body in these extrinsic perturbations.

Chapter 3 addressed the question of whether the virtual pivot point can be observed in the double support phase of walking. For this purpose, subjects walked at a self-selected speed along a level walkway. It was found that the ground reaction forces, in contrast to the single support phase, pointed with a small spread into the center of mass.

Finally, in **Chapter 4**, running was investigated. Experiments were performed in which the subjects were asked to run over a level track as well as over a drop of 10 cm. In addition, human running was investigated numerically with the help of simulation, for which the spring-loaded inverted pendulum model with a trunk was used. It could be shown that the ground reaction forces pointed with a small spread below the center of mass. The implementation of the experimental results in the simulation resulted in a stable system, both for level running and for running down a step.

The main results of the previous chapters concerning the virtual pivot point were summarized in **Chapter 5**. In addition, the results were compared and the influence of the input variables on the position and the spread of the virtual pivot point was investigated. For this purpose, methodological differences in data collection and evaluation as well as measurement inaccuracies were considered and their effects on the results were analyzed. Finally, limitations and possibilities for further development of the virtual pendulum concept were listed.

Table of Contents

Acknowledgments	I
Zusammenfassung	III
Abstract	V
Nomenclature	IX
1 General introduction	1
1.1 Human bipedal locomotion	1
1.1.1 Walking and running	1
1.1.2 Perturbations	5
1.2 Models describing human locomotion	6
1.3 VPP model	8
1.3.1 VPP in simulation and robotics	9
1.3.2 VPP in experiments	9
1.3.3 Calculation of the VPP	11
1.3.4 Differences in the VPP analysis	13
1.4 Methodic aspects	14
1.4.1 Considered part of the stride	14
1.4.2 Blur size of the VPP	15
1.4.3 Further aspects	16
1.5 Preparatory work	17
1.6 Dissertation outline	17
2 Article I: Ground reaction forces intersect above the center of mass even when walking down visible and camouflaged curbs	19
3 Article II: Ground reaction forces intersect above the center of mass in single support, but not in double support of human walking	29
4 Article III: Postural stability in human running with step-down perturbations: an experimental and numerical study	37

5	General conclusion	69
5.1	Summary	69
5.2	Comparison of the studies	72
5.2.1	Influence of the input variables	72
5.2.2	Influence of the calculation methods	77
5.2.3	Error estimation	80
5.2.4	Conclusion	81
5.3	Improvements of the VPP concept	83
5.4	Limitations and further considerations	85
	List of literature	87
A	Appendix: Summary	i
B	Appendix: Influence of the input variables between the studies	v
C	Appendix: Influence of the input variables within the studies	xi
D	Appendix: Error estimation	xv
	Publications	xvii
	Erklärung	xix

Nomenclature

Gait parameters

BW	body weight in Newton
CoM	center of mass of the whole body
CoM _{ZTD}	vertical CoM position relative to the CoP at TD
CoP	center of pressure
CoP _{CoM}	horizontal CoP relative to the CoM
DSP	double support phase
g	standard gravity
GRF	ground reaction force
l	leg length
\vec{L}_{wb}	centroidal angular momentum of the whole body
$\vec{p}_{normalized}$	normalized impulse
SSP	single support phase
TD	touch down
TO	take-off

Models

BSLIP	bipedal SLIP
d	minimal distance between VPP and GRF vector
DP	divergent point
FMCH	leg force modulated compliant hip
IP	intersection point
nmF	neuromuscular FMCH
R ²	coefficient of determination

SLIP	spring-loaded inverted pendulum
TSLIP	trunk SLIP
VP concept	virtual pendulum concept
VPP_RMSD	root mean squared distance of the VPP to the GRF vector
VPP	virtual pivot point
VP	virtual point

Experiments

ampl	accuracy of the amplifier
C10	gait over a camouflaged curb (walking)/drop (running) of 10 cm
cross	crosstalk error of the force plates
Δ	absolute error
EMG	electromyography
M	bending moment of the force plate
post	contact after the DSP
pre	contact previous to the DSP (walking)/perturbed contact (running)
θ	angle between the theoretical force vector and the measured GRF vector
TI25	walking with a trunk inclination of $31.9 \pm 5.4^\circ$
TI50	walking with a trunk inclination of $47.1 \pm 5.4^\circ$
TI _{max}	walking with a trunk inclination of $72.5 \pm 8.1^\circ$
V0	visible, level, unperturbed gait
V10	gait over a visible curb (walking)/drop (running) of 10 cm
V20	walking over a visible curb of 20 cm
x	horizontal component in gait direction
z	vertical component

1 General introduction

1.1 Human bipedal locomotion

1.1.1 Walking and running

Locomotion is the active movement of the animal's whole body mass through aerial, aquatic, or terrestrial space (Cappozzo et al., 1976). Even over a level, smooth surface, locomotion is a complex task because a large number of muscles acting over numerous joints must be coordinated (Jordan and Newell, 2008). Most of the terrestrial animals use four or six legs for their locomotion, while bipedal locomotion is relatively uncommon (Alexander, 1976). The disadvantage of bipedalism is the loss of static stability compared to quadrupeds or animals with even more legs and a greater need of neural control (Inman et al., 2006). However, there are species which locomote successfully on two legs, such as birds and occasionally bears, primates, marsupials, and some lizards (Kaufman and Sutherland, 2006; Alexander, 2004). Notably the human being performs a bipedal gait that is uniquely efficient and functional (Kaufman and Sutherland, 2006). Human bipedalism has probably become established because of its minimum energy requirement (Inman et al., 2006). This means that humans could hunt animals by following them for days until their complete exhaustion. It might also have been useful to have one's hands free for carrying infants or handling tools (Simonsen, 2014).

There are several modes of bipedal locomotion, which are used by humans and animals, as walking, running, hopping, jumping, and galloping (Alexander, 2004; Peck and Turvey, 1997). They are rhythmic displacements of body parts that maintain a constant forward progression (Alexander, 2004; Inman et al., 2006), where in antero-posterior direction, braking and propulsion forces alternate (Nilsson and Thorstensson, 1989). This repetition of rhythmic movements involves a gait cycle (Bonney and Armand, 2015). The normal human gaits for everyday use are walking and running. Here, the feet move symmetrically alternating in contrast to hopping, jumping and galloping, so that each limb experiences a sequence of support and nonsupport during each cycle (Alexander, 2004; Enoka, 2008). Besides these similarities, there are determining differences between walking and running. A decisive difference is speed (in adults, the average self-selected speed is about 1.4 ms^{-1} when walking and about 5 ms^{-1} when running (Götz-Neumann, 2011)), which also influences the duty factor¹ and the energy requirement. While the duty factor is greater than

¹The duty factor is the fraction of the time for which each foot is on the ground (Alexander, 2004).

0.5 in walking and less than 0.5 in running (Alexander, 2004), the energy efficiency in human walking is greater than in human running (Muir et al., 1996). This dynamic difference is caused by the oscillating exchanges between potential and kinetic energy while walking, and the exchanges between elastic and kinetic energy in running, because in the latter the leg acts as a spring (Muir et al., 1996). The distinguishing kinetic characteristic between walking and (aerial²) running is the presence of a double support phase. While walking requires a double support phase due to the duty factor >0.5 , running has only single support phases (Marquardt, 2012).

A gait cycle of human walking can be divided into eight phases, where stance phase and swing phases alternate (Marquardt, 2012). The stance phase starts with the *initial contact*. The instant of the beginning of the stance phase is called touch down (TD). The TD additionally initiates the double support phase. The following *loading response*, *mid stance*, and *terminal stance*, are single-leg supported. The instant when terminal stance ends is called take-off (TO; Enoka, 2008). The second double support phase follows with the *pre-swing*. Afterwards, the swing phase with the *initial swing*, the *mid swing* and the *terminal swing* is executed. The phases are illustrated in figure 1.1. The ratio of stance to swing phase is approximately 3:2, with each double support phase accounting for 10% of one gait cycle (Perry and Burnfield, 1993).

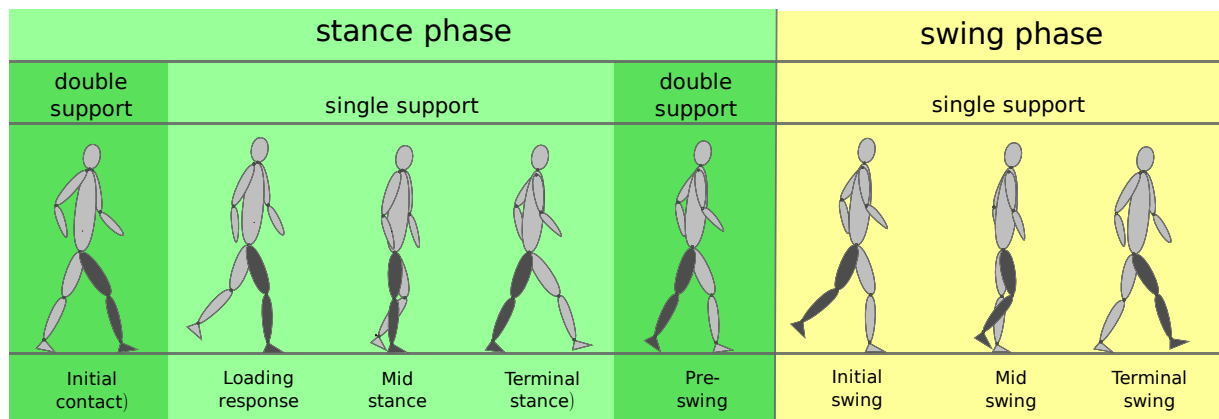


Figure 1.1: Phases of one stride of human walking adapted from Marquardt (2012).

For human running, the 6-phases-model by Mann et al. (1986) consists of a stance phase and a swing phase for each cycle. The stance phase is at any time single-leg supported and can be divided into *foot contact*, *mid support* (or mid stance), and *toe-off*. The following swing phase is composed of the *follow through*, *forward swing*, and *foot descent*. This model is shown in figure 1.2.

²The term *aerial* was chosen to distinguish from grounded running. In the following, the term *running* refers to aerial running. For the definition of *grounded running* see Rubenson et al. (2004).

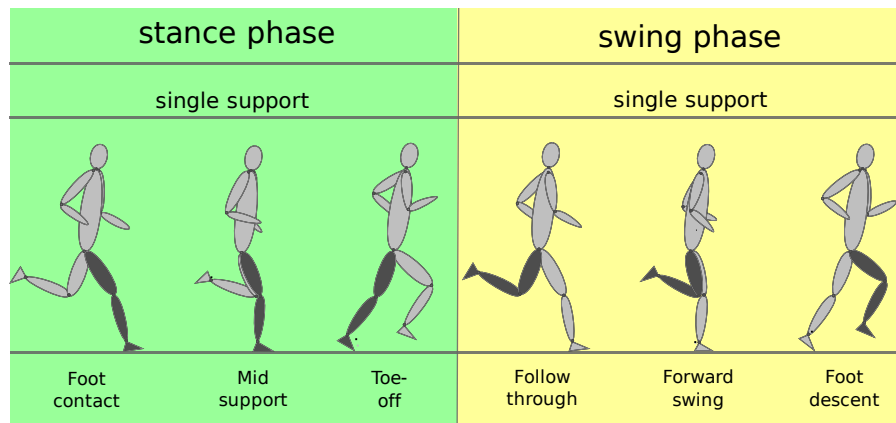


Figure 1.2: Phases (6-phases model) of one stride of human running adapted from Mann et al. (1986).

To investigate human walking and running, there are various gait analysis methods. The applied method depends on the research question and object. Common methods are the analysis of the kinematic and kinetic (or dynamic) data. Kinematics describes the bodies in motion without considering internal and external forces causing the body movement, i.e. the movement geometry. Thus, positions, orientations, angles, velocities, and accelerations of the body segments and joints are analyzed. Electrogoniometers, 2D cameras and 3D infrared camera systems can be used to measure kinematic data (Götz-Neumann, 2011; Marquardt, 2012). Kinetics studies the forces that cause the movements of the bodies. Here, ground reaction forces (GRFs) and joint movements are measured. If, in addition, anthropometric data of the subject are known, it is also possible to calculate net joint moments using inverse dynamics (Bonneyoy and Armand, 2015; Whittle, 1993). An extensively used kinetic measuring device is the ground reaction force measuring plate (Götz-Neumann, 2011). Furthermore, there are additional components that could be measured, as the pressure beneath the foot, the muscle activity via electromyography (EMG), and the energy consumption (Götz-Neumann, 2011; Whittle, 1993).

For this work, kinematic analysis by a 3D infrared camera system and kinetic analysis by ground reaction force measuring plates were used. Therefore, the measured variables will be mentioned below. The obtained kinematic data include the joint positions and orientations. Besides the GRFs, the kinetic analysis provides the center of pressure (CoP) of the feet. By using the GRFs, various variables can be calculated, as the contact time, the duty factor, the TD, TO and mid stance, and, in walking, the double support time. Additionally, there are variables that can be calculated by combining the kinematic and the kinetic data. The combined variables that are relevant for this work are presented in the following. The center of mass of the whole body (CoM) was determined with a body segment parameters method according to Plagenhoef et al. (1983). Typical curves of the variables GRFs, CoM, and the horizontal CoP relative to the CoM (CoP_{CoM}) for walking and running are illustrated in figure 1.3.

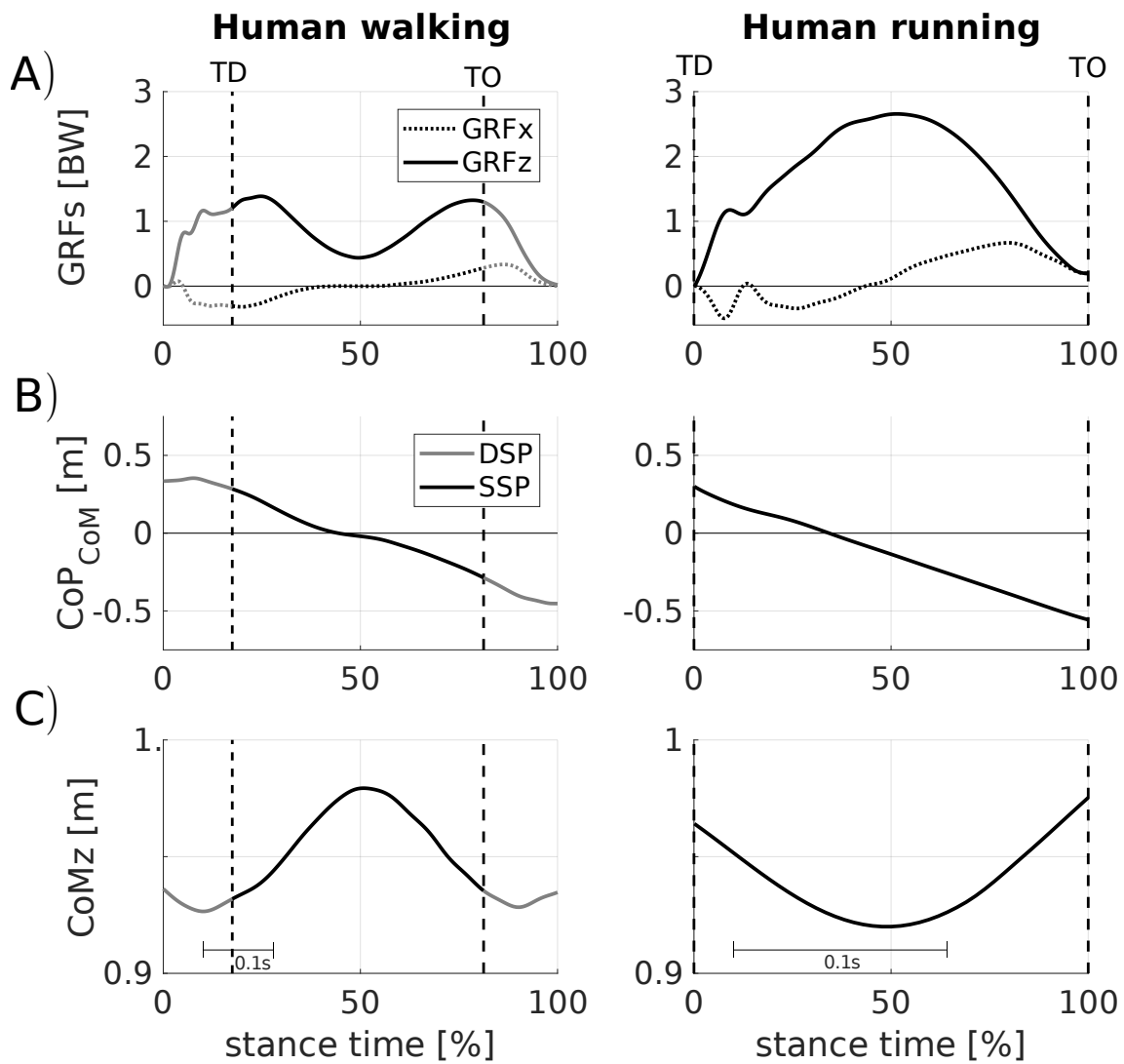


Figure 1.3: Exemplary gait parameters of human walking and running. A) Horizontal (x, dotted line) and vertical (z, solid line) ground reaction forces (GRFs) normalized to body weight (BW), B) horizontal center of pressure (CoP) relative to the center of mass (CoM) of the whole body (CoP_{CoM}), and C) vertical CoM position during the stance time of one leg are shown. For walking, the gray lines illustrate the double support phases (DSP) and the black lines the single support phase (SSP). The vertical, dashed lines indicate the touch down (TD) and the take-off (TO). The data come from two different female subjects, who match in the anthropometric data (walking/running: age: 25/21 years, height: 170/172 cm, and body mass: 68/69 kg; speed: 1.9/4.7 ms^{-1}). The walking curves are an example of the data published in Müller et al., 2012, the running curves are an example of the data published in Müller et al., 2014.

In order to compare GRFs during the braking and the propulsion intervals, it is reasonable to consider horizontal and vertical impulses \vec{p} as the integrals of the GRFs. The braking interval is defined from TD to zero-crossing of the horizontal GRFs and the propulsion interval from zero-crossing of the horizontal GRFs to TO, respectively. To compare the impulses between different subjects, they are normalized to each subject's body weight BW , the leg length l and the standard gravity g as denoted in equation 1.1 (Hof, 1996):

$$\vec{p}_{\text{normalized}} = \frac{\vec{p}}{BW \cdot \sqrt{l/g}}. \quad (1.1)$$

Another variable for describing the body movement while walking and running is the centroidal angular momentum of the whole body \vec{L}_{wb} . \vec{L}_{wb} can be calculated as the sum of individual segment angular momenta about the CoM with the following equation 1.2 (Herr and Popovic, 2008):

$$\vec{L}_{\text{wb}} = \sum_{i=1}^N \left[(\vec{r}_{\text{CoM}}^i - \vec{r}_{\text{CoM}}) \times m_i \cdot (\vec{v}^i - \vec{v}_{\text{CoM}}) + \vec{I}^i \vec{\omega}^i \right]. \quad (1.2)$$

In equation 1.2, $(\vec{r}_{\text{CoM}}^i - \vec{r}_{\text{CoM}})$ is the CoM position of the i -th segment relative to the whole body CoM position, m_i is the i -th segment's mass, and $(\vec{v}^i - \vec{v}_{\text{CoM}})$ is the velocity of the i -th segment relative to the whole body CoM velocity. Thus, this first term of the sum is the angular momentum due to the i -th segment's CoM movement. The second term is the angular momentum of the i -th segment around its CoM position. Here, \vec{I}^i is the i -th segment's inertia tensor with 3×3 dimensions and $\vec{\omega}^i$ the 3×1 dimensional angular velocity around the segment's CoM. To reduce the variance across subjects, \vec{L}_{wb} can be normalized to each subject's body mass, the vertical CoM position, and the mean gait speed across the trials (Herr and Popovic, 2008). From the non-normalized angular momentum the whole body angle γ_{wb} can be calculated as the integral of \vec{L}_{wb} . However, before these variables are taken up again in chapters 2-4, human walking and running under the influence of perturbations will be examined.

1.1.2 Perturbations

In everyday life, there are very rarely level, smooth surfaces for walking and running. Humans are more often exposed to uneven terrains which include compliant surfaces as sand and grass, slippery surfaces as puddles or ice, and uneven ground as rocks, curbs or cobbled sidewalks (Gates et al., 2012; Blair et al., 2018). Besides these extrinsic perturbations, there are also intrinsic perturbations. This could be a changed speed or an alternate posture, which occurs for example in various pathologies (Grasso et al., 2000; Saha et al., 2008; Hicks et al., 2008). For a better understanding of the human gait, it is helpful to study these perturbations in more detail.

Various methods have been used in the literature to reconstruct extrinsic perturbations on walking and running. Studies including stepping up and down curbs, drops and steps are very present (e.g. Barbieri et al., 2013; van Dieën et al., 2008; Hortobágyi and DeVita, 2000; Müller and Blickhan, 2010; Peng et al., 2016), even when the obstacle is camouflaged (e.g. van Dieën et al., 2007; van der Linden et al., 2009; Müller et al., 2012, 2014; Shinya et al., 2009). Furthermore, there are perturbations as bumps (Panizzolo

et al., 2017), protuberances (Thies et al., 2007) and irregular surfaces (Blair et al., 2018). In order to analyze intrinsic perturbations of walking, on the one hand, patients who have an altered posture due to pathological causes were examined (e.g. cerebral palsy, Hicks et al., 2008). On the other hand, healthy people were instructed to walk with a modified posture as, for example, knee-flexed, knee- and trunk-flexed (Grasso et al., 2000), and trunk-flexed (Saha et al., 2008). In those investigations, different walking speeds were examined as well, but there are also studies focussing primarily on the speed effect on gait parameters (e.g. Hak et al., 2012; Keller et al., 1996; Kirtley et al., 1985; Lu et al., 2017a).

The investigated biomechanical parameters, for instance GRFs, CoP, CoM, angular momentum, and muscle activity, are comprehensive for describing the perturbed gait. A crucial question, however, is how stability and robustness can be ensured in case of perturbation, since the aim is always not to fall. The given biomechanical parameters only provide insufficient information on stability. A universal stability and robustness criterion is required here. Therefore, it is advisable to take a look at models that describe human gait because they focus explicitly on stability.

1.2 Models describing human locomotion

To understand human locomotion, it is not invariably sufficient to merely observe and measure human individuals. The data should also be edited in a useful way. Especially for the development of legged robots, a detailed analysis of animal and human locomotion is necessary (Sharbafi et al., 2013b). Thus, simple, conceptual models called *templates* were established for legged locomotion (Full and Koditschek, 1999). These templates are as complex as necessary and as simple as possible to ensure a trade-off between describing processes accurately and both understanding and modeling general mechanisms. Practical experience in robotics shows that implementing templates or using them as a control mechanism leads to functioning robots (e.g. Raibert, 1986; Saranli et al., 2001; Poulakakis and Grizzle, 2007).

A template for human running and hopping is the spring-mass model (Blickhan, 1989; McMahon and Cheng, 1990). The model consists of a point-mass body at the CoM and a leg that is modeled by a massless spring, as illustrated in figure 1.4A. This template is called *Spring-Loaded Inverted Pendulum* (SLIP). As human running and walking were initially treated as different mechanical paradigms (Geyer et al., 2006), walking was also modeled as a point mass on an inverted pendulum, but with one massless stiff leg (Alexander, 1976; Mochon and McMahon, 1980), as illustrated in figure 1.4B. Later it was found that extending the SLIP by a second spring in the double support phase was more suitable to model walking. The template is called *Bipedal SLIP* (BSLIP) and is illustrated in figure 1.4C (Geyer et al., 2006).

The SLIP template was refined in several directions to model the human locomotion more accurately. There were extensions in the form of a swing leg control (Blum et al., 2007), a more realistic hip-motor torque (Seipel and Holmes, 2007), roller feet (Whittington and Thelen, 2009), and a compliant ankle joint (Maykranz et al., 2009), respectively.

A considerable change of the (B)SLIP template was the extension of the point mass to a rigid body to characterize the trunk (Sharbafi et al., 2013b; Poulakakis and Grizzle, 2007). The template exists with one spring for running and two springs for walking and is called *Trunk SLIP*³ (TSLIP, figure 1.4D). Only with a rigid trunk postural control can be addressed, as vertical body alignment plays a major role in stabilizing the human locomotion (Maus et al., 2010; Sharbafi and Seyfarth, 2015).

Geyer and Herr (2010) introduced a muscle-reflex model as a neuromuscular extension of the TSLIP template. This models human walking more precisely, but also leads to a remarkable increase in complexity (Geyer and Herr, 2010). Another extension of the TSLIP template to improve postural stability involves adjusting the hip torques so that the GRFs intersect at a point above the CoM. The point is named *Virtual Pivot Point* (VPP) and the template *Virtual Pendulum (VP) concept* or *VPP model* (Maus et al., 2010). The concept is based on observations in animals and humans and is illustrated in figure 1.4E (Maus et al., 2010). Although it was successfully implemented with a passive hip spring in the simulation of human locomotion (Rummel and Seyfarth, 2010; Sharbafi et al., 2013a; Maus et al., 2008; Sharbafi and Seyfarth, 2014), the model disregards the non-linear behavior of human hip torque-angle (Sharbafi and Seyfarth, 2015). Therefore, *Leg Force Modulated Compliant Hip* (FMCH) was introduced as a new neuromuscular template for postural control in walking (Sharbafi and Seyfarth, 2015). Further developments followed, for example the *neuromuscular FMCH (nmF) model* (Davoodi et al., 2019), which was more physiological, as well as models that make adaptations to show more stable and robust walking (Lee et al., 2017; Vu et al., 2017).

Since the new templates are based on the VPP model with more complex extensions, all of these models assume a VPP in human and humanlike locomotion. Thus, the VPP model and its implementation in simulation and robots will be presented in more detail in the next chapter. Additionally, the experimental situations in which a VPP could be observed in humans and animals will be discussed, including calculation and analysis of the VPP.

³Poulakakis and Grizzle (2007) called it ASLIP, for *Asymmetric SLIP*.

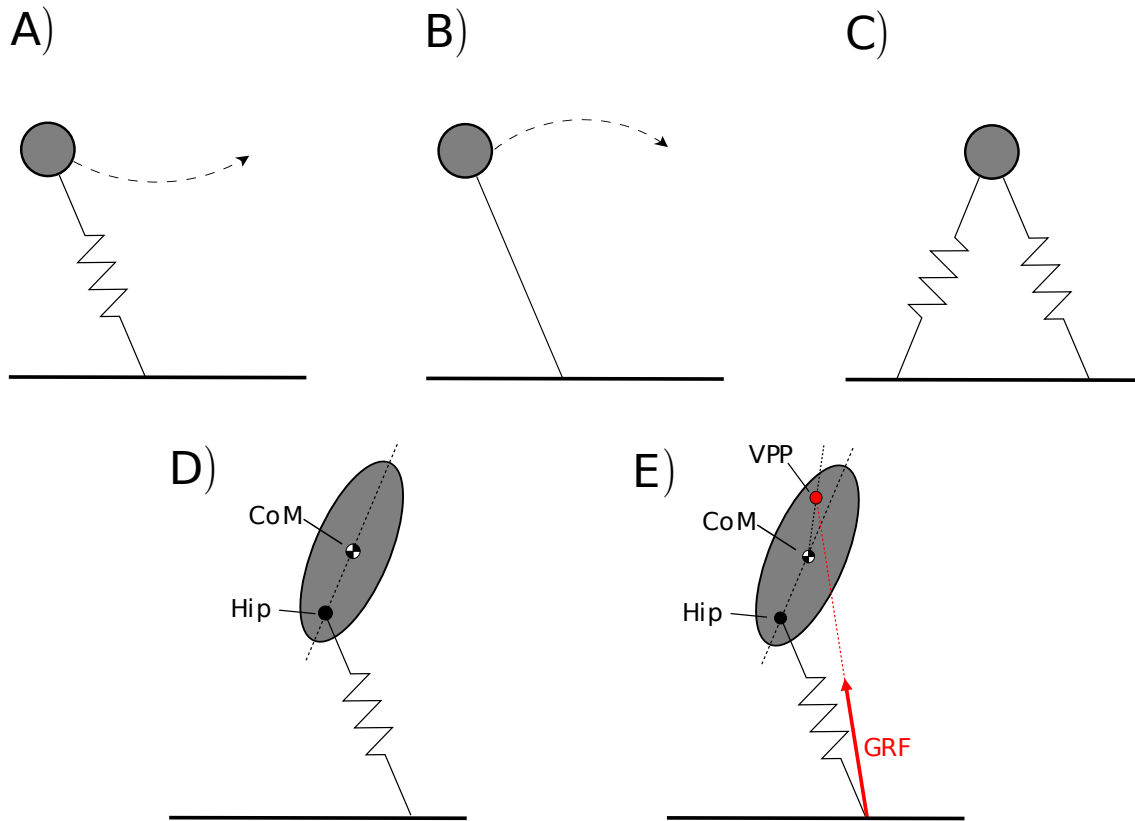


Figure 1.4: Schematic illustrations of human locomotion models. A) Spring-loaded inverted pendulum (SLIP), B) Inverted pendulum with stiff leg, C) Bipedal SLIP (BSLIP), D) Trunk SLIP (TSLIP), and E) virtual pivot point (VPP) model. CoM is the center of mass of the whole body and GRF is the ground reaction force vector. Note that TSLIP and VPP models also exist with two springs (legs). The figures are adapted from A, B: Geyer et al. (2006), C: Geyer and Herr (2010), and D, E: Sharbafi et al. (2013b).

1.3 VPP model

Unlike the quadrupedal gait, the upright bipedal gait has a smaller area of support and an elevated CoM, which poses a major challenge for the balance control system (Maus et al., 2010; Winter, 1995; Gruben and Boehm, 2012). For static scenarios or quasi-static locomotion (e.g. with wheels on a Segway), this behavior could be described by an inverted pendulum, which stands for an increased instability. However, human gaits such as walking and running are dynamic patterns of locomotion. That means that the CoP as point of application of the GRFs moves with respect to the CoM and thus, the stabilization mechanism does not depend on the instantaneous area of support. The behavior can be described by a regular physical pendulum which is suspended at a point above the CoM, the VPP. The system becomes more stable against perturbations than an inverted pendulum (Maus et al., 2010). Neural control and body mechanics provide stability by using the GRFs and torques stabilizing the trunk (Gruben and Boehm, 2012; Blickhan et al., 2015).

Before the VPP model is presented in more detail, the different terminology existing in the literature concerning the *Virtual Pivot Point* shall be introduced. The denotation *VPP* was established by Maus et al. (2008, 2010) for simulation and experiments and has been used by several authors (e.g. Andrada et al., 2014; Rummel and Seyfarth, 2010; Müller et al., 2017). Other denotations are for example *Divergent Point* (DP, Gruben and Boehm, 2012), or *Virtual Point* (VP, Drama and Badri-Spröwitz, 2019). In this work the name VPP will be used for the simulation of the model and for the experiments unless stated otherwise.

1.3.1 VPP in simulation and robotics

The BSLIP model explains the dynamics of the legs, but does not include trunk stabilization. However, since the human trunk is not a point mass, it was expanded to a rigid body (TSLIP model). For this purpose, a new control strategy was presented, namely the VP concept, which was introduced to stabilize biped robots (Maus et al., 2008). When implementing the VP concept in simulation, stable solutions for walking and running were found. Additionally, the model predicts hip torque patterns for walking that fit to corresponding data in human walking (Maus et al., 2008). Thereafter, the VPP model has been successfully used in other simulation studies, e.g. for human walking (Rummel and Seyfarth, 2010; Kenwright et al., 2011), running (Sharbafi and Seyfarth, 2014; Drama and Badri-Spröwitz, 2019), and hopping (Sharbafi et al., 2013a,b).

Nevertheless, the VP concept has hardly ever actually been implemented in robots. Worth mentioning are the robot ATRIAS (Peekema, 2015), the humanoid robot BioBiped (Seyfarth et al., 2012), and the exoskeleton LOPES II (Zhao et al., 2017), in which the VP concept was used. However, there have been some studies on humans and animals to investigate whether a VPP could be observed in experiments to analyze how well the model describes reality.

1.3.2 VPP in experiments

The VPP was observed in several experimental studies with humans and animals (Andrada et al., 2014; Gruben and Boehm, 2012; Maus et al., 2010; Müller et al., 2017). The first research was done to see whether the model was plausible and fitted human data (Maus et al., 2008, 2010). The study considered human walking and running on the treadmill. A VPP was reported for both gaits. Previously, Herr and Popovic (2008) had investigated how the angular momentum of the whole body is controlled in walking. However, this was done without focusing on VPP analyses, but rather on whether the GRFs intersect at the CoM. The findings are nevertheless worth mentioning, because they virtually represent a VPP at the CoM. Gruben and Boehm (2012) also observed a VPP in human walking on the treadmill. The analyses were made in different reference

frames, which are described in more detail in section 1.3.4. Figure 1.5A shows a typical walkway measurement setup and the variables belonging to the VPP. In figure 1.5B, a representative VPP plot of human walking is shown.

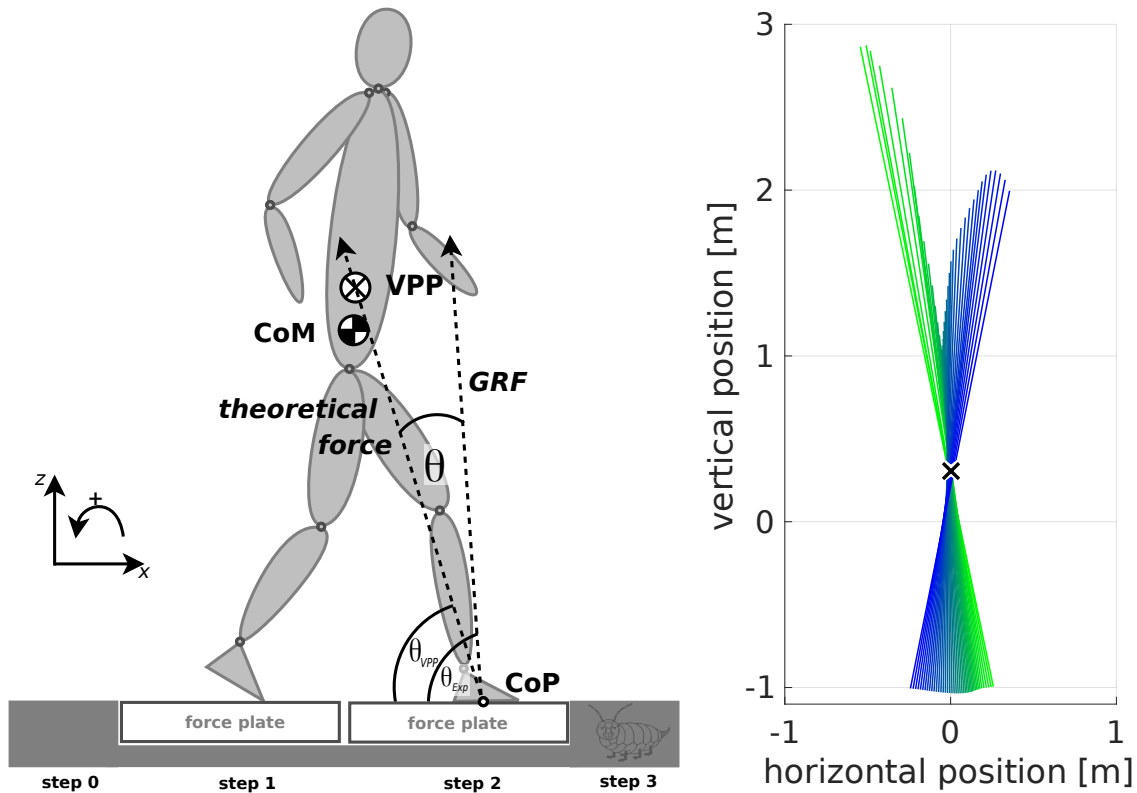


Figure 1.5: Virtual pivot point (VPP) in experiments. Left: Exemplary setup for human walking experiments and the VPP input variables (center of mass (CoM), ground reaction force (GRF) and center of pressure (CoP)) are shown. The theoretical force intersects the CoP and the calculated VPP. θ is the angle between the theoretical force vector and the measured GRF vector for each time frame. Right: Exemplary VPP plot of one subject for the single support phase of walking in a CoM-centered coordinate system. The GRF vectors start for each time of measurement (green to blue) at the CoP. The black cross indicates the calculated VPP.

The existence of a VPP was also been investigated in animals. Maus et al. (2010) examined running chickens and walking dogs. Both showed a VPP, but for the dogs the force vectors displayed a greater spread around that point than for humans or chickens. Andrada et al. (2014) considered quails during walking, running and grounded running. A VPP was observed in all gaits (Andrada et al., 2014). In the next section, the calculation of the VPP for humans and animals from the experimentally measured variables will be presented.

1.3.3 Calculation of the VPP

In the experiments, the calculation of the VPP in the sagittal plane is similar in all known studies (Andrada et al., 2014; Gruben and Boehm, 2012; Maus et al., 2010; Müller et al., 2017). It is calculated as the point where the sum (or mean) of the squared perpendicular distances between force vectors and the point is minimal (figure 1.6). In doing so, the force vectors start in the CoP in a CoM-centered coordinate system.

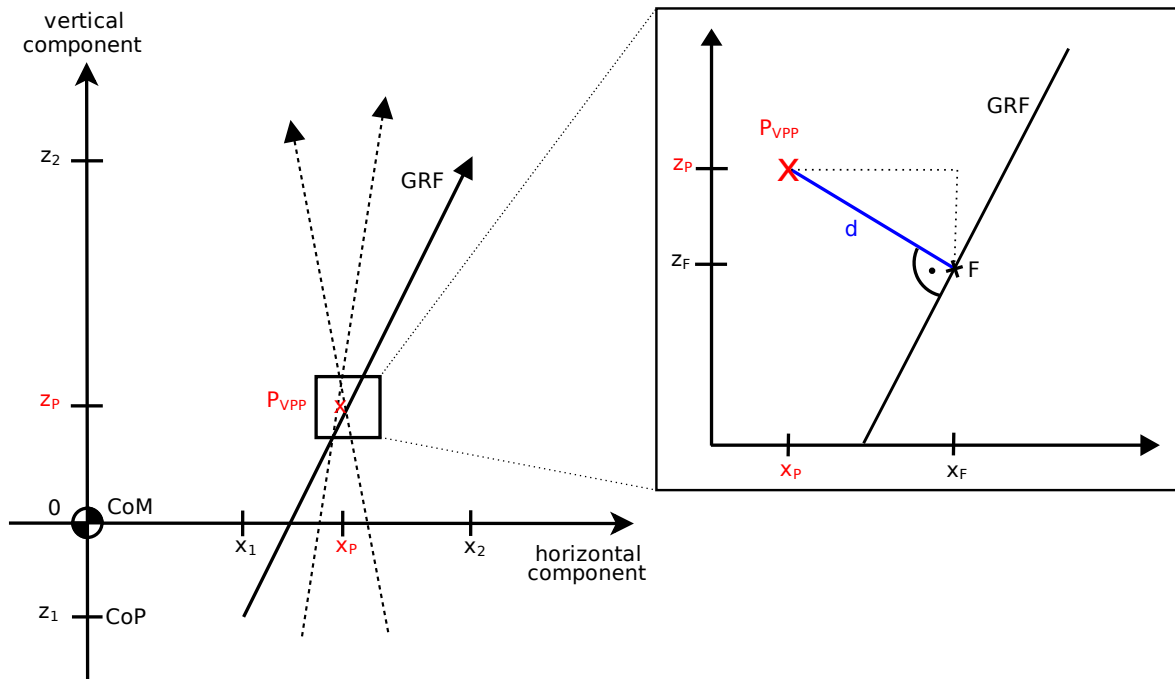


Figure 1.6: Virtual pivot point (VPP) calculation for three points in time of measurement. CoM is the center of mass of the whole body. The ground reaction force (GRF) vector starts at the center of pressure (CoP) relative to the CoM at every point in time. The dashed lines represent the GRF vectors of different instants of measurement with different CoPs relative to the CoM. $x_{1/2}$ and $z_{1/2}$ denote the horizontal and vertical starting/terminal point of GRF. F is the point on the vector GRF where the distance d to P_{VPP} is minimal. P_{VPP} could be every point in the plane with the condition that the mean of d of all instants of measurement is minimal.

For calculation of the VPP, first one GRF vector starting at the CoP in a CoM-centered coordinate system in the sagittal plane is considered. In this coordinate system x is the horizontal component in walking direction and z the vertical component of the vector. Considering that, the following variables are defined,

$$\begin{aligned}
 x_1 &= x_{\text{CoP}} - x_{\text{CoM}}, \\
 x_2 &= x_{\text{CoP}} - x_{\text{CoM}} + x_{\text{GRF}}, \\
 z_1 &= z_{\text{CoP}} - z_{\text{CoM}}, \\
 z_2 &= z_{\text{CoP}} - z_{\text{CoM}} + z_{\text{GRF}}, \\
 \vec{u} &= \begin{pmatrix} x_1 - x_2 \\ z_1 - z_2 \end{pmatrix}, \\
 \vec{f} &= \begin{pmatrix} x_2 \\ z_2 \end{pmatrix} + \lambda \vec{u}, \quad \lambda \in \mathbb{R}, \\
 P_{\text{VPP}} &= \begin{pmatrix} x_{\text{P}} \\ z_{\text{P}} \end{pmatrix}.
 \end{aligned} \tag{1.3}$$

Then, the perpendicular distance d from the vector \vec{f} to the target variable P_{VPP} is calculated. Note that GRF and \vec{f} point in the same direction. In addition, they have the same magnitude if $\lambda=1$. As the scalar product of the connection vector and the direction vector \vec{u} by definition is zero, for a given P_{VPP} follows

$$\begin{aligned}
 (\vec{f} - P_{\text{VPP}}) \cdot \vec{u} &= 0 \\
 \Leftrightarrow \left(\begin{pmatrix} x_2 - x_{\text{P}} \\ z_2 - z_{\text{P}} \end{pmatrix} + \lambda \begin{pmatrix} x_1 - x_2 \\ z_1 - z_2 \end{pmatrix} \right) \begin{pmatrix} x_1 - x_2 \\ z_1 - z_2 \end{pmatrix} &= 0 \\
 \Leftrightarrow \begin{pmatrix} x_2 - x_{\text{P}} \\ z_2 - z_{\text{P}} \end{pmatrix} \begin{pmatrix} x_1 - x_2 \\ z_1 - z_2 \end{pmatrix} + \lambda \begin{pmatrix} x_1 - x_2 \\ z_1 - z_2 \end{pmatrix} \begin{pmatrix} x_1 - x_2 \\ z_1 - z_2 \end{pmatrix} &= 0 \\
 \Leftrightarrow (x_2 - x_{\text{P}})(x_1 - x_2) + (z_2 - z_{\text{P}})(z_1 - z_2) + \lambda((x_1 - x_2)^2 + (z_1 - z_2)^2) &= 0 \\
 \Leftrightarrow - \frac{(x_2 - x_{\text{P}})(x_1 - x_2) + (z_2 - z_{\text{P}})(z_1 - z_2)}{(x_1 - x_2)^2 + (z_1 - z_2)^2} &= \lambda.
 \end{aligned}$$

Using this relationship for λ , F is the point on \vec{f} where the distance d to P_{VPP} is minimal,

$$x_F = x_2 + \lambda(x_1 - x_2), \quad z_F = z_2 + \lambda(z_1 - z_2). \tag{1.4}$$

Then, the distance d can be calculated with the Pythagorean theorem,

$$d = \sqrt{(x_{\text{P}} - x_F)^2 + (z_{\text{P}} - z_F)^2} \tag{1.5}$$

This calculation is implemented for every time of measurement. Afterwards, the mean of all values d is minimized to get the optimal P_{VPP} . Here, the Matlab function *fminuc* was used for minimizing the mean of d with the starting point $P_{VPP} = \begin{pmatrix} 0 \\ 0.2 \end{pmatrix}$. Thus, both the position of the VPP and the mean distances d of the force vectors to the VPP are derived.

Differences between the studies appear in the number and range of the involved force vectors and the chosen reference frame. Furthermore, d is included in the evaluation in different ways. These aspects are examined in more detail in the following section.

1.3.4 Differences in the VPP analysis

There are differences in the time segment of one stride considered for the VPP calculation. Since in the VPP model force vectors are adjusted to always point to the VPP at a fixed position, the VPP is naturally at the same position for the whole stride. It is not clear, however, whether this is the case in the human experiments. Maus et al. (2010) reported a VPP for the stance phase of one leg and found that “if the impact force around touchdown [...] is omitted, a very clear intersection point would occur” (Maus et al., 2010, p. 4). Andrada et al. (2014) and Müller et al. (2017) investigated 10% to 90% of the stance phase of one leg. This cut-off was most likely used to examine only the single support phase and to avoid the spread of the force vectors due to the impact peak. Gruben and Boehm (2012) analyzed the single support phase of each leg “to avoid the static indeterminacy which can alter F [ground reaction force] direction during double leg support” (Gruben and Boehm, 2012, p. 653).

The reference frame chosen to calculate the VPP is also relevant for the VPP position. It can be aligned to the environment or body aligned and can have different origins. Advantages and disadvantages of the different reference frames are presented by Gruben and Boehm (2012). Both the VPP model and the experimental analyses in the literature used a coordinate system, where the vertical axis is parallel to gravity and the origin is at the CoM (Andrada et al., 2014; Gruben and Boehm, 2012; Maus et al., 2010; Maus, 2008; Müller et al., 2017). Additionally, Gruben and Boehm (2012) compared four different reference frames: vertically aligned coordinate systems with the origin at the CoM and the hip, respectively; furthermore, a body aligned system with the origin at the CoM and a trunk aligned system with the origin at the hip. They found that all reference frames are well suited to predict the directions of the forces with the VPP model. Nevertheless, the second and third of the reference frames provided significantly better predictions than the other two (Gruben and Boehm, 2012).

Another aspect concerns the differences in the assessment of the VPP spread. This obviously appears only in the experimental analyses. Maus et al. (2010) and Andrada et al.

(2014) did not evaluate the spread of the VPP with a specific variable. Müller et al. (2017) used the minimized mean of the distance d (equation 1.5) and named it VPP_RMSD (root mean squared distance). Gruben and Boehm (2012) used a coefficient of determination (R^2) to quantify the model's ability to describe the observed force direction, especially for each reference frame. To analyze whether a VPP is obtained and to compare how spread out that VPP is under different experimental setups, it is necessary to quantify it. Since this issue, as provided above, has hardly been considered in studies so far, the following chapter will take a closer look at this methodological part. Furthermore, other methodic aspects will be mentioned, which, in the interest of greater consistency, should receive more attention than before in the literature.

1.4 Methodic aspects

1.4.1 Considered part of the stride

It seems that the authors cited above wanted to calculate the VPP for the single support phase. Considering this, they used different methodical approaches. The method of cutting off the impact peak (Maus et al., 2010) is probably slightly imprecise as there are no clear boundaries and therefore it is difficult to generalize. Furthermore, in a strict sense, the end of the stance phase would also have to be cut off in order to investigate only the single support phase.

Another observed method is to use 10% to 90% of the whole stance phase to cut off the double support phase (Andrada et al., 2014; Müller et al., 2017). This alternative was presumably introduced because only two force plates were available for measurement (Andrada et al., 2013). Hence, it is not possible to calculate the exact single support phase of both force plates by using only the kinetic data. For this purpose, each force plate would need two additional force plates surrounding it. However, if there exist prominent features in the kinematic data⁴, the exact single support phase could be calculated without the necessity of additional force plates. For example, in human walking a characteristic apex in the speed curve of the malleolus lateralis could be used for this issue (O'Connor et al., 2007). If the percentage cut-off method is used nevertheless, one disadvantage is that only an estimate of the single support phase can be obtained. On the other hand, this method has the advantage that the ratio of single and double support does not matter. This issue is important for the comparison between different setups. To make the VPP comparable between setups, the time segment of GRFs used for analysis should not vary too much and the distorting impact peaks mentioned by Maus et al. (2010) should be excluded. Due to this desired comparability, the cut-off method was also chosen by Müller et al.

⁴This depends presumably on the type of locomotion (e.g. walking, running, hopping) and the studied species (e.g. human, avian, quadruped).

(2017).

If only level walking without various setups is examined, it is advisable to consider the exact single support phase, as Gruben and Boehm (2012), without specifying the concrete procedure, did. For human running, the missing double support phase makes it simple and obvious to evaluate the exact single support phase as the whole stance phase.

1.4.2 Blur size of the VPP

For assessing the spread of the vectors around the VPP, it is suitable to use a quantity for better comparison. Here, it is appropriate to use the minimized mean of the distance d , which was needed to calculate the VPP. This method was used by Müller et al. (2017), the variable is called VPP_RMSD. It enables a quantitative comparison between the setups of the study. However, this approach has the disadvantage that the variable VPP_RMSD has a non-normalized unit (millimeter) and is therefore not comparable between studies with different premises (e.g. varying mean heights of subjects or the comparison of humans and birds). Thus, a normalized variable is preferable, as the coefficient of determination R^2 used by Gruben and Boehm (2012). Unfortunately, Gruben and Boehm (2012) did not explain the calculation of R^2 . However, it is likely to be based on the study of Herr and Popovic (2008).

Herr and Popovic (2008) investigated particularly the angular momentum in human walking with the assumption that the GRFs are regulated to point to the CoM⁵. The coefficient of determination R^2 was used to quantitatively evaluate this assumption (Herr and Popovic, 2008),

$$R^2 = 1 - \frac{\sum_{i=1}^{N_{\text{Trial}}} \sum_{j=1}^{N_{\text{Percent}}} \left(F_{\text{Exp}}^{ij} - F_{\text{Mod}}^{ij} \right)^2}{\sum_{i=1}^{N_{\text{Trial}}} \sum_{j=1}^{N_{\text{Percent}}} \left(F_{\text{Exp}}^{ij} - \bar{F}_{\text{Exp}} \right)^2} \quad (1.6)$$

with at least one pair of i, j , so that $F_{\text{Exp}}^{ij} \neq \bar{F}_{\text{Exp}}$.

Here, F_{Exp}^{ij} are the experimentally measured horizontal forces. The forces F_{Mod}^{ij} of the model-predicted data are those horizontal forces which point to the calculated target variable (e.g. CoM or VPP) for each measurement time. For each subject, the R^2 value was calculated by summing over all trials (N_{Trial}) and gait percentage times analyzed (N_{Percent}). The experimental mean \bar{F}_{Exp} is the grand mean over all trials and gait percentage times analyzed.

The fraction in equation 1.6 becomes minimal when $F_{\text{Exp}}^{ij} = F_{\text{Mod}}^{ij}$ for each i, j . Then, it has zero value and therefore R^2 equals 1. This means that if there is a perfect fit between the model forces and the experimentally measured forces, R^2 reaches its maximum of 1. The

⁵This can be interpreted as the VPP coinciding with the CoM.

fraction can theoretically become infinitely large, meaning, there is no lower bound for R^2 . However, already for a zero R^2 the numerator equals the denominator and therefore the model's estimate would be worse than using the mean experimental value as an estimate. A minor weakness in calculating R^2 using forces is that the magnitude of the forces is included in the calculation. If, for example, the magnitude of the GRFs is significantly larger before than after mid stance, the whole body would rotate around its own axis. This means that, in addition to the direction, the magnitude of the GRFs is also decisive for the stabilization of the whole body. However, the magnitude is not considered in the VPP calculation, where only body angles are determining. Therefore, R^2 should also exclude the magnitude of the forces and rather consider the angles between the forces instead of the forces themselves. Thus, R^2 is calculated as follows:

$$R^2 = \left(1 - \frac{\sum_{i=1}^{N_{\text{Trial}}} \sum_{j=1}^{N_{\text{Percent}}} \left(\theta_{\text{Exp}}^{ij} - \theta_{\text{VPP}}^{ij} \right)^2}{\sum_{i=1}^{N_{\text{Trial}}} \sum_{j=1}^{N_{\text{Percent}}} \left(\theta_{\text{Exp}}^{ij} - \bar{\theta}_{\text{Exp}} \right)^2} \right) \times 100\% \quad (1.7)$$

with at least one pair of i, j , so that $\theta_{\text{Exp}}^{ij} \neq \bar{\theta}_{\text{Exp}}$.

θ_{Exp}^{ij} are the angles between the GRFs and the floor and θ_{VPP}^{ij} are the angles between the theoretical forces and the floor which point to the calculated target variable for each trial and measurement time, as illustrated in figure 1.5A. The mean experimental angle $\bar{\theta}_{\text{Exp}}$ is the grand mean over all trials and measurement times. Note, that the value of R^2 is converted to percentage for presentation purposes and that its maximum is 100%.

Another small change to the formula seems advisable and concerns the considered measurement times. When normalizing the measurement time N_{Percent} to 100% as done in equation 1.6 and 1.7, it seems to neglect the aspect of occasionally clearly varying time windows. This occurs, for example, when comparing different time segments of a contact (the double support phase is about four times shorter than the single support phase). Therefore, it is recommended to rename the variable N_{Percent} as N_{Time} and to choose both N_{Time} and the associated time steps in, for example, milliseconds for a measurement frequency of 1 kHz.

1.4.3 Further aspects

There are a few more methodic aspects that have been treated differently in the studies. Probably most of the differences are small and therefore not conspicuous, but nevertheless affect the results. However, one obvious fact is the choice of surface. While some studies investigated the gait on an overground walking track (Andrada et al., 2014; Herr and Popovic, 2008; Müller et al., 2017), others used a treadmill (Maus et al., 2010; Maus,

2013; Gruben and Boehm, 2012). Differences in the gait parameters can be observed here (e.g. Lu et al., 2017b; Nigg et al., 1995; Sinclair et al., 2013; White et al., 1998) and should be considered in their assessment and discussion. The chosen method to calculate the CoM affects the results as well (e.g. sacral marker method, body segment method, and the method of double integration of the GRFs, for details see Gard et al., 2004). A similarity between all the studies mentioned above is the investigation of the VPP in the sagittal plane. Another aspect could be the analysis of the VPP in the frontal plane, as introduced by Firouzi et al. (2019) for human walking.

1.5 Preparatory work

As own preparatory work for this thesis, walking with intrinsic perturbation was investigated (Müller et al., 2017). This study, where the subjects walked with altered trunk orientations, analyzed whether a VPP could be observed even in the perturbed cases. The change of the trunk orientation was chosen because the trunk makes up a large proportion of the total body weight (Winter, 2009) and thus has a major impact on the posture. Additionally, in the VPP model, the whole body mass is concentrated in the trunk (Maus et al., 2008). It was presumed that because of the changed posture the position of the VPP is also shifted. The examined trunk inclinations (TI) were upright ($7.4 \pm 3.1^\circ$), TI25 ($31.9 \pm 5.4^\circ$), TI50 ($47.1 \pm 5.4^\circ$), and TI_{max} ($72.5 \pm 8.1^\circ$). For all trunk orientations, a VPP above the CoM could be observed, albeit without significant differences in height between the setups. However, the blur size of the VPP increased for larger trunk inclinations.

These findings suggest that the VPP concept is used for the investigated perturbations. This introduced the question for the present work whether the VPP mechanism is also used in other situations that differ from normal walking.

1.6 Dissertation outline

The previous chapters, in particular section 1.1.2, have shown that perturbations can affect the stability of human gait and, in the worst case, can lead to falls and injuries. Therefore it is of scientific interest to analyze how the perturbations influence the gait stability and its robustness. For this purpose, the VPP should be further examined, because if in case of a perturbation a VPP cannot be observed, then obviously another mechanism is used at the expense of energy or stability. Since the VPP has been well studied for experiments of human level walking (e.g. Gruben and Boehm, 2012; Maus et al., 2010), and in the preparatory work also for intrinsic perturbations (Müller et al., 2017), extrinsic perturbations on walking should be investigated.

Hypothesis 1 assumes that extrinsic perturbations affect both the position and the blur size

of the VPP, whereby the blur size will probably increase, possibly even up to the point where the VPP cannot be observed anymore.

In **Chapter 2**, extrinsic perturbations will be considered, more precisely walking down visible and invisible (camouflaged) curbs. Here, in addition to the wide variety of studies concerning balance while stepping down curbs and drops (e.g. van Dieën et al., 2007; Müller et al., 2014), this should be investigated with regard to the VPP. While the position and blur size of the VPP may be preserved when descending a visible curb, changes at least in the blur size of the VPP will certainly occur if the curb is camouflaged and thus not visible.

Hypothesis 2 supposes that no VPP will be observed in the double support phase of human walking.

While in the known literature only the single support phase of human walking was considered or the support phases were not explicitly separated, **Chapter 3** explicitly examines the double support phase with regard to the VPP. In the VPP model, there is no separation between single and double support, the VPP is the whole time at the same position. Since human locomotion is more complex than the model, the support phases have different purposes and thus, maybe different VPP positions. While in the single support phase the pendulum mechanism is used to maintain the stability, in the double support phase the CoM has to be shifted forward in a short time period with less demands on stability.

Hypothesis 3 assumes that a VPP (above the CoM) can also be observed in running.

As mentioned above, the VPP has been well studied for walking, whereas it has hardly been examined for human running. **Chapter 4** will take a look at the VPP model in human running simulations and the VPP in human running experiments. Even if this aspect is very rare in the literature (only shortly mentioned in Blickhan et al., 2015), a VPP (above the CoM) is suggested there.

Taken as a whole, the VPP can provide an indication of gait stability and its maintenance, together with general robustness of the system in all situations examined. Hence, in **Chapter 5** the separate findings of this work will be summarized and analyzed collectively. Additionally, conclusions, limitations and further considerations will be given.

2 Article I: Ground reaction forces intersect above the center of mass even when walking down visible and camouflaged curbs

	Contributor
Conceptualization	R.M.
Methodology	J.V.; E.G.; R.M.
Software	J.V.; E.G.; R.M.
Validation	J.V.; E.G.; R.M.
Formal analysis	J.V.; E.G.
Investigation	J.V.; E.G.; R.M.
Data curation	J.V.; E.G.
Writing - original draft	J.V.
Writing - review & editing	J.V.; E.G.; R.M.
Visualization	J.V.; E.G.
Supervision	R.M.
Project administration	R.M.
Funding acquisition	R.M.

<https://doi.org/10.1242/jeb.204305>

RESEARCH ARTICLE

Ground reaction forces intersect above the center of mass even when walking down visible and camouflaged curbs

Johanna Vielemeyer^{1,2,*}, Eric Griebach² and Roy Müller^{1,2}

ABSTRACT

A main objective in bipedal walking is controlling the whole body to stay upright. One strategy that promotes this objective is to direct the ground reaction forces (GRFs) to a point above the center of mass (COM). In humans, such force patterns can be observed for unperturbed walking, but it is not known whether the same strategy is used for a walkway that changes in height. In this study, 11 volunteers stepped down off a visible (0, 10 and 20 cm) and a camouflaged (0 or 10 cm) curb while walking at two different speeds (1.2 ± 0.1 and 1.7 ± 0.1 m s⁻¹). The results showed that in all conditions the GRFs pointed predominantly above the COM. Vectors directed from the center of pressure (COP) to the intersection point (IP) closely fitted the measured GRF direction not only in visible conditions ($R^2 > 97.5\%$) but also in camouflaged curb negotiation ($R^2 > 89.8\%$). Additional analysis of variables included in the calculation of the IP location showed considerable differences for the camouflaged curb negotiation: compared with level walking, the COP shifted posterior relative to the COM and the vertical GRFs were higher in the beginning and lower in later parts of the stance phase of the perturbed contact. The results suggest that IP behavior can be observed for both visible and camouflaged curb negotiation. For further regulation of the whole-body angle, the asymmetrical vertical GRFs could counteract the effect of a posterior shifted step.

KEY WORDS: Angular momentum, Bipedal gait, Perturbation, Stability, Uneven ground, Virtual pivot point

INTRODUCTION

Walking is widely present in human everyday life, but it is nonetheless a complex task for the neural and mechanical systems (Capaday, 2002; Gruben and Boehm, 2012a; Nielsen, 2003; Winter, 1995, 2009). Maintaining an upright position and thus controlling the whole-body angle is challenging. Hence, the angular momentum of the whole body seems to be highly controlled when walking (Herr and Popovic, 2008). If the regulation of the upright position is perturbed, e.g. by stumbling over obstacles (Pijnappels et al., 2004) or stepping down unexpected (van Dieën et al., 2007) or camouflaged (Müller et al., 2014) changes in ground level, it may lead to falls or fall-related injuries, particularly in the elderly (e.g. Berg et al., 1997; Menz et al., 2003; Pijnappels et al., 2005). Therefore, the use of a model or the analysis of specific target variables to describe walking characteristics can be important tools to understand the mechanism of stability (e.g. Alexander, 1995; Roos and Dingwell, 2013).

A mechanical strategy to stabilize the body while walking is to direct the forces to a point above the center of mass of the whole body (COM). Based on this, in the virtual pivot concept the body is conceived like a pendulum with a single rigid mass representing the trunk along with massless legs (Maus et al., 2010). In this model, a trunk-fixed virtual pivot point (VPP) is the target variable controlling the direction of the ground reaction forces (GRFs). However, the fluctuations of the model's trunk pitch angle were 180 deg out of phase with the upper body angle of humans (Gruben and Boehm, 2012a; Müller et al., 2017). A physical model with the appropriate phase relationship between GRF behavior and whole-body motion is a rocking rigid block. However, that model would predict an intersection point (IP) with a fixed height (Gruben and Boehm, 2012a). The general idea for the stabilizing effect is that across time the GRFs can provide a torque around the lateral axis in the upright direction (Lee et al., 2017).

In human walking, a stabilizing strategy based on neural control seems to generate such an IP of GRFs. This point has been examined in various studies, at least in the sagittal plane, but named differently [e.g. VPP in Maus et al. (2010) or divergent point (DP) in Gruben and Boehm (2012a)]. The studies showed that such a point seems to be important for controlling upright walking, because different environmental situations and perturbations during walking can be compensated for to some degree (Gruben and Boehm, 2012a; Maus et al., 2008, 2010). However, the vertical position of the IP seems to show a high variance between and within the studies, possibly related to the different walking speeds used (Müller et al., 2017).

In addition to speed, other factors may affect the position of the IP. In this context, Müller et al. (2017) studied walking with altered trunk orientations (see also Aminiaghdam et al., 2017). For this internal (body-related), geometrical perturbation, the data still suggest that the GRFs intersect near a point above the COM, although with greater spread of the force vectors around this point than in upright walking. In addition to internal perturbations, external (environment-related) perturbations such as ground level changes (e.g. gaps in the ground, curbs or stairs) may also cause alterations in the gait pattern. These alterations have been biomechanically well studied (e.g. van Dieën et al., 2008; Müller et al., 2014; Peng et al., 2016; Reeves et al., 2008; Silverman et al., 2014), but not with a focus on an IP. That consideration is worthwhile, notably because the simulation of the VPP showed a stabilizing effect only for a small perturbation such as a 5 mm curb (Maus et al., 2010).

Furthermore, unexpected level changes while walking, e.g. when a curb is not noticed, often lead to falls (Berg et al., 1997). Possibly as a result of a lack of anticipative adaptations, such perturbation may place high demands on the regulation of linear momentum and angular momentum in order to avoid falling (Buckley et al., 2008). For example, van Dieën et al. (2007) observed that the sum over time of the angular momenta of the whole body during a stride while stepping down off a camouflaged curb is smaller than for level

¹Klinikum Bayreuth GmbH, 95445 Bayreuth, Germany. ²Friedrich-Schiller-University Jena, 07737 Jena, Germany.

*Author for correspondence (johanna.vielemeyer@uni-jena.de)

 J.V., 0000-0003-1282-3576; R.M., 0000-0002-4688-1515

List of symbols and abbreviations

bw	body weight
C10	camouflaged curb of 10 cm
COM	center of mass of the whole body
COM _z	vertical COP-centered COM position
COP	center of pressure
COP _{10,x}	horizontal COM-centered COP position at 10% of the stance phase
COP _{90,x}	horizontal COM-centered COP position at 90% of the stance phase
DP	divergent point
<i>g</i>	standard gravity
GRFs	ground reaction forces
IP	intersection point
IP _x	horizontal IP position
IP _z	vertical IP position
<i>l</i>	distance between lateral malleolus and trochanter major of the leading leg
<i>L</i> _{wb}	angular momentum of the whole body
<i>N</i> _%	number of gait percentage times analyzed
<i>N</i> _{trial}	number of trials
$\bar{p}_{\text{brake},x}$	horizontal braking impulse
$\bar{p}_{\text{brake},z}$	vertical braking impulse
$\bar{p}_{\text{normalized}}$	normalized impulse
$\bar{p}_{\text{prop},x}$	horizontal propulsion impulse
$\bar{p}_{\text{prop},z}$	vertical propulsion impulse
<i>R</i> ²	coefficient of determination
TD	touchdown
<i>t</i> _{double}	double stance time
TO	take-off
V0	visible curb of 0 cm
V10	visible curb of 10 cm
V20	visible curb of 20 cm
VPP	virtual pivot point
γ_{wb}	whole-body angle
$\gamma_{\text{wb},10}$	whole-body angle at 10% of the stance phase
$\gamma_{\text{wb},90}$	whole-body angle at 90% of the stance phase
θ	angle between the model forces and the GRFs
θ_{Exp}	angle of the experimentally measured GRFs in the sagittal plane
$\bar{\theta}_{\text{Exp}}$	mean experimental angle of GRFs
θ_{Mod}	angle of the model forces

walking, thus resulting in a more clockwise rotation of the body. Not falling means that there is a strategy to keep the balance and that kinetic and kinematic adjustments are made (Müller et al., 2014). Nevertheless, stepping down off a curb has not been investigated in the context of whole-body angle or IP regulation. The IP control is a supportive strategy, but neither necessary nor sufficient to stay upright; hence, there could be other strategies (Gruben and Boehm, 2012a).

Based on these considerations, it is possible that during camouflaged curb negotiation the stabilizing IP control is lost and the GRFs do not intersect near a point anymore or the IP is not found above the COM. However, we hypothesize that both for visible and camouflaged curb negotiation, the GRFs intersect above the COM. Additionally, we assume that the deviation of the measured GRF lines of action from the calculated IP is larger in the camouflaged than in the visible walking conditions.

MATERIALS AND METHODS**Subjects**

Eleven volunteers (3 female, 8 male; mean±s.d., age: 25.8±4.8 years, mass: 68.3±8.1 kg, height: 178.9±9.4 cm) took part in this experiment. Because of missing data regarding the COM, which

is necessary for the IP calculation, only 10 of the 11 subjects were considered in the evaluation. All of them were physically active and had no known restrictions which could have affected their performance or behavior in the study. Prior to participation, an informed consent form was signed by each subject. The experiment was approved by the local ethics committee (University of Jena, 3532-08/12) and conducted in accordance with the Declaration of Helsinki.

Measurements

The subjects were asked to walk along an 8 m walkway with two consecutive force plates in its center (Fig. 1). They were instructed to reach the first force plate with the left foot (trailing leg) and the second force plate with the right foot (leading leg) while walking with two different constant speeds: slow ($1.2\pm 0.1 \text{ m s}^{-1}$) and fast ($1.7\pm 0.1 \text{ m s}^{-1}$), as controlled by an examiner. To comply with the requirements, several practice trials took place before beginning the experiment. The force plate of the first contact (9281B, Kistler, Winterthur, Switzerland) was fixed at ground level for the first part of the walkway. The force plate of the second contact (9287BA, Kistler) was adjustable in height, as was the subsequent part of the walkway. The GRFs of both force plates were sampled at 960 Hz.

First, the subjects had to walk over three visible settings: for one, the track was even (V0, visible level); for the other two, the force plate on the second contact and the subsequent walkway were both lowered by either 10 cm (V10, visible curb of 10 cm) or 20 cm (V20, visible curb of 20 cm). The order of the settings was block randomized as well as the order of the walking speed for each

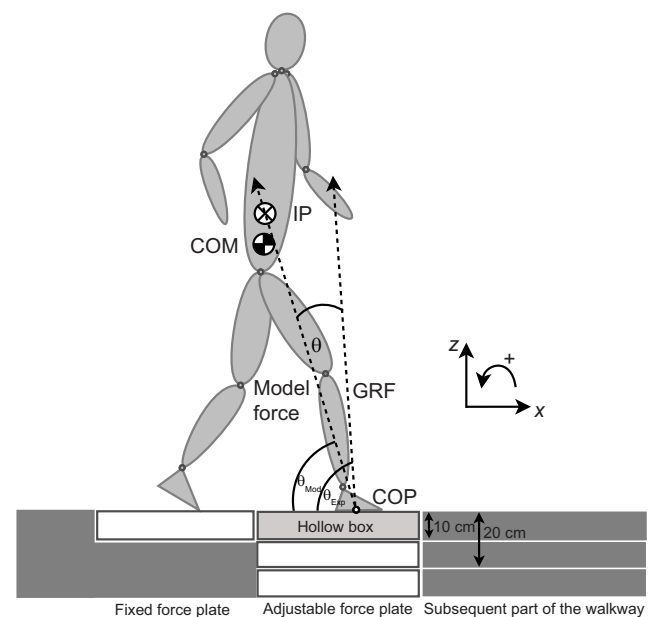


Fig. 1. Side view of the walkway. In the visible conditions, the second force plate (adjustable) and the subsequent walkway were set at elevations of 0 cm (V0, visible level), -10 cm (V10, visible curb of 10 cm) and -20 cm (V20, visible curb of 20 cm) relative to the first force plate (fixed). For the camouflaged curb negotiation, a 10 cm high block was randomly either present or absent on the adjustable force plate (10 cm below the fixed force plate). The block was camouflaged with a hollow box covered with an opaque sheet of paper (light gray rectangle). Here, the subsequent walkway was always set at an elevation of -10 cm. The model force goes through the center of pressure (COP) and the calculated intersection point (IP). The angle θ is between the model force vector and the measured ground reaction force (GRF) vector for each time frame ($\theta = \theta_{\text{Exp}} - \theta_{\text{Mod}}$). COM is the center of mass of the whole body.

setting. In each visible condition, the subjects had to accomplish eight trials. Thereafter, for the camouflaged setting, the basic setup was the same as for the V10 condition but a wooden block with a height of 10 cm was randomly either present or absent on the force plate of the second contact; the top surface was camouflaged with an opaque sheet of paper, so that the subjects did not know whether they were stepping down 10 cm (C10, camouflaged curb of 10 cm) or walking one more step on the same level before stepping down. In the camouflaged setting, the participants had to accomplish 10 trials at each velocity, while the order of the four block-absent and six block-present trials was randomized. A trial (visible or camouflaged) was only analyzed when the subject hit the corresponding force plates with the correct foot without losing any reflective joint markers. The spherical markers (19 mm diameter) were placed on the tip of the fifth toe, lateral malleolus, epicondylus lateralis femoris, trochanter major, anterior superior iliac spine, acromion, epicondylus lateralis humeri and ulnar styloid processus on both sides of the body as well as on L5 and C7 process spinosus.

All trials were recorded with eight cameras (240 Hz) by a 3D infrared system (MCU 1000, Qualisys, Gothenburg, Sweden) and synchronized using the trigger of the Kistler software and hardware (for more details regarding the experimental setup, see AminiAghdam et al., 2019).

Data processing

All data were analyzed with custom-written Matlab codes (The Mathworks, Inc., Natick, MA, USA). The raw kinetic data were filtered at a 50 Hz cut-off frequency and kinematic data were filtered at 12 Hz with a bidirectional fourth-order low-pass Butterworth filter. Kinetic data were normalized by individual body weight (bw). The moments of touchdown (TD) and take-off (TO) were calculated as the instants when the GRFs exceeded or fell below the threshold of 0.02 bw, respectively, for first and second contacts. The COM was determined with a body segment parameters method according to Plagenhoef et al. (1983).

To compute the IP, we used the GRF vectors starting in the center of pressure (COP) for every instant of measurement in a COM-centered coordinate frame, where the vertical axis is parallel to gravity, as delineated by Müller et al. (2017). The chosen reference frame was evaluated by Gruben and Boehm (2012a) because of the mechanical significance of the COM and the omnipresence of the gravity force field. Although other examined reference frames provided significantly better predictions of the DP model, the quality was nevertheless high in all reference frames (Gruben and Boehm, 2012a). Therefore, in this study the COM-centered coordinate system was chosen because of its simple linking to the angular momentum of the whole body. The position of the IP with respect to the COM is the point where the sum of the squared perpendicular distances to the GRFs from 10% to 90% of stance is minimal. This time frame of 80% of the stance phase was chosen based on the literature (Andrada et al., 2014; Müller et al., 2017) to make the different conditions more comparable, because the double stance time (t_{double}) varied (see below). As the data were normalized to 250 samples per stance phase per trial, 200 samples of measured GRF lines of action were included in the calculation. The IP was computed only for the second (perturbed) contact, separately for each trial. Because the COP could not be determined exactly in the block-present condition, the IP was not calculated here.

The calculated model forces go through the COP and the computed IP (Fig. 1). To estimate the amount of agreement between model forces and experimentally measured GRFs, we considered

the angle of the GRF θ_{Exp} and of the model forces θ_{Mod} for each trial ($N_{\text{trial}}=8$ for visible conditions and $N_{\text{trial}}=4$ for camouflaged conditions, respectively) and measurement time ($N_{\%}=100$). The mean experimental angle $\bar{\theta}_{\text{Exp}}$ is the mean over all trials and measurement times. Based on this, we calculated the coefficient of determination R^2 , as suggested by Herr and Popovic (2008):

$$R^2 = \left(1 - \frac{\sum_{i=1}^{N_{\text{trial}}} \sum_{j=1}^{N_{\%}} (\theta_{\text{Exp}}^{ij} - \theta_{\text{Mod}}^{ij})^2}{\sum_{i=1}^{N_{\text{trial}}} \sum_{j=1}^{N_{\%}} (\theta_{\text{Exp}}^{ij} - \bar{\theta}_{\text{Exp}})^2} \right) \times 100\%. \quad (1)$$

Note that $R^2=100\%$ would mean that the angle of the GRFs and the angle of the model forces match for each trial and each measurement time. An R^2 value of 0% or smaller would mean that the estimation of the model is equal to or even worse than the use of $\bar{\theta}_{\text{Exp}}$ as an estimate (Herr and Popovic, 2008). We also calculated the angle θ between the model forces and the GRFs (Fig. 1) for each measurement time to quantify the force difference over time.

To determine changes in variables needed for IP calculations (IP-related variables), we also computed horizontal and vertical impulses \vec{p} for two time intervals (braking and propulsion) as the integrals of the GRFs. The braking interval went from TD to zero-crossing of the horizontal GRFs and the propulsion interval from the zero-crossing of the horizontal GRFs to TO, respectively. For better comparability, impulses were normalized to each subject's body weight bw, leg length l (distance between lateral malleolus and trochanter major of the leading leg) and standard gravity g as denoted in Eqn 2 (Hof, 1996):

$$\vec{p}_{\text{normalized}} = \frac{\vec{p}}{\text{bw} \cdot \sqrt{l/g}}. \quad (2)$$

As an additional variable, the angular momentum of the whole body L_{wb} was calculated as the sum of individual segment angular momenta about the COM (Herr and Popovic, 2008) and was normalized to each subject's body weight and the mean vertical COM position of the fast visible level walking to reduce data variance between the subjects (Herr and Popovic, 2008). The whole-body angle γ_{wb} was determined as the integral of the non-normalized angular momentum. The integration constant was chosen so that γ_{wb} was zero at mid-stance of the trailing leg in the step before perturbation. Mid-stance was defined as the frame when the COM was above the lateral malleolus.

To compare IP variables, IP-related variables and additional variables, we used repeated measures ANOVA ($P<0.05$; SPSS®, Chicago, IL, USA) with *post hoc* analysis (Šidák correction) regarding the factors 'speed' (slow and fast) and 'ground condition' (V0, V10, V20, C10). To analyze whether the IP was above the COM, we performed a one-sample *t*-test compared with zero (separately for each condition with Šidák correction).

RESULTS

The results and statistical values of 10 subjects are listed in Table 1 and illustrated in Figs 2–6. Figs 2–4 show IP variables, Fig. 5 shows IP-related variables and Fig. 6 shows additional variables. For clarity, only data for the fast conditions are shown in Figs 4–6. Figures for the slow conditions differ only slightly from those of the fast conditions (see Figs S1 and S2). Additionally, significant mean differences will be highlighted in the following sections of the Results.

Table 1. Statistical analysis of investigated IP parameters

	Speed	Ground condition				P-value F-value/ η^2		
		V0	V10	V20	C10	Ground	Speed	Interaction
IP variables								
IP _x (cm)	Slow	0.3±1.1	-0.2±1.8	0.7±1.2 ^a	-2.7±1.8 ^{a,b}	0.000	0.001	0.269
	Fast	-1.4±2.1	-1.2±2.1	-0.3±1.4	-3.5±2.0	73.62/0.89	22.10/0.71	1.42/0.14
IP _z (cm)	Slow	18.5±5.7	13.2±6.3 ^a	9.9±6.2 ^a	19.7±11.4	0.026	0.563	0.436
	Fast	15.0±4.8	11.8±5.3 ^a	11.9±7.6	19.5±16.7	6.12/0.41	0.36/0.04	0.74/0.08
R ² (%)	Slow	97.7±0.9	97.9±0.9	98.1±0.8	94.6±2.9 ^a	0.000	0.013	0.013
	Fast	97.5±1.0	97.9±1.0	97.6±0.9	89.8±5.3 ^{a,b}	24.66/0.73	9.67/0.52	9.19/0.51
IP-related variables								
COP _{10,x} (m)	Slow	0.31±0.02	0.27±0.02	0.27±0.03 ^a	0.20±0.04 ^{a,b}	0.000	0.034	0.077
	Fast	0.33±0.02	0.30±0.03	0.28±0.04	0.19±0.02	60.62/0.87	6.21/0.41	3.47/0.28
COP _{90,x} (m)	Slow	-0.28±0.02	-0.30±0.03 ^a	-0.32±0.02 ^a	-0.36±0.03 ^{a,b}	0.000	0.000	0.383
	Fast	-0.32±0.02	-0.35±0.03 ^a	-0.37±0.03 ^a	-0.40±0.06 ^a	28.48/0.76	32.40/0.78	0.95/0.10
$\bar{p}_{brake,x}$	Slow	-0.14±0.02	-0.16±0.02 ^a	-0.15±0.02	-0.11±0.02 ^{a,b}	0.000	0.458	0.000
	Fast	-0.15±0.01	-0.18±0.02 ^a	-0.15±0.03	-0.09±0.02 ^{a,b}	38.15/0.81	0.60/0.06	14.13/0.61
$\bar{p}_{prop,x}$	Slow	0.13±0.02	0.13±0.02	0.15±0.03	0.10±0.03 ^{a,b}	0.000	0.003	0.014
	Fast	0.12±0.02	0.13±0.01	0.13±0.03	0.08±0.03 ^{a,b}	34.81/0.78	16.34/0.65	4.25/0.32
$\bar{p}_{brake,z}$	Slow	1.15±0.08	1.24±0.08 ^a	1.21±0.07	1.12±0.07	0.000	0.000	0.017
	Fast	1.00±0.05	1.10±0.04 ^a	1.13±0.06 ^a	0.94±0.10 ^b	11.90/0.57	47.80/0.84	4.03/0.31
$\bar{p}_{prop,z}$	Slow	0.99±0.09	0.85±0.05 ^a	0.91±0.08	0.71±0.10 ^{a,b}	0.000	0.000	0.007
	Fast	0.76±0.06	0.70±0.05 ^a	0.67±0.06 ^a	0.55±0.10 ^{a,b}	31.12/0.78	465.27/0.98	5.03/0.36
Additional variables								
$\gamma_{wb,10}$ (deg)	Slow	-0.30±0.11	-0.59±0.14 ^a	-0.73±0.20 ^a	-0.99±0.14 ^{a,b}	0.000	0.000	0.002
	Fast	-0.31±0.06	-0.65±0.13 ^a	0.96±0.14 ^{a,b}	-1.09±0.15 ^{a,b}	64.30/0.88	29.40/0.77	6.67/0.43
$\gamma_{wb,90}$ (deg)	Slow	-0.48±0.14	-0.68±0.07 ^a	-0.90±0.10 ^{a,b}	-1.34±0.22 ^{a,b}	0.000	0.491	0.539
	Fast	-0.46±0.11	-0.66±0.11 ^a	-0.98±0.19 ^a	-1.37±0.39 ^a	73.31/0.89	0.52/0.05	0.53/0.06

V0, visible level walking; V10,20, visible curb of 10 or 20 cm; C10, camouflaged curb of 10 cm; IP, horizontal (x) and vertical (z) positions of the intersection point relative to the center of mass (COM); R², coefficient of determination of the angles between measured ground reaction forces (GRFs) and model forces [through center of pressure (COP) and IP]; COP_{10,x}, COP_{90,x}, horizontal COM-centered COP position at 10% or 90% of stance phase; $\bar{p}_{brake,x}$, braking impulse in the x- and z-direction; \bar{p}_{prop} , propulsion impulse in the x- and z-direction; γ_{wb} , whole-body angle at 10% and 90% of stance phase.

Data are means±s.d. across all included subjects (N=10). Post hoc analysis with Šidák correction revealed significant differences between ground conditions: differences from V0 and V10 are indicated with 'a' and 'b', respectively (P<0.05). The same denotation is used for the interaction, here across each speed. Underlined values indicate a significant difference from the slow walking speed condition. Bold indicates P<0.05.

IP variables

In the visible conditions, the IP height decreased with a larger curb drop. However, the IP was always above the COM. The R² was high in all conditions, but significantly lower in the camouflaged compared with the visible conditions.

The horizontal IP position (IP_x) showed a significant main effect for ground condition and speed (Table 1). In V20, the IP_x was 0.8 cm more posterior than in V0 (P=0.027). In the camouflaged condition (C10), it was 2.6 and 2.4 cm more posterior compared with V0 and V10 (P<0.001). In fast walking, the IP_x was 1.1 cm more posterior. The vertical IP position (IP_z; Fig. 3A) showed a significant main effect for ground condition. It was 4.3 cm lower in V10 (P=0.001) and 5.9 cm lower in V20 (P=0.002) compared with V0. There were no significant differences between C10 and the visible conditions nor speed effects in any conditions. The IP_z was in all conditions

significantly above the COM (P<0.039). In Fig. 2, exemplary illustrations of the IP for single trials of different subjects are shown.

In R² (Fig. 3B), there was an interaction between ground condition and speed (Table 1). The mean value in C10 was 3.1 and 7.7 percentage points lower than in V0 (slow: P=0.033; fast: P=0.025). Additionally, in fast walking, the R² in C10 was 8.1 percentage points lower than in V10 (P=0.025). However, at fast C10, the variance between subjects was high, with 76.1% being the lowest and 95.3% being the highest value (Fig. 3B). In V20, R² was 0.5 percentage points lower in fast walking (P=0.017). The generally high R² mean values (89.8–98.1%) indicate good agreement between model forces and measured forces and therefore a small angle θ between them.

The absolute value of the angle θ between model forces and GRFs was in some cases more than 3 times higher in the first and the

Table 2. Walking velocity and double stance time (t_{double})

	Speed	Ground condition				P-value F-value/ η^2		
		V0	V10	V20	C10	Ground	Speed	Interaction
Velocity (m s ⁻¹)	Slow	1.17±0.07	1.21±0.07	1.20±0.08	1.28±0.08 ^a	0.002	0.000	0.780
	Fast	1.66±0.09	1.68±0.13	1.70±0.08	1.77±0.15	6.39/0.42	385.56/0.98	0.36/0.04
t_{double} (s)	Slow	0.14±0.01	0.12±0.01 ^a	0.10±0.01 ^{a,b}	0.04±0.02 ^{a,b}	0.000	0.000	0.060
	Fast	0.10±0.01	0.09±0.01 ^a	0.07±0.01 ^a	0.02±0.09 ^a	167.47/0.95	231.54/0.96	4.24/0.32

Data are means±s.d. across all included subjects (N=10). Post hoc analysis with Šidák correction revealed significant differences between ground conditions: differences from V0 and V10 are indicated with 'a' and 'b', respectively (P<0.05). The same denotation is used for the interaction, here across each speed. Underlined values indicate a significant difference from the slow walking speed condition. Bold indicates P<0.05.

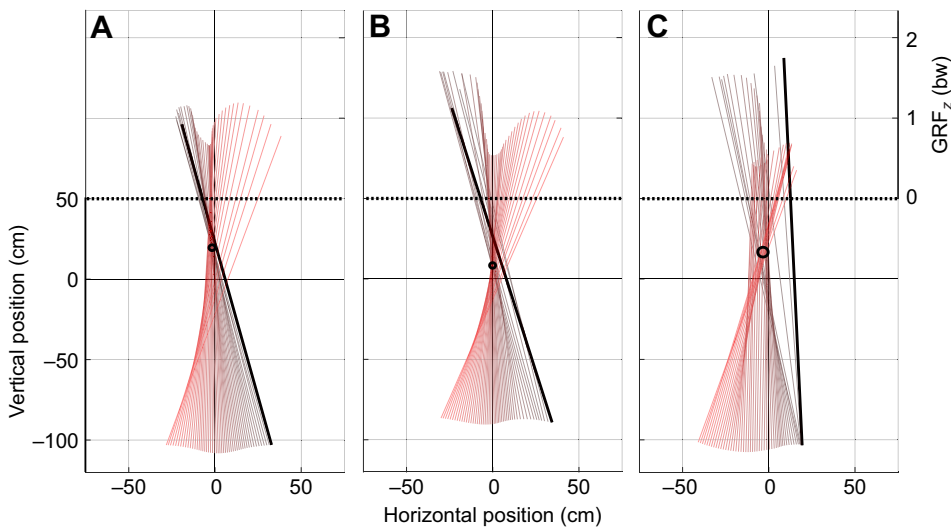


Fig. 2. Examples of the IP in a COM-centered coordinate system for different subjects and conditions. Lines show the GRFs at different measurement times (10–90% of the single support phase; black to red, thicker line indicates the first vector), originating at the COP. The midpoints of the circles indicate the mean spread of the GRFs relative to the IP; the radii represent the mean spread of the GRFs relative to the IP. (A) Fast visible level walking (V0). (B) Fast walking with a visible curb of 10 cm (V10). (C) Fast walking with a camouflaged curb of 10 cm (C10). For each condition, the trial with the spread around the IP nearest to the 50th percentile of all subjects was chosen. Above 50 cm, the vertical length of the vector represents the vertical GRF. Animated versions of these graphs can be found in the supplementary information (Movies 1–3).

last 10% of the stance phase than in the remaining 80% (Fig. 4). There, θ did not exceed 6 deg in any condition; the highest values were reached at the beginning and at the end of the single stance phase. The angle of C10 was almost always larger than that of the other conditions.

IP-related variables

The horizontal COP shifted in the posterior direction with a larger curb drop and from visible to camouflaged conditions. From visible

level to 10 cm curb walking, the braking impulses increased and the vertical propulsion impulses decreased. In the camouflaged condition, the impulses became smaller compared with those for visible level walking.

The horizontal position of the COM-referenced COP showed significant main effects for ground condition and speed for both 10% and 90% of the stance phase (Table 1). The COP was, relative to the COM, significantly more posterior in all curb conditions compared with V0, for both 10% (except V10; V20: -4.5 cm, $P=0.020$; C10: -12.5 cm, $P<0.001$) and 90% (V10: -2.5 cm, $P=0.004$; V20: -4.5 cm, $P=0.001$; C10: -8.0 cm, $P=0.025$). Additionally, the COP was more posterior for C10 compared with V10 (10%: -9.0 cm, $P<0.001$; 90%: -5.5 cm, $P=0.035$). Fig. 5A shows that the horizontal COP was more posterior for larger curb heights and for camouflaged compared with visible conditions for the whole stance phase. In fast walking, $COP_{10,x}$ was 2.0 cm more anterior in the visible conditions and 1.0 cm more posterior in C10 compared with that in slow walking. $COP_{90,x}$ was 4.5 cm more posterior in fast walking. The COM_z position with respect to the floor showed only minor differences between the conditions (Fig. 5B).

For the horizontal and vertical impulse \vec{p}_{brake} and \vec{p}_{prop} , there was an interaction between ground condition and speed (Table 1). The horizontal braking impulse was significantly larger in V10 than in V0 (slow: $P=0.004$; fast: $P=0.033$). It was lower in C10 than in V0 (slow: $P=0.010$; fast: $P<0.001$) and in V10 ($P<0.001$). In V0 and V10, it was larger ($P\leq 0.040$), and in C10 it was lower ($P=0.016$) for fast walking. The horizontal propulsion impulse was significantly lower in C10 than in V0 ($P\leq 0.021$) and V10 ($P\leq 0.035$). The horizontal forces for each condition for fast walking are shown in Fig. 5C. In V20 and C10, GRF_x was smaller for fast walking. The vertical impulse during the braking phase $\vec{p}_{brake,z}$ was larger in V10 than in V0 ($P\leq 0.024$). In fast walking, it was larger in V20 than in V0 ($P=0.011$) and lower in C10 than in V10 ($P=0.019$). The vertical impulse during the propulsion phase $\vec{p}_{prop,z}$ was lower in all curb conditions than in V0 ($P\leq 0.031$), except for the slow V20. In C10, it was lower than in V10 ($P\leq 0.007$). In all conditions, $\vec{p}_{brake,z}$ and $\vec{p}_{prop,z}$ were lower in fast walking ($P\leq 0.001$). Fig. 5D suggests that $\vec{p}_{prop,z}$ increased and $\vec{p}_{brake,z}$ decreased with the lower visible curb condition and even more so in C10 compared with the visible conditions. Therefore, GRF_z became more asymmetrical.

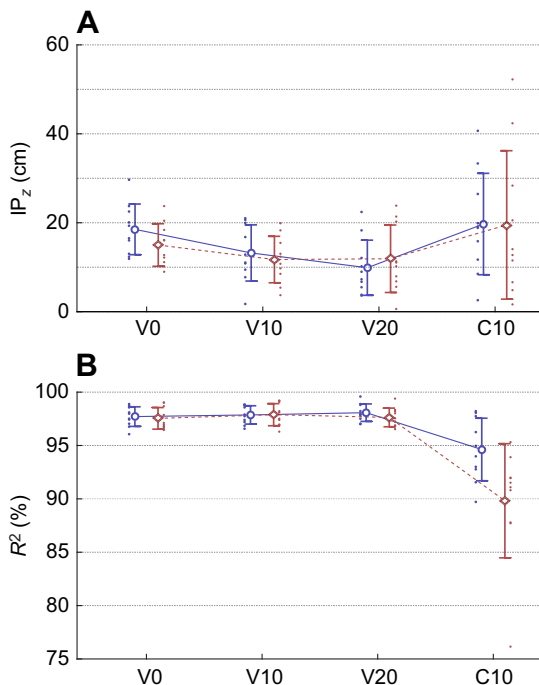


Fig. 3. Mean \pm s.d. IP variables between subjects for each walking condition (V0, V10, V20 and C10). Blue circles indicate slow walking and red diamonds indicate fast walking. (A) Vertical position of the intersection point (IP_z) relative to the COM. Each dot is the median over all trials of one condition for one subject. (B) R^2 represents the ratio of the angle between measured and model forces and their variance. Each dot represents one subject. Notice that the R^2 value of one subject is strikingly lower in fast C10.

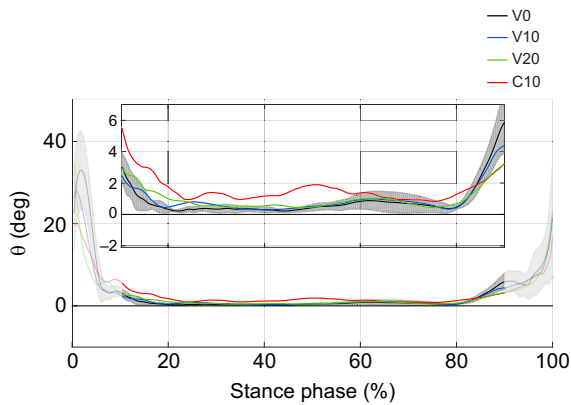


Fig. 4. Absolute angle θ between model forces and GRFs. Mean (\pm s.d. for visible level walking, V0) data across the subjects ($N=10$) for fast conditions (V0, V10, V20 and C10). The darker curve representing 10–90% of stance phase of the leading leg is shown on an enlarged scale in the inset.

Additional variables

The angular momentum in the camouflaged condition differed from that in the other conditions. Additionally, the subjects rotated more anterior with a larger curb drop and from visible to camouflaged conditions. However, the differences were smaller than 2 deg.

The angular momentum in the sagittal plane L_{wb} differed between the conditions before the stance phase of the leading leg (Fig. 6A). In the visible conditions, L_{wb} increased with the larger curb height around the TD of the leading leg. However, shortly after, the TO of the trailing leg L_{wb} was similar for all conditions. Only in C10 was there a larger L_{wb} after the TO in the posterior direction and thereafter a larger L_{wb} in the anterior direction compared with the visible conditions, like an overshoot. In all conditions, a deficit in

L_{wb} over the whole stride and the subsequent double stance phase (extended stride) could be observed.

The range of the whole-body angle γ_{wb} did not exceed 2 deg. For $\gamma_{wb,10}$ in the sagittal plane, there was an interaction between ground condition and speed (Table 1). $\gamma_{wb,10}$ in all curb conditions was significantly larger than in V0 (mean difference from 0.29 deg in V10 slow to 0.78 deg in C10 fast; $P \leq 0.035$). In the fast condition, it was larger in V20 than in V10 ($P < 0.001$). Additionally, the angle was larger in C10 than in V10 ($P \leq 0.002$). In the curb conditions, $\gamma_{wb,10}$ was larger when walking faster ($P \leq 0.042$). $\gamma_{wb,90}$ showed significant main effects for ground condition. It was significantly larger in all curb conditions compared with V0 (mean difference from 0.20 deg in V10 to 0.88 deg in C10; $P \leq 0.001$). Additionally, $\gamma_{wb,90}$ was significantly larger in V20 and C10 than in V10 ($P < 0.001$). The differences between the conditions after the TD of the leading leg are illustrated in Fig. 6B. An anterior shift of 0.5 deg (V0) to 1.5 deg (C10) from 0% to 100% of the extended stride was observed.

DISCUSSION

In this study, the force direction patterns while stepping down off a visible or camouflaged curb at slow and fast walking speeds were analyzed. Although in all conditions there was the tendency to generate an IP, related variables (COM-referenced COP and GRFs) changed considerably. We did not observe a significant speed effect on the results.

Forces intersect above the COM

As was hypothesized, in all conditions the GRFs intersected above the COM. Thus, we assume that a similar stabilization strategy is used in the camouflaged curb negotiation as in the visible conditions. For the visible trials, the high R^2 (mean $>97.5\%$) indicates that the deviation of the GRF from the calculated IP is small. The results are comparable to those of Gruben and Boehm

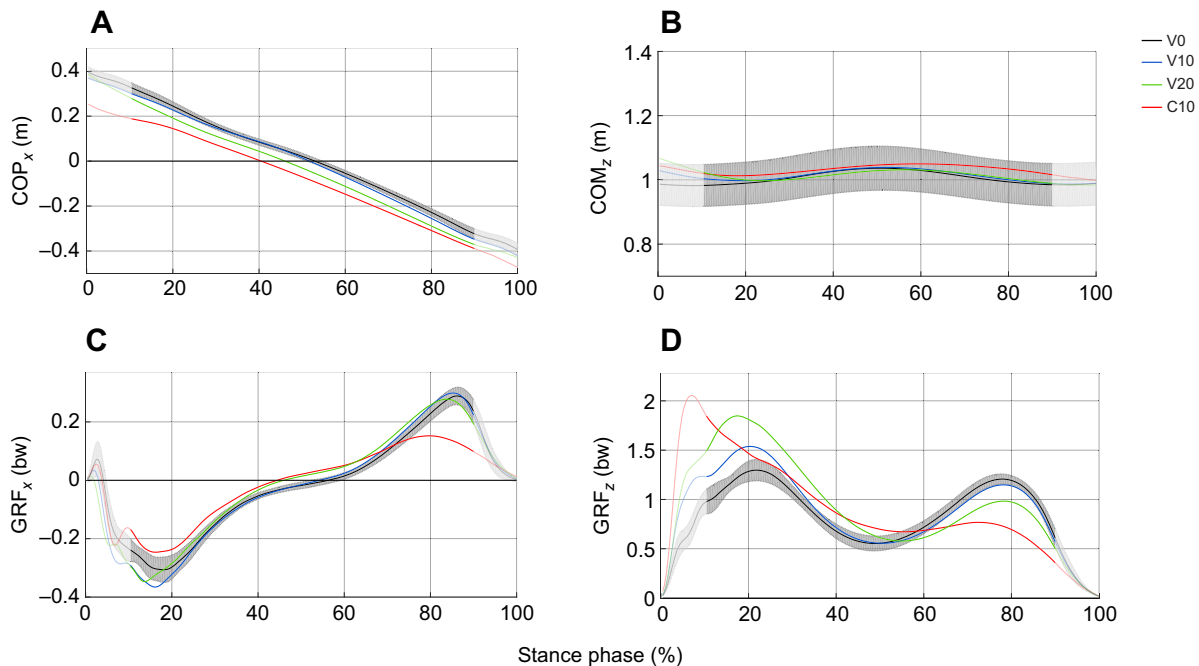


Fig. 5. Variables included in the calculation of the IP (IP-related variables). (A) Horizontal, COM-related COP position. (B) Vertical, COP-related COM position. (C) Horizontal GRFs. (D) Vertical GRFs. Mean (\pm s.d. for visible level walking, V0) data between the subjects ($N=10$) for fast walking (V0, V10, V20 and C10). The darker curve is 10–90% of stance phase of the leading leg, which is included in the calculations.

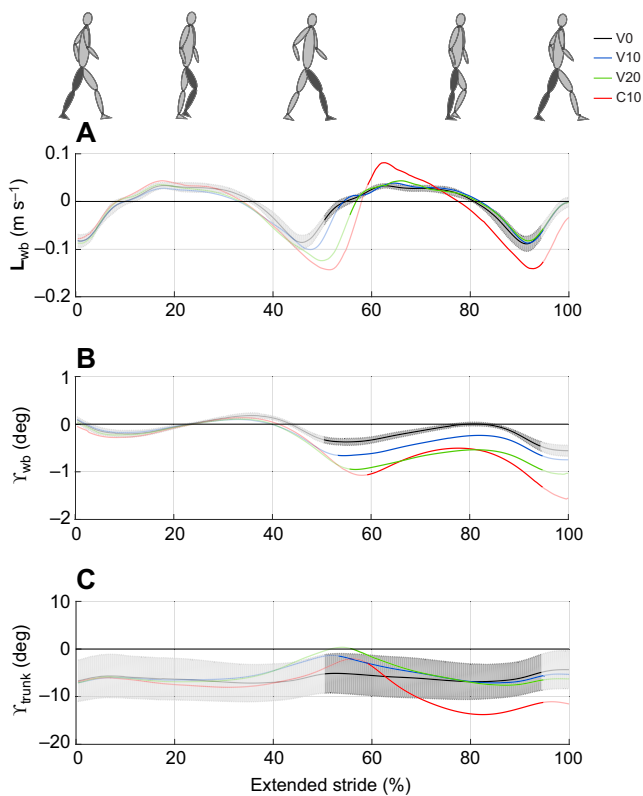


Fig. 6. Whole-body angle γ_{wb} and angular momentum L_{wb} for the extended stride. Extended stride was taken from touchdown (TD) of the trailing leg to take-off (TO) of the leading leg. Mean (\pm s.d. for visible level walking, V0) data between the subjects ($N=10$) for fast conditions (V0, V10, V20 and C10). The darker curve is 10–90% of stance phase of the leading leg. (A) L_{wb} in the sagittal plane. (B) γ_{wb} in the sagittal plane, defined as zero at mid-stance of the trailing leg. (C) Trunk angle (γ_{trunk}) in the sagittal plane. Negative values indicate a clockwise rotation.

(2012a), which also achieved high R^2 values ($>98.5\%$) for level walking in a COM-centered reference frame. In the camouflaged conditions, the R^2 was lower than in the visible conditions. Even though the R^2 value of one subject was noticeably low in fast C10 (76.1%), the mean value was still high ($>89.8\%$). The difference between model forces and measured forces (angle θ ; Fig. 4) was higher for C10 than for the visible conditions, which produced smaller R^2 values. The graph of θ suggests higher deviations of the forces for C10 in the first two-thirds of the stance phase, with missing noticeable peaks in the beginning. A reflex-based reactive approach after the TD would probably cause short and high fluctuations early in the stance phase. It may be that in the camouflaged condition, suitable adaptations of motor behavior were made before the TD. The additional fall time to react to a camouflaged curb was short [approximately 143 ± 23 ms for slow walking, 107 ± 197 ms for fast walking, and 110 ms in a previous study (van Dieën et al., 2007)]. A delayed TD showed time-dependent motor adaptations in prior studies, like changes in muscle activation (walking: van der Linden et al., 2007; or running: Müller et al., 2010, 2015) or leg retraction, creating a more vertical leg position with different joint moment requirements (van Dieën et al., 2007). Both these and possibly other mechanisms could facilitate the relatively smooth transition of GRF angles to the early stance phase. To summarize, the R^2 values suggest that the GRFs pass near an IP, in both visible and camouflaged conditions.

Because the mean IP_x value was maximally up to 4 cm posterior to the COM (Table 1), the IP was located nearly on a vertical line above the COM in all conditions. Basically this agrees with the results of previous studies (Gruben and Boehm, 2012a; Maus et al., 2010; Müller et al., 2017). However, the IP_z position varies in the literature. Gruben and Boehm (2012a) observed an IP height of approximately 44 ± 13 cm above the COM at a walking speed of 0.5 m s⁻¹ (IP_z was estimated using the percentage vertical COM position of the mean body height of all subjects calculated in that study). Maus et al. (2010) calculated the IP 5–70 cm above the COM at walking speeds between 0.8 and 1.7 m s⁻¹. The IP determined by Müller et al. (2017) was located 21 ± 7 cm above the COM at a walking speed of 1.5 ± 0.1 m s⁻¹. Therefore, we expected a lower IP height above the COM at a higher walking speed.

In this study, the IP_z position of 18 ± 6 cm (slow walking speed) and 15 ± 5 cm (fast walking speed) above the COM for visible level walking matches the data of Maus et al. (2010) (lower third) and Müller et al. (2017) and is considerably below the values calculated by Gruben and Boehm (2012a). The speed effect assumed from the above-mentioned data was not observed in the speed range of this study. However, it is possible that slower or faster walking could affect IP height. Furthermore, the chosen reference frame could also have an effect on the IP position. Gruben and Boehm (2012a) evaluated a lower IP position for a hip- or body-related reference frame. Thus, comparison between the different studies should consider which reference frame was used. While the chosen reference frame of Gruben and Boehm (2012a) and Müller et al. (2017) was also COM centered and aligned to the vertical, Maus et al. (2010) used a COM-centered reference frame that was aligned to the trunk.

Presumably, there are other factors that affect the IP height. However, the trunk orientation investigated by Müller et al. (2017) does not seem to have a major effect on IP height; the mean height increases only slightly with increasing trunk inclination. Other studies (Gruben and Boehm, 2012a; Maus et al., 2010) have suggested that raising the IP increases stability but also the energy cost. Hence, a higher IP_z position in C10 compared with the visible conditions could be expected in this study to negotiate the larger perturbation. However, this was not confirmed. In addition to speed, we also examined the effect of curb height on the IP_z position. Here, we found a significantly lower IP_z position in the visible curb conditions compared with level walking. Therefore, curb height seems to be the only previously investigated factor that affects IP height.

Regulation of the IP and the whole-body angle

When calculating the IP, solely the COM-referenced COP and the GRFs in the sagittal plane were considered and thus control its position. For the GRFs, only the ratio of the horizontal and vertical components had an effect.

In the visible conditions, there were changes in the IP-related variables that could be associated with the IP height. The ratio of the GRF components seems to have the greatest effect on the IP_z position compared with the other IP-related variables. When describing it by the ratio of vertical impulse to horizontal impulse (Table 1), a decrease from V0 to the curb conditions can be observed in all cases, except the fast V20. This decrease presumably causes the lower IP height found in the curb conditions (Table 1). We noticed that most subjects negotiated the level track and the 10 cm curb (visible and camouflaged) with heel landing and the 20 cm curb with toe landing. [For visible level walking, 0% (V10: 14%, C10: 9%) of all trials were accomplished with toe landing. In the 20 cm curb condition, we observed toe landing in 64% of the trials. Toe landing was defined as proposed by Knorz et al. (2017).] This could

affect the kinetics and kinematics at landing (van Dieën et al., 2007, 2008). Gruben and Boehm (2012b, 2014) observed that, when both standing and walking, the GRFs point more anterior with the COP near the heel and more posterior with the COP near the toe. However, from a mechanical point of view a shift of the GRF independent of the COP would be required to affect the IP position. Besides mechanics, other components also produce the GRF direction during walking. For example, neural control is an important factor that coordinates the direction of the GRF by torques (Gruben and Boehm, 2014). Thus, in prior work and this study, an emergent behavior of mechanical and neural control can be suggested, which ensures that the IP_x position does not change from V10 to V20 (Gruben and Boehm, 2014).

While IP height changes were not significant in C10, the camouflaged curb condition showed the most pronounced differences in IP-related variables. The greatest of these was the horizontal shift in the COM-referenced COP in the posterior direction, which means that the COP was nearer to the COM at TD and further away at the end of the stance phase compared with the visible conditions. This asymmetrical step behavior could again be associated with a delayed TD in the perturbed step and a continuous leg retraction in this longer fall time, producing a more vertical leg position at TD (van Dieën et al., 2007). When the IP is generated in level walking, forces directed in front of the COM produce a moment angularly accelerating the body in the posterior direction and forces behind the COM produce a moment angularly accelerating the body in the anterior direction, until force angle and COM are aligned. Note that γ_{wb} is in a more anterior rotation at TD in C10 compared with V0 and V10 (Fig. 6B). The COP posterior shift would allow less time to generate a posterior moment and more time to generate an anterior moment and therefore complicate the handling of the perturbed body state. However, in our discussion so far, changes in the force amplitude have not been considered. In C10, there were higher vertical forces in the beginning of the stance phase and lower vertical forces in the second half of the stance phase (Fig. 5D). This asymmetrical force behavior partially counters the effect of a higher anterior rotated γ_{wb} prior to the TD, as in this case higher forces at the beginning can produce higher moments for posterior rotation in the shortened time frame. With all these changes, γ_{wb} did not return to level walking range values, remaining more anterior even in the visible curb conditions. This could possibly be compensated in later steps.

Future considerations

While the VPP model assumes exactly one single point as the IP, the experimentally measured forces intersect with spread around one point, so that an intersection area of force vectors occur. However, no one has clearly defined up to what spread the intersection area can still be denoted as a point as introduced by the model. That would have to be examined in a simulation of the model with an intersection area instead of an intersection point. We suggest the R^2 as defined by Herr and Popovic (2008) rather than the squared distance r (Maus et al., 2010; Müller et al., 2017) to determine the accuracy of intersection, because it normalizes the spread with regard to variability of the measured variables and is comparable between the studies. Here, the angle approach seems to be more suitable than the force approach proposed by Herr and Popovic (2008), because it disregards the magnitude of the forces. Nevertheless, there is no clear limit up to which value of R^2 the intersection area can be denoted as a point. These limits should be methodically researched and specified.

Another methodological problem is the definition of the included single stance time. The constant cutting off of 10% as performed in previous studies (Andrada et al., 2014; Müller et al., 2017) does not represent the exact single support phase. This can also be observed in the graph of the angle θ between model forces and experimentally measured GRFs (Fig. 4), which indicates that the deviations mainly occur at the beginning and the end of the considered contact time. This possibly represents a superposition of the GRFs at double stance phase. However, considering the pure single support phase, the different contact and t_{double} (Table 2) in the visible versus camouflaged conditions would affect the position and precision of the IP and make conditions less comparable. Furthermore, it might also be worth analyzing the IP for the double stance phase.

A limitation of this study is that the subjects could have chosen a new strategy that differs from level-ground walking because they were aware of the possible perturbation. Future studies might consider investigating larger curb heights or other perturbations to the angular momentum. Noteworthy is a study in which subjects tripped over an unexpected obstacle at mid-stance phase (Pijnappels et al., 2004). The high moment in the anterior direction produced by tripping was countered by some subjects with a posterior moment in the second half of the stance phase. As force vectors would be below the COM here, this force regulation suggests the possibility of other control strategies. One possibility would be that the IP is just an emerging variable, where another control strategy would produce the IP as a side effect. This assumption is supported by experimental and modeling approaches (Gruben and Boehm, 2014; Maus et al., 2010; Müller et al., 2017; Rummel and Seyfarth, 2010; Sharbafi and Seyfarth, 2015). Gruben and Boehm (2014) showed the IP above the COM to be an emerging variable produced by the interaction of (a) ankle torques that generate the typical heel-to-toe roll-over and (b) a neural coordination of the remaining joint torques. The resulting behavior, it was argued, has favorable energetic and stability properties. There could be a switch in the neural control approach for highly perturbed situations. A more precise determination of different control strategies could be the subject of future studies.

These experiments could also be adapted for the elderly or patients with a neurological disorder, because they have a higher risk of falling (Berg et al., 1997; Menz et al., 2003). Additionally, it may be investigated whether the proximity of the GRF lines of action to the calculated IP could be used as a stabilizing parameter for walking.

Acknowledgements

We would like to thank Isabel Kolkka, Christian Rimpau and Will Murray for proof reading the manuscript.

Competing interests

The authors declare no competing or financial interests.

Author contributions

Conceptualization: R.M.; Methodology: J.V., E.G., R.M.; Software: J.V., E.G.; Validation: J.V., E.G., R.M.; Formal analysis: J.V., E.G.; Investigation: J.V., E.G., R.M.; Data curation: J.V., E.G.; Writing - original draft: J.V., E.G.; Writing - review & editing: J.V., E.G., R.M.; Visualization: J.V., E.G.; Supervision: R.M.; Project administration: R.M.; Funding acquisition: R.M.

Funding

This project was supported by the Deutsche Forschungsgemeinschaft (MU 2970/4-1 to R.M.).

Data availability

Kinetic and kinematic data are available from the figshare repository: <https://doi.org/10.6084/m9.figshare.7558586.v1>

Supplementary information

Supplementary information available online at
<http://jeb.biologists.org/lookup/doi/10.1242/jeb.204305.supplemental>

References

- Alexander, R. M. N.** (1995). Simple models of human movement. *Appl. Mech. Rev.* **48**, 461-470. doi:10.1115/1.3005107
- Aminiaghdam, S., Rode, C., Müller, R. and Blickhan, R.** (2017). Increasing trunk flexion transforms human leg function into that of birds despite different leg morphology. *J. Exp. Biol.* **220**, 478-486. doi:10.1242/jeb.148312
- Aminiaghdam, S., Griessbach, E., Vielemeyer, J. and Müller, R.** (2019). Dynamic postural control during (in)visible curb descent at fast versus comfortable walking velocity. *Gait Posture* **71**, 38-43. doi:10.1016/j.gaitpost.2019.04.014
- Andrada, E., Rode, C., Sutedja, Y., Nyakatura, J. A. and Blickhan, R.** (2014). Trunk orientation causes asymmetries in leg function in small bird terrestrial locomotion. *Proc. R. Soc. B* **281**, 20141405. doi:10.1098/rspb.2014.1405
- Berg, W. P., Alessio, H. M., Mills, E. M. and Tong, C.** (1997). Circumstances and consequences of falls in independent community-dwelling older adults. *Age Ageing* **26**, 261-268. doi:10.1093/ageing/26.4.261
- Buckley, J. G., MacLellan, M. J., Tucker, M. W., Scally, A. J. and Bennett, S. J.** (2008). Visual guidance of landing behaviour when stepping down to a new level. *Exp. Brain Res.* **184**, 223-232. doi:10.1007/s00221-007-1096-8
- Capaday, C.** (2002). The special nature of human walking and its neural control. *Trends Neurosci.* **25**, 370-376. doi:10.1016/S0166-2236(02)02173-2
- Gruben, K. G. and Boehm, W. L.** (2012a). Force direction pattern stabilizes sagittal plane mechanics of human walking. *Hum. Mov. Sci.* **31**, 649-659. doi:10.1016/j.humov.2011.07.006
- Gruben, K. G. and Boehm, W. L.** (2012b). Mechanical interaction of center of pressure and force direction in the upright human. *J. Biomech.* **45**, 1661-1665. doi:10.1016/j.jbiomech.2012.03.018
- Gruben, K. G. and Boehm, W. L.** (2014). Ankle torque control that shifts the center of pressure from heel to toe contributes non-zero sagittal plane angular momentum during human walking. *J. Biomech.* **47**, 1389-1394. doi:10.1016/j.jbiomech.2014.01.034
- Herr, H. and Popovic, M.** (2008). Angular momentum in human walking. *J. Exp. Biol.* **211**, 467-481. doi:10.1242/jeb.008573
- Hof, A. L.** (1996). Scaling gait data to body size. *Gait Posture* **4**, 222-223. doi:10.1016/0966-6362(95)01057-2
- Knorz, S., Kluge, F., Gelse, K., Schulz-Drost, S., Hotfiel, T., Lochmann, M., Eskofier, B. and Krinner, S.** (2017). Three-dimensional biomechanical analysis of rearfoot and forefoot running. *Orthopaedic J. Sports Med.* **5**, 2325967117719065. doi:10.1177/2325967117719065
- Lee, J., Vu, M. N. and Oh, Y.** (2017). A control method for bipedal trunk spring loaded inverted pendulum model. in 13th international conference on autonomic and autonomous systems (ICAS 2017) (ed. C. B. Westphall, M. Mendonca and R. O. Vasconcelos), pp. 24-29. Barcelona, May 21-25, 2017.
- Maus, H.-M., Rummel, J. and Seyfarth, A.** (2008). Stable upright walking and running using a simple pendulum based control scheme. In *Advances in Mobile Robotics* (ed. L. Marques, A. T. de Almeida, M. O. Tokhi and G. S. Virk), pp. 623-629. World Scientific.
- Maus, H.-M., Lipfert, S. W., Gross, M., Rummel, J. and Seyfarth, A.** (2010). Upright human gait did not provide a major mechanical challenge for our ancestors. *Nat. Commun.* **1**, 70. doi:10.1038/ncomms1073
- Menz, H. B., Lord, S. R. and Fitzpatrick, R. C.** (2003). Acceleration patterns of the head and pelvis when walking are associated with risk of falling in community-dwelling older people. *J. Gerontol. Ser. A Biol. Sci. Med. Sci.* **58**, M446-M452. doi:10.1093/gerona/58.5.M446
- Müller, R., Grimmer, S. and Blickhan, R.** (2010). Running on uneven ground: leg adjustments by muscle pre-activation control. *Hum. Mov. Sci.* **29**, 299-310. doi:10.1016/j.humov.2010.01.003
- Müller, R., Tschiesche, K. and Blickhan, R.** (2014). Kinetic and kinematic adjustments during perturbed walking across visible and camouflaged drops in ground level. *J. Biomech.* **47**, 2286-2291. doi:10.1016/j.jbiomech.2014.04.041
- Müller, R., Häufle, D. F. B. and Blickhan, R.** (2015). Preparing the leg for ground contact in running: the contribution of feed-forward and visual feedback. *J. Exp. Biol.* **218**, 451-457. doi:10.1242/jeb.113688
- Müller, R., Rode, C., Aminiaghdam, S., Vielemeyer, J. and Blickhan, R.** (2017). Force direction patterns promote whole body stability even in hip-flexed walking, but not upper body stability in human upright walking. *Proc. R. Soc. A* **473**, 20170404. doi:10.1098/rspa.2017.0404
- Nielsen, J. B.** (2003). How we walk: central control of muscle activity during human walking. *Neuroscientist* **9**, 195-204. doi:10.1177/1073858403009003012
- Peng, J., Fey, N. P., Kuiken, T. A. and Hargrove, L. J.** (2016). Anticipatory kinematics and muscle activity preceding transitions from level-ground walking to stair ascent and descent. *J. Biomech.* **49**, 528-536. doi:10.1016/j.jbiomech.2015.12.041
- Pijnappels, M., Bobbert, M. F. and van Dieën, J. H.** (2004). Contribution of the support limb in control of angular momentum after tripping. *J. Biomech.* **37**, 1811-1818. doi:10.1016/j.jbiomech.2004.02.038
- Pijnappels, M., Bobbert, M. F. and van Dieën, J. H.** (2005). Push-off reactions in recovery after tripping discriminate young subjects, older non-fallers and older fallers. *Gait Posture* **21**, 388-394. doi:10.1016/j.gaitpost.2004.04.009
- Plagenhoef, S., Evans, F. G. and Abdelnour, T.** (1983). Anatomical data for analyzing human motion. *Res. Q Exerc. Sport* **54**, 169-178. doi:10.1080/02701367.1983.10605290
- Reeves, N. D., Spanjaard, M., Mohagheghi, A. A., Baltzopoulos, V. and Maganaris, C. N.** (2008). The demands of stair descent relative to maximum capacities in elderly and young adults. *J. Electromyogr. Kinesiol.* **18**, 218-227. doi:10.1016/j.jelekin.2007.06.003
- Roos, P. E. and Dingwell, J. B.** (2013). Using dynamic walking models to identify factors that contribute to increased risk of falling in older adults. *Hum. Mov. Sci.* **32**, 984-996. doi:10.1016/j.humov.2013.07.001
- Rummel, J. and Seyfarth, A.** (2010). Passive stabilization of the trunk in walking. In *Proceedings of SIMPAR 2010 Workshops: International Conference on Simulation, Modeling, and Programming for Autonomous Robots*, Darmstadt, Germany, 15-16 November 2010, Darmstadt, Germany: Technische Universität Darmstadt.
- Sharbafi, M. A. and Seyfarth, A.** (2015). Fmch: a new model for human-like postural control in walking. In *IEEE/RSJ International Conference on Intelligent Robots and Systems (IROS)*, pp. 5742-5747. IEEE.
- Silverman, A. K., Neptune, R. R., Sinitski, E. H. and Wilken, J. M.** (2014). Whole-body angular momentum during stair ascent and descent. *Gait Posture* **39**, 1109-1114. doi:10.1016/j.gaitpost.2014.01.025
- van der Linden, M. H., Marigold, D. S., Gabreëls, F. J. M. and Duysens, J.** (2007). Muscle reflexes and synergies triggered by an unexpected support surface height during walking. *J. Neurophysiol.* **97**, 3639-3650. doi:10.1152/jn.01272.2006
- van Dieën, J. H., Spanjaard, M., Konemann, R., Bron, L. and Pijnappels, M.** (2007). Balance control in stepping down expected and unexpected level changes. *J. Biomech.* **40**, 3641-3649. doi:10.1016/j.jbiomech.2007.06.009
- van Dieën, J. H., Spanjaard, M., Könemann, R., Bron, L. and Pijnappels, M.** (2008). Mechanics of toe and heel landing in stepping down in ongoing gait. *J. Biomech.* **41**, 2417-2421. doi:10.1016/j.jbiomech.2008.05.022
- Winter, D. A.** (1995). Human balance and posture control during standing and walking. *Gait Posture* **3**, 193-214. doi:10.1016/0966-6362(96)82849-9
- Winter, D. A.** (2009). *Biomechanics and Motor Control of Human Movement*. John Wiley & Sons.

3 Article II: Ground reaction forces intersect above the center of mass in single support, but not in double support of human walking

	Contributor
Conceptualization	J.V.; R.M.
Methodology	J.V.; R.M.; D.R.
Software	J.V.; N.-S.S.; D.R.
Validation	J.V.; N.-S.S.
Formal analysis	J.V.
Investigation	R.M.
Data curation	J.V.
Writing - original draft	J.V.
Writing - review & editing	J.V.; R.M.; N.-S.S.; D.R.
Visualization	J.V.
Supervision	R.M.; R.A.
Project administration	R.M.; R.A.
Funding acquisition	R.M.

<https://doi.org/10.1016/j.jbiomech.2021.110387>



Contents lists available at ScienceDirect

Journal of Biomechanics

journal homepage: www.elsevier.com/locate/jbiomech
www.JBiomech.com

Ground reaction forces intersect above the center of mass in single support, but not in double support of human walking



Johanna Vielemeyer^{a,b,*}, Roy Müller^{a,b}, Nora-Sophie Staufenberg^c, Daniel Renjewski^c, Rainer Abel^d

^a GaitLab, Klinikum Bayreuth GmbH, Hohe Warte 8, 95445 Bayreuth, Germany

^b Motionscience, Institute of Sport Sciences, Friedrich Schiller University Jena, Seidelstraße 20, 07749 Jena, Germany

^c Institute of Applied Mechanics, Technical University of Munich, Boltzmannstr. 15, 85748 Garching, Germany

^d Department of Orthopedic Surgery, Klinikum Bayreuth GmbH, Hohe Warte 8, 95445 Bayreuth, Germany

ARTICLE INFO

Article history:
Accepted 9 March 2021

Keywords:
Double support
Human walking
Stability
Virtual pivot point (VPP)

ABSTRACT

There are various simplifying models that describe balance strategies of human walking. In one model it is assumed that ground reaction forces are directed to a point (virtual pivot point) above the center of mass during the whole stride. This was observed in several experimental investigations, but only for the single support phase. It has not yet been concretely considered whether humans use the same stabilization strategy during the double support phase. For analyzing this, nine volunteers walked at self-selected speed while kinetic and kinematic data were measured. We found that in contrast to the single support phase, where the virtual pivot point was significantly above the center of mass, in the double support phase of human walking the ground reaction forces point around the center of mass with a small spread ($R^2 = 92.5\%$). The different heights of the virtual pivot point in the different support phases could be caused by the vertical movement of the center of mass, which has a lower amplitude in the double support phase. This is also reflected in the ground reaction forces, whereby the ratio of the horizontal and vertical ground reaction forces can explain the height of the virtual pivot point. In the double support phase the ratio is shifted in favor of the horizontal component compared to the single support phase, because of a shorter contact time and a delayed braking impulse. Thus, the whole body seems to rotate around the center of mass, which presumably minimizes required energy.

© 2021 Elsevier Ltd. All rights reserved.

1. Introduction

The human bipedalism presents complex challenges for the stability while walking. Different strategies to balance the whole body are possible and could be described with various simplifying models, e.g. the inverted pendulum (Alexander, 1976; Mochon and McMahon, 1980; Pratt et al., 2006) or the bipedal spring-loaded inverted pendulum with the whole body mass concentrated in a point (Geyer et al., 2006) or in a trunk as rigid body (Maus et al., 2010; Poulakakis and Grizzle, 2007; Sharbafi et al., 2013). Besides models with compliant hips (e.g. Rummel and Seyfarth, 2010; Sharbafi and Seyfarth, 2015), in the model of Maus et al. (2010), the hip torques were adjusted so that the ground reaction forces (GRFs) intersect at a point (virtual pivot point – VPP) above the center of mass of the whole body (CoM) during the stride. In several human walking experiments, it was supposed that this control

mechanism is used (Maus et al., 2010; Gruben and Boehm, 2012; Müller et al., 2017; Vielemeyer et al., 2019). That means that the GRFs intersect near a VPP above the CoM. The same stabilization strategy could be observed when coping with perturbations, e.g. walking with altered trunk orientations (Müller et al., 2017) or walking over visible and camouflaged curbs (Vielemeyer et al., 2019).

However, in most of the experimental investigations, only the single support phase (SSP) was considered or there was no explicit separation between the support phases in the evaluation. Therefore, it is not clear if humans use the VPP strategy also in the double support phase (DSP). It is possible that, similar to the VPP model, the control mechanism with a VPP above the CoM is maintained. Furthermore, the position of the VPP could vary and be below the CoM, as it was observed in human running (Drama et al., 2020), or even at the CoM as assumed by Herr and Popovic (2008).

A study on a bipedal robot found no VPP at all in the SSP (Staufenberg et al., 2019). It is analogously possible that in the DSP of human walking the stabilization by a pendulum mechanism is not necessary since bipedal support ensures presumably a higher

* Corresponding author at: GaitLab, Klinikum Bayreuth GmbH, Hohe Warte 8, 95445 Bayreuth, Germany.

E-mail address: johanna.vielemeyer@uni-jena.de (J. Vielemeyer).

Nomenclature

CoM	center of mass of the whole body
CoP	center of pressure
CoP _{CoM}	CoP relative to the horizontal CoM position
DSP	double support phase
GRFs	ground reaction forces
GRFx	horizontal component of the GRFs
GRFz	vertical component of the GRFs
N_{Time}	duration of the support phase
N_{Trial}	number of trials
R^2	coefficient of determination
SSP	single support phase
SSP _{post}	single support phase after double support

SSP _{pre}	single support phase before double support
TD	touchdown
TO	take-off
θ	angle between the theoretical forces and the GRFs
θ_{Exp}	angle of the experimentally measured GRFs in the sagittal plane relative to the ground
$\bar{\theta}_{Exp}$	mean experimental angle of GRFs
θ_{VPP}	angle of the theoretical forces relative to the ground
VPP	virtual pivot point
VPPx	horizontal VPP position
VPPz	vertical VPP position

control authority than the monopodal stand in the SSP (Cui et al., 2020). Hence, we will analyze whether a VPP could be found as intersection point of the GRFs in the DSP of human walking.

2. Material and methods

Nine physically active volunteers took part in these investigations (4 female, 5 male, mean ± s.d. age: 24.6 ± 1.0 years, mass: 67.0 ± 7.5 kg, height: 171.1 ± 7.7 cm). An informed written consent was signed by each volunteer. The experiment was approved by the local ethics committee (University of Jena, 3532–08/12) and in accordance to the Declaration of Helsinki. The subjects were instructed to walk at self-selected speed (1.7 ± 0.2 ms⁻¹) over a 15 m walkway with two consecutive force plates in its center (Fig. 1). All trials were recorded by a 3D infrared system. A detailed description of the methods can be found in Müller et al. (2014).

2.1. Data processing

The kinetic data were filtered at a 50 Hz cut-off frequency and kinematic data were filtered at 12 Hz with a bidirectional fourth-order low-pass Butterworth filter. The GRFs were normalized by individual body weight and the instances of touchdown (TD) and take-off (TO) of the first and second contacts were calculated as the instances when the GRFs exceeded or fell below the threshold of 0.05 body weight. Due to missing of additional force plates, the TO of step zero (TO₀) and the TD of step three (TD₃) were computed using the kinematic data, more precisely using a characteristic apex in the velocity curve of the malleolus lateralis (O'Connor et al., 2007). The CoM was determined with a body segment parameters method according to Plagenhoef et al. (1983), adapted by Winter (2009).

To calculate the VPP position, we used the GRF vectors starting at the center of pressure (CoP) for every instant of measurement in a CoM-centered coordinate frame, where the vertical axis is parallel to gravity. The position of the VPP with respect to the CoM is the point where the sum of the squared perpendicular distances to the GRFs from TO to the following TD in the SSP and vice versa in the DSP is minimal. The calculated theoretical forces are the linear connections between the CoP and the computed VPP. To estimate the amount of agreement between theoretical forces and experimentally measured GRFs, we considered the angle of the GRFs θ_{Exp} and of the theoretical forces θ_{VPP} relative to the ground for each trial ($N_{Trial}=10$) and measurement time (N_{Time} =duration of the support phase in milliseconds), as illustrated in

Fig. 1. The mean experimental angle $\bar{\theta}_{Exp}$ is the grand mean over all trials and measurement times. Then, the coefficient of determination R^2 was calculated as follows, adapted from Herr and Popovic (2008):

$$R^2 = \left(1 - \frac{\sum_{i=1}^{N_{Trial}} \sum_{j=1}^{N_{Time}} (\theta_{Exp}^{ij} - \theta_{VPP}^{ij})^2}{\sum_{i=1}^{N_{Trial}} \sum_{j=1}^{N_{Time}} (\theta_{Exp}^{ij} - \bar{\theta}_{Exp})^2} \right) \times 100\%. \quad (1)$$

with at least one pair of i, j , so that $\theta_{Exp}^{ij} \neq \bar{\theta}_{Exp}$. The centroidal angular momentum of the whole body was calculated analogously to Vielemeyer et al. (2019).

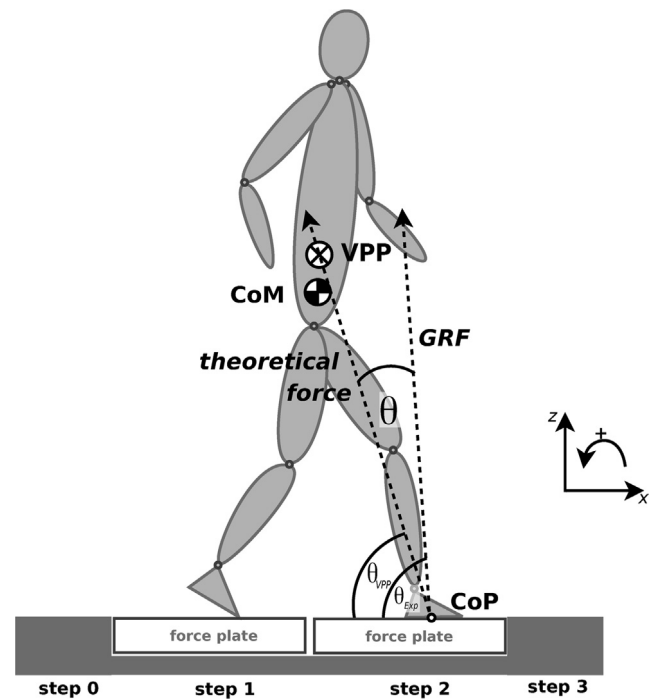


Fig. 1. Side view of the walkway with two consecutive force plates in its center. The theoretical force goes through the center of pressure (CoP) and the calculated virtual pivot point (VPP). The angle θ is between the theoretical force vector and the measured ground reaction force (GRF) vector for each time frame ($\theta = \theta_{Exp} - \theta_{VPP}$). CoM is the center of mass of the whole body.

To compare the VPP and corresponding variables between SSP and DSP, we used an analysis of variance (ANOVA; SPSS®, Chicago, IL, USA; $p < 0.05$) with post hoc analysis (Sidak correction). To analyze if the VPP is above, below or at the CoM, and anterior or posterior to it, we performed one-sample t-tests compared to zero, separated for each support phase.

3. Results

The vertical VPP position VPPz is with a mean of 43.3 cm and 27.7 cm in both SSPs significantly above the CoM ($p < 0.001$, Table 1). Here, the VPPz of the SSP before DSP (SSP_{pre}, step 1 in Fig. 1) is significantly higher than the VPPz of the SSP after DSP (SSP_{post}, step 2 in Fig. 1; $p = 0.004$). However, in the DSP, there is no significant difference between the CoM and the VPPz (Fig. 2). The VPPz differs significantly between the SSPs and the DSP ($p < 0.001$). In all support phases, the R^2 represents with more than 92.5% a good agreement between theoretical and measured forces. In the SSPs, it is with more than 98.7% even remarkably good (Herr and Popovic, 2008) and significantly higher than in the DSP ($p < 0.001$). The horizontal VPP position VPPx also differs between the SSPs and the DSP ($p < 0.001$). In the DSP, the VPPx is with 5.1 cm significantly before (anterior to) the CoM ($p < 0.001$, Fig. 2). This is up to 6.8 cm more anterior than in the SSPs, where only the VPPx position of SSP_{post} significantly differs from the CoM (with 1.7 cm posterior, $p = 0.018$).

4. Discussion

In the double support phase, the GRFs intersect near a point ($R^2 = 92.5\%$, Fig. 2). Because of the high R^2 value, this point is probably a VPP at the height of the CoM (0.0 ± 7.2 cm). Both the VPP position and the R^2 in the DSP differ significantly from those in the SSPs. Here, both intersection points can be denoted as a VPP above the CoM because of the high R^2 values ($\geq 98.7\%$) and the position of 43.3 and 27.7 cm above the CoM.

The CoP_{CoM} (CoP relative to the horizontal CoM position) and the GRFx (horizontal GRFs) should move relatively smoothly over time to obtain fan-like oriented vectors that intersect in a VPP (Fig. 3). This behavior can be observed in the SSPs and the DSP (Fig. 5A,C). The quality of the VPP as intersection point is represented by the R^2 and depends on the symmetry of the VPP related variables. If CoP_{CoM} and GRFx are point-symmetric to zero-crossing and GRFz (vertical GRFs) and $CoMz$ (vertical CoM position) are axisymmetric to the middle of the support phase, then only the intersection height can vary. A distinct symmetrical behavior can be noticed in the SSPs, while this is less represented in the DSP. The differences in symmetry may have their origin in the different

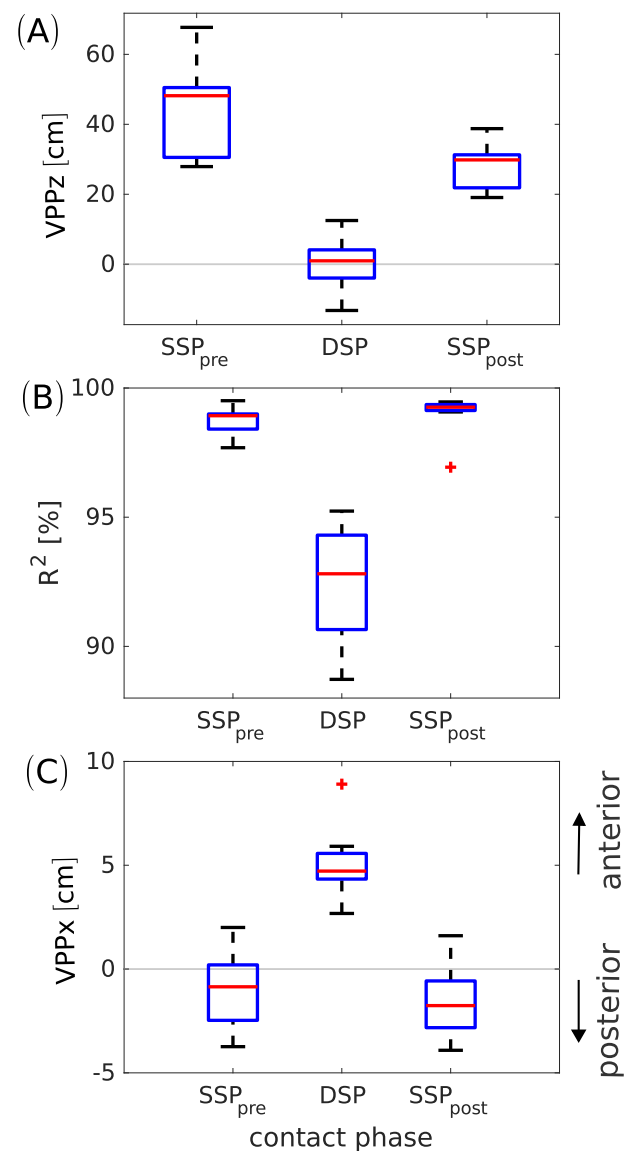


Fig. 2. Descriptive statistics of the virtual pivot point (VPP) data of all subjects ($N = 9$). (A) Vertical VPP (VPPz), (B) R^2 , the coefficient of determination of the angles between measured ground reaction forces and theoretical forces [through center of pressure and VPP] and (C) horizontal VPP (VPPx) are illustrated for the single support phases (SSP_{pre} before double support and SSP_{post} after double support) and the double support phase (DSP). Median (red line), 25th to 75th percentile (blue box), extreme data points (black whisker) and outliers (red '+') are shown. (For interpretation of the references to colour in this figure legend, the reader is referred to the web version of this article.)

Table 1

Statistical analysis of selected parameters. VPP, horizontal (x) and vertical (z) positions of the virtual pivot point relative to the center of mass (CoM) in a vertical-aligned coordinate system. R^2 , coefficient of determination of the angles between measured ground reaction forces and theoretical forces [through center of pressure and VPP] for each measurement time (distance: 1 ms). Data are means \pm s.d. across all included subjects ($N = 9$). Post-hoc analysis with Sidak correction revealed significant differences between the support phases: significant differences to single support pre are underlined, significant differences to double support are cursive. Bold indicates $p < 0.05$.

	Single support pre	Double support	Single support post	p-value
VPPx (cm)	-1.0 ± 1.9	<u><i>5.1 ± 1.7</i></u>	-1.7 ± 1.7	0.000
VPPz (cm)	43.3 ± 13.5	<u><i>0.0 ± 7.2</i></u>	<u><i>27.7 ± 6.4</i></u>	0.000
R^2 (%)	98.7 ± 0.6	<u><i>92.5 ± 2.3</i></u>	99.0 ± 0.8	0.000
duration (s)	0.380 ± 0.019	<u><i>0.102 ± 0.013</i></u>	0.391 ± 0.019	0.000

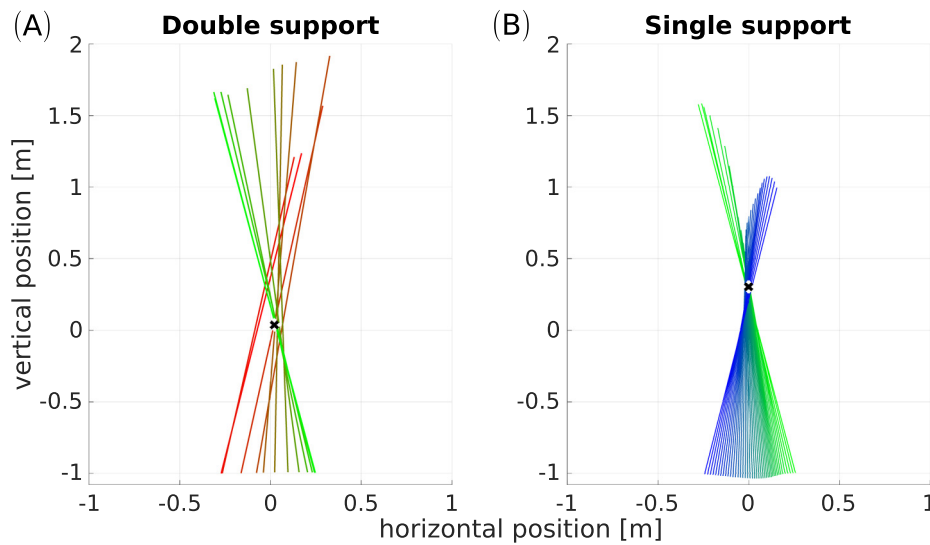


Fig. 3. Exemplary plot of the virtual pivot point (VPP) of a representative subject (the individual with the median of the spread around the VPP in the double support phase over all trials and subjects). Colored lines show the ground reaction forces (GRFs) scaled by factor two at different measurement times, originating at the center of pressure in a center of mass -centered coordinate system. Distance of the vectors: 10 ms, the black crosses indicate the calculated VPP. (A) double support phase (TD₂ to TO₁), red to green, and (B) single support phase after double support (TO₁ to TD₃), green to blue. (For interpretation of the references to colour in this figure legend, the reader is referred to the web version of this article.)

requirements on the stability. In the SSP, the swing leg must be swung forward while standing on only one leg. Thus, a symmetric behavior could support stability and avoid falls. The DSP is more robust against perturbations (Cui et al., 2020) and must restore stable initial conditions for the next SSP. For the SSP, an asymmetric behavior in the peak heights of the GRFz is observed (Fig. 5B), signifying that the vertical braking at the beginning of the SSP is more distinctive than the vertical propulsion at the end of the SSP. This causes in different ways also the DSP behavior. For example, the CoP_{CoM} is weighted by these asymmetric GRFz and is therefore, together with the VPPx, shifted in the anterior direction.

The significantly different VPP heights of both SSPs ($p = 0.004$) can have several reasons. Fig. 5 and 6 suggest that in SSP_{pre} compared to SSP_{post} the slightly smaller GRFx and slightly larger GRFz component until mid stance provide steeper resulting force vectors. This causes an upward shift of the VPP. However, the changes in other variables are rather small. Besides, it cannot be excluded that measurement uncertainties of the force plates possibly somewhat influence results as well. Considerable differences in VPPz of SSP (between 15 and 45 cm) can also be observed between previous studies (Gruben and Boehm, 2012; Maus et al., 2010; Müller et al., 2017; Vielemeyer et al., 2019).

It remains to be examined, why not only the quality of the VPP but also its height varies between SSP and DSP. Firstly, the range of the CoP_{CoM} can affect VPPz. But since the CoP_{CoM} has to act between the feet, it does not cause the differences in VPPz between SSP and DSP. Secondly, the amplitude of $CoMz$ could have an effect on VPPz. Fig. 5D shows that a lower amplitude is observed for the

DSP compared with the SSP. This is caused by the underlying mechanics that with two legs on the floor (a closed kinetic chain for the lower body) the CoM cannot be raised as in the SSP with the same energetic effort. Finally, the $CoMz$ movement directly affects the GRFs. Here, the ratio of GRFx to GRFz can explain the VPPz position. It is noticeable that in DSP the ratio is shifted in favor of the horizontal component, compared to the SSP (Fig. 5A, B and Fig. 6). The GRFx seem to have a greater effect than the GRFz, possibly related to the magnitude of the components. This results in a lower VPPz position in DSP. Most likely, the reason for the higher GRFx amplitude is that the forces from two legs add up in a short time window (Table 1). Additionally, the horizontal braking in the beginning of the DSP seems to start slightly delayed. Thus, the whole body is rotated around the CoM in the DSP, which is supported by the delayed horizontal braking and the small $CoMz$ movement. This can also be observed in the angular momentum of the whole body (Fig. 4B illustrates this exemplarily), where for the DSP a clockwise movement is shown. Thus, it is conceivable that the rotation of the whole body around the CoM minimizes required energy. This would explain the VPPz position at the height of the CoM in the DSP. Yet, one fact contradicts this simplified mechanism: Especially the vectors at the edges of the phase point to the VPP of the SSPs, so that it is rather a pointing around the CoM . That means, there are also vectors that point below the CoM to compensate these edge vectors. In conclusion it can be stated that a VPP in DSP at the same position as in SSP should be possible for human walking (as in simulations), though it is unnecessarily energy-intensive in favor of additional unneeded stability.

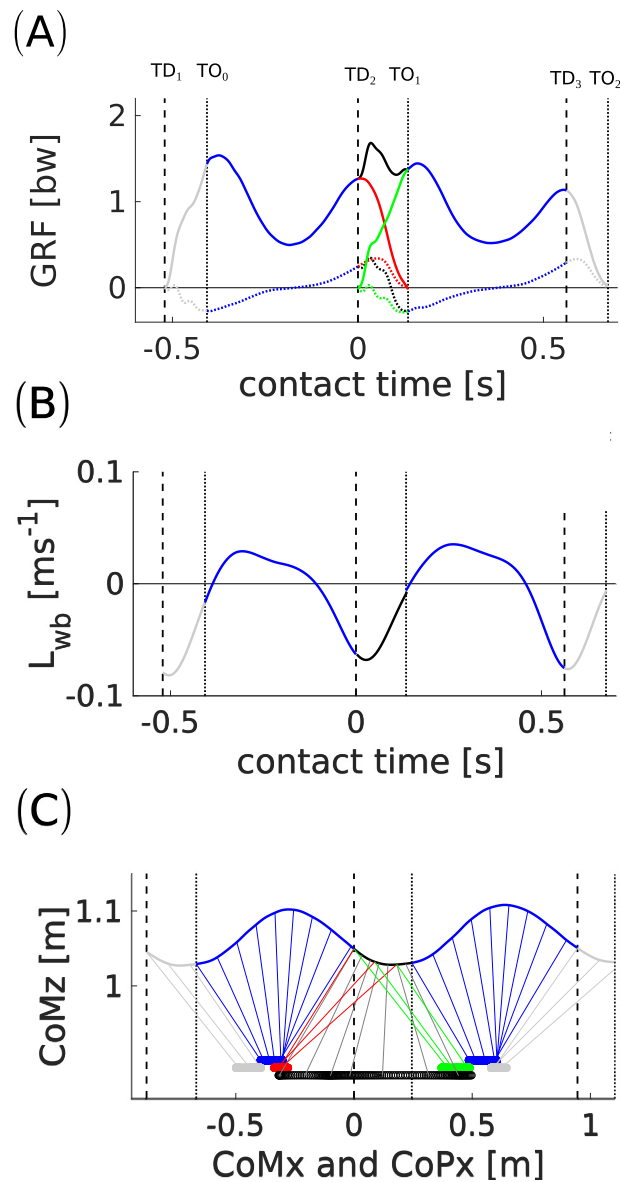


Fig. 4. Exemplary curves of a representative subject (the individual with the median of the spread around the virtual pivot point in the double support phase over all trials and subjects). (A) horizontal (dotted line) and vertical (solid line) ground reaction force (GRF; $TD_2 = 0$ s). In the double support phase, the resulting forces are the added GRFs of the first and the second contact. (B) Centroidal angular momentum (L_{wb}) of the whole body, negative values indicate clockwise rotation, (C) Center of mass (CoM) and CoM-centered center of pressure (CoP; TD_2 relative to the CoM = 0 m), CoM and CoP of the same time points are linearly connected each 0.5 s, x: horizontal, z: vertical; the resulting CoP in the double support phase is the sum of the CoPs of the first and second contact weighted by the vertical GRFs. (A–C): curves from TD_1 to TO_2 , double support phase (DSP) pre and post in gray, first and second single support phase (SSP) in blue, double support in red (first contact) and green (second contact), sum in black. The vertical lines represent the TD (dashed) and TO (dotted). (For interpretation of the references to colour in this figure legend, the reader is referred to the web version of this article.)

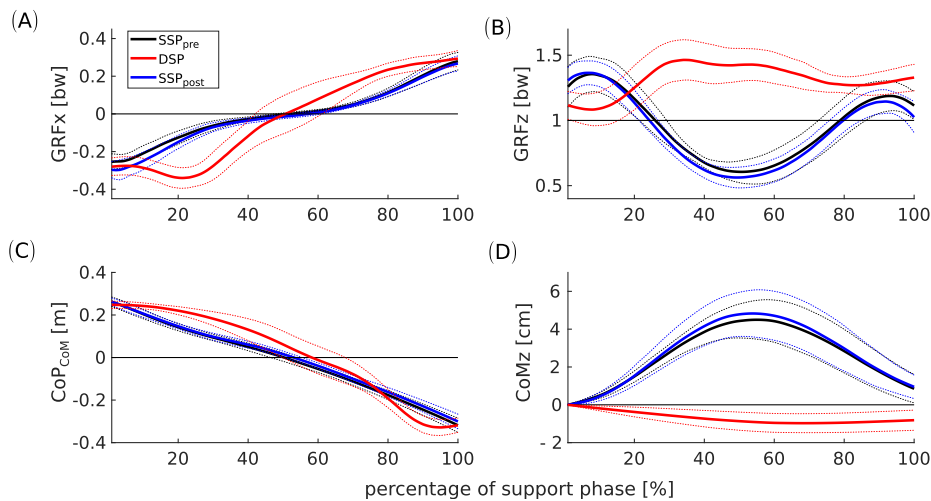


Fig. 5. Comparison of virtual pivot point-related variables of the single support phase before double support (SSP_{pre} , black line), the double support phase (DSP, red line) and the single support phase after double support (SSP_{post} , blue line). The solid line is the mean, the dotted line the standard deviation of all subjects ($N = 9$). (A) shows the horizontal (x) ground reaction force (GRF) normalized to body weight (the curve of the double support phase is mirrored on the x-axis for better comparability) and (B) the vertical (z) GRF normalized to body weight. (C) Shows CoP_{CoM} , the horizontal center of pressure (CoP) relative to the center of mass (CoM), here, the curve of the double support is mirrored on the vertical line of 50% for better comparability. D) shows the vertical position of the CoM relative to the position of the CoM at the beginning of the support phase. (For interpretation of the references to colour in this figure legend, the reader is referred to the web version of this article.)

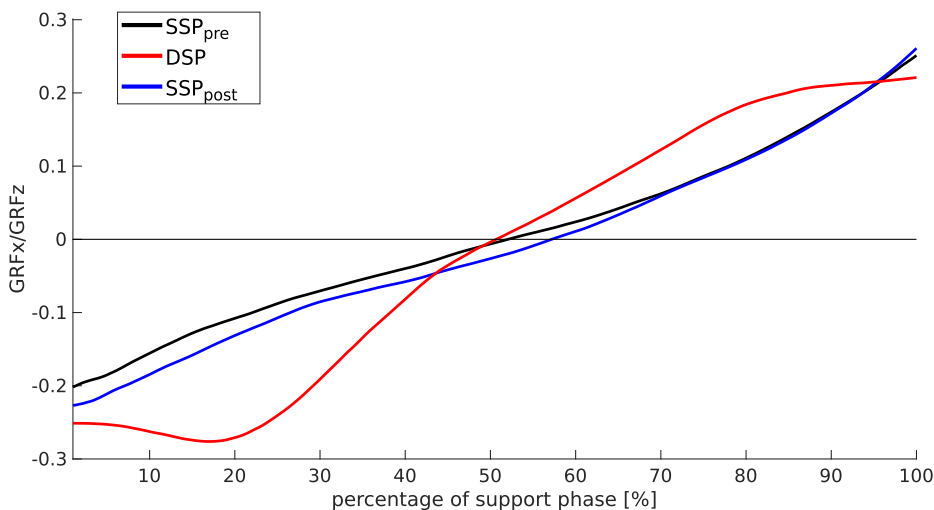


Fig. 6. Ratio of horizontal ground reaction forces (GRFx) to vertical ground reaction forces (GRFz). The mean of all subjects ($N = 9$) is shown for the single support phase before double support (SSP_{pre} , black line), the double support phase (DSP, red line) and the single support phase after double support (SSP_{post} , blue line). The curve of the double support phase is mirrored on the x-axis for better comparability. (For interpretation of the references to colour in this figure legend, the reader is referred to the web version of this article.)

Data accessibility

Kinetic and kinematic data are deposited at <https://figshare.com/s/5940bb3888b05e4551f2>.

Declaration of Competing Interest

The authors declare that they have no known competing financial interests or personal relationships that could have appeared to influence the work reported in this paper.

Acknowledgements

We would like to thank Kevin Moll for conducting the experiments, Reinhard Blickhan for the helpful comments, and Isabel

Kolkka for proof reading the manuscript. This project was supported by the German Research Foundation (MU 2970/4-1 to R.M.).

References

Alexander, R., 1976. Mechanics of bipedal locomotion. *Perspect. Exp. Biol.* 1, 493–504.
 Cui, C., Kulkarni, A., Rietdyk, S., Barbieri, F., Ambike, S., 2020. Synergies in the ground reaction forces and moments during double support in curb negotiation in young and older adults. *J. Biomech.*, 109837
 Drama, Ö., Vielemeyer, J., Badri-Spröwitz, A., Müller, R., 2020. Postural stability in human running with step-down perturbations: an experimental and numerical study. *Roy. Soc. Open Sci.* 7, 200570.
 Geyer, H., Seyfarth, A., Blickhan, R., 2006. Compliant leg behaviour explains basic dynamics of walking and running. *Proc. Roy. Soc. B: Biol. Sci.* 273 (1603), 2861–2867.
 Gruben, K.G., Boehm, W.L., 2012. Force direction pattern stabilizes sagittal plane mechanics of human walking. *Hum. Mov. Sci.* 31 (3), 649–659.
 Herr, H., Popovic, M., 2008. Angular momentum in human walking. *J. Exp. Biol.* 211 (4), 467–481.

- Maus, H.-M., Lipfert, S., Gross, M., Rummel, J., Seyfarth, A., 2010. Upright human gait did not provide a major mechanical challenge for our ancestors. *Nature Commun.* 1, 70.
- Mochon, S., McMahon, T.A., 1980. Ballistic walking. *J. Biomech.* 13 (1), 49–57.
- Müller, R., Rode, C., Aminiaghdam, S., Vielemeyer, J., Blickhan, R., 2017. Force direction patterns promote whole body stability even in hip-flexed walking, but not upper body stability in human upright walking. *Proc. R. Soc. A* 473 (2207), 20170404.
- Müller, R., Tschiesche, K., Blickhan, R., 2014. Kinetic and kinematic adjustments during perturbed walking across visible and camouflaged drops in ground level. *J. Biomech.* 47 (10), 2286–2291.
- O'Connor, Ciara M., Thorpe, Susannah K., O'Malley, Mark J., Vaughan, Christopher L., 2007. Automatic detection of gait events using kinematic data. *Gait & posture* 25, 469–474.
- Plagenhoef, S., Gaynor, E.F., Abdelnour, T., 1983. Anatomical data for analyzing human motion. *Res. Quart. Exercise Sport* 54 (2), 169–178.
- Poulakakis, I., Grizzle, J., 2007. Formal embedding of the spring loaded inverted pendulum in an asymmetric hopper. In: 2007 European Control Conference (ECC). IEEE, pp. 3159–3166.
- Pratt, J., Carff, J., Drakunov, S., Goswami, A., 2006. Capture point: A step toward humanoid push recovery. In: 2006 6th IEEE-RAS international conference on humanoid robots. IEEE, pp. 200–207.
- Rummel, J., Seyfarth, A., 2010. Passive stabilization of the trunk in walking. In: International Conference on Simulation, Modeling and Programming for Autonomous Robots, Darmstadt, Germany, 2010, Proceedings, 180(190), 200.
- Sharbafi, M.A., Maufroy, C., Ahmadabadi, M.N., Yazdanpanah, M.J., Seyfarth, A., 2013. Robust hopping based on virtual pendulum posture control. *Bioinspiration Biomimetics* 8 (3), 036002.
- Sharbafi, M.A., Seyfarth, A., 2015. FMCH: a new model for human-like postural control in walking. In: 2015 IEEE/RSJ International Conference on Intelligent Robots and Systems (IROS). IEEE, pp. 5742–5747.
- Staufenberg, N.-S., Vielemeyer, J., Müller, R., Renjewski, D., Rixen, D.J., 2019. Virtual pivot point analysis of the humanoid robot Lola. In: Dynamic Walking 2019.
- Vielemeyer, J., Griefsbach, E., Müller, R., 2019. Ground reaction forces intersect above the center of mass even when walking down visible and camouflaged curbs. *J. Exp. Biol.* 222(14), jeb204305. <https://doi.org/10.1242/jeb.204305>.
- Winter, D.A., 2009. Biomechanics and motor control of human movement. John Wiley & Sons.

4 Article III: Postural stability in human running with step-down perturbations: an experimental and numerical study

	Contributor
Conceptualization	Ö.D.; J.V.; A.B.-S.; R.M.
Methodology	Ö.D.; J.V.
Software	Ö.D.; J.V.
Validation	Ö.D.; J.V.; A.B.-S.; R.M.
Formal analysis	Ö.D.; J.V.
Investigation	R.M.
Data curation	Ö.D.; J.V.
Writing - original draft	Ö.D.; J.V.
Writing - review & editing	Ö.D.; J.V.; A.B.-S.; R.M.
Visualization	Ö.D.; J.V.
Supervision	A.B.-S.; R.M.
Project administration	A.B.-S.; R.M.
Funding acquisition	A.B.-S.; R.M.

<http://dx.doi.org/10.1098/rsos.200570>

Research



Cite this article: Drama Ö, Vielemeyer J, Badri-Spröwitz A, Müller R. 2020 Postural stability in human running with step-down perturbations: an experimental and numerical study. *R. Soc. Open Sci.* **7**: 200570.
<http://dx.doi.org/10.1098/rsos.200570>

Received: 7 April 2020

Accepted: 23 October 2020

Subject Category:

Physics and biophysics

Subject Areas:

Biomechanics

Keywords:

Bipedal locomotion, human running, step-down perturbation, postural stability, TSLIP model, virtual point (VP, VPP)

Author for correspondence:

Özge Drama

e-mail: drama@is.mpg.de

Postural stability in human running with step-down perturbations: an experimental and numerical study

Özge Drama^{1,†}, Johanna Vielemeyer^{2,3,†},
Alexander Badri-Spröwitz¹ and Roy Müller^{2,3}

¹Dynamic Locomotion Group, Max Planck Institute for Intelligent Systems, Stuttgart, Germany

²Department of Neurology/Orthopedic Surgery, Klinikum Bayreuth GmbH, Germany

³Department of Motion Science, Friedrich Schiller University-Jena, Jena, Germany

ÖD, 0000-0001-7752-0950; RM, 0000-0002-4688-1515

Postural stability is one of the most crucial elements in bipedal locomotion. Bipedals are dynamically unstable and need to maintain their trunk upright against the rotations induced by the ground reaction forces (GRFs), especially when running. Gait studies report that the GRF vectors focus around a virtual point above the centre of mass (VP_A), while the trunk moves forward in pitch axis during the stance phase of human running. However, a recent simulation study suggests that a virtual point below the centre of mass (VP_B) might be present in human running, because a VP_A yields backward trunk rotation during the stance phase. In this work, we perform a gait analysis to investigate the existence and location of the VP in human running at 5 m s^{-1} , and support our findings numerically using the spring-loaded inverted pendulum model with a trunk. We extend our analysis to include perturbations in terrain height (visible and camouflaged), and investigate the response of the VP mechanism to step-down perturbations both experimentally and numerically. Our experimental results show that the human running gait displays a VP_B of $\approx -30\text{ cm}$ and a forward trunk motion during the stance phase. The camouflaged step-down perturbations affect the location of the VP_B . Our simulation results suggest that the VP_B is able to encounter the step-down perturbations and bring the system back to its initial equilibrium state.

1. Introduction

Bipedal locomotion in humans poses challenges for stabilizing the upright body owing to the under-actuation of the trunk and the hybrid dynamics of the bipedal structure (table 1).

[†]Shared first authorship.

Table 1. Nomenclature.

general terminology	
CoM	centre of mass
TSLIP	spring loaded inverted pendulum model extended with a trunk
VP	virtual point
VP _A	virtual point above the centre of mass
VP _B	virtual point below the centre of mass
VP _{BL}	virtual point below the centre of mass and below the leg axis at touch-down
g	$g = 9.81 \text{ m s}^{-2}$, standard acceleration due to gravity
symbols related to the experiment	
l	distance between lateral malleolus and trochanter major of the leg in contact with the ground
CoP	centre of pressure
GRFs	ground reaction forces
V0	experiment with level ground
V10	experiment with 10 cm visible step-down perturbation
C10	experiment with 10 cm camouflaged step-down perturbation
R^2	coefficient of determination
γ	the trunk angle estimated from markers on L5 and C7. The trunk angle γ corresponds to the θ_c in the TSLIP model
N_{trial}	number of trials
$N_{\%}$	number of gait percentage times analysed
θ_{exp}	angle of the experimental measured GRFs
$\bar{\theta}_{\text{exp}}$	mean experimental angle of GRFs
θ_{theo}	angle of theoretical forces
\vec{p}	impulse
$\vec{p}_{\text{normalized}}$	normalized impulse
\vec{P}_{brake}	braking impulse
\vec{P}_{prop}	propulsion impulse
symbols related to the simulations	
$[x_G, z_G, \theta_G]$	state vector of the centre of mass
$[r_{FG}, r_{FV}, r_{FH}]$	position vectors from foot to the centre of mass, virtual point and hip joint, respectively
Δz	step-down height
m	mass
J	moment of inertia
l	leg length
θ_L	leg angle
τ_H	hip torque
F_{sp}	leg spring force
F_{dp}	leg damper force
${}_f\mathbf{F}_a$	axial component of the ground reaction force in foot frame
${}_f\mathbf{F}_t$	tangential component of the ground reaction force in foot frame
r_{VP}	VP radius, the distance between the centre of mass and virtual point
θ_{VP}	VP angle, the angle between trunk axis and VP _A , or the vertical axis passing from CoM and VP _B
superscripts	
AP	apex event, where the centre of mass reaches to its maximum height

TD	leg touch-down event
TO	leg take-off event
Des	desired value of the variable
subscripts	
i	current step
$i - 1$	previous step

Human gait studies investigate the underlying mechanisms to achieve and maintain the postural stability in symmetrical gaits such as walking and running. One major observation states that the ground reaction forces (GRFs) intersect near a virtual point (VP) above the centre of mass (CoM) [1]. Subsequent gait studies report that the VP is 15–50 cm above the CoM (VP_A) in the sagittal plane for level walking [1–5]. Among those, only a single study reports a limited set of level walking trials with a VP below the CoM (VP_B) [1]. The VP_A strategy is also observed when coping with the step-down perturbations in human walking, even when walking down a camouflaged curb [5]. A similar behaviour is observed for the avians, where a VP_A of 5 cm is reported for level walking, grounded running, and running of the quail [6,7]. Unlike in the studies with healthy subjects, it is reported that humans with Parkinson's disease display a VP_B when walking [8]. In addition, a VP_B was identified in the frontal plane for human level walking [9]. The existing literature for human running report a VP_A [7,10]. However, these experiments are limited to a small subset of subjects and trials, hence are not conclusive.

The observation of the GRFs intersecting at a VP suggests that there is potentially a control mechanism to regulate the whole-body angular momentum [1,11,12]. Based on this premise, the behaviour of a VP-based postural mechanism would depend on the location and adjustment of the VP. It also raises the question whether the VP position depends on the gait type, locomotor task (e.g. control intent) and terrain conditions.

The spring loaded inverted pendulum model (SLIP) is extensively used in gait analysis owing to its capability to reproduce the key features of bipedal locomotion. The SLIP model is able to reproduce the CoM dynamics observed in human walking [13] and running [14–16]. This model can be extended with a rigid body (TSLIP) to incorporate the inertial effects of an under-actuated trunk, where the trunk is stabilized through a torque applied at the hip [1,10,12].

Based on the experimental observations, the VP is proposed as a control method to determine the hip torque in the TSLIP model to achieve postural stability [12]. The VP as a control mechanism in the TSLIP model has been implemented for human walking [4,17–20], hopping [21,22], running [12,23,24] and avian gaits [6,25]. It is also implemented and tested on the ATRIAS robot for a walking gait [26]. However, the currently deployed robotic studies are limited to a small set of gait properties (e.g. forward speed) and simple level terrain conditions.

In the simulation model, the selection of the VP position influences the energetics of the system by distributing the work performed by the leg and the hip [23,25]. A VP_B in the human TSLIP model reduces the leg loading at the cost of increased peak hip torques for steady-state gaits. A VP_A yields lower duty factors and hence higher peak vertical GRF magnitudes, whereas a VP_B yields larger peak horizontal GRF magnitudes. Consequently, a VP_A can be used to reduce the kinetic energy fluctuations of the CoM, and a VP_B to reduce the potential energy fluctuations.

In human gait, the trunk moves forward during the single stance phase of walking and running, which is reversed by a backward trunk motion in the double stance phase of walking [27] and flight phase of running [10,27]. In TSLIP model simulations of human running, the trunk moves forward during the stance phase if a VP_B is used, whereas it moves backward for a VP_A [12,23,25,28].

One potential reason for the differences between the human and the model may be that the TSLIP model does not distinguish between the trunk and whole-body dynamics. In human walking, the trunk pitching motion is reported to be 180° out-of-phase with the whole body [2]. A VP_A in the TSLIP model predicts the whole-body dynamics with backward rotation, and it follows that the trunk rotation is in the opposite direction (i.e. forward). The phase relationship between the trunk and whole-body rotation has not been published for human running, to our knowledge. However, we can indirectly deduce this relationship from the pitch angular momentum patterns. In human running, the pitch angular momentum of the trunk and the whole body are inphase, and they both become negative during stance phase, i.e. clockwise rotation of the runner [11]. The negative angular

momentum indicates that the GRFs should pass below the CoM. Therefore, a VP_B in the TSLIP model can predict the whole-body dynamics with forward rotation, and the trunk rotation is in the same direction (i.e. forward).

The VP can also be used to manoeuvre, when the VP target is placed out of the trunk axis [12,21]. A simulation study proposes to shift the VP position horizontally as a mechanism to handle stairs and slopes [29]. The gait analyses provide insights into the responses of GRFs to changes in terrain. In human running, step-down perturbations increase the magnitude of the peak vertical GRF. The increase gets even higher if the drop is camouflaged [30]. However, there is no formalism to describe how the VP position relates to the increase in GRFs in handling varying terrain conditions.

In the first part of our work, we perform an experimental analysis to acquire trunk motion patterns and ground reaction force characteristics during human running. Our gait analysis involves human-level running, and running over visible and camouflaged step-down perturbations of -10 cm. We expect to see a VP below the CoM (VP_B) shaped by the ground reaction forces, based on the results in [27], and a net forward trunk pitch motion during the stance phase, based on previous results from level running [27]. If the mechanism leading to a VP_B in level running remains active, it should also extend to camouflaged, step-down perturbations. Consequently, we hypothesize to observe a VP_B also in the step-down experiments.

In the second part, we perform a simulation analysis using the TSLIP model with the gait parameters estimated from our experiments. We generate an initial set of gaits that match to the experimental set-up, and extend our analysis to larger set of step-down perturbations up to -40 cm, which is close to the maximum achievable perturbation magnitude in avians [31]. We investigate whether a VP_B controller is able to stabilize the gait against the step-down perturbations, and if so, how does it contribute to the energy flow in counteracting the perturbation.

2. Methods

2.1. Experimental methods

In this section, we describe the experimental set-up and measurement methods. In our experiments, 10 physically active volunteers (nine male, one female, mean \pm s.d., age: 24.1 ± 3.4 years, mass: 73.8 ± 7.3 kg, height: 179.9 ± 7.6 cm) are instructed to run over a 17 m track. Prior to participation, an informed consent form was obtained from each volunteer. The experiment was approved by the local ethics committee and was in accordance to the Declaration of Helsinki. The running track has two consecutive force plates in its centre, where the first plate is fixed at ground-level, and the second one is height adjustable. We designed three sets of experiments, where the subjects were asked to run at their self-selected velocity¹ (4.9 ± 0.5 m s⁻¹, table 2). In the first experiment, the subjects were asked to run on a track with an even ground (V0). In the second experiment, the second force plate was lowered -10 cm, which was visible to the subjects (V10). In the third experiment, the second force plate was lowered -10 cm, and an opaque sheet was added on top of the plate on ground level to camouflage the drop. A wooden block was randomly placed between the second force plate and the opaque sheet during the course of the experiment without subject's knowledge. In other words, the subjects were not aware whether the step would be on the ground level (C0), or would be a step-down drop (C10). The step corresponding onto the first force plate is referred to as step -1 , and the step to the second force plate as step 0.

All trials were recorded with eight cameras by a three-dimensional motion capture system working with infrared light. In summary, 12 spherical reflective joint markers (19 mm diameter) were placed on the tip of the fifth toe [A], malleolus lateralis [B], epicondylus lateralis femoris [C], trochanter major [D], and acromion [E] on both sides of the body as well as on L5 [F] and C7 [G] processus spinosus (figure 1). The CoM was determined with a body segment parameter method according to Winter [32]. The trunk angle γ was calculated from the line joining C7 to L5 with respect to the vertical [33].

Further information concerning the participants, and the technical details of the measurement equipment (i.e. force plates, cameras) can be found in Müller *et al.* [30] and partly in Ernst *et al.* [34].

The method for analysing the gait data and estimating a potential VP is analogous to the gait analysis carried out for the human walking in [5]. Here, we denote the intersection point of the GRF vectors as a VP without implications for this point being above or below the CoM. To compute the VP, we use the

¹The velocity was calculated for the stance phases of both contacts.

Table 2. Statistical analysis of VP, R^2 , impulse and gait properties. (V0, visible level running; V10 visible drop of -10 cm; C10, camouflaged drop of -10 cm; VP, horizontal (x) and vertical (z) positions of the virtual point relative to the centre of mass for the 90% and the 100% dataset; R^2 , coefficient of determination of the angles between measured ground reaction forces and forces through centre of pressure and VP; \vec{p}_{brake} , braking impulse and \vec{p}_{prop} , propulsion impulse in the x - and z -direction. Data are means \pm s.d. across all included subjects ($n = 10$; exception: duty factor is only calculated for nine subjects) for step -1 (pre-perturbed contact) and step 0 (perturbed contact). *Post hoc* analysis with Šidák correction revealed significant differences between ground conditions: differences from V0 and V10 are indicated with 'a' and 'b', respectively ($p < 0.05$).

	V0	V10	C10	p -value	F -value/ η^2
step -1					
VP variables					
VP $x_{100\%}$ [cm]	-2.9 ± 2.9	-8.5 ± 3.5^a	-8.6 ± 3.1^a	0.000	224.38/0.01
VP $x_{90\%}$ [cm]	-3.4 ± 2.8	-8.7 ± 3.4^a	-9.1 ± 3.2^a	0.000	146.41/0.01
VP $z_{100\%}$ [cm]	-31.5 ± 4.9	-31.3 ± 5.0	-31.7 ± 6.6	0.965	0.04/0.00
VP $z_{90\%}$ [cm]	-30.8 ± 5.8	-30.7 ± 5.2	-31.5 ± 6.5	0.997	0.23/0.00
$R^2_{100\%}$ [%]	76.0 ± 14.6	79.0 ± 12.1	77.3 ± 13.2	0.424	0.90/0.00
$R^2_{90\%}$ [%]	88.1 ± 3.4	89.4 ± 3.4	88.5 ± 3.1	0.411	1.45/0.00
impulse					
$\vec{p}_{\text{brake},x}$	-0.05 ± 0.02	-0.05 ± 0.02	-0.04 ± 0.02	0.162	2.02/0.00
$\vec{p}_{\text{brake},z}$	0.53 ± 0.11	0.47 ± 0.10	0.49 ± 0.06	0.051	3.53/0.01
$\vec{p}_{\text{prop},x}$	0.11 ± 0.01	0.12 ± 0.02	0.11 ± 0.01	0.078	2.94/0.00
$\vec{p}_{\text{prop},z}$	0.56 ± 0.02	0.57 ± 0.04	0.55 ± 0.04	0.421	0.91/0.00
step 0					
VP variables					
VP $x_{100\%}$ [cm]	-2.8 ± 4.5	-4.0 ± 4.6^a	-7.1 ± 5.1^a	0.014	7.95/0.01
VP $x_{90\%}$ [cm]	-2.6 ± 4.6	-4.3 ± 4.7	-7.0 ± 5.0^a	0.018	7.17/0.01
VP $z_{100\%}$ [cm]	-35.2 ± 6.1	-38.8 ± 5.6^a	-24.6 ± 14.5	0.047	5.17/0.10
VP $z_{90\%}$ [cm]	-35.0 ± 6.3	-37.6 ± 5.7	-24.0 ± 16.4	0.074	4.04/0.10
$R^2_{100\%}$ [%]	81.9 ± 11.3	64.1 ± 15.9^a	65.1 ± 13.4	0.021	6.87/0.17
$R^2_{90\%}$ [%]	92.0 ± 2.1	83.0 ± 5.9^a	$69.4 \pm 8.7^{a,b}$	0.000	70.13/0.13
impulse					
$p_{\text{brake},x}$	-0.10 ± 0.02	-0.11 ± 0.03	$-0.04 \pm 0.02^{a,b}$	0.000	40.27/0.01
$p_{\text{brake},z}$	0.69 ± 0.08	0.83 ± 0.12^a	0.63 ± 0.12^b	0.000	20.92/0.10
$p_{\text{prop},x}$	0.09 ± 0.02	0.09 ± 0.01	$0.06 \pm 0.01^{a,b}$	0.000	14.26/0.00
$p_{\text{prop},z}$	0.46 ± 0.08	0.48 ± 0.05	0.45 ± 0.06	0.309	1.19/0.01
gait properties					
velocity [m s^{-1}]	4.9 ± 0.5	4.9 ± 0.5	5.1 ± 0.4	0.148	2.13/0.11
stance time [s]	0.18 ± 0.02	0.17 ± 0.02^a	$0.14 \pm 0.01^{a,b}$	0.000	62.67/0.00
duty factor [%]	26.7 ± 2.0	24.8 ± 1.6^a	$22.4 \pm 1.5^{a,b}$	0.008	37.20/0.01

instantaneous GRF vectors, which have an origin at the centre of pressure (CoP) and are expressed in a CoM-centred coordinate frame that aligns with the gravity vector in the vertical axis [3]. The CoP is calculated from the kinetic data using the method described in Winter [32]. Then, the VP is estimated as the point, which minimizes the sum of the squared distances between the GRF vectors and itself. For the camouflaged setting with a wooden block placed on the force plate (C0), we can not calculate the CoP accurately. Thus, the VP is not estimated for the C0 case.

The human gait data involves impact forces at the leg touch-down, which introduces an additional behaviour in the GRF pattern [30,35,36]. In order to see the influence of the impact on VP, we are presenting our recorded data in two ways. The first calculation involves the full GRF data from leg touch-down to take-off (100% dataset), whereas the second calculation involves the GRF data starting from 10% of the stance to the leg take-off (90% dataset).

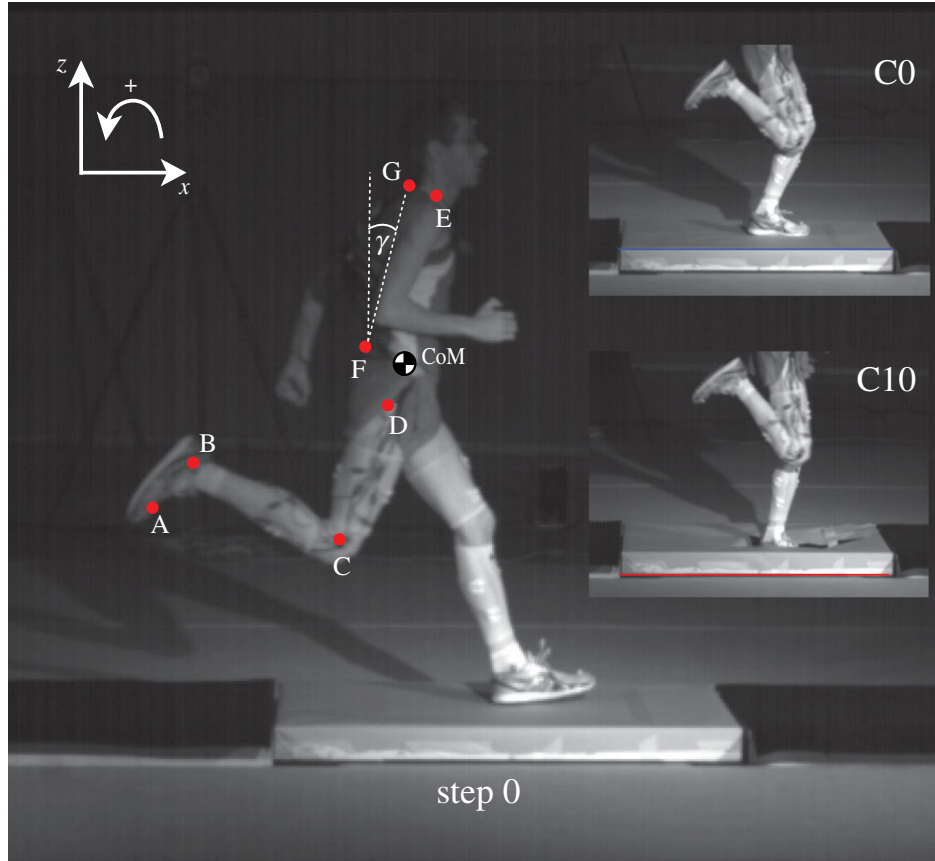


Figure 1. Experimental set-up. The first force plate is on the ground level, whereas the second force plate is height adjustable (step 0). The camouflaged setting for the second force plate is shown on the right for elevations of 0 cm (C0, blue) and –10 cm (C10, red). The placement of the motion capture markers is given on the left, where the markers are denoted the letters A–G. The trunk angle is shown with γ and is positive in the counterclockwise direction.

In the VP concept, all of the GRF vectors start from the CoP and point to a single VP. However, the human gait data differs from this theoretical case, as the human is more complex. To evaluate the amount of agreement between the theoretical VP-based forces and experimentally measured GRFs, we use a measure called the *coefficient of determination* (R^2) similar to Herr & Popovic [37]:

$$R^2 = \left(1 - \frac{\sum_{i=1}^{N_{\text{trial}}} \sum_{j=1}^{N_{\%}} (\theta_{\text{exp}}^{ij} - \theta_{\text{theo}}^{ij})^2}{\sum_{i=1}^{N_{\text{trial}}} \sum_{j=1}^{N_{\%}} (\theta_{\text{exp}}^{ij} - \bar{\theta}_{\text{exp}})^2} \right) \times 100\%. \quad (2.1)$$

The $(\theta_{\text{exp}}, \theta_{\text{theo}})$ are the experimental GRF and theoretical force vector angles, N_{trial} is the number of trials, and $N_{\%} = 100$ is the measurement time. Here, $\bar{\theta}_{\text{exp}}$ is the grand mean of the experimental GRF angles over all trials and measurement times. The number of trials is equal to 30 for visible conditions (15 for V0 and 15 for V10) and 20 for the camouflaged conditions (12 for C0 and 8 for C10).

Note that $R^2 = 100\%$ if there is a perfect fit for the experimental GRF and the theoretical force vector angles. The value of R^2 approaches zero as the estimation of the model is equal to the use of θ_{exp} as an estimator [37].

We also compute the horizontal and vertical impulses \vec{p} for two intervals (braking and propulsion) by integrating the GRFs over time. The braking interval went from touch-down to mid-stance (zero-crossing of the horizontal GRFs) and the propulsion interval mid-stance onwards. We report the values for brake-propulsion intervals individually in §3.1. To enable the comparison among subjects, we normalize the impulses to each subject's body weight (BW), leg length (l , the distance between lateral malleolus and trochanter major of the leg in contact with the ground) and standard gravity (g) in accordance with [38] as,

$$\vec{p}_{\text{normalized}} = \frac{\vec{p}}{\text{BW} \cdot \sqrt{l/g}}. \quad (2.2)$$

Because of the inaccuracy in calculating the CoP, we did not analyse the C0 statistically. For all other experimental settings (V0, V10 and C10), we used repeated measures ANOVA ($p < 0.05$) with post hoc

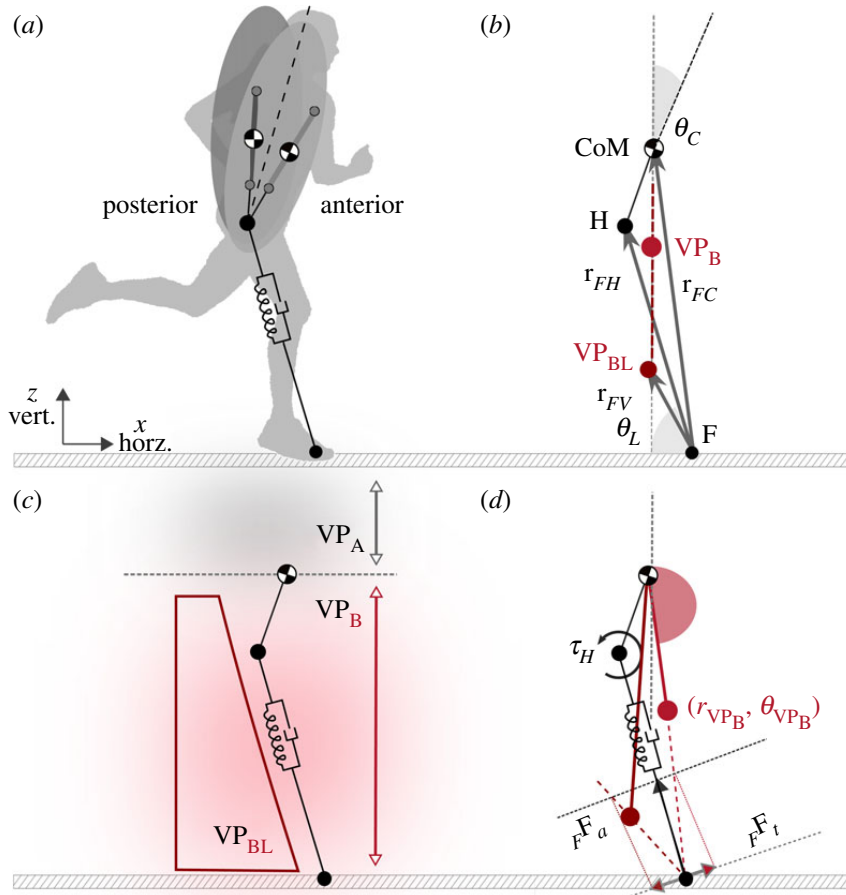


Figure 2. (a) TSLIP model that shows the forward (anterior) and backward (posterior) trunk motion. (b) Vector notations used in equations of motion. (c) The parameter space for the VP is divided into two regions: the virtual points above the centre of mass (VP_A) and below (VP_B). VP_A causes backward and VP_B causes forward trunk rotation during the stance phase. Each subspace is divided further with respect to the leg axis, where the sign of the hip torque changes. (d) For VP_B , the points above the leg axis yield a negative and points below (VP_{BL}) yield a positive hip torque at touch-down. The VP is described with the radius (r_{VP}) and angle (θ_{VP}) that is expressed in the CoM centred world coordinate frame. Here, presented human running experiments reveal that the VP is -30 cm below the CoM (see §3.1). This corresponds to the VP_{BL} region with -180° VP angle in our simulation.

analysis (Šidák correction) to test the statistical significance of the estimated VP position, the impulses and additional gait properties. In order to verify whether the VP is above or below the CoM (VP_A or VP_B), we performed a one-sample t -test compared with zero, separately for each condition with Šidák correction as the *post hoc* test.

2.2. Simulation methods

In this section, we describe the TSLIP model that we use to analyse how the VP reacts to the step-down perturbations in human running. The TSLIP model consists of a trunk with mass m and moment of inertia J , which is attached to a massless leg of length l and a massless point foot F (figure 2a). The leg is passively compliant with a parallel spring-damper mechanism, whereas the hip is actuated with a torque τ_H . The dynamics of the system is hybrid, which involves a flight phase that has ballistic motion, followed by a stance phase that reflects the dynamics of the spring-damper-hip mechanism. The phases switch when the foot comes in contact with the ground at touch-down, and when the leg extends to its rest length l_0 at take-off.

The equations of motion for the CoM state (x_C, z_C, θ_C) during the stance phase can be written as in equation (2.3), where the linear leg spring force $F_{sp} = k(l - l_0)$ and bilinear leg damping force $F_{dp} = c\dot{l}(l - l_0)$ generate the axial component of the GRF in foot frame ${}_F\mathbf{F}_a = (F_{sp} - F_{dp})[-\cos\theta_L \sin\theta_L]^T$. Here, k refers to the spring stiffness and c to the damping coefficient. The hip torque τ_H creates the tangential component of the GRF ${}_F\mathbf{F}_t = (-\tau_H/l_L)[\sin\theta_L \ -\cos\theta_L]^T$ (figure 2d):

$$\begin{aligned} m \begin{bmatrix} \ddot{x}_C \\ \ddot{z}_C \end{bmatrix} &= {}_F\mathbf{F}_a + {}_F\mathbf{F}_t + \mathbf{g}, \\ J \ddot{\theta}_C &= -\mathbf{r}_{FC} \times ({}_F\mathbf{F}_a + {}_F\mathbf{F}_t). \end{aligned} \quad (2.3)$$

The leg and the hip maintain the energy balance of the system. The hip increases the system energy to propel the body forward, whereas the leg damper removes an equivalent energy in return. We determine τ_H , such that the GRF points to a VP, which is characterized by the radius r_{VP} (i.e. distance between the hip and CoM) and angle θ_{VP} , as shown in figure 2*d* (red circle). The hip torque as a function of the VP is written as,

$$\begin{aligned}\tau_H = \tau_{VP} &= {}_P\mathbf{F}_a \times \frac{\begin{bmatrix} \mathbf{r}_{FV} \times \mathbf{r}_{FH} \\ \mathbf{r}_{FV} \cdot \mathbf{r}_{FH} \end{bmatrix}}{\|\mathbf{r}_{FV} \cdot \mathbf{r}_{FH}\|} \times l, \\ \mathbf{r}_{FV} &= \mathbf{r}_{FC} + r_{VP} \begin{bmatrix} -\sin(\theta_C + \theta_{VP}) \\ \cos(\theta_C + \theta_{VP}) \end{bmatrix}.\end{aligned}\quad (2.4)$$

We use two linear controllers: one for the leg angle at touch-down θ_L^{TD} , and the other for the VP angle θ_{VP} , both of which are executed at the beginning of the step at apex, as shown in appendix A.2., figure 12. The leg angle is regulated as,

$$\theta_L^{TD} |_{i} = \theta_L^{TD} |_{i-1} + k_{\dot{x}_0}(\Delta \dot{x}_C^{AP} |_{i-1}) + k_{\dot{\theta}}(\Delta \dot{\theta}_C^{AP} |_{i-1}), \quad (2.5)$$

with $\Delta \dot{x} |_{i-1}$ being the difference in apex velocity \dot{x} between time steps -1 and i . The VP angle is defined with respect to a CoM-centred, stationary coordinate frame that is aligned with the global vertical axis, if the VP is set below the CoM (figure 2*b,d*) [25]. It is adjusted based on the difference between the desired mean body angle θ_C^{Des} , and the mean body angle observed in the last step $\Delta \theta_C$ as,

$$\theta_{VP} |_{i} = \theta_{VP} |_{i-1} + k_{VP}(\theta_C^{Des} - \Delta \theta_C). \quad (2.6)$$

The model parameters are selected to match a 80 kg human with 1 m leg length (see appendix A.1., table 4 for details). The damping coefficient is set to $c = 680 \text{ kNsm}^{-1}$ to match the trunk angular excursion of 4.5° reported in [27,39,40]. The forward speed and VP radius are set to 5 m s^{-1} and -30 cm , respectively, to match our estimated gait data in table 2. A VP radius of -30 cm becomes below the leg axis at leg touch-down with the model parameters we chose. Because the position of VP relative to the leg axis affects the sign of the hip torque, the VP_B region is separated into two and the points below the leg axis are called VP_{BL} (figure 2*c,d*), in accordance with [23].

First, we generate a base gait for level running using the framework in [23], which corresponds to the V0 in our human running experiments. Then, we introduce step-down perturbations of $\Delta z = [-10, -20, -30, -40 \text{ cm}]$ in step 0. The -10 cm drop corresponds to the V10 and C10 of the human running experiments. In the simulations, the VP controller is blind to the changes in step 0, because the controller update happens only at the apex of each step. During step 0, the state of the CoM diverges from the equilibrium conditions. The postural correction starts at step 1, as the leg touch-down angle and VP angle are adjusted in response to the changes in the CoM apex state. By contrast, small adaptations might already be active at step 0 in the human experiments, e.g. resulting from swing leg retraction dynamics [16,30].

The step-down perturbation increases the total energy of the system. The added energy can be either dissipated e.g. via the hip torque or leg damper, or converted to other forms of energy e.g. change in speed or hopping height. In the latter case, we need to update the desired forward speed in the leg angle control (equation (2.5)) until all excess energy is converted to kinetic energy.

We implemented the TSLIP model in MATLAB[®] using variable step solver ode113 with a relative and absolute integrator error tolerance of 1×10^{-12} .

3. Results

3.1. Experimental results

The results and statistical values of the experiments are listed in table 2 and are illustrated in figures 3–5, and connected with simulation results, in figures 9–11. Additionally, significant mean differences will be highlighted in the following.

In figure 3, exemplary illustrations of the VP for single trials (V0 and C10) of different subjects at step 0 are shown. Here, the GRF vectors are plotted in a CoM-centred coordinate frame where the vertical axis is parallel to gravity. The VP is calculated as the point which minimizes the sum of squared perpendicular distances to the GRFs for each measurement time point. To avoid biases caused by the impact peak, the VP was additionally calculated for only 90% of the dataset. That means that the GRFs of the first 10%

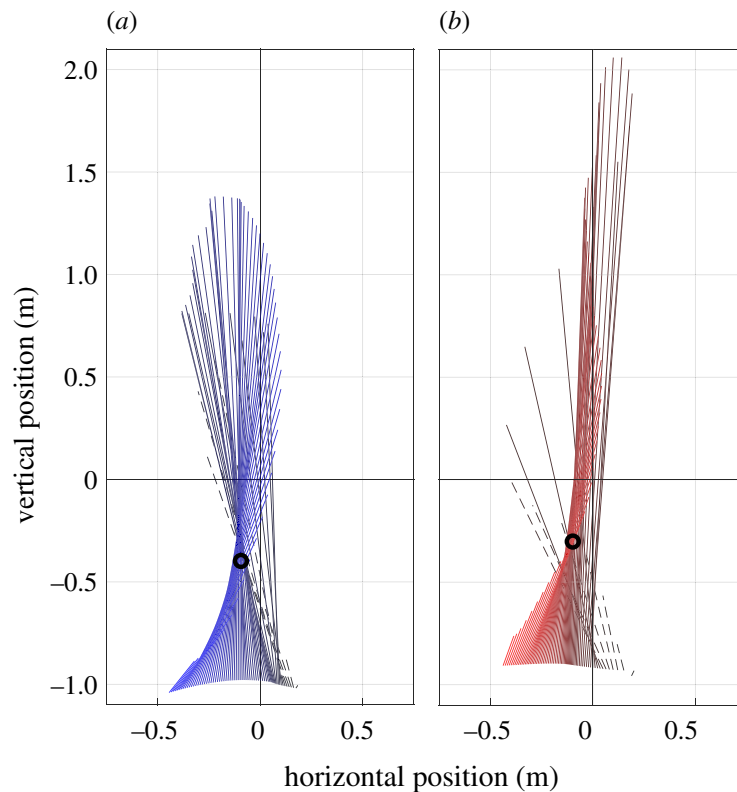


Figure 3. Examples of the ground reaction force vectors (GRFs) and the estimated virtual point (VP) for step 0 of V0 (a) and C10 (b) conditions of the human running experiments. The GRFs and VP are plotted with respect to a CoM-centred, stationary coordinate frame. Lines show the GRFs at different measurement times, originating at the CoP. The 90% dataset consists only of GRF data plotted as solid lines, the 100% dataset includes the entire stance phase GRF data. The black circle indicates the calculated VP for the 90% dataset. (a) V0: visible level running, black to blue, (b) C10: running with a camouflaged drop of -10 cm, black to red. For each condition, the trial with the spread around the VP nearest to the 50th percentile of all subjects was chosen.

of the stance phase (dashed lines) were neglected in this VP calculation (figure 3). Hence, the VP was computed for 90% and 100% datasets and the results for both VP are given in this section.

The VP in step -1 (pre-perturbed) and step 0 (perturbed) was below the CoM ($p \leq 0.001$, Cohen's $D \leq -1.486$) and between -38.8 ± 5.6 cm and -24.0 ± 16.4 cm (figure 4a). For step -1 , there were no differences between the ground conditions in the vertical VP position VPz (-31.0 cm) and the R^2 (88.7%; table 2). However, the horizontal VP position VPx was 5.5 cm (V10) and 5.7 cm (C10) more posterior in the drop conditions than in the level condition ($p < 0.001$). At step 0, VPx was 4.4 cm more posterior in C10 compared to V0 ($p < 0.028$), and for the 100% dataset 0.8 cm more posterior in V10 than in V0 ($p = 0.038$; table 2). There were only differences in VPz for the 100% dataset, it was 3.6 cm lower in V10 compared to V0 ($p = 0.029$). R^2 has the largest value for V0 ($92.0 \pm 2.1\%$; 90% dataset) and the smallest one for C10 ($64.1 \pm 8.7\%$; 100% dataset, figure 4b).

There were no significant differences between the ground conditions in the impulses of step -1 (table 2). For step 0, figure 5 suggests that the vertical GRFs are higher in the step conditions compared to V0, especially for the braking phase. The vertical braking impulse was higher in V10 than in V0 ($p = 0.008$) and in C10 ($p < 0.001$). We observe 2.9 BW peak vertical GRFs in V0, which yield to a vertical braking impulse of 0.69. In V10, the peak vertical GRFs were at 3.4 BW with a braking impulse of 0.83. In C10, the peak was the highest with 3.9 BW, but here, the peak is overlapping with the impact peak and therefore not comparable with that of the visible ground conditions (figure 5). Because of the shorter stance time in C10 (table 2), the braking impulse of 0.63 does not differ from the value of V0 despite the high impact peak. The vertical propulsion impulse of step 0 does not differ significantly between the ground conditions. The amounts of the horizontal braking and propulsion impulses were lower in C10 than in the visible conditions ($p \leq 0.004$). The sum of the horizontal braking and propulsion impulses of step 0 is in all ground conditions around zero. It means that there is no forward acceleration or deceleration.

The vertical CoM position relative to the CoP at the touch-down of step 0 is 3.5 cm higher in the drop conditions compared to V0 ($p < 0.001$) with 104.9 ± 5.2 cm and 1 cm higher in C10 than in V10 ($p = 0.019$).

The forward running velocity measured at step 0 does not vary between the experiments V0, V10 and C10, and is within the range of 5.0 ± 0.5 m s $^{-1}$. Despite the constant velocity, the stance time and the duty factor of step 0 show a variation between these experiments. The stance time gets shorter ($p = 0.029$) and

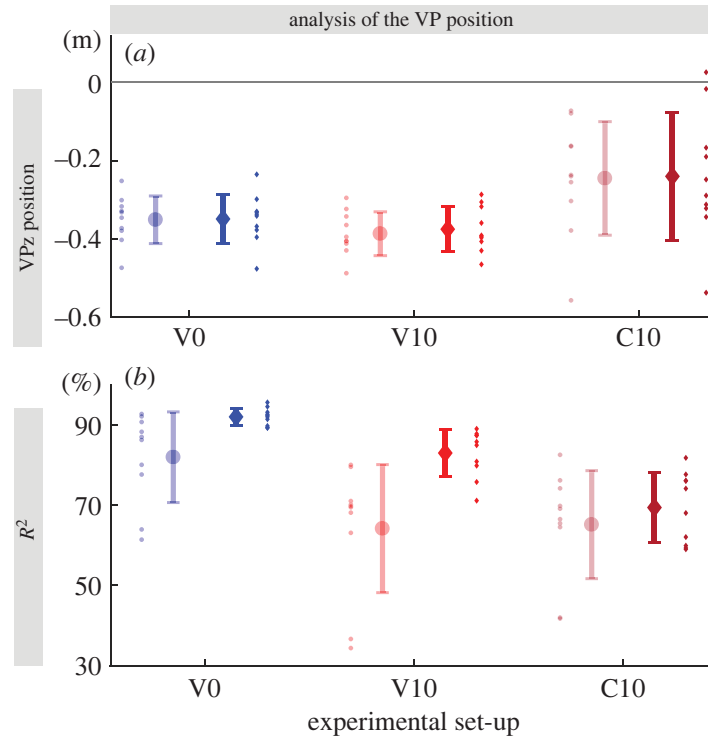


Figure 4. Mean \pm s.d. of the vertical virtual point position VPz (a), and R^2 values (b) between subjects ($n = 10$) for each ground condition (V0, V10 and C10) for step 0. (a) Each small dot is the median over all trials of one condition for one subject. (b) R^2 represents the ratio of the angle between measured and ideal forces and their variance. Each small dot represents one subject. Transparent circle: 100% dataset, non-transparent diamond: 90% dataset.

the duty factor lower ($p < 0.001$) when running down the visible drop and even shorter and lower when the drop is camouflaged ($p < 0.006$).

3.2. Simulation results

In this section, we present our simulation results and our analysis on how the VP reacts to step-down perturbations. The simulation gaits are generated for 5 m s^{-1} running with a VP target -30 cm below the CoM (VP_{BL}), which correspond to the estimated values of our experiments in §3.1.

The temporal properties of the base gait for the level running are given in table 3, where the duty factor is calculated as 26.2% with a stance phase duration of 0.16 s. The CoM trajectory of the base gait is shown in figure 7a₀ and its respective GRF vectors are plotted with respect to a hip centred stationary coordinate frame in figure 7b₀.

The base gait is subjected to step-down perturbations of $\Delta z = [-10, -20, -30, -40 \text{ cm}]$ at step 0. The leg angle controller in equation (2.5) and VP angle controller in equation (2.6) update on a step-to-step basis, therefore are informed about the deviation from the base gait at the beginning of step 1. At step 0, the state of the CoM at leg touch-down diverges from the equilibrium conditions: the trunk pitch angle is smaller (i.e. smaller trunk lean), and vertical speed is higher (see dark grey lines in appendix A.3., figure 13a,c). The VP position relative to the hip shifts downwards, as seen with circle marker in figure 7c_{1–c₄}. The perturbed state leads to an increase in trunk angular excursion during the stance, whereas the step ends with a higher forward speed, smaller trunk lean, and higher trunk angular velocity (see dark grey lines in appendix A.3., figure 13a,b,d). At step 1, the leg angle at touch-down is adjusted to a flatter angle and the VP angle to a larger angle (i.e. VP rotates clockwise). The VP position relative to the hip joint shifts backwards, as seen with dark cross marker in figure 7c_{1–c₄}. The backward VP_{BL} shift helps to restore the desired trunk lean and leads to a more pronounced forward trunk motion at step 1 (see red lines in appendix A.3., figure 13a). This restoring behaviour can also be inferred from the absence of a counterclockwise rotation towards the leg take-off, i.e. the GRF vectors are not coloured teal towards leg take-off in figure 7b_{1–b₄}, in contrast to figure 7b₀. We see that the VP_{BL} is able to counteract the step-down perturbations in the following steps by using only local controllers for the VP angle (equation (2.6)) and the leg angle (equation (2.5)), as shown in figure 7a_{1–a₄}. As we increase the magnitude of the step-down perturbations, we decrease the coefficients $k_x, k_{\dot{x}_0}$ in the leg angle control, so that the speed correction is slower and the postural control is prioritized (see appendix A.2). The generated gaits are able to converge to the initial equilibrium state (i.e. the initial energy level) within 15 steps after the step-down perturbation at step 0.

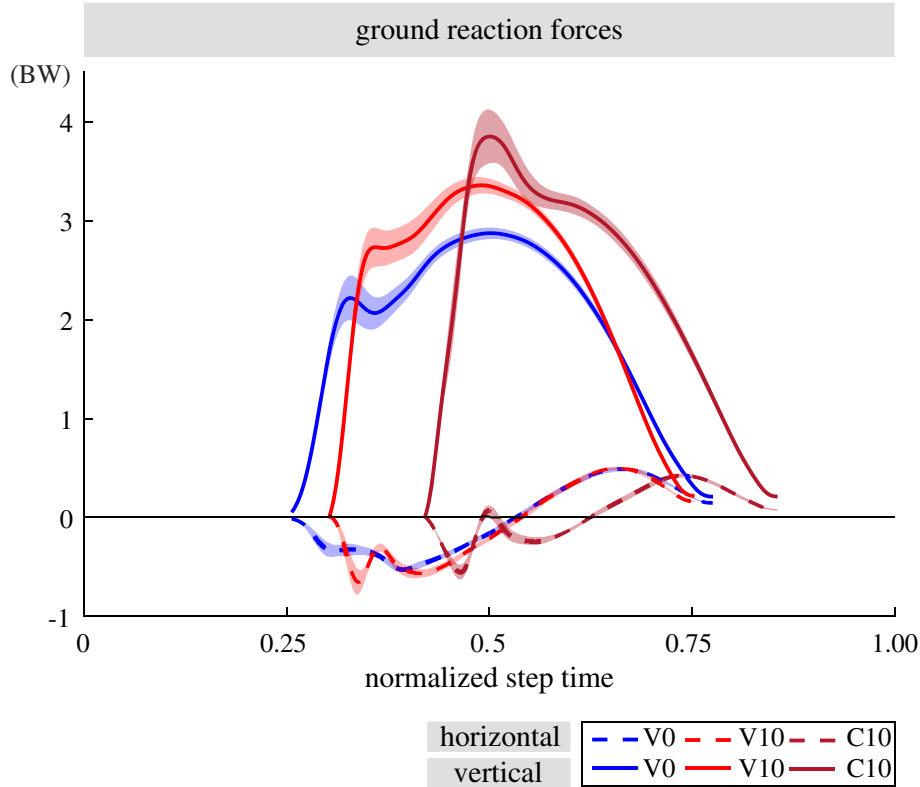


Figure 5. The ground reaction forces (GRFs) of step 0 for human running experiments V0 (blue), V10 (red) and C10 (brown). The GRFs are normalized to body weight (BW) of the subjects ($n = 10$). The mean values of the vertical and horizontal GRFs are plotted with solid and dashed lines, respectively. The \pm standard error is shown with the shaded area. For the C10 condition, the vertical GRF peak coincides with the peak caused by the impact peak forces. The duty factor of the V0 condition is $26.7 \pm 2.0\%$, whereas it is $24.8 \pm 1.6\%$ for the V10 condition and $22.4 \pm 1.5\%$ for the C10 condition.

Table 3. Gait properties of the simulated trajectories. (In the presence of step-down perturbations, the VP_{BL} method is able to bring the system back to its initial equilibrium state. Therefore, the gait properties are the same for the even ground and perturbed terrain, after reaching the steady-state condition.)

property	unit	value	property	unit	value
duty factor	%	26.2	VP angle	$^{\circ}$	-180
stance time	s	0.16	trunk angular excursion	$^{\circ}$	4.45
forward speed	$m s^{-1}$	5	leg angle at touch-down	$^{\circ}$	66

3.2.1. Energy regulation

In order to assess the response of the VP controller, we plot the VP position with respect to a hip centred non-rotating coordinate frame that is aligned with the global vertical axis, as it can be seen in figure 7 c_{1-c_4} . For a VP_{BL} target, a backward shift in VP position indicates an increase in the negative hip work.

The step-down perturbation at step 0 increases the total energy of the system by the amount of potential energy introduced by the perturbation, which depends on the step-down height. The position of the VP with respect to the hip shifts downwards by 0.5–1.9 cm depending on the drop height (see circle markers in figure 7 c_{1-c_4}). Consequently, the net hip work remains positive and its magnitude increases by 0.7 to 1.7 fold² (see solid lines in figures 6 c and 14 c). The leg deflection increases by 0.95 to 3 fold, whose value is linearly proportional to the leg spring energy as $E_{SP} = 1/2 k \Delta l_L^2$ (see solid lines in figures 6 a and appendix A.4., 14 a). The leg damper dissipates 1.5 to 6 fold more energy compared to its equilibrium condition (see solid lines in figures 6 b and appendix A.4., 14 b).

The reactive response of the VP starts at step 1, where the target VP is shifted to backwards by 1.2–2.8 cm and downwards by 0.6–2.9 cm depending on the drop height (see cross markers in figure 7 c). The backward shift in VP causes a 1.4 to 3.8 fold increase in the negative hip work, and the *net* hip work

²For quantities A and B, the fold change is given as $(B-A)/A$.

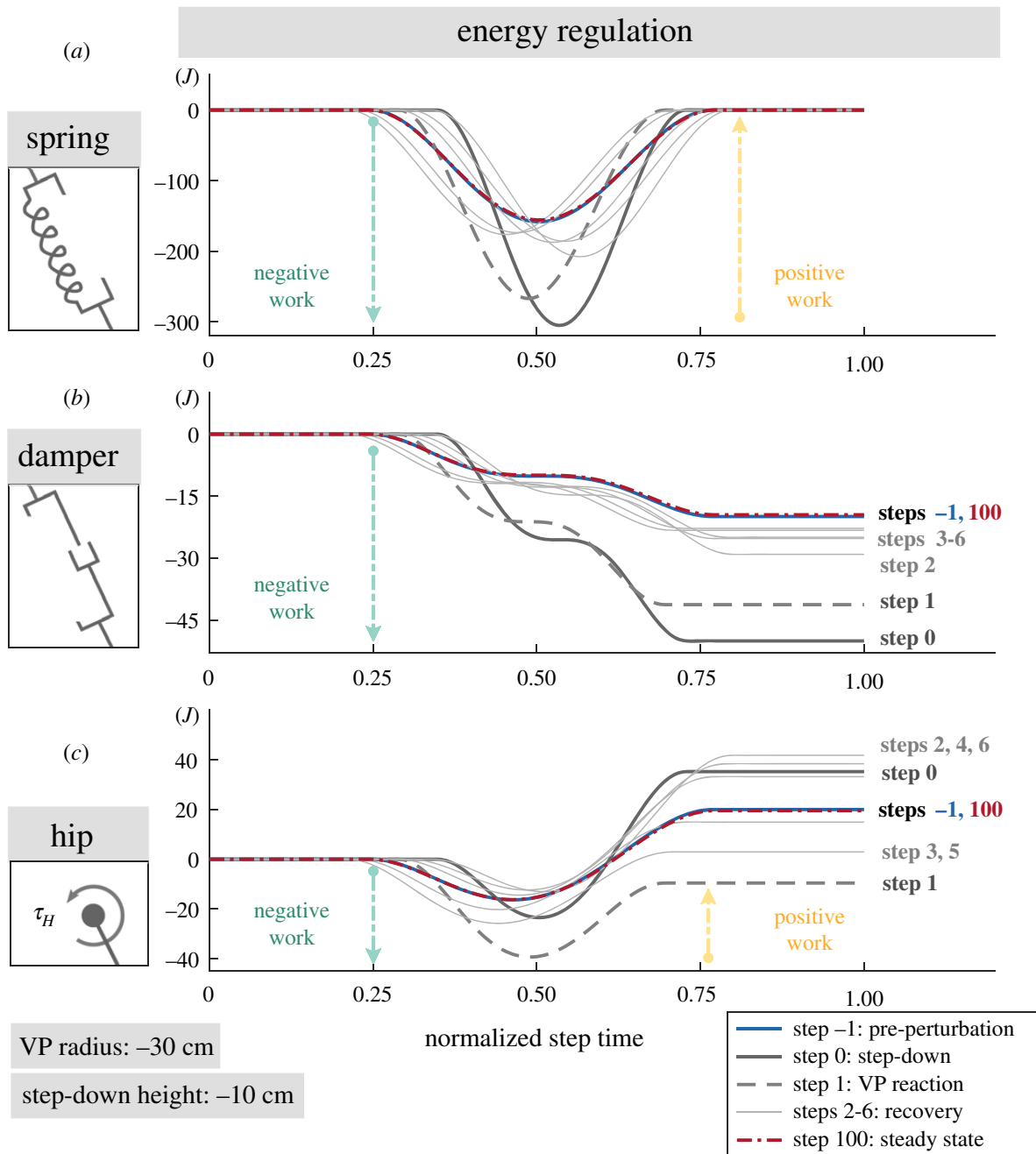


Figure 6. The energy levels for the leg spring (a), leg damper (b) and hip actuator (c) for -10 cm step-down perturbation. The step-down perturbation at step 0 increases the energy of the system, which causes an increase in leg deflection and a larger fluctuation in spring energy (a, solid dark grey line). The leg damper dissipates more energy and the hip actuator injects more energy than during its equilibrium condition (b–c, solid dark grey line). Starting with step 1, the VP begins to react to the energy change and the hip actuator starts to remove energy from the system (c, dashed line). In the following steps (solid grey line), the hip regulates the energy until the system reaches to the initial equilibrium state (solid blue line). Extended plots for the step-down height of $\Delta z = [-20, -30, -40$ cm] can be found in appendix A.4.

becomes negative (see dashed lines in figures 6c and appendix A.4., 14c). In other words, the hip actuator starts to remove energy from the system. As a result, the trunk leans more forward during the stance phase (see yellow coloured GRF vectors in figure 7b). The leg deflects 0.7 to 2.3 fold more than its equilibrium value, and the leg damper removes between 1 and 4.1 fold more energy. However, the increase in leg deflection and damper energy in step 1 are lower in magnitude compared to the increase in step 0. In step 1, we see the VP_{BL}'s capability to remove the energy introduced by the step-down perturbation.

In the steps following step 1, the target VP position is continued to be adjusted with respect to the changes in the trunk angle at apices, as expressed in equation (2.6) and shown with cross markers in figure 7c. The VP position gradually returns to its initial value, and the gait ultimately converges to its initial equilibrium, see coinciding markers diamond, rectangle in figure 7c. During this transition,

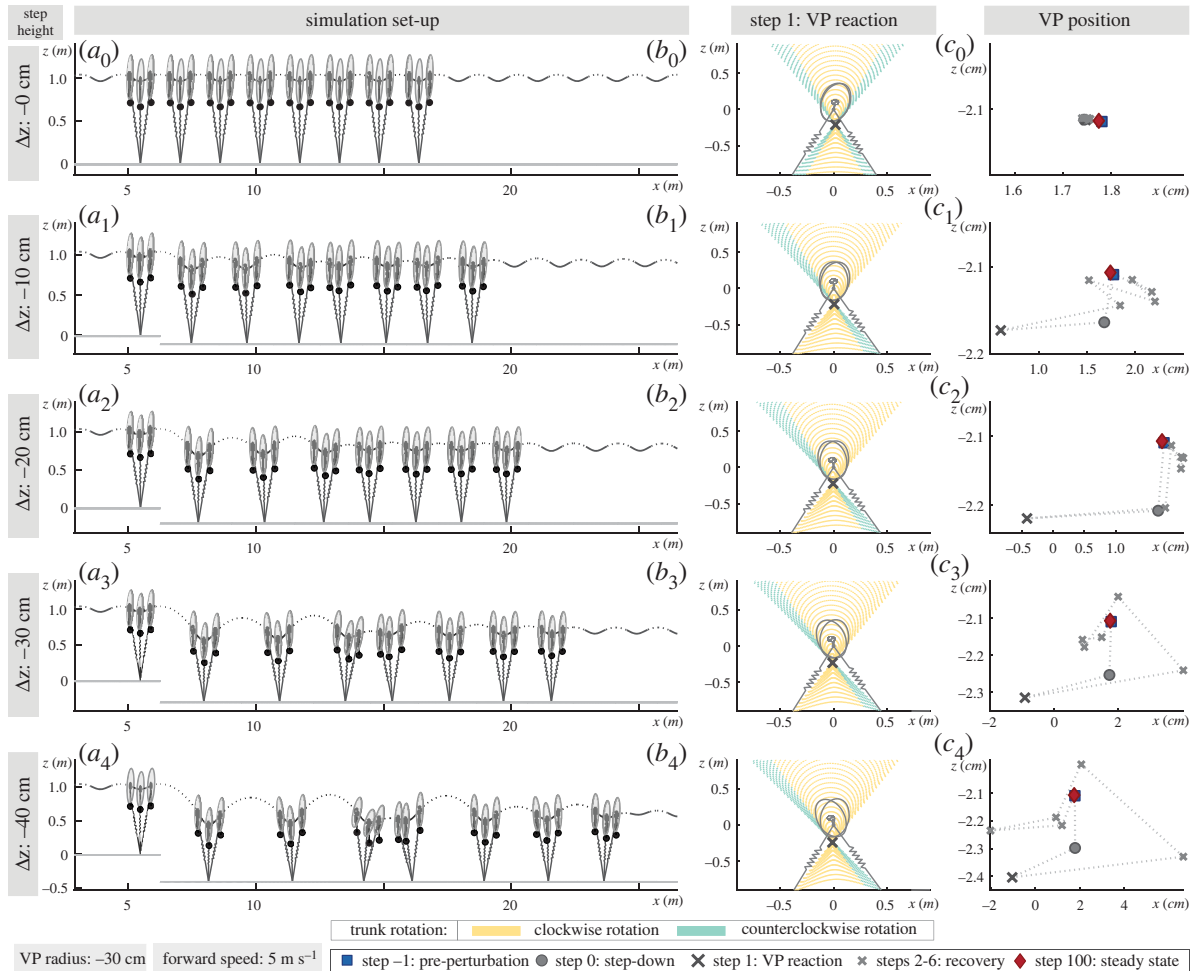


Figure 7. The analysis begins with a base gait a_0 based on the human running experiment V0, which has a VP target of -30 cm with a forward speed of 5 m s^{-1} . This base gait is then subjected to step-down perturbations of $\Delta z = [-10, -20, -30, -40 \text{ cm}]$ at step 0. The -10 cm perturbation corresponds to V10–C10 of the human running experiments. The model state at touch-down, mid-stance and take-off instances of steps -1 to 6 are drawn in a_0 – a_4 to display the changes in the trunk angle. At the perturbation step, the VP position shifts downwards with respect to a hip centred stationary coordinate frame (circle in c_1 – c_4). VP_{BL} counteracts to the perturbation at step 1 with a backward shift, which depletes the energy added by the stepping down (dark cross marker in c_1 – c_4). The GRF vectors of step 1 causes a forward trunk lean of 5 to 10° , which is shown in b_1 – b_4 . In the following steps, VP position is regulated to achieve the energy balance (cross marker), and gaits ultimately reach to the equilibrium state. The equilibrium state is given in table 3. A single gait involves 100 successful steps (diamond markers in figure c_1 – c_4).

the energy interplay between the hip and leg successfully removes the energy added to the system, as shown in figure 6*b,c* and in appendix A.4., figure 14*b,c* for larger step-down perturbation magnitudes.

3.2.2. Ground reaction force analysis

The energy increment owing to the step-down perturbation and the energy regulation of the VP_{BL} control scheme can also be seen in the GRF and impulse profiles.

The peak vertical GRF magnitude of the equilibrium state is 3 BW. It increases to 4.2–6.1 BW at step 0 with the step-down (figure 8*c,a*). The peak magnitude decreases gradually to its initial value in the following steps, indicating that the VP is able to bring the system back to its equilibrium. In a similar manner, the normalized vertical impulse increases from 1 to 1.4–2.2 at step 0 (see circle marker in figure 8*d,b*) and decreases to 1 in approximately 15 steps.

The peak horizontal GRF magnitude of the equilibrium state amounts to 0.6 BW. It increases to 0.9–1.4 BW at step 0 (figures 8*a* and appendix A.5., 15*a*). The sine shape of the horizontal GRF and its peak magnitude depend on the change in VP position. Therefore, the horizontal GRF impulse provides more information. The net horizontal GRF impulse is zero at the equilibrium state (see rectangle in figures 8*b* and appendix A.5., 15*b*). It becomes positive at the step-down perturbation (circle), leading to a net horizontal acceleration of the CoM. Consequently, the forward speed increases at the end of step 0 (see dark grey lines in appendix A.3., figure 13*b*). In step 1, the VP_{BL} and leg touch-down angle are adjusted with respect to the change in the state, which leads to a negative net horizontal GRF impulse (dark cross marker) and decelerates the

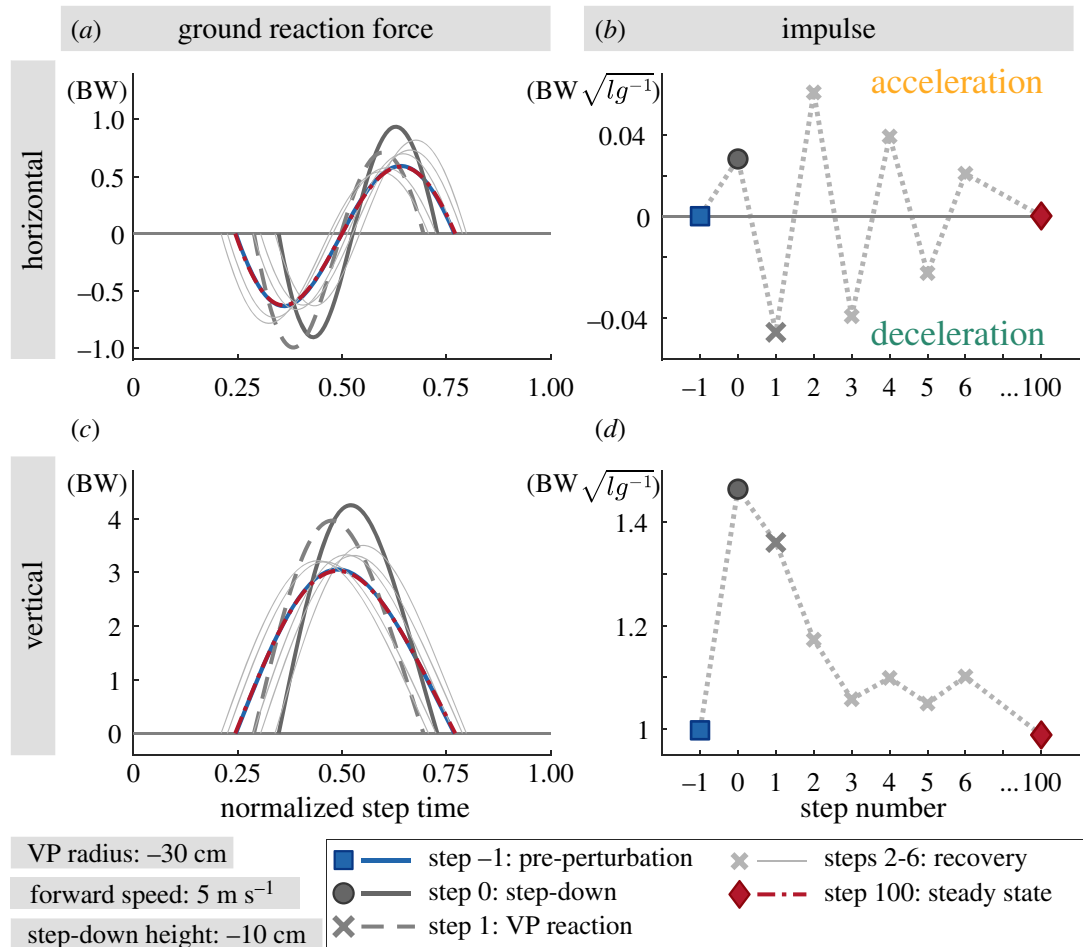


Figure 8. Numerical simulation results: the ground reaction forces (a,c) and the corresponding net impulses (b,d) for -10 cm step-down perturbation. The GRFs are normalized to body weights (BW), whereas the impulses are normalized to their $BW\sqrt{l/g}$ values. The effect of the VP_{BL} control can be seen in the horizontal GRF and impulse. VP_{BL} alters the net horizontal impulse, and causes either net horizontal acceleration or deceleration after the step-down perturbation. Consequently, the excess energy introduced by the perturbation is removed from the system. The vertical GRF and impulse increase with the perturbation and decrease gradually to its equilibrium value approximately within 15 steps. Extended plots for the step-down height of $\Delta z = [-20, -30, -40]$ cm can be found in appendix A.5.

body (see red lines in appendix A.3., figure 13b). In the following transient steps, the leg and VP angle adjustment yields successive net accelerations and decelerations (cross marker) until the system returns to its equilibrium state (diamond), where the net horizontal GRF impulse and forward acceleration is zero.

4. Discussion

In this study, we performed an analysis of experimental and simulation results regarding the force direction patterns during human-level running, and running onto a visible or camouflaged step-down. Our experimental results show that humans tend to generate a VP below the CoM (VP_B) for all terrain conditions. Our simulations support these experimental observations, and show that the VP_B as a controller can cope with step-down perturbations up to 0.4 times the leg length. In this section, we will address the VP location in connection with the gait type, and will discuss how our experimental results compare to our simulation results for the running gait.

4.1. Virtual point quality and location in human gait

In the first part, we discuss the validity of a VP estimated from the GRF measurements of the human running. We only consider step 0 of the 90% dataset, because the 100% dataset is biased by the additional effects of the impact forces and has low R^2 values [7]. In the second part, we discuss how the VP position is correlated to the gait type.

To determine the quality of the VP estimation, we used the coefficient of determination R^2 . In our experiments, the R^2 values for level running are high, where $R^2 \approx 92\%$ (see V0 in figure 4b). The

values of the R^2 get significantly lower for the visible drop condition, where $R^2 \approx 83\%$ (see V10 in figure 4b). On the other hand, the R^2 of the camouflaged drop conditions are even lower than for the visible drop conditions, where $R^2 \approx 69\%$ (see C10 in figure 4b). An R^2 value of $\approx 70\%$ is regarded as ‘reasonably well’ in the literature ([37], p. 475). Based on the high R^2 values, we conclude that the measured GRFs intersect near a *point* for the visible and camouflaged terrain conditions. We can also confirm that this point is as hypothesized below the CoM (VP_B), as the mean value of the estimated points is -32.2 cm and is significantly below the CoM.

We find a difference in the estimated VP position between the human walking and our recorded data of human running. The literature reports a VP above the CoM (VP_A) for human walking gait [1–3,5], some of which report a VP_A in human running as well [7,10]. By contrast, our experiments show a VP_B for human-level running at 5 m s^{-1} and running over a visible or camouflaged step-down perturbation. Previous studies only reported single trials of single subjects and no statistical analysis. We also did observe a few trials as outliers with a VP above the CoM, which are statistically not significant. Additionally, different ways for cropping the contact phase were considered in the previous studies, which affects the estimation of the vertical VP position. Here, we consistently remove the first 10% of the contact phase. Our experimental set-up and methodology are identical to [5], which reports results from human walking. Thus, we can directly compare the R^2 values for both walking and running. The R^2 value of the level running is 6 percentage points lower than the R^2 reported in [5] for level walking. The R^2 value for V10 running is 15 percentage points lower than V10 walking, whereas the R^2 for C10 running is up to 25 percentage points lower compared to C10 walking. In summary, we report that the spread of the R^2 is generally higher in human running at 5 m s^{-1} , compared to human walking.

4.2. Experiments versus model

In this section, we discuss how well the TSLIP simulation model predicts the CoM dynamics, trunk angle trajectories, GRFs and energetics of human running. A direct comparison between the human experiments and simulations is possible for the level running. The V0 condition of the human experiments corresponds to step -1 of the simulations (also to the base gait). Overall, we observe a good match between experiments and simulations for the level running (see figures 9–11). On the other hand, a direct comparison for the gaits with perturbed step is not feasible owing to the reasons given in §4.3 in detail. Here, we present perturbed gait data to show the extent of the similarities and differences between the V10 and C10 conditions of the experiments and step 0 and 1 of the simulations.

Concerning the CoM dynamics, the predicted CoM height correlates closely with the actual CoM height in level running, both of which fluctuate between 1.05–1 m with 5 cm vertical displacement (figure 9a_{1–a2}). The vertical displacement of the CoM is larger for the perturbed step, where the CoM height alternates between 1–0.9 m in the experiments (figure 9a₃) and 1.05–0.85 m in the simulations (figure 9a₄). The differences can be attributed to the visibility of the drop. Human runners visually perceiving changes in ground level and lowered their CoM by about 25% of the possible drop height for the camouflaged contact [41]. The mean forward velocity at leg touch-down is 5.2 m s^{-1} in the experiments (figure 9b₁). In the simulations, the leg angle controller adjusts the forward speed at the apex to a desired value. We set the desired speed to 5 m s^{-1} (figure 9b₂), which is the mean forward velocity of the step estimated from the experiments. For level running, both the experiments and simulations show a 0.2 m s^{-1} decrease in forward velocity between the leg touch-down and mid-stance phases (figure 9b_{1–b2}). As for the perturbed running, human experimental running shows a drop in forward speed of 4.5% for V10, and 0.1% for the C10 condition (figure 9b₃). Namely, there is no significant change in forward velocity during the stance phase for the C10 condition. The simulation shows a drop in forward speed of 9.5% for step 0, and 11.1% in step 1 (figure 9b₄).

The trunk angle is the least well-predicted state, since the S-shape of the simulated trunk angle is not recognizable in the human running data (figure 9c_{1–c2}). One of the reasons may be the simplification of the model. The flight phase of a TSLIP model is simplified as a ballistic motion, which leads to a constant angular velocity of the trunk. The human body, on the other hand, is composed of multiple segments, and intra-segment interactions lead to more complex trunk motion during flight phase. Furthermore, the model does not distinguish between the trunk and whole-body dynamics [42]. The large variance observed in the trunk angle trajectories between different subjects and trials might obscure small trunk angle tendencies, particularly for the C10 condition. Consequently, the mean trunk angle profiles do not provide much information about the trunk motion pattern, especially for the perturbed step for C10. Therefore, we cannot clarify to what extent the VP position is used for regulating the trunk motion in humans. However, a trend of trunk moving forward is visible in both simulation and

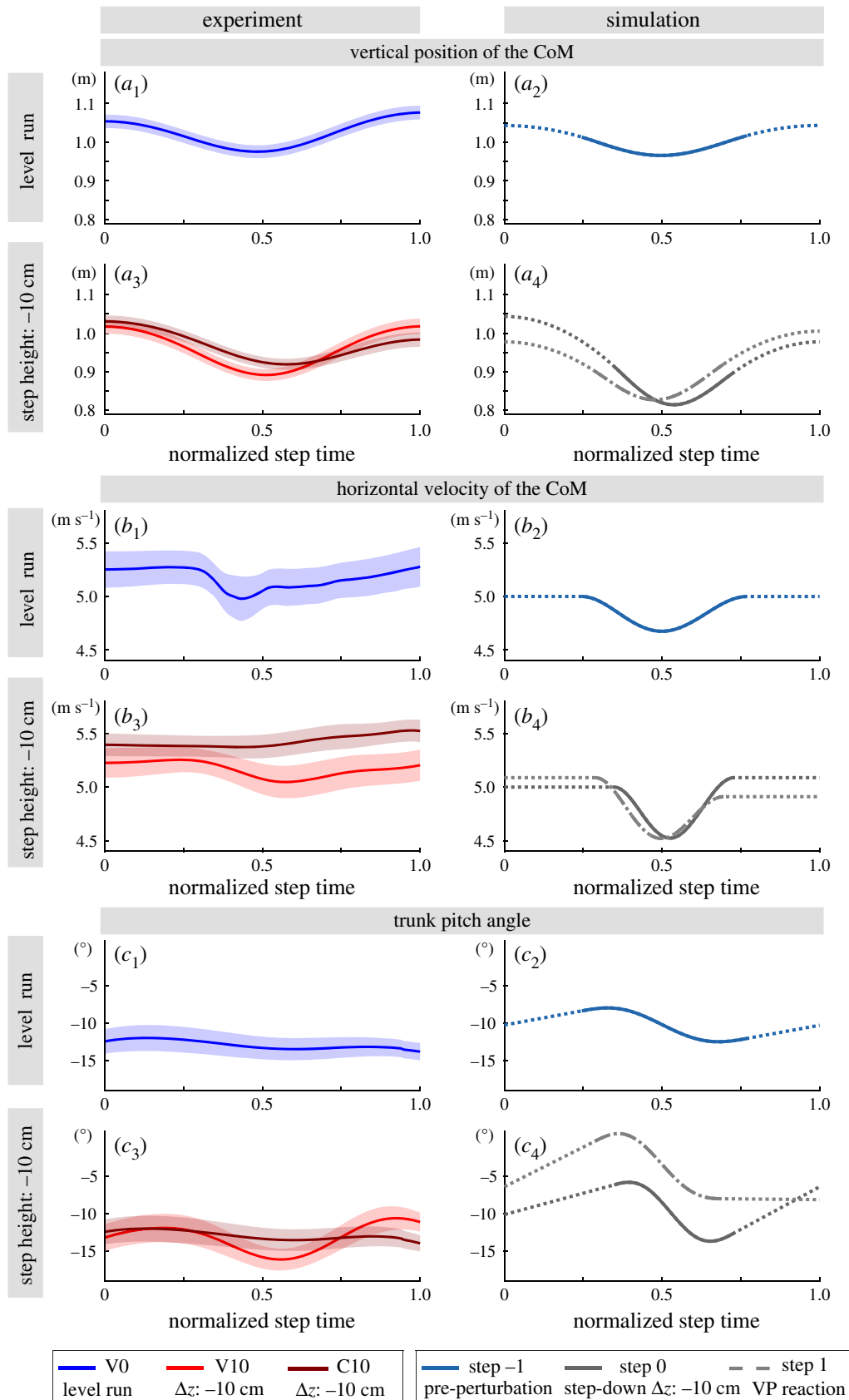


Figure 9. The CoM height (*a*), horizontal CoM velocity (*b*), and trunk angle (*c*) for step 0 of the experiments V0, V10 and C10 are shown on the left, and the steps -1, 0 and 1 of the simulation are shown on the right column. The mean is shown with a line and the standard error is indicated with the shaded region. The standard error equals to the standard deviation divided by the square root of number of subjects. The TSLIP model is able to predict the CoM height and forward speed. Its prediction capability is reduced for the trunk motion, as the flight phase involves ballistic motion and the trunk angular velocity is constrained to be constant.

experiments. The mean trunk angular excursion at step 0 of the experiments is 1.8° for V0, 5.5° for V10 and 1.9° for the C10 condition (figure 9*c*_{1–3}). The S-shaped pattern of the trunk motion becomes more perceivable in the experiments with a visible perturbed step (figure 9*c*₃). In the simulations, the trunk angular excursion is set to 4.5° for level running based on [27,39,40]. The magnitude of the trunk

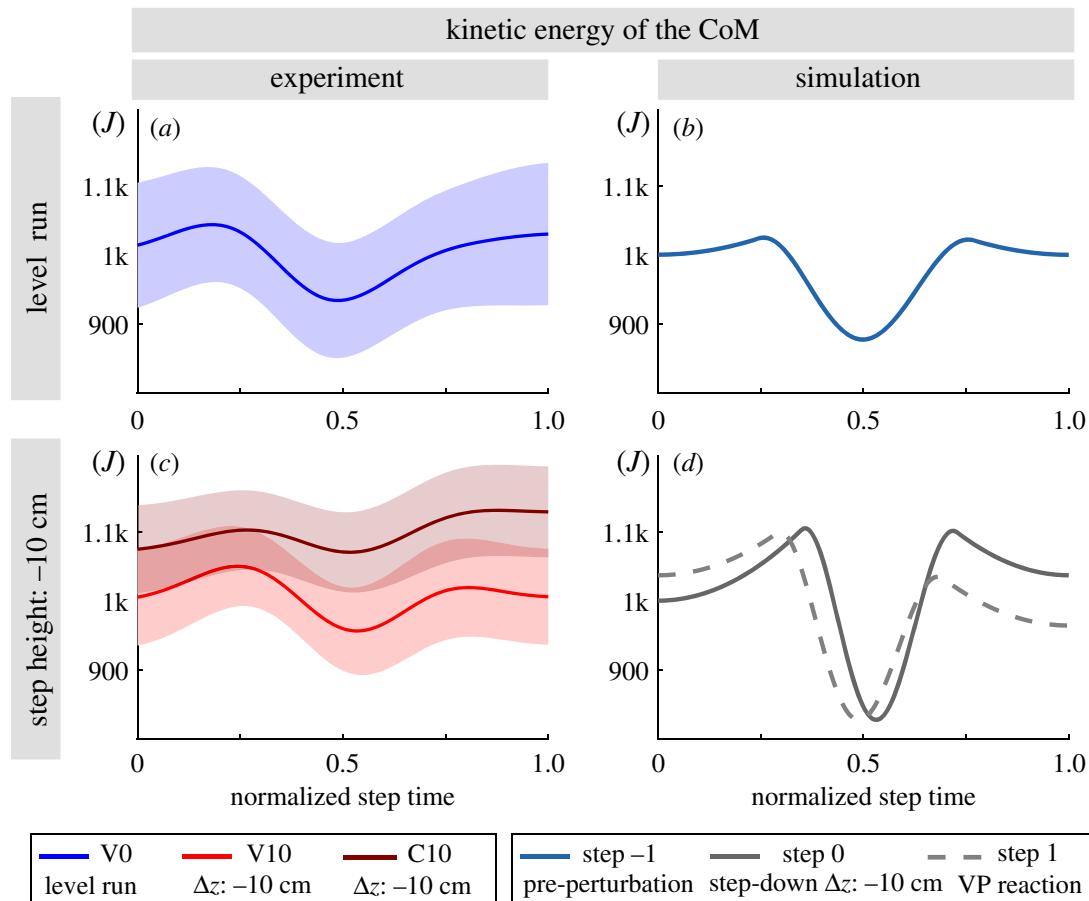


Figure 10. Kinetic energy of the CoM for the human running experiments (left) and simulated model (right). The mean is shown with a line and the standard error is indicated with the shaded region. The standard error equals to the standard deviation divided by the square root of number of subjects. The TSLIP model is able to predict the kinetic energies for the unperturbed and visible perturbed step well. The simulation yields larger energy fluctuations during the stance phase compared to experiments. Experiments with camouflaged perturbation (C10) yield higher mean kinetic energy compared to the ones with visible perturbations (V10).

rotation at the perturbation step is higher in simulations, and amounts to 7.8° at step 0 and 8.6° at step 1 (figure 9_{c2-c4}).

There is a good agreement between the simulation-predicted and the recorded GRFs for level running. The peak horizontal and vertical GRFs amount to 0.5 BW and 3 BW, respectively, in both experiments and simulations (see figures 5, 8*a,d* and appendix A.7., 19). As for the step-down perturbation, the simulation model is able to predict the peak vertical GRF, but the prediction becomes less accurate for the peak horizontal GRF. The peak vertical GRF of the -10 cm step-down perturbation case is 3.5 BW for the V10 condition and 4 BW for the C10 condition, whereas it is 4 BW for the simulation. In the C10 condition, the vertical GRF peak occurs at the foot impact and its peak is shifted in time, to the left. The numerical simulation leads to over-simplified horizontal GRF profiles, in the step-down condition. The human experiments show an impact peak. The experiments have a peak horizontal GRF magnitude of 0.5 BW, which remains the same for all perturbation conditions. By contrast, the peak horizontal GRF increases up to 1 BW in simulations.

In level running the GRF impulses of the experiments and the simulation are a good match (see table 2 and appendix A.5., figures 15*b* and 16*b*). The normalized horizontal impulses for both braking and propulsion intervals are the same at 0.1, while the normalized net vertical impulse in experiments are 15% higher than in the simulation. For the step-down conditions, the simulation predicts higher normalized net vertical impulse values of 1.46 at step 0 and 1.36 at step 1, as opposed to 1.31 for the V10 condition and 1.18 for C10 condition in experiments. The change in the horizontal impulses during the step-down differs significantly between the simulation and experiments. The V10 condition shows no significant change in the horizontal impulses, while in the C10 condition they decrease to 0.04 for braking and 0.06 for propulsion. By contrast, the simulations show an increase in the horizontal impulses (appendix A.5., figure 15*b*). In particular, for a step-down perturbation of -10 cm, the normalized braking impulse increases to 0.15 at step 0 and 0.18 at step 1, whereas for propulsion it increases to 0.15 and 0.12.

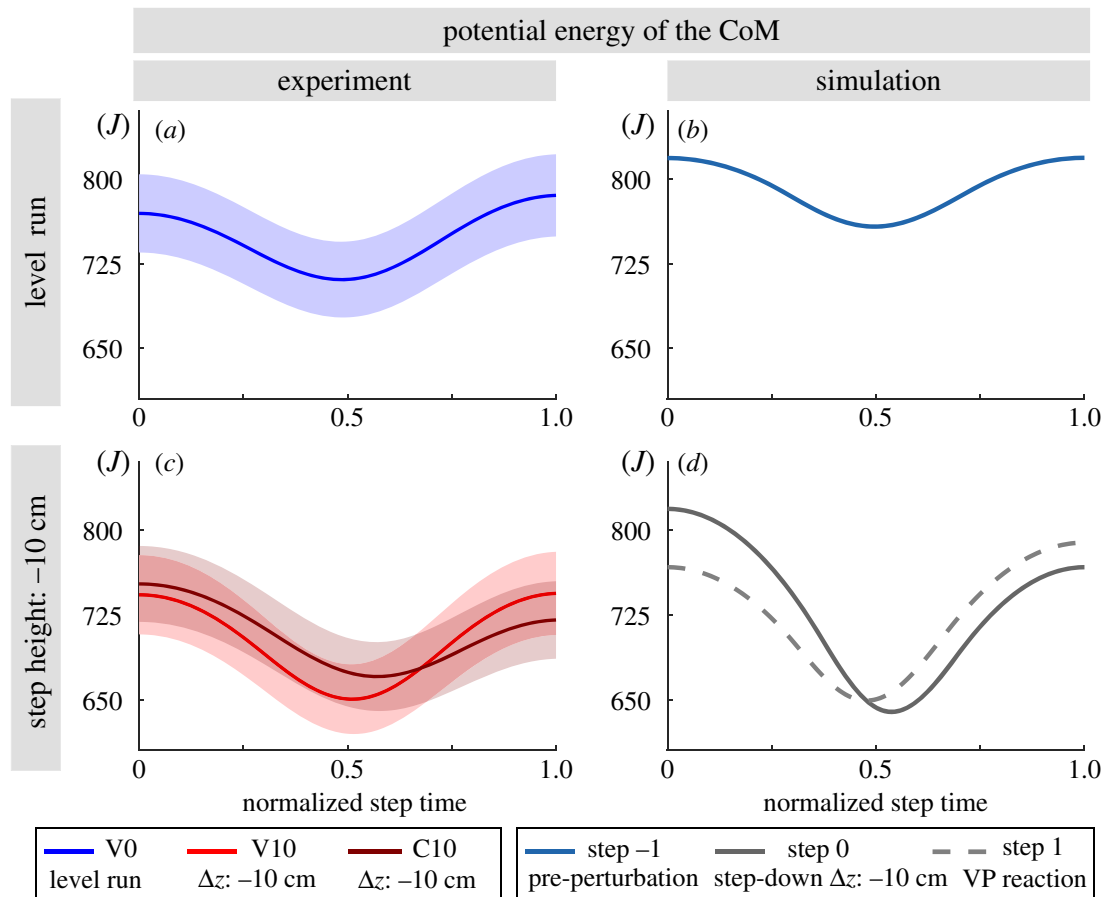


Figure 11. Potential energy of the CoM for the human running experiments (left) and simulated model (right). The mean is shown with a line and the standard error is indicated with the shaded region. The standard error equals to the standard deviation divided by the square root of number of subjects. Overall, the TSLIP model predicts the CoM height and its related potential energy well.

The different behaviour we observe in horizontal impulses at step-down for the experiments and simulations may be owing to different leg angles at touch-down. We expect that a steeper leg angle of attack at touch-down would decrease the horizontal and increase the vertical braking impulse. However, we observe with 66° a 9° steeper angle of attack in the simulations for level running than it was reported for V0 for the same experiments [30]. Nevertheless, no corresponding changes in the braking impulses could be observed. On the other hand, in the perturbed condition, the angle of attack is with 66° nearly the same in the simulation and C10, but here the braking impulses differ. However, differences in the definition of the leg also affect the angle of attack. In the literature, an angle of attack between 57° and 82° was reported for level running [16], which fits the model's leg angle of attack. Additionally, no corresponding changes in the braking impulses could be observed. In the perturbed condition, the angle of attack in the experiments is 9° steeper compared to V0, which could be caused by the swing leg retraction, while the angle of attack in the simulation is the same in V0 and C10. Here, also the braking impulses between experiment and simulation differ. Therefore, we conclude that the simulation could potentially be improved by implementing a swing leg retraction as observed in humans [30,43,44].

Another reason for the limited prediction capabilities of the model for step-down drops might be related to the heel strike and impact dynamics during the leg touch-down. The impact peak (i.e. first peak) of the horizontal GRF in the braking interval is smaller than the active peak (i.e. second peak) for V0, and larger for V10 and C10 conditions (appendix A.7., figure 19*b₀-b₁*). In particular, the C10 condition displays a M-shaped horizontal GRF during braking interval, where the impact dynamics becomes dominant. The absence of impact dynamics and associated GRF peaks in the simulation model might contribute to the discrepancy observed in peak GRF magnitudes while stepping down. Therefore, we conclude that additional factors have to be involved in the explanation of the different peaks and impulses between simulation and experiments, and further investigations are needed.

In terms of the CoM energies, there is a good match between the kinetic energies of the experiments and simulations for the unperturbed step (V0 and step -1 in figure 10*a,b*). The simulated energies of the perturbed step are closer to the experiments with visible perturbations (V10 and steps 0 and 1 in figure 10*c,d*). Human experiments show a drop in kinetic energy of 9% for V10, 3% for C10. The simulation shows a drop in kinetic energy of about 25% for step 0 and step 1. The C10 condition shows a higher

mean kinetic energy compared to visible perturbations and there is no obvious decrease of energy in the stance phase (figure 10c).

The potential energy estimate of the simulations lies in the upper boundary of the experiments for the unperturbed step (V0 and step -1 in figure 10a,b). The experiments with visible and camouflaged perturbations, as well as the TSLIP model, result in similar potential energy curves (figure 10c,d).

4.3. Limitations of this study

The human experiments and the numerical simulations differ in several points, and conclusions from a direct comparison must be evaluated carefully. We discuss details for our choice of human experimental and numerical simulation conditions in this section.

First of all, there is a difference in terrain structure. After passing step 0, the human subjects face a different terrain structure type, compared to the TSLIP simulation model. The experimental set-up is constructed as a pothole: a step-down followed by a step-up. However, an identical step-up in the numerical simulation would require an additional set of controllers to adjust the TSLIP model's leg angle and push off energy. Hence for the sake of simplicity, the TSLIP model continues running on the lower level and without a step-up. After the step-down perturbation, the simulated TSLIP requires several steps to recover. An experimental set-up for an equivalent human experiment would require a large number of force plates, which were not available here.

In the V10 condition, the subjects have a visual feedback and hence the prior knowledge of the upcoming perturbation. This additional information might affect the chosen control strategy. In particular, because there is a step-up in the human experiments, subjects might account for this upcoming challenge prior to the actual perturbation.

In the C10 condition, some subjects might prioritize safety in the case of a sudden and expected drop, and employ additional reactive strategies [45]. By contrast, the simulations with a VP controller cannot react to changes during the step-down and only consider the changes of the previous step when planning for the next.

Furthermore, in the human experiments, we cannot set a step-down higher than -10 cm owing to safety reasons, especially in the camouflaged setting. Instead, we can evaluate these situations in numerical simulations and test whether a hypothesized control mechanism can cope with higher perturbations. However, one has to keep in mind that the TSLIP model that we use in our analysis is simplified. Its single-body assumption considers neither intra-segment interactions, nor leg dynamics from impacts and leg swing. A future model can be improved by including swing leg dynamics, collision dynamics and ankle torque to capture the heel-strike and ankle push-off effects [46–48]. Finally, our locomotion controller applied does not mimic specific human neural locomotion control or sensory feedback strategy.

4.4. Potential uses for the virtual point

Our previous study in [23] offers an explanation why different VP behaviours can be observed in human-level running, by suggesting that different VP targets lead to a trade-off between the energy requirements of the leg and hip. In particular, a VP below the CoM (VP_{BL}) with prominent forward trunk motion at ground contact might indicate weaker leg actuation (e.g. caused by injuries), whereas a VP_B closer to the CoM or a VP_A might indicate weaker hip actuation (e.g. caused by hip extensor strength deficit). Robots and rehabilitation devices could be designed with smaller actuators, after adopting VP positions leading to lower joint loads.

If the VP is an existing function in human gait, the VP-based controllers establish biomechanically similar patterns to humans. Consequently, VP-based controllers can provide natural reference trajectories for exoskeletons to assist the human gait with a greater efficiency. For example, VP inspired controllers implemented in the lower limb exoskeleton LOPEZ II [49] and soft passive exosuit in [50] are able to reduce leg muscle activations and decrease the metabolic cost by 10% and 4%, respectively. Our current work can provide the foundation for a VP-based control approach to assist the human gait in the presence of step-down perturbations.

5. Conclusion

In this work, we investigated the existence and position of a VP in human running gait, and analysed the implications of the observed VP location to postural stability and energetics with the help of a numerical simulation.

In addition to level running, we also inquired into the change of VP position when stepping down on a -10 cm visible or camouflaged drop. Our novel results are twofold: first, the ground reaction forces focus around a point that is -30 cm below the CoM for the human running at 5 m s^{-1} . The VP position does not change significantly when stepping down a visible or camouflaged drop of -10 cm. Second, the TSLIP model simulations show that a VP target below the CoM is able to stabilize the body against step-down perturbations without any need to alter the state or model parameters.

Ethics. The experiment was approved by the local ethics committee and was in accordance to the Declaration of Helsinki.

Data accessibility. Kinetic and kinematic data of the human running experiments are available from the figshare repository: <https://doi.org/10.6084/m9.figshare.12034350.v1>.

Authors' contribution. J.V. performed the gait analysis for human running. Ö.D. shares first authorship owing to generation of the simulation model and analysis. Both J.V. and Ö.D. wrote the manuscript and all authors discussed the results and contributed to the final manuscript.

Competing interests. We declare we have no competing interests.

Funding. The human running project was supported by the German Research Foundation (Bl 236/21 to Reinhard Blickhan and MU 2970/4-1 to R.M.). The International Max Planck Research School for Intelligent Systems (IMPRS-IS) supported Ö.D. This work was partially made possible thanks to a Max Planck Group Leader grant awarded to A.B.-S. by the Max Planck Society.

Acknowledgements. We thank Martin Götze and Michael Ernst for supporting the experiments.

Appendix A

A.1. Simulation: spring loaded inverted pendulum model extended with a trunk parameters

The TSLIP model parameters are presented in table 4 (see [23] for the parameters for the human model and [25] for the avian model).

Table 4. TSLIP model parameters.

name	symbol	units	literature	chosen	reference
mass	m	kg	60–80	80	[21]
moment of inertia	J	kg m^2	5	5	[21,42]
leg stiffness	k	kN m^{-2}	16–26	18	[15,21]
leg length	l	m	1	1	[21]
leg angle at TD	θ_l^{TD}	°	78–71	$f_H(\dot{x})$	[15,21]
distance Hip-CoM	r_{HC}	m	0.1	0.1	[21,51]

A.2. Simulation: flowchart for leg angle and virtual point angle control

The linear controller for the leg angle θ_L and VP angle θ_{VP} is presented in figure 12. The leg angle control coefficients ($k_{\dot{x}}, k_{x_0}$) in equation (2.5) are decreased from $(0.25, 0.5k_{\dot{x}})$ to $(0.2, 0.3k_{\dot{x}})$, as the step-down height is increased from -10 cm to -40 cm. The reduction of the coefficients slows down the adjustment of the forward speed, and enables us to prioritize the postural correction in the presence of larger perturbations.

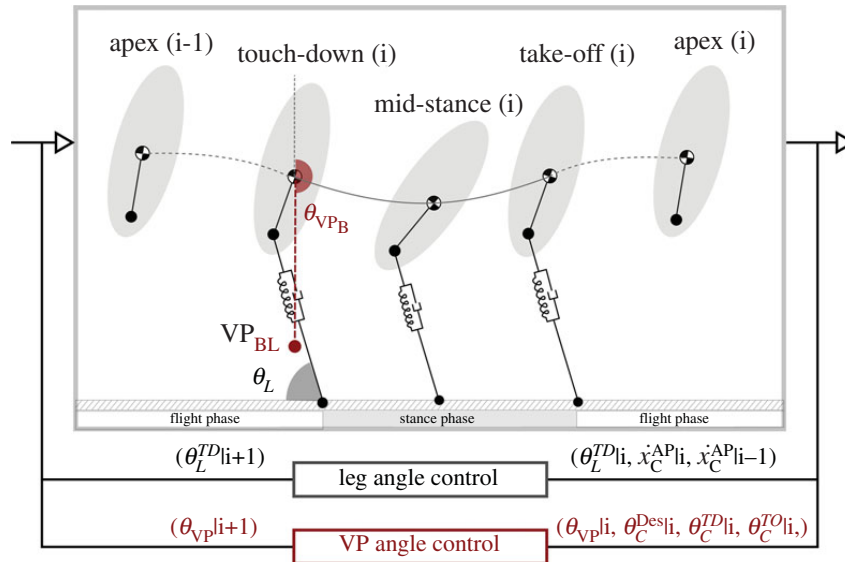


Figure 12. The linear feedback control scheme for the leg angle in equation (2.5) and the VP angle in equation (2.6) are presented. Both controllers update step-to-step at the apex event where the CoM reaches to its maximum height.

A.3. Simulation: the centre of mass state

The centre of mass trajectory of the simulated gaits are plotted in figure 7, where we can infer its position and height. In figure 13, we provide the time progression of the remaining state parameters: the trunk pitch angle, forward speed, vertical speed and trunk angular velocity.

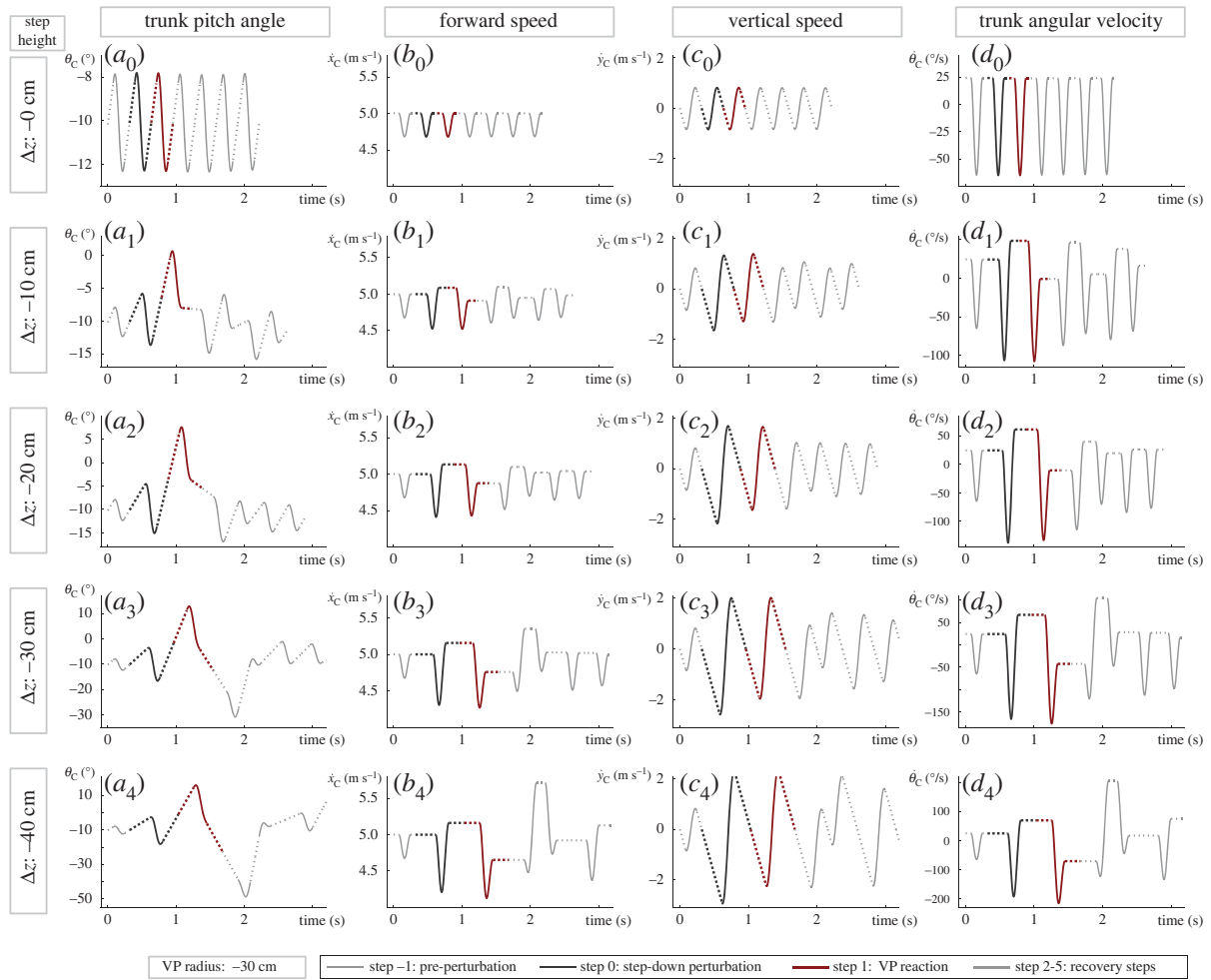


Figure 13. The trunk pitch angle (*a*), forward speed (*b*), vertical speed (*c*), and trunk angular velocity (*d*) of the simulated gaits. The figure is complementary to figure 7*a*, which provides the centre of mass trajectories. The solid lines correspond to the stance phase, whereas dotted lines correspond to the flight phase of running in simulation. The step-down perturbation leads to a deviation from the equilibrium state. At the end of the perturbed step (dark grey lines), the forward trunk lean is less, forward speed is higher, and trunk angular velocity is higher than the equilibrium conditions. The step after perturbation (red lines) is the step, where the leg angle and VP controllers react to the changes in state.

In figure 14, we present the energy levels of the leg spring, leg damper and the hip actuator for the entire set of step-down perturbations ($\Delta z = [-10, -20, -30, -40 \text{ cm}]$).

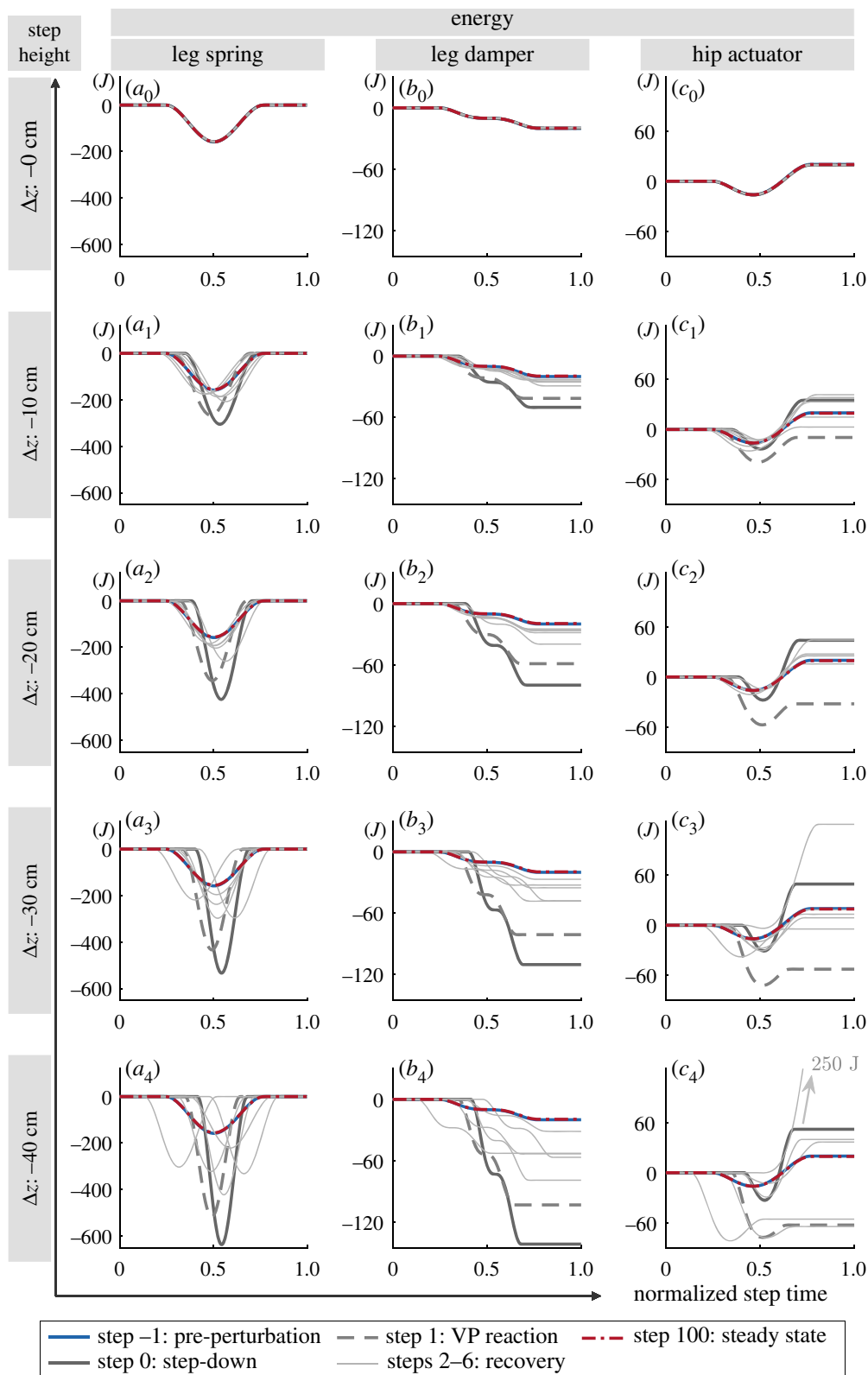


Figure 14. The energy curves for the leg spring (a_0 – a_4), leg damper (b_0 – b_4) and hip actuator (c_0 – c_4). In subplot c_4 , the maximum value of steps 7–11 is indicated with a text and arrow because of the scaling issues. The sub-index ‘0’ indicates the trajectory belongs to the equilibrium state. With the increase of the system’s energy at step-down (solid black line), the leg deflects more, the leg damper dissipates more energy and the hip actuator injects more energy compared to its equilibrium condition. During the reaction step (dashed line), the hip actuator reacts to energetic change and starts to remove energy from the system. In the following steps (solid grey line), the hip regulates the energy until the system reaches to the initial equilibrium state (solid blue line). In subplot c_4 , the maximum value of steps 7–11 is indicated with a text and arrow because of the scaling issues.

A.5. Simulation: ground reaction forces and impulses

We provide the vertical and horizontal ground reaction forces for the entire set of step-down perturbations ($\Delta z = [-10, -20, -30, -40 \text{ cm}]$) in figures 15 and 16, respectively.

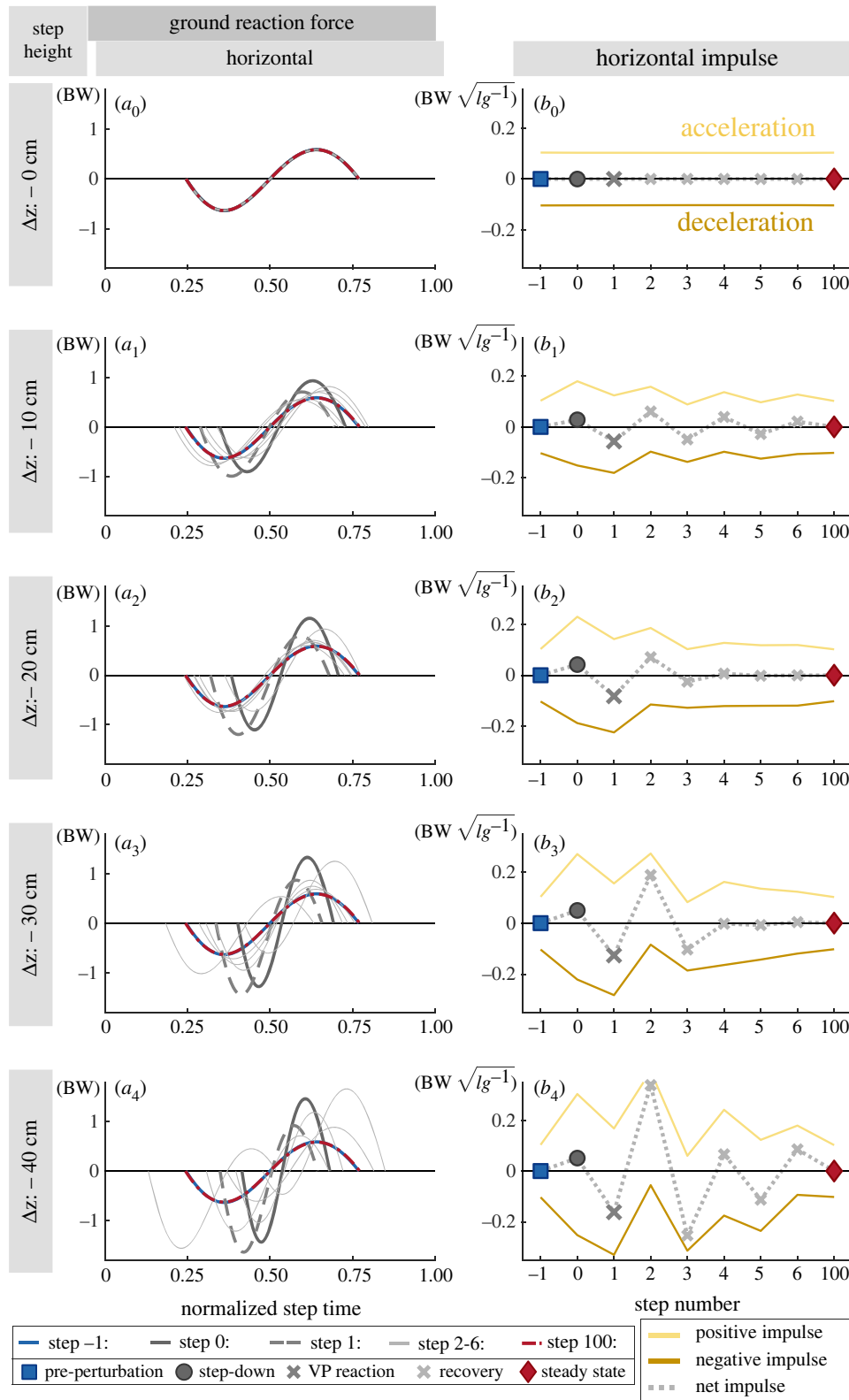


Figure 15. The horizontal ground reaction forces over normalized step time are shown (a_0 – a_4). The peak horizontal GRF increases with the step-down perturbation. The area under this curve is the horizontal impulse, which corresponds to the acceleration and deceleration of the main body (b_0 – b_4). The step-down perturbation at step 0 increases the energy of the system. The increase in energy influences the net horizontal impulse, as the impulse attains a positive value (circles) and causes the body to accelerate forwards. In response, the VP position changes to create net negative impulse in the following step (i.e. step 1, dark cross marker) and decelerates the body. The VP position is adjusted until all the excess energy is removed from the system (cross markers) and the gait reaches to an equilibrium state (diamonds).

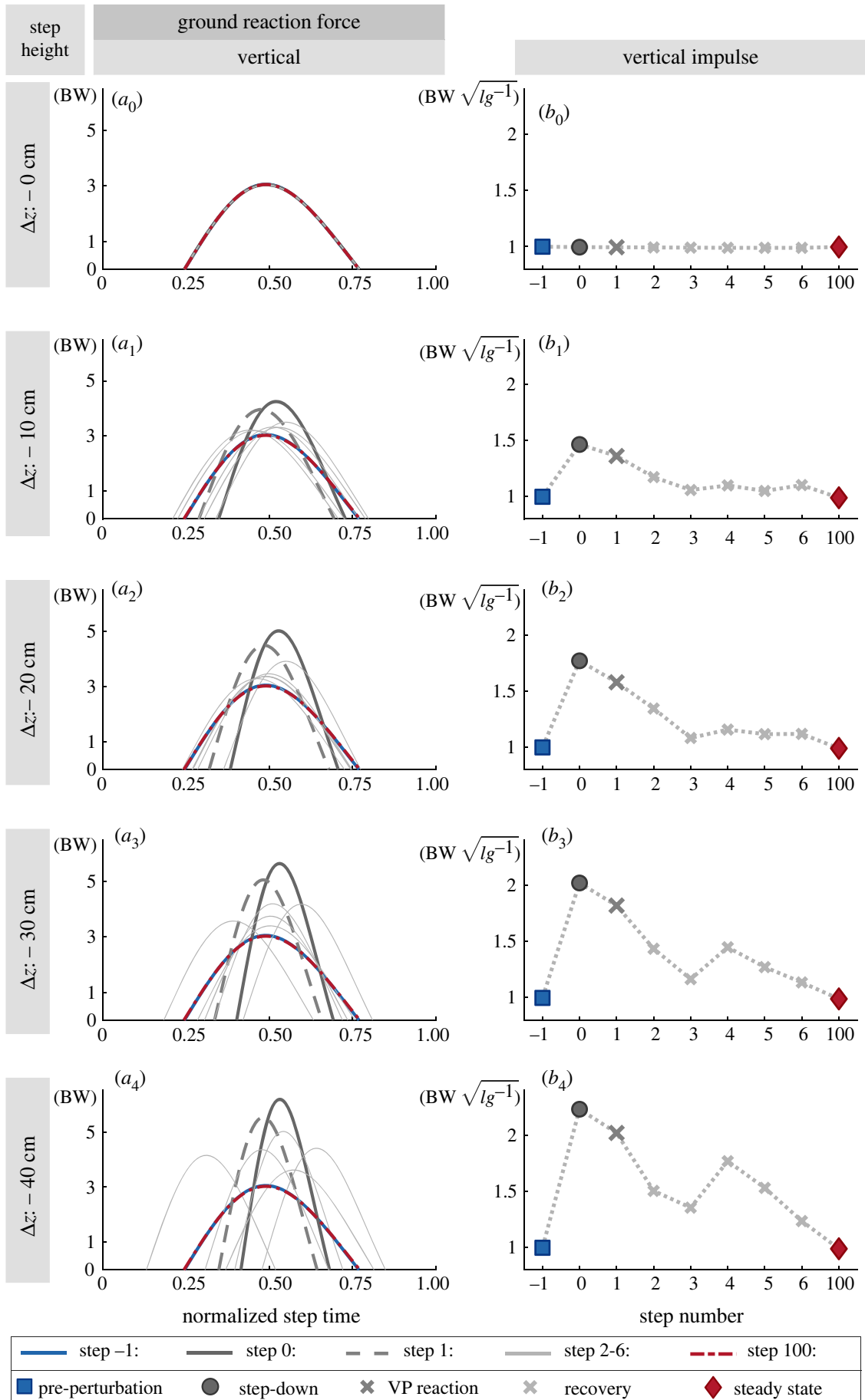


Figure 16. The vertical ground reaction forces over normalized step time are shown (a_0 – a_4). The peak vertical GRF increases with the step-down perturbation. During the following steps, the impulse decreases to its initial value through the regulation of the VP position. The increase in the peak GRF after step-down is proportional to the step-down height. Between steps 4 and 5, the peak vertical GRF increases 1.4 fold for -10 cm drop and twofold for -40 cm drop. In accordance, the vertical impulse increases with the step-down perturbation and returns to its initial value (b_0 – b_4). As the step-down height increases from -10 to -40 cm the vertical impulse increases 1.53-fold from its initial value for step 0 (circle) and 1.48 fold for step 1 (dark cross markers).

A.6. Standard deviation of the experiments

In §4, we provided the standard error (SE) of the measurements from the human running experiments (see the patched areas in figures 9–11). The SE is calculated by dividing the standard deviation (STD) by the square root of number of subjects. The SE shows how good the mean estimate of the measurements is.

On the other hand, STD shows how spread out our different measurements are. The STD is an important measure, especially for the trunk angle measurements, where the trajectories of each subject significantly varies. Therefore, we provide the STD values here for the CoM state in figure 17 and CoM energy in figure 18.

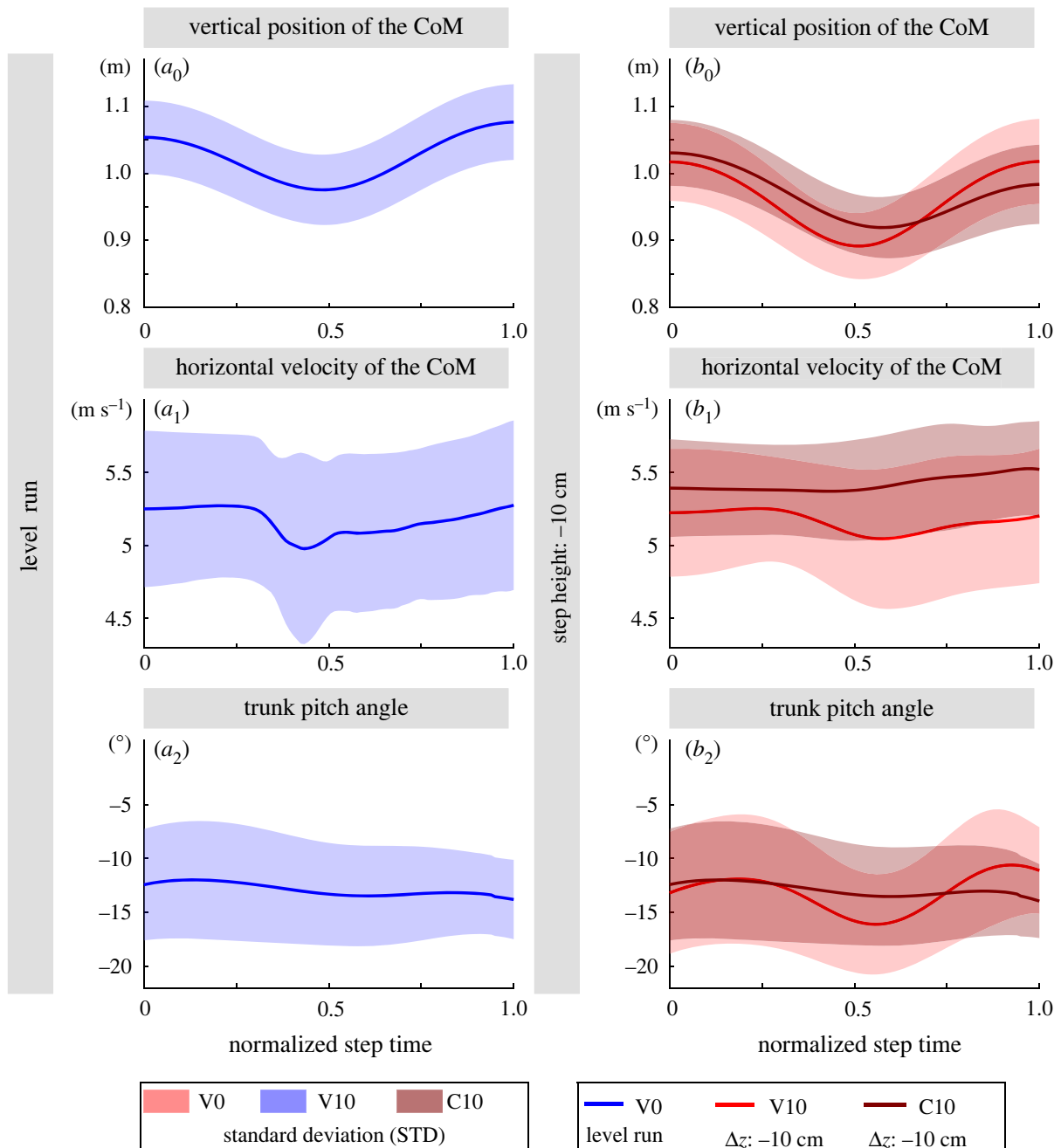


Figure 17. This figure is an extension of figure 9, with the difference that the standard deviation is plotted with the patches instead of the standard error.

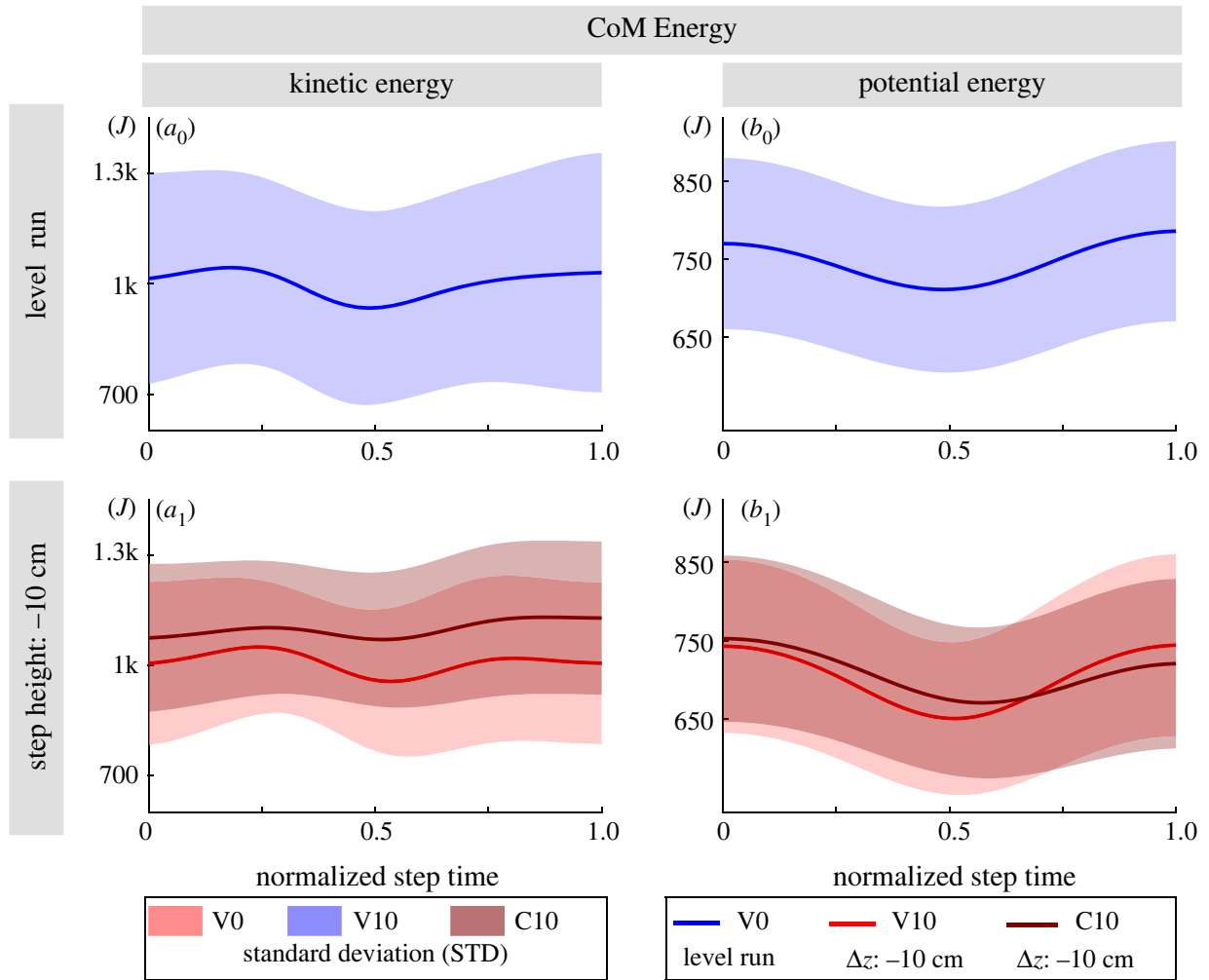


Figure 18. This figure is an extension of figures 10 and 11, with the difference that the standard deviation is plotted as patches instead of the standard error.

A.7. Ground reaction forces: simulation versus experiment

We present the vertical (a) and horizontal (b) GRFs belonging to the step 0 of the human running experiments (V0, V10, C10) and steps -1 , 0 and 1 of the simulations with a -10 cm step-down height, plotted on top of each other in figure 19.

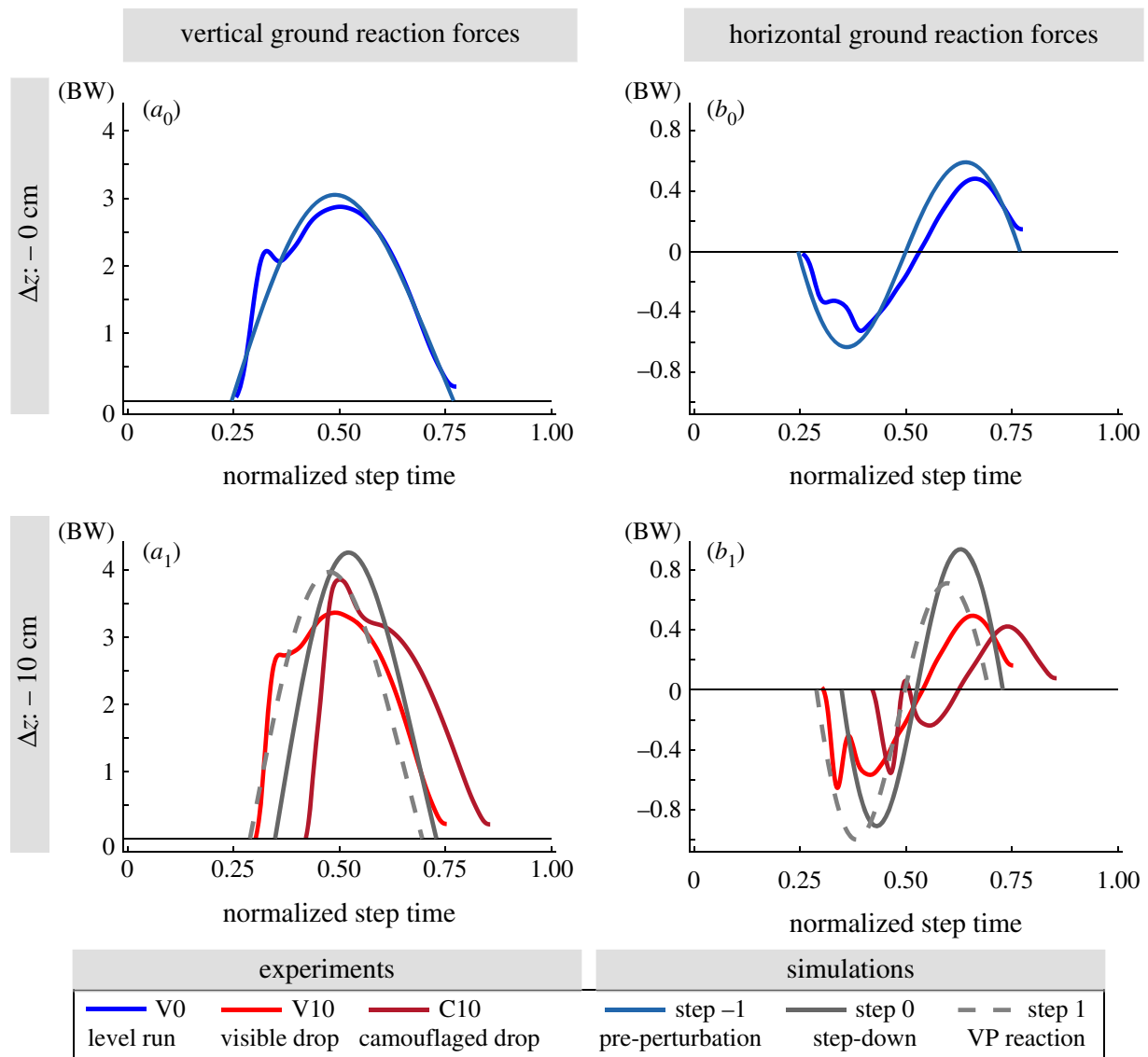


Figure 19. The vertical (a) and horizontal (b) ground reaction forces (GRFs) are plotted over normalized step time. The mean of the experimental results are shown. The TSLIP model simulation is able to capture the characteristics of the GRF in level running (a_0 , b_0). For the step-down perturbation, the model predicts higher values for the peak vertical (a_1) and horizontal (b_1) GRF, compared to the mean values of the experiments.

1. Maus H-M, Lipfert S, Gross M, Rummel J, Seyfarth A. 2010 Upright human gait did not provide a major mechanical challenge for our ancestors. *Nat. Commun.* **1**, 70. (doi:10.1038/ncomms1073)
2. Gruben KG, Boehm WL. 2012 Force direction pattern stabilizes sagittal plane mechanics of human walking. *Hum. Mov. Sci.* **31**, 649–659. (doi:10.1016/j.humov.2011.07.006)
3. Müller R, Rode C, Aminiaghdam S, Vielemeyer J, Blickhan R. 2017 Force direction patterns promote whole body stability even in hip-flexed walking, but not upper body stability in human upright walking. *Proc. R. Soc. A* **473**, 20170404. (doi:10.1098/rspa.2017.0404)
4. Sharbafi MA, Seyfarth A. 2015 Mimicking human walking with 5-link model using hzd controller. In *IEEE Int. Conf. on Robotics and Automation (ICRA)*, pp. 6313–6319. New York, NY: IEEE.
5. Vielemeyer J, Griebßach E, Müller R. 2019 Ground reaction forces intersect above the center of mass even when walking down visible and camouflaged curbs. *J. Exp. Biol.* **222**, jeb204305. (doi:10.1242/jeb.204305)
6. Andrada E, Rode C, Sutedja Y, Nyakatura JA, Blickhan R. 2014 Trunk orientation causes asymmetries in leg function in small bird terrestrial locomotion. *Proc. R. Soc. Lond. B* **281**, 20141405.
7. Blickhan R, Andrada E, Müller R, Rode C, Ogihara N. 2015 Positioning the hip with respect to the COM: consequences for leg operation. *J. Theor. Biol.* **382**, 187–197. (doi:10.1016/j.jtbi.2015.06.036)
8. Scholl P. 2018 Modeling postural control in Parkinson's disease. Msc thesis, Technical University of Darmstadt, Darmstadt, Germany.
9. Firouzi V, Seyfarth A, Sharbafi MA. 2019 Tip model: a combination of unstable subsystems for lateral balance in walking. In *IEEE/RSJ Int. Conf. on Intelligent Robots and Systems (IROS)*, pp. 476–482. New York, NY: IEEE.
10. Maus MH. 2008 Stabilisierung des Oberkörpers beim Rennen und Gehen. Diploma thesis. Friedrich Schiller University, Jena, Germany.
11. Hinrichs RN. 1987 Upper extremity function in running. II: angular momentum considerations. *Int. J. Sport Biomech.* **3**, 242–263. (doi:10.1123/ijsb.3.3.242)
12. Maus H-M, Rummel J, Seyfarth A. 2008 Stable upright walking and running using a simple pendulum based control scheme. In *Advances in Mobile Robotics* (eds L Marques, A de Almeida, MO Tokhi, GS Virk), pp. 623–629. Singapore: World Scientific.
13. Geyer H, Seyfarth A, Blickhan R. 2006 Compliant leg behaviour explains basic dynamics of walking and running. *Proc. R. Soc. B* **273**, 2861–2867. (doi:10.1098/rspb.2006.3637)
14. Blickhan R. 1989 The spring-mass model for running and hopping. *J. Biomech.* **22**, 1217–1227. (doi:10.1016/0021-9290(89)90224-8)
15. McMahon TA, Cheng GC. 1990 The mechanics of running: how does stiffness couple with speed? *J. Biomech.* **23**, 65–78. (doi:10.1016/0021-9290(90)90042-2)
16. Müller R, Birn-Jeffery AV, Blum Y. 2016 Human and avian running on uneven ground: a model-based comparison. *J. R. Soc. Interface* **13**, 20160529. (doi:10.1098/rsif.2016.0529)
17. Lee J, Vu MN, Oh Y. 2017 A control method for bipedal trunk spring loaded inverted pendulum model. In *The 13th Int. Conf. on Autonomic and Autonomous Systems*, pp. 1–6. IARIA XPS Press.
18. Maufroy C, Maus HM, Seyfarth A. 2011 Simplified control of upright walking by exploring asymmetric gaits induced by leg damping. In *IEEE Int. Conf. on Robotics and Biomimetics (ROBIO)*, pp. 491–496. New York, NY: IEEE.
19. Vu MN, Lee J, Oh Y. 2017a Control strategy for stabilization of the biped trunk-slip walking model. In *14th Int. Conf. on Ubiquitous Robots and Ambient Intelligence (URAI)*, pp. 1–6. New York, NY: IEEE.
20. Vu MN, Lee J, Oh Y. 2017b Walking control algorithm of the 5-link robot based on operational space control. In *IEEE Int. Conf. on Mechatronics and Automation (ICMA)*, pp. 1532–1537. New York, NY: IEEE.
21. Sharbafi MA, Maufroy C, Ahmadabadi MN, Yazdanpanah MJ, Seyfarth A. 2013 Robust hopping based on virtual pendulum posture control. *Bioinspir. Biomim.* **8**, 036002. (doi:10.1088/1748-3182/8/3/036002)
22. Sharbafi MA, Maufroy C, Maus HM, Seyfarth A, Ahmadabadi MN, Yazdanpanah MJ. 2012 Controllers for robust hopping with upright trunk based on the virtual pendulum concept. In *IEEE/RSJ Int. Conf. on Intelligent Robots and Systems*, pp. 2222–2227. New York, NY: IEEE.
23. Drama Ö, Badri-Spröwitz A. 2019 Trunk pitch oscillations for joint load redistribution in humans and humanoid robots. In *2019 IEEE-RAS 19th Int. Conf. on Humanoid Robots (Humanoids)*, pp. 531–536. New York, NY: IEEE.
24. Van Bommel L. 2011 Virtual pivot point control for running robots. Msc thesis, Delft University of Technology (TU Delft), Delft, The Netherlands.
25. Drama Ö, Badri-Spröwitz A. 2020 Trunk pitch oscillations for energy trade-offs in bipedal running birds and robots. *Bioinspir. Biomim.* **15**, 036013. (doi:10.1088/1748-3190/ab7570)
26. Peekema AT. 2015 Template-based control of the bipedal robot ATRIAS. Msc thesis, Oregon State University, Oregon, USA.
27. Thorstensson A, Nilsson J, Carlson H, Zomlefer MR. 1984 Trunk movements in human locomotion. *Acta Physiol. Scand.* **121**, 9–22. (doi:10.1111/j.1748-1716.1984.tb10452.x)
28. Sharbafi MA, Seyfarth A. 2014 Stable running by leg force-modulated hip stiffness. In *5th IEEE RAS/EMBS Int. Conf. on Biomedical Robotics and Biomechatronics*, pp. 204–210. New York, NY: IEEE.
29. Kenwright B, Davison R, Morgan G. 2011 Dynamic balancing and walking for real-time 3d characters. In *Motion in Games* (eds JM Allbeck, P Faloutsos), pp. 63–73. Berlin, Heidelberg: Springer.
30. Müller R, Ernst M, Blickhan R. 2012 Leg adjustments during running across visible and camouflaged incidental changes in ground level. *J. Exp. Biol.* **215**, 3072–3079. (doi:10.1242/jeb.072314)
31. Birn-Jeffery AV, Hubicki CM, Blum Y, Renjewski D, Hurst JW, Daley MA. 2014 Don't break a leg: running birds from quail to ostrich prioritise leg safety and economy on uneven terrain. *J. Exp. Biol.* **217**, 3786–3796. (doi:10.1242/jeb.102640)
32. Winter DA. 2009 *Biomechanics and motor control of human movement*. Hoboken, NJ: John Wiley & Sons.
33. Müller R, Tschiesche K, Blickhan R. 2014 Kinetic and kinematic adjustments during perturbed walking across visible and camouflaged drops in ground level. *J. Biomech.* **47**, 2286–2291. (doi:10.1016/j.jbiomech.2014.04.041)
34. Ernst M, Götze M, Müller R, Blickhan R. 2014 Vertical adaptation of the center of mass in human running on uneven ground. *Hum. Mov. Sci.* **38**, 293–304. (doi:10.1016/j.humov.2014.05.012)
35. Günther M, Sholukha VA, Kessler D, Wank V, Blickhan R. 2003 Dealing with skin motion and wobbling masses in inverse dynamics. *J. Mech. Med. Biol.* **3**, 309–335. (doi:10.1142/S0219519403000831)
36. van der Linden MH, Hendricks HT, Bloem BR, Duysens J. 2009 Hitting a support surface at unexpected height during walking induces loading transients. *Gait Posture* **29**, 255–260. (doi:10.1016/j.gaitpost.2008.08.017)
37. Herr H, Popovic M. 2008 Angular momentum in human walking. *J. Exp. Biol.* **211**, 467–481. (doi:10.1242/jeb.008573)
38. Hof AL. 1996 Scaling gait data to body size. *Gait Posture* **3**, 222–223. (doi:10.1016/0966-6362(95)01057-2)
39. Heitkamp L. 2012 *The role of the gluteus maximus on trunk stability in human endurance running*. PhD thesis, University of Cincinnati, Ohio, USA.
40. Schache AG, Bennell KL, Blanch PD, Wrigley TV. 1999 The coordinated movement of the lumbo pelvic hip complex during running: a literature review. *Gait Posture* **10**, 30–47. (doi:10.1016/S0966-6362(99)00025-9)
41. Ernst M, Götze M, Blickhan R, Müller R. 2019 Humans adjust the height of their center of mass within one step when running across camouflaged changes in ground level. *J. Biomech.* **84**, 278–283. (doi:10.1016/j.jbiomech.2018.12.036)
42. de Leva P. 1996 Adjustments to Zatsiorsky-Seluyanov's segment inertia parameters. *J. Biomech.* **29**, 1223–1230. (doi:10.1016/0021-9290(95)00178-6)
43. Blum Y, Lipfert SW, Rummel J, Seyfarth A. 2010 Swing leg control in human running. *Bioinspir. Biomim.* **5**, 026006. (doi:10.1088/1748-3182/5/2/026006)
44. Seyfarth A, Geyer H, Herr H. 2003 Swing-leg retraction: a simple control model for stable running. *J. Exp. Biol.* **206**, 2547–2555. (doi:10.1242/jeb.00463)

45. Müller R, Häufle DFB, Blickhan R. 2015 Preparing the leg for ground contact in running: the contribution of feed-forward and visual feedback. *J. Exp. Biol.* **218**, 451–457. (doi:10.1242/jeb.113688)
46. Kim M, Collins SH. 2017 Once-per-step control of ankle push-off work improves balance in a three-dimensional simulation of bipedal walking. *IEEE Trans. Rob.* **33**, 406–418. (doi:10.1109/TRO.2016.2636297)
47. Suzuki Y, Geyer H. 2018 A simple bipedal model for studying control of gait termination. *Bioinspir. Biomim.* **13**, 036005. (doi:10.1088/1748-3190/aaae8e)
48. Zamani A, Bhounsule PA. 2017 Foot placement and ankle push-off control for the orbital stabilization of bipedal robots. In *2017 IEEE/RSJ Int. Conf. on Intelligent Robots and Systems (IROS)*, pp. 4883–4888. New York, NY: IEEE.
49. Zhao G, Sharbafi M, Vlutters M, van Asseldonk E, Seyfarth A. 2017 Template model inspired leg force feedback based control can assist human walking. In *2017 Int. Conf. on Rehabilitation Robotics (ICORR)*, pp. 473–478. New York, NY: IEEE.
50. Barazesh H, Sharbafi MA. 2020 A biarticular passive exosuit to support balance control can reduce metabolic cost of walking. *Bioinspir. Biomim.* **15**, 036009. (doi:10.1088/1748-3190/ab70ed)
51. Wojtusich J, von Stryk O. 2015 Humod - a versatile and open database for the investigation, modeling and simulation of human motion dynamics on actuation level. In *Proc. of the IEEE-RAS Int. Conf. on Humanoid Robots*, pp. 74–79. New York, NY: IEEE.

5 General conclusion

The main issue of all performed studies was the intersection of ground reaction force vectors during various human locomotion. Herein, the horizontal and vertical positions and the blur size of the intersection point, the virtual pivot point (VPP), were analyzed (VPP variables). In the preparatory work, the VPP was investigated for walking with trunk inclinations as intrinsic perturbations (Müller et al., 2017). Due to its close proximity to the content of this work, this study will also be taken into account in the discussion (see figure A.1-A.3 and table A.1 for summary). However, different calculation methods were used in Müller et al. (2017) than in the other studies, which will be discussed in more detail in section 5.2.2. Therefore, the VPP variables of Müller et al. (2017) were recalculated again for the following comparison to exclude methodological causes for differences.

5.1 Summary

The first study focused on extrinsic perturbations (visible and camouflaged curbs) while walking (Vielemeyer et al., 2019). The second study considered the VPP in the double support phase of walking (Vielemeyer et al., 2021), and the third study examined the VPP in level and step down running of humans and simulated human running (Drama et al., 2020). The summarized main results of all these studies are listed in table A.1 and are illustrated in figure 5.1 and 5.2.

In figure 5.1, it can be seen that in most analyzed settings the VPP was above the CoM, between 9.9 and 43.3 cm (mean values). One exception is the double support phase of walking, where the VPP was at the height of the CoM (Vielemeyer et al., 2021). The other exception represents running with a VPP below the CoM (mean values between -37.6 and -24.0 cm, Drama et al., 2020). In all studies, the VPP was denoted as a point because of its small spread, as illustrated in figure 5.2. The blur size of the VPP, represented by R^2 , was *remarkably good*¹ for the visible curb conditions and trunk inclinations up to TI50 of the single support phase of human walking (mean value between 95.5 and 99.0%). R^2 of C10, TI_{max} and the double support phase of walking, as well as of the level contacts (including previous to step down) of running were at least *good* (mean value between 88.1 and 94.6%). The worst R^2 values were achieved for the visible (83.0%) and camouflaged drop (69.4%) conditions in running. However, Herr and Popovic (2008) denoted an R^2 of about 70% still as *reasonably well*.

¹following the denotation of Herr and Popovic (2008)

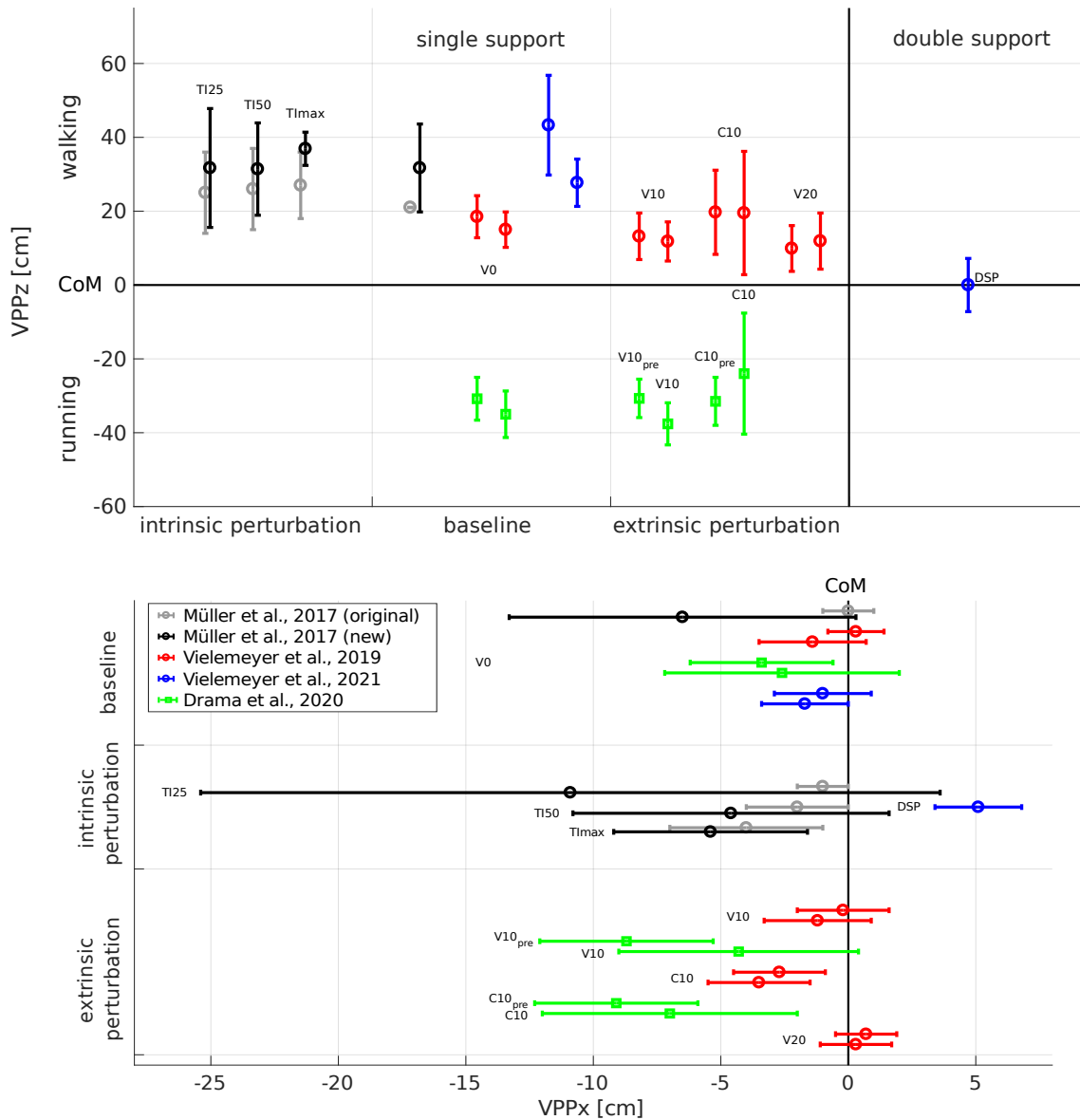


Figure 5.1: Position (top: vertical (z) and bottom: horizontal (x)) of the virtual pivot point (VPP) relative to the center of mass (CoM) for all studies, median of all trials (T) and subsequent mean and standard deviation of all subjects (N) are illustrated. For the original data of Müller et al. (2017), the grand mean over N and T is shown. The baseline denotes the single support phase of normal level walking or running (visible level - V0). The intrinsic perturbations measured by Müller et al. (2017) are different trunk inclinations. Here, TI25 stands for a trunk inclination of $31.9 \pm 5.4^\circ$, TI50 for $47.1 \pm 5.4^\circ$, and TImax for $72.5 \pm 8.1^\circ$ (N=10, T=8 for each TI). For Müller et al. (2017), the original data (gray circles) and the methodically adapted data (black circles) are shown. Vielemeyer et al. (2019) measured visible and camouflaged curbs of different heights (red circles) as extrinsic perturbation. V10 and V20 stand for the step down of visible curbs of 10 cm and 20 cm, respectively. C10 describes the perturbed contact of a camouflaged curb of 10 cm. The left-hand circles of the red pairs of a setting are the results of walking at $1.2 \pm 0.1 \text{ ms}^{-1}$, the right-hand ones at $1.7 \pm 0.1 \text{ ms}^{-1}$ (N=10, T=8 for visible/T=4 for C10). In Vielemeyer et al. (2021), the VPP was calculated for the double support phase of walking (DSP, blue circle). Additionally, the two single support phases surrounding the DSP were analyzed in V0 (N=9, T=10). In Drama et al. (2020), running was analyzed (green squares). The extrinsic perturbations are defined analogously to Vielemeyer et al. (2019). Here, the subscript *pre* denotes the contact previous to the perturbed contact (N=10, T=15 for visible/T=8 for C10).

The horizontal VPP position was in the most settings with -1.0 to -10.9 cm posterior to the CoM, as shown in figure 5.1. Only in the slow, visible conditions and additionally the fast visible curb of 20 cm (Vielemeyer et al., 2019), the VPPx was at the horizontal CoM position (± 0.7 cm). In the double support phase, the VPP was 5.1 cm anterior to the CoM.

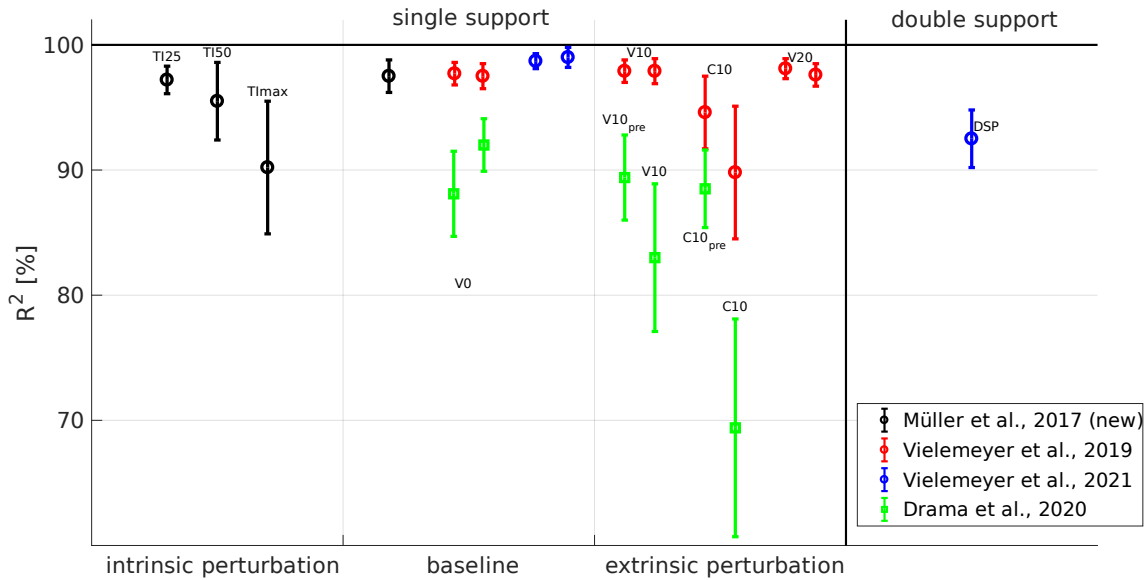


Figure 5.2: Coefficient of determination, R^2 , for all studies, median of all trials (T) and subsequent mean and standard deviation of all subjects (N) are illustrated. The baseline denotes the single support phase of normal level walking or running (visible level - V0). The intrinsic perturbations measured by Müller et al. (2017) are different trunk inclinations. Here, TI25 stands for a trunk inclination of $31.9 \pm 5.4^\circ$, TI50 for $47.1 \pm 5.4^\circ$, and TI_{max} for $72.5 \pm 8.1^\circ$ ($N=10$, $T=8$ for each TI). For Müller et al. (2017), the methodically adapted data (black circles) are shown. Vielemeyer et al. (2019) measured visible and camouflaged curbs of different heights (red circles) as extrinsic perturbation. V10 and V20 stand for the step down of visible curbs (walking)/drops (running) of 10 cm and 20 cm, respectively. C10 describes the perturbed contact of a camouflaged curb (walking)/drop (running) of 10 cm. The left-hand circles of the red pairs of a setting are the results of walking at $1.2 \pm 0.1 \text{ ms}^{-1}$, the right-hand ones at $1.7 \pm 0.1 \text{ ms}^{-1}$ ($N=10$, $T=8$ for visible/ $T=4$ for C10). In Vielemeyer et al. (2021), the VPP was calculated for the double support phase of walking (DSP, blue circle). Additionally, the two single support phases surrounding the DSP were analyzed in V0 ($N=9$, $T=10$). In Drama et al. (2020), running was analyzed (green squares). The extrinsic perturbations are defined analogously to Vielemeyer et al. (2019). Here, the subscript *pre* denotes the contact previous to the perturbed contact ($N=10$, $T=15$ for visible/ $T=8$ for C10).

Therefore, in all settings a VPP could be observed, but the point was on different positions, and its blur size varied. In the following it will be discussed whether the hypotheses from section 1.6 can be confirmed.

In part one of *Hypothesis 1* it was assumed that extrinsic perturbations affect the position of the VPP. This can be observed partly. However, no clear directional trend is apparent. Furthermore, in part two of the hypothesis it was assumed that the blur size of the VPP would increase, possibly even up to the point where the VPP cannot be observed

anymore. This can not be observed for visible curbs. These perturbations are too small to significantly affect the VPP. In contrast, a significantly increased spread around the VPP in the larger perturbations (C10) was observed, but the VPP could still be denoted as a point. In case of intrinsic perturbations, the VPPx position and the spread around the VPP were affected by large trunk inclinations (TI50 and TImax). Although the blur size was increasing for larger perturbations, the VPP could be denoted as a point as well. In summary it can be said that (major) perturbations seem to affect the position and the blur size of the VPP, albeit the VPP is still present.

Hypothesis 2 stated that no VPP would be observed in the double support phase of human walking. An intersection point at the height of the CoM with an R^2 of 92.5% was found in Vielemeyer et al. (2021). Thus, it can be concluded that there is a VPP in the double support phase, and the hypothesis is rejected. However, the question arises whether this intersection point should still be called a *VPP* due to its position.

The assumption of *Hypothesis 3* was that a VPP above the CoM could be observed in running. For level running and running over visible and camouflaged drops, an intersection point could be found. However, in all settings it was significantly below the CoM. Thus, the intersection point cannot be denoted as *VPP* in the conventional sense.

In the following section the similarities and differences between the studies are analyzed.

5.2 Comparison of the studies

Although in all experiments the VPP was calculated for the level, upright gait, there are noticeable differences between the VPP variables even in the unperturbed setups. Therefore, the influence of the input variables will be analyzed. Subsequently, the effect of the calculation methods is taken up in section 5.2.2. A detailed analysis of the input variables within the studies can be found in the appendix (chapter C).

5.2.1 Influence of the input variables

The input variables for the calculation of the VPP are the GRFs, the CoP, and the CoM. Since the trajectory of the CoM reflects the GRFs², the remaining crucial variables are the CoM-centered horizontal CoP position (CoP_{CoM}) and its range, the GRFs, and the vertical CoM position relative to the CoP at TD (CoMz_{TD}). For the GRFs, the ratio of the horizontal and the vertical components determines the VPP position and its blur size. The influence of the input variables on the VPP position is illustrated schematically in figure 5.3.

²This is because of the theoretical equivalence of the acceleration of the CoM and the GRFs (see section 5.2.2).

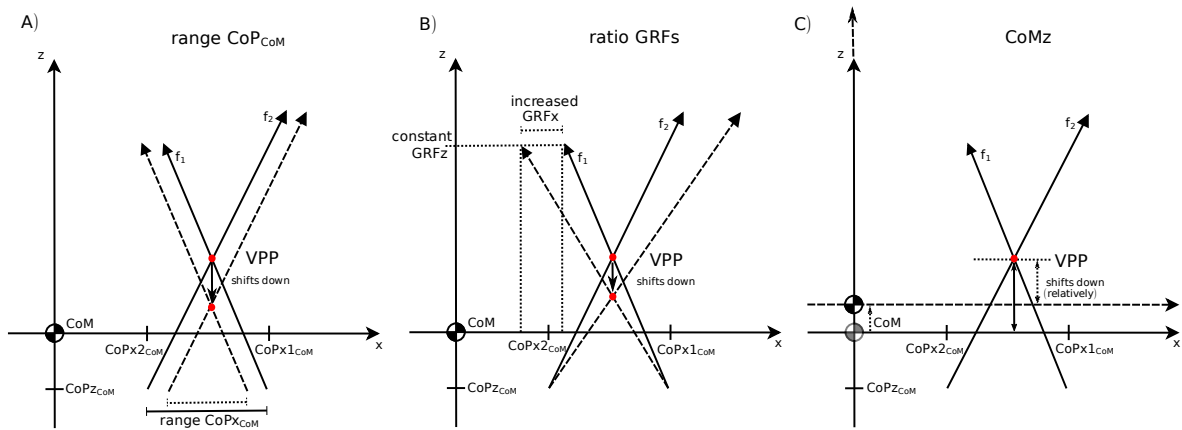


Figure 5.3: Schematic illustration of the influences of the input variables on the vertical (z) position of the virtual pivot point (VPP). The vectors f_1 and f_2 are ground reaction force (GRF) vectors starting at the center of pressure (CoP_{CoM}) for two instants of measurement. The coordinate system is centered with respect to the center of mass of the whole body (CoM). A) The effect of a reduced horizontal (x) CoP_{CoM} range on VPPz is shown. Here, f_1 and f_2 are the first and the last vectors considered in the calculation. B) The effect of a larger GRFx -component for a constant GRFz -component on VPPz is illustrated. C) A shift of the CoMz implies a vertical shift of the whole coordinate system and thus, the VPPz is also shifted relatively to the point of origin.

Considering the time evolution of the ratio of GRFx to GRFz , it is worthwhile taking a closer look at the *relative horizontal impulse*. This quantity is useful for comparing the influence of horizontal contributions of the GRF on vertical VPP position between different setups. It is calculated as the time integral of $|\text{GRFx}/\text{GRFz}|$. This is illustrated in figure 5.4, the gray area represents the relative horizontal impulse. A larger relative horizontal impulse indicates a larger horizontal contribution, and thus a lower VPP, as illustrated in figure 5.3B.

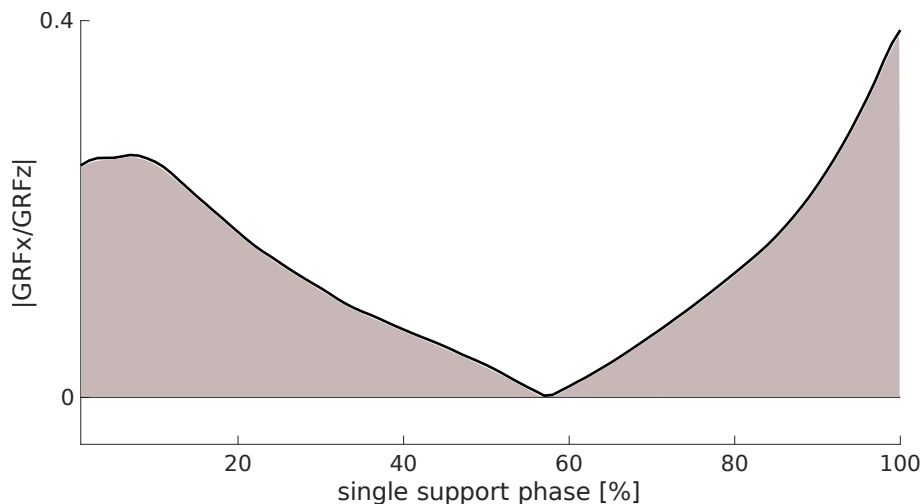


Figure 5.4: Schematic illustration of the relative horizontal impulse (gray area). The absolute values of the time-dependent ratio of the horizontal (x) relative to the vertical (z) ground reaction forces (GRF) are shown.

The most obvious difference in the VPPz positions can be observed between walking and running. This difference can be explained quite simply by the input variables. Here, the CoP_{CoM} and the CoMz_{TD} play nearly no role, they are very similar for walking and running (figure B.1 and table B.1). The main difference can be observed in the GRFs (figure B.2) and the ratio of their horizontal and vertical components (relative horizontal impulse, figure 5.5). The monomodal shape of GRFz in running, compared to the bimodal one in walking, combined with larger amplitudes and a noticeable impact peak in GRFx in running lead to different relative horizontal impulses in running and walking. In the visible running conditions, the contribution of the horizontal component increases considerably from mid stance as the GRFz flattens out sharply. In walking however, GRFx and GRFz both grow from mid stance and fall again simultaneously after reaching their maximum. Additionally, there are small differences at the beginning of the single support phase because of the impact peak in GRFx in running. Therefore, in total, the ratio of the GRFs in running compared to walking shifts distinctly in favor of the horizontal component. This, however, causes the VPP to move sharply downward. The deviations for the camouflaged conditions can be explained with a higher impact peak in the beginning of single support and a lower peak in GRFx at the end, because less propulsion impulse is needed. Consequently, the magnitude of the GRFx decreases slightly here, and thus the VPP moves a bit upward again. These main differences in the GRFs come from different speeds in walking and running. Therefore, it is possible that small differences in walking speed also affect VPP variables, although no significant speed effects were found in Vielemeyer et al. (2019) for VPPz. This will be taken into consideration when comparing the baseline (level) conditions of the walking studies.

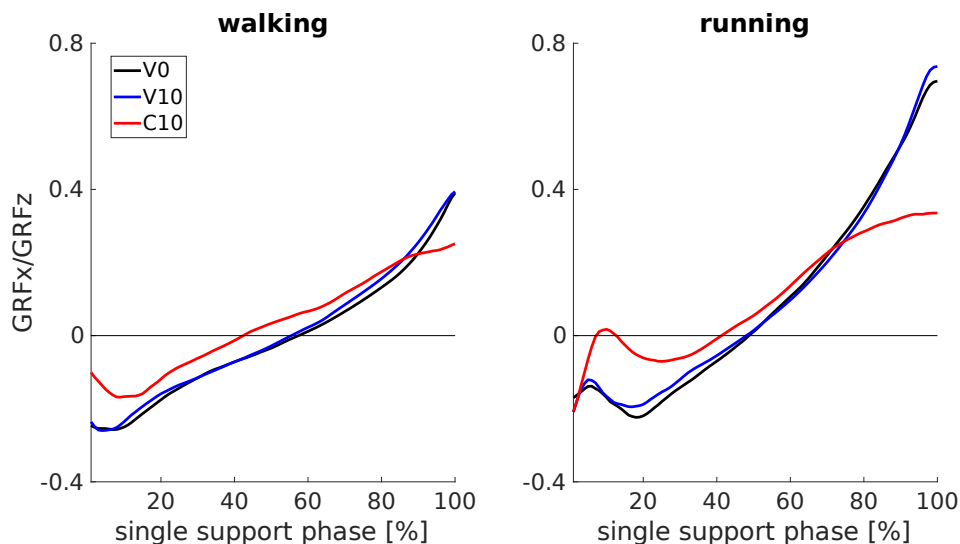


Figure 5.5: Ratio of the horizontal (x) and vertical (z) ground reaction forces (GRF) for the single support phase of walking at $1.7 \pm 0.1 \text{ ms}^{-1}$ (left) and running (right), median of all trials and mean of all subjects. The black lines represent the baseline (V0 - level) conditions. The blue/red lines stand for visible/camouflaged curbs (walking)/drops (running) of 10 cm (V10/C10).

The CoMz_{TD} does not show noticeable differences between the walking studies (table B.1). Considering the ratio of the GRFs, as illustrated in figure 5.6, the relative horizontal impulse increases from the data of the first single support of Vielemeyer et al. (2021) to the data of the fast condition of Vielemeyer et al. (2019), as shown in table B.2. A larger relative horizontal impulse is related to a greater contribution of the GRFx component, which should shift the VPPz downwards. This relation could be observed for all baseline data, except for the data of Müller et al. (2017).

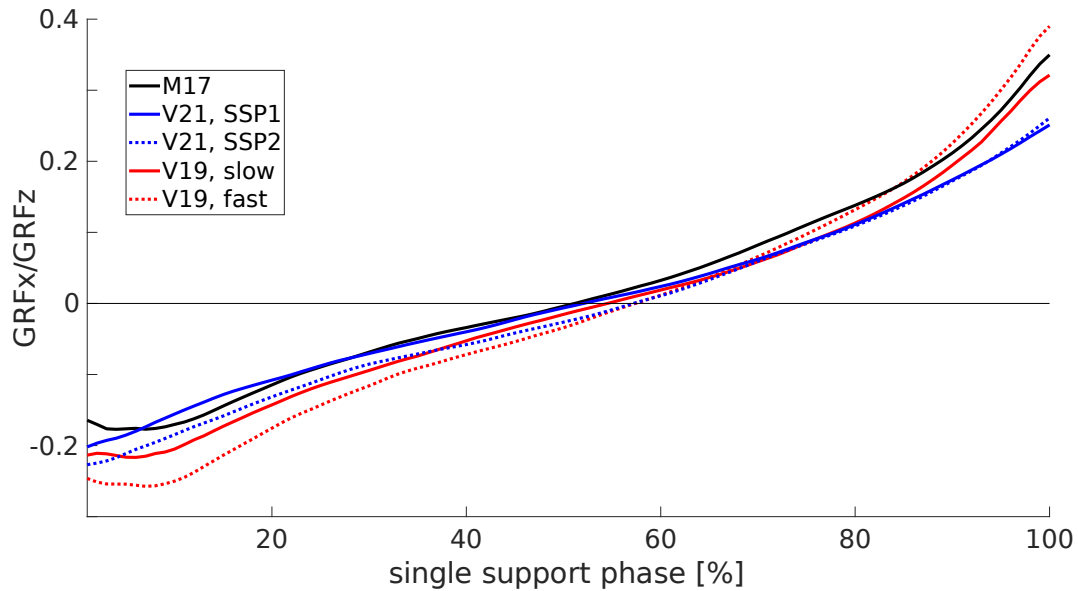


Figure 5.6: Ratio of the horizontal (x) and vertical (z) ground reaction forces (GRF) for the single support phase of walking (level, unperturbed), median of all trials and mean of all subjects. The black line illustrates the data of Müller et al. (2017) - M17. The solid blue line shows the data of the first contact (single support phase - SSP1), the dotted blue line shows the data of the second contact, SSP2, (Vielemeyer et al., 2021) - V21. The red lines represent the data of Vielemeyer et al. (2019) - V19 - with different speeds (solid line: $1.2 \pm 0.1 \text{ ms}^{-1}$, *slow*; dotted line: $1.7 \pm 0.1 \text{ ms}^{-1}$, *fast*).

The ranges of the CoP_{CoM} also display differences between the studies (figure 5.7). However, the relation of these values does not match the VPPz positions. Thus, it is conceivable that the input variables compensate each other to an unknown degree. It is likely that there is a control loop in which the input variables adapt to each other to be able to compensate perturbations without active control. For the VPPx position, there seems to be a clearer relation to the input variable CoP_{CoM} . Here, the more posterior the CoP_{CoM} is, the more posterior the VPPx is located. It is nevertheless unknown why the CoP_{CoM} is not balanced around the CoM. It could be because only the torques are balanced for the whole body stabilization (e.g. Blickhan et al., 2015; Gruben and Boehm, 2014), but these are not directly reflected in the VPP because it only indicates the control of the force vector direction. Thus, the VPP may not be a target variable, but rather an emergent variable (Vielemeyer et al., 2019). On the other hand, this shift could result

from asymmetries in the experimental setup, which will be discussed later. However, the question remains as to why there are differences in the input variables of the studies in the first place. One explanation could be that the speed has an effect. The CoP_{CoM} depends on the stride length and this in turn depends on the walking speed (e.g. Kirtley et al., 1985). Additionally, the GRFs differ with changing speeds (Nilsson and Thorstensson, 1989). Since the walking speed for the baseline conditions in the studies is between 1.17 and 1.70 ms^{-1} , the different GRFs (figure B.3), and thus ratios of their components can be explained well by the speed effects.

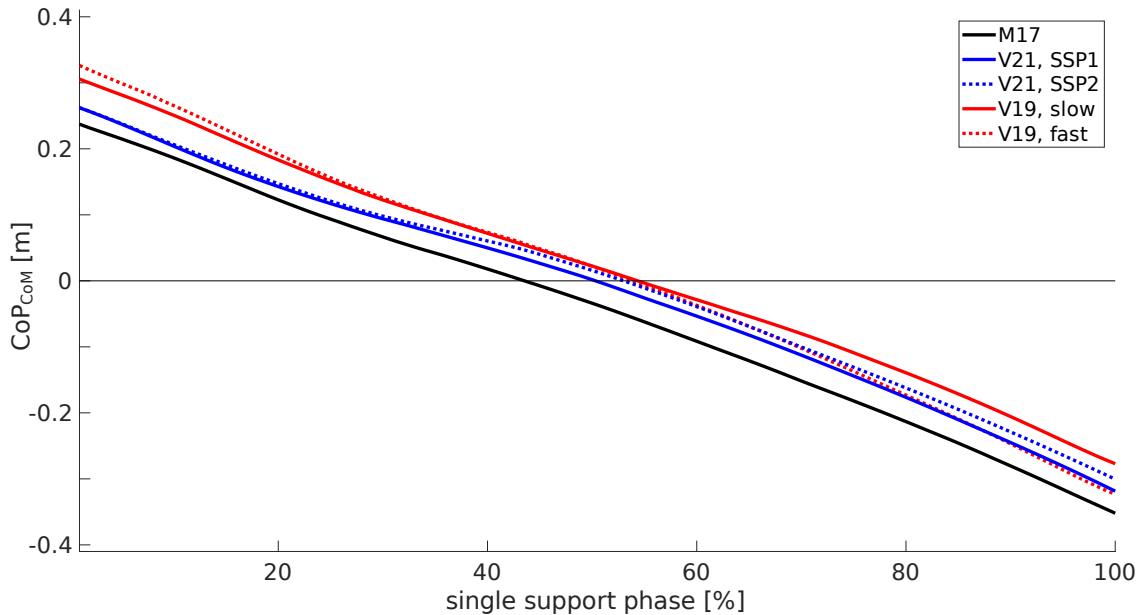


Figure 5.7: Horizontal position of the center of pressure (CoP) relative to the center of mass (CoM) for the single support phase of walking (level, unperturbed), median of all trials and mean of all subjects. The black line illustrates the data of Müller et al. (2017) - M17. The solid blue line shows the data of the first contact (single support phase - SSP1), the dotted blue line shows the data of the second contact, SSP2, (Vielemeyer et al., 2021) - V21. The red lines represent the data of Vielemeyer et al. (2019) - V19 - with different speeds (solid line: $1.2 \pm 0.1 \text{ ms}^{-1}$, *slow*; dotted line: $1.7 \pm 0.1 \text{ ms}^{-1}$, *fast*).

Nevertheless, there are further factors that may have influenced the input variables. Firstly, the anthropometric data differ between the studies, which could lead to systematic deviations (e.g. mean body height, leg length or footedness). However, these effects should be small due to the high homogeneity between the groups (see also section 5.4). Secondly, the arrangement of the walking track and the force plates varies between the studies. This could affect the stride length and the braking and propulsion behavior. Thirdly, there are errors resulting from the measurement systems that will be analyzed in section 5.2.3. Finally, slightly different calculation methods make the results less comparable.

5.2.2 Influence of the calculation methods

As mentioned in section 1.4, the used calculation methods can affect the results. Here, attention was given to the considered part of the stride, the computation of the CoM, and the blur size parameter. Since the used blur size parameters VPP_RMSD and R^2 are not comparable, R^2 was calculated for the data of Müller et al. (2017). Therefore, only the other two aspects will be compared between the studies in the following.

In two of the walking studies the considered part of the stride was 10% to 90% of the contact phase (to exclude double support phases, Müller et al., 2017; Vielemeyer et al., 2019) and in one study the calculated single support phase (Vielemeyer et al., 2021). In the running study, 10% to 100% of the contact phase was taken into account to exclude the impact peak. However, it is not clear whether these are good estimates. In Vielemeyer et al. (2021), the calculated double support phase makes up between $16.1 \pm 1.6\%$ and $17.5 \pm 1.4\%$ of the contact phase, grand mean \pm s.d. of the first and the second contact, respectively. This could explain differences between the studies regarding VPP position and blur size. In order to assess the influence of the considered part of the stride, the VPP data of Vielemeyer et al. (2021) were calculated again with the 10%-method and are shown in table 5.1. The small differences in the results could be due to the fact that the vectors at the edge regions either have only a small influence or point in the same direction for both phases. Figure 3 in the paper rather supports the second assumption (Vielemeyer et al., 2021).

Table 5.1: Virtual pivot point (VPP) data of Vielemeyer et al. (2021), calculated considering 10% to 90% of the contact phase. The values of the exact phase duration are put in brackets. Horizontal (x) and vertical (z) components of the VPP and the coefficient of determination, R^2 , are given. *Pre* stands for previous to and *post* for after the double support phase.

	method	Single support pre	Double support	Single support post
VPPx (cm)	10-90%	-0.9 ± 1.9	5.0 ± 1.7	-1.6 ± 1.7
	exact	(-1.0 ± 1.9)	(5.1 ± 1.7)	(-1.7 ± 1.7)
VPPz (cm)	10-90%	43.0 ± 13.6	1.0 ± 7.3	27.6 ± 6.4
	exact	(43.3 ± 13.5)	(0.0 ± 7.2)	(27.7 ± 6.4)
R^2 (%)	10-90%	98.4 ± 0.8	92.2 ± 2.3	98.9 ± 0.9
	exact	(98.7 ± 0.6)	(92.5 ± 2.3)	(99.0 ± 0.8)
part of contact (%)	10-90%	80	10	80
	exact	(65.1 ± 2.5)	(17.4 ± 1.4)	(66.6 ± 2.8)

Another reason for differences could be how the input variables for the VPP calculation (GRFs, CoP and CoM) are determined. The GRFs and the CoP are given directly by the force plates and thus only variations due to measurement inaccuracies are to be expected here. This will be discussed in more detail in section 5.2.3. Regarding the calculation of the CoM, there are some discrepancies, though. In all studies, the body segment

method was used. However, while the original study of Müller et al. (2017) considered the anthropometric tables of Zatsiorsky–Seluyanov modified by de Leva (Gard et al., 2004; de Leva, 1996), the other studies used the parameter method according to Plagenhoef et al. (1983), adapted by Winter (2009)³. The crucial difference is that the underlying data of de Leva (1996) were collected on living humans, whereas Plagenhoef et al. (1983) considered cadavers. To compare both methods and their influence on the VPP, the CoM and the VPP data of Müller et al. (2017) were calculated again with the method of 1) de Leva, 1996 (*living method*) and 2) Plagenhoef et al., 1983 (*cadaver method*). The mean positions of the CoM at the beginning of the single support phase are shown in figure 5.8. Here, the different heights between the methods (5-10 cm lower for the cadaver method) are particularly striking and get larger with a greater trunk inclination. Table 5.2 shows the VPP data computed with a CoM calculated by the cadaver method. The mean VPPx positions differ by 1-10 cm (more posterior for cadaver method), the mean VPPz positions differ by 7-11 cm (higher for cadaver method, which results directly from the lower CoMz position). Nevertheless, the values of both methods agree within the standard deviations.

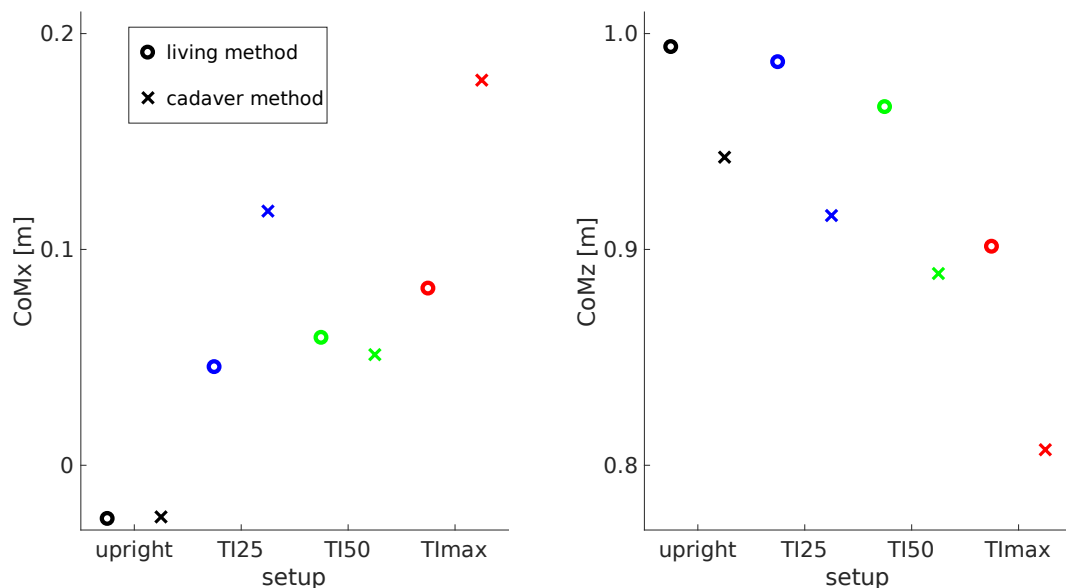


Figure 5.8: Horizontal (x, left) and vertical (z, right) position of the center of mass of the whole body (CoM) for the beginning of the single support phase, mean of all subjects and trials. The positions are calculated with the living method (circles), according to de Leva (1996) and the cadaver method (crosses) according to Plagenhoef et al. (1983) using the data of Müller et al. (2017). The black circles represent the upright walking ($7.4 \pm 3.1^\circ$). TI25 (blue) stands for a trunk inclination of $31.9 \pm 5.4^\circ$, TI50 (green) for $47.1 \pm 5.4^\circ$, and TImax (red) for $72.5 \pm 8.1^\circ$.

The trajectory of the CoM can be validated by the method of double integration of the GRFs or its inverse operation. Thus, for both conducted CoM calculation methods, the CoM position was twice differentiated with respect to time and compared with the GRFs (Crowe et al., 1993; Eames et al., 1999). Figure 5.9 shows exemplary data. The

³Vielemeyer et al. (2019) only used Plagenhoef et al. (1983).

mean trajectories agree reasonably well for both methods, even if the correlation is only between 0.27 and 0.71, probably due to the high fluctuations of the CoM acceleration. The correlation increases by considering only 70% of the contact time (adjustment according to table 5.1) to 0.44 - 0.78, the highest correlations are achieved for the upright conditions. Nevertheless, with this comparison offsets of the CoM position cannot be examined, since this information gets lost in the differentiation. Thus, it can only be presumed that the estimate of the cadaver method is more precise, because here single body segments instead of the whole body are used for the calculations.

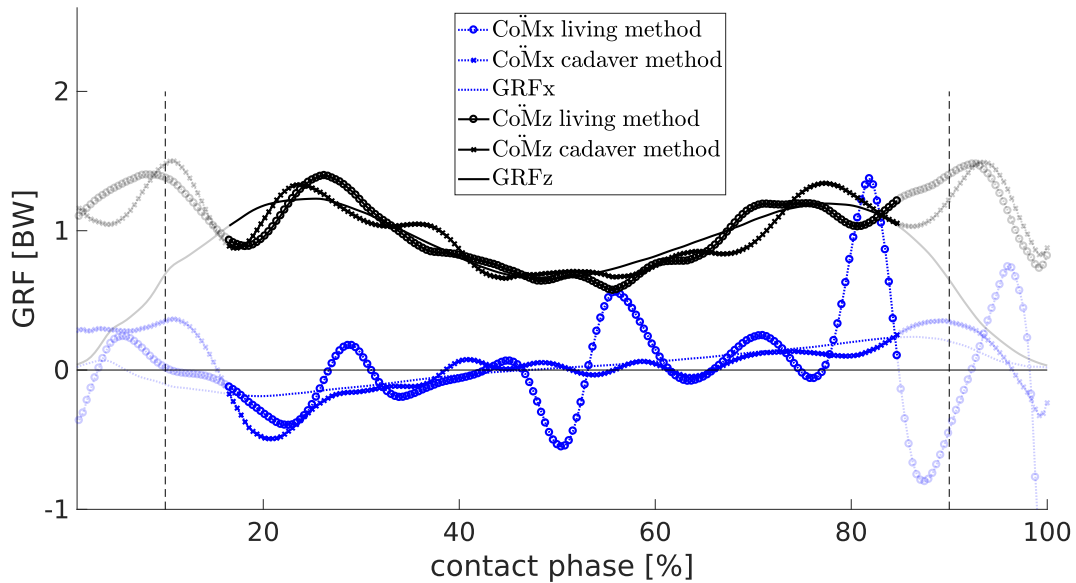


Figure 5.9: Exemplary validation of the position of the center of mass of the whole body (CoM) for the contact phase of one subject (upright walking, first trial of subject “anna” of Müller et al., 2017). The blue dotted/black solid lines show the horizontal (x)/vertical (z) components. The plain lines represent the ground reaction forces (GRF) in body weight (BW), while the lines with circles/crosses stand for the double differentiation of the CoM position (calculated with the living/cadaver method) with respect to time (CoM). The non-transparent area represents 15-85% of the contact phase, the vertical dashed lines indicate 10% and 90%. Note that the z-trajectories differ in the transparent area (double support phase), because CoMz considers both legs, while GRFz represents only one leg.

Table 5.2: Virtual pivot point (VPP) data of Müller et al. (2017), computed with the center of mass (CoM) calculation by the cadaver method. The original data (CoM calculation by the living method) are put in brackets. Horizontal (x) and vertical (z) component of the VPP and the coefficient of determination, R^2 , are given. *Upright* stands for a trunk inclination of $7.4 \pm 3.1^\circ$, *TI25* for $31.9 \pm 5.4^\circ$, *TI50* for $47.1 \pm 5.4^\circ$, and *TI_{max}* for $72.5 \pm 8.1^\circ$.

	method	upright	TI25	TI50	TI _{max}
VPPx (cm)	cadaver	-6.5 ± 6.8	-10.9 ± 14.5	-4.6 ± 6.2	-5.4 ± 3.8
	living	(0 ± 1)	(-1 ± 1)	(-2 ± 2)	(-4 ± 3)
VPPz (cm)	cadaver	31.7 ± 11.9	31.7 ± 16.1	31.4 ± 12.5	36.9 ± 4.5
	living	(21 ± 7)	(25 ± 11)	(26 ± 11)	(27 ± 9)
R^2 (%)	cadaver	97.5 ± 1.3	97.2 ± 1.1	95.5 ± 3.1	90.2 ± 5.3

The last methodic aspect to be considered concerns the descriptive statistic. While Müller et al. (2017) calculated the mean over trials and subjects, the other studies used the median for the trials to give less weight to outliers. However, across the subjects, the mean value was calculated, as outliers must also be taken into account here. The expected differences due to this calculation methods are nevertheless small.

5.2.3 Error estimation

The following error estimation is performed exemplarily for the data of Vielemeyer et al. (2021). It will show the effect on the input variables and the resulting changes in the VPP data.

The maximum error in the CoM⁴ is directly determined by the maximum deviation in the marker positions. The average measurement error for most kinematic measurement systems is given with 2-3 mm per dimension (Whittle, 1993). In addition, the position of the marker can be inaccurate, caused, for example, by not exactly determined landmarks or skin movement. Thus a resulting error of up to ± 1.5 cm is assumed for the CoM.

For the kinetic system, there are crosstalk errors and deviations in the accuracy of the amplifier. These are given in the data sheet of the force plates (Kistler, 2008a,b).

$$\begin{aligned}\Delta F_x &= (1 + \text{ampl}) \cdot (\text{cross}_{y \rightarrow x} \cdot |\text{GRF}_y| + \text{cross}_{z \rightarrow x} \cdot |\text{GRF}_z|), \\ \Delta F_z &= (1 + \text{ampl}) \cdot (\text{cross}_{x \rightarrow z} \cdot |\text{GRF}_x| + \text{cross}_{y \rightarrow z} \cdot |\text{GRF}_y|), \\ \Delta M_y &= (1 + \text{ampl}) \cdot (\text{cross}_{x \rightarrow y} \cdot |M_x| + \text{cross}_{z \rightarrow y} \cdot |M_z|),\end{aligned}\tag{5.1}$$

where *ampl* and *cross* are given in table D.1.

This results in a maximum absolute error of $\Delta F_x = \pm 0.02$ BW for GRFx and $\Delta F_z = \pm 0.01$ BW for GRFz for all trials and subjects. In equation 5.1, *M* are the bending moments, which are calculated by the force plates.

The horizontal position of the CoP is calculated with equation 5.2 (Winter, 2009).

$$\text{CoP} = \frac{\text{GRF}_x \cdot z_0 + M_y}{\text{GRF}_z},\tag{5.2}$$

where *M_y* is the bending moment with respect to the axis of rotation of support and *z₀* is the distance between the support axis and the force plate surface, as shown in figure D.1 (Winter, 2009). The absolute error of the CoP can be calculated taking into account the error limits as follows

⁴Errors arising from model assumptions are neglected in these considerations.

$$\Delta\text{CoP} = \frac{|(\text{GRF}_x + \text{sgn}(\text{GRF}_x) \cdot \Delta\text{F}_x) \cdot z_0 + (\text{M}_y + \text{sgn}(\text{M}_y) \cdot \Delta\text{M}_y)|}{|\text{GRF}_z| - \Delta\text{F}_z} - |\text{CoP}|, \quad (5.3)$$

with the sign function *sgn*. This results in the absolute error $\Delta\text{CoP} = \pm 0.03$ m (equation 5.3), as mean value over the trajectory for all trials and subjects.

From these errors in the input variables, the uncertainty in the VPP can be estimated. To get the maximum range of the VPPz, the possible errors were added up and the VPPz was calculated with equation 1.3 for the minimum (maximum) CoP_{CoM} range, GRFs with a ratio in favor of GRFx (GRFz) and a maximum (minimum) CoMz position. This results in the technical lower (upper) limit of the VPP. The mechanisms are illustrated schematically in figure 5.3. The results and the contribution of the particular components are shown in table 5.3. It is noticeable that the influence of the CoMz height is directly represented in the VPPz position, while the errors of the GRFs and the CoP_{CoM} have an influence of ± 2.5 to 3.0 cm. This results in a shift of the VPPz of up to about ± 7 cm only due to measurement errors. However, this is only the cumulative error when all components shift the VPP in the same direction.

Table 5.3: Vertical (z) virtual pivot point (VPP) range due to measurement system errors (mean values of all trials and subjects, all values in cm) according to the data of Vielemeyer et al. (2021). SSP1 (SSP2) is the single support phase of the first (second) contact. CoP_{CoM} describes the center of mass (CoM) - centered center of pressure (CoP), GRFs are the ground reaction forces.

	VPPz	CoP_{CoM}	GRFs	CoMz	sum	$\text{VPPz}_{\text{min}} \dots \text{VPPz}_{\text{max}}$
SSP1	43.3	± 2.7	± 3.0	± 1.5	± 7.2	36.1...50.5
SSP2	27.7	± 2.5	± 2.5	± 1.5	± 6.5	21.2...34.2

In summary, it is essential to pay attention to the errors that can arise from the measurement systems, as their influence on the results is considerable, and not to overinterpret the exact calculated VPP position.

5.2.4 Conclusion

As a result of the above considerations, the relation between the VPP and the gait stability will be discussed now. Can the VPP or related data provide information about robustness against perturbations? How does the gait stability relate to the VPP position, and is the VPP possibly even a target variable of control?

In principle, there are different possibilities with respect to the VPP. For one thing, the family of force vectors might not point in any defined direction, then no VPP exists and no statement can be made regarding stability. For another thing, the force vectors can

intersect near a point, the VPP. Then the system can be denoted as regular pendulum if the VPP is above the CoM, and as inverted pendulum, if the VPP is at or below the CoM. Since R^2 was sufficiently high in all investigated situations for the VPP to be regarded as a point, the pendulum mechanism could be observed in all setups. In the literature, an upward shift of the VPP was expected to increase both stability and energy costs (Gruben and Boehm, 2012; Maus et al., 2010). Thus, the pendulum mechanism presumably ensures the stability of at least human walking. In human running, the inverted pendulum seems to be used for energy reasons (Drama et al., 2020). Therefore, a VPP above the CoM can be used to reduce the kinetic energy fluctuations of the CoM, and a VPP below the CoM to reduce the potential energy fluctuations (Drama et al., 2020). In the single support phase of walking, a forward leaning of the trunk indicates a positive offset in the hip torque pattern and thus, a counterclockwise angular momentum (Maufroy et al., 2011). The purpose of leaning forward with a VPP posterior to the trunk axis is probably to increase stability (Maufroy et al., 2011). In running, the clockwise angular momentum indicates that the GRFs should pass below the CoM (Drama et al., 2020). In the double support phase of walking, also a clockwise angular momentum could be observed (Vielemeyer et al., 2021). However, the whole body is rotated around the CoM in a short time window, presumably to decrease energy effort and increase stability (Vielemeyer et al., 2021) and robustness against perturbations (Cui et al., 2020).

Differences, especially in the blur size parameter R^2 , can be found between the unperturbed settings and the perturbed ones. The lower R^2 in the highly perturbed situations could be explained by the fact that more energy is needed to balance the whole body in these situations. The assumption of higher energy requirements is based on the observation that a higher GRFz or impulse effort is needed for braking, for example in the C10 and TImax conditions. Additionally, for these setups, the CoP_{CoM} is more posterior and not well balanced around the CoM. As mentioned above, these factors reduce R^2 . Thus, there is probably an overregulation at the expense of energy and in favor of maintaining stability. However, a more detailed investigation of this hypothesis is required. If proven correct, R^2 might be a good indicator whether more energy was needed to balance the whole body without measuring the energy effort directly. A smaller R^2 could indicate a more energy-consuming, unstable gait and thus a greater likelihood of falling, making R^2 a highly beneficial diagnostic tool. However, it is not possible to use the VPP and its blur size as a quantitative parameter for evaluating stability.

The high R^2 suggests that the VPP model is robust against the investigated perturbations. This was also found in simulations, albeit to varying degrees. The first simulation of the VPP model for walking was robust against a step down perturbation of 5 mm without further adjustments (Maus et al., 2010). Remarkably, one simulation of human running was even robust for a step down perturbation of up to 40 cm (Drama et al., 2020). Both simulations differ in the VPPz position relative to the CoM (Maus et al., 2010: 25 cm

above the CoM, Drama et al., 2020: 30 cm below the CoM). Thus, it can be assumed that the VPPz position has an effect on the robustness of the model. In particular, it seems to be decisive whether the VPP is located above, at, or below the CoM. Since, for example, there are simulations for running with a VPP below the CoM and also with a VPP above the CoM (Maus et al., 2008; Sharbafi and Seyfarth, 2014), both approaches seem to work. However, there are probably differences in robustness against perturbation, which unfortunately has not yet been investigated systematically.

It is probably not appropriate to compare different gaits or gait phases based on the VPP position. Human walking has single support and double support phases with different purposes and thus, varying VPPz positions in these particular phases. Here, a lower R^2 in the double support phase does not necessarily mean that the system is less stable, since both legs having contact to the ground provides a closed kinetic chain for the lower body. On the other hand, human running only has single support phases, where stability always has to be maintained. Therefore, the different VPPz positions could be explained by the different purposes and may not directly be a sign of stability. Analogous considerations can be made for the VPPx. The VPPx can be at, anterior or posterior to the CoM. A greater distance from the CoM indicates more rotation of the whole body (depending on VPPz). The differences between the gaits or the gait phases can also be explained by the different purposes. However, the variability of the system presumably increases for greater deviations of the VPPx from the CoM due to higher rotation.

Therefore, the VPP is probably not a target variable, because its position and blur size vary, but rather arises from the interaction of various factors, as Gruben and Boehm (2014), Müller et al. (2017) and Vielemeyer et al. (2019) already argued.

In summary, the VPPz position cannot provide any indication of stability, but only of the type of pendulum and the purpose of the gait. R^2 and VPPx, however, can indicate the quality of stability: a lower R^2 and a greater distance of the VPPx to the CoM represent a presumably lower stability of human gait. It is nevertheless impossible to measure stability with the VPP or its blur size.

5.3 Improvements of the VPP concept

In the known literature, the VPP concept is very rarely represented. This is because, on the one hand, it is currently only a bit more than ten years old, and, on the other hand, it exists parallel to other models. Here, no model can obviously be preferred to another, as they all simplify the human body. Nevertheless, the VPP model can make an important contribution to a better understanding of human locomotion. Thus, the studies performed for this work provide exciting new insights in the dynamic stabilization of human gait. Besides exploring different experimental setups, a main purpose was to

methodically develop and improve the VPP concept. This includes a detailed documentation of the calculation of the VPP (chapter 1.3.3) and the introduction of the blur size parameters VPP_RMSD and R^2 . However, there are several points in which the model can be further developed and improved.

From the perspective of simulation of the VPP model, step-by-step changes of the VPP position could improve gait stability and robustness against perturbations (Sharbafi et al., 2013b). That means, for example, that different VPP positions for the single support phase and the double support phase could be considered. Overall, the simulation can certainly be enhanced by considering more human parameters (see section 5.4). When analyzing the experiments, it could be examined more closely which alignment of the reference frame gives more accurate results. While Sharbafi et al. (2013b) aligned the coordinate system to the trunk axis, Andrada et al. (2014); Drama et al. (2020); Maus et al. (2010); Maus (2008) and Vielemeyer et al. (2019, 2021) chose a vertically aligned coordinate system. However, both Gruben and Boehm (2012) and Müller et al. (2017) did not observe any obvious differences when comparing the reference frames. Another aspect is the percentage of the GRFs that are considered for the VPP calculation, since it could provide more precise results if the impact peak is excluded. Therefore some studies have cut a fixed percentage of GRFs (Andrada et al., 2014; Drama et al., 2020; Müller et al., 2017; Vielemeyer et al., 2019), other included only GRFs within a certain angular range (Maus, 2008). Both approaches do not seem to be methodologically very sound and could be improved further.

A decisive further development of the VPP concept in simulation and experiments could be to no longer consider the VPP as a point but as a 2D or 3D domain. For example, instead of a single intersection point of the GRFs over time a set of intersection points of the GRFs with the vertical or the trunk axis could be considered for each time frame. This might result in a trajectory in the sagittal plane or in space. In doing so, it could be investigated whether this construct better explains reality. In particular, this could be the case for situations like double support, where it is not clear whether the intersection can be denoted as a VPP or even as a point (Vielemeyer et al., 2021). Following this, the term *VPP* should once again be given considerable attention. Although there are several different denotations (e.g. *divergent point*, *intersection point*, *virtual point*, *virtual pivot point*), there does not seem to be a superior one; the choice of denotation rather reflects personal preferences. The term *virtual pivot point* was chosen in this study, because it describes well the concept of stabilizing the body as physical pendulum, for example in human walking. On the other hand, the term seems inappropriate when the point is at or below the CoM and thus, an inverted pendulum is observed. In these cases, the term *intersection point* seems to be more general and appropriate. However, this issue of notation can certainly only be properly addressed by further developing the VPP concept as a whole, as emphasized in the previous section.

5.4 Limitations and further considerations

The design of the experiments performed for this work have a few limitations that should be mentioned. Firstly, in all studies there participated only homogeneous groups of physically active, healthy, and young adults. However, this allows a good comparability between the studies. Secondly, there were no automatic mechanisms to control speed. It is therefore possible that braking and propulsion occurred during the single trials, although a constant gait speed was assumed in the analyses. Thirdly, in the studies where unexpected drops or curbs occurred (Drama et al., 2020; Vielemeyer et al., 2019), the subjects were aware that something would happen and thus, it was not completely unexpected. It is possible that in these conditions the gait pattern was already different from the level condition before the perturbation. In all experiments it was defined that the first force plate had to be hit with the left foot and the second force plate with the right foot. As a result, the gait was no longer completely natural⁵. Another limitation was that the order of the settings was not randomized, except for Vielemeyer et al. (2019). This could lead to order effects or learning effects.

One general weakness of using an overground gait track compared to a treadmill is the restriction to only a few evaluable steps. In the experiments performed for the present work, only two force plates were available, although it is known that a high stride-to-stride variance can be observed in human gait (Kluitenberg et al., 2012). To mitigate this problem, the results were averaged over several trials. Moreover it is possible that in the experiments with drops and curbs the normalization of the gait pattern occurs in the steps after the perturbation, which were not examined. This issue could be measured better on the treadmill, but neither visible nor camouflaged drops and curbs can be realized in such a setup.

Since Maus et al. (2010) and Gruben and Boehm (2012) conducted their measurements to determine the VPP on the treadmill (walking on level ground), it will be briefly analyzed whether differences between overground and treadmill walking can be expected in the VPP-relevant parameters. For the vertical GRFs, it was reported that the patterns were nearly identical, while the magnitudes during mid- and late-stance of individual subjects and trials may differ slightly but significantly (White et al., 1998). The CoM motion relative to the CoP is qualitatively similar between overground and treadmill walking (Lu et al., 2017b). Therefore, the surface has only a small effect on the VPP-related variables in walking, but as shown in Vielemeyer et al. (2021), this can nevertheless shift the VPP considerably. The results for the VPP-related variables while running are similar (Firminger et al., 2018; Kluitenberg et al., 2012). This should be considered when comparing the studies.

⁵For a detailed discussion of this issue see Müller et al. (2014), who provided the experimental data for Vielemeyer et al. (2021).

Additionally, measurement inaccuracy of the kinetic and kinematic systems cannot be excluded. The effect of expectable measurement inaccuracies on the calculation of the VPP was discussed in section 5.2.3. Furthermore, the model-based computations (for instance the parameter model for CoM calculation) are only simplifications. For both the running and the double support studies, the subject's arms were not included in the kinematic measurements, which makes the CoM model less precise. However, the double check of comparing the second derivative of the CoM with the GRFs suggests that the inaccuracies are not very large, as shown in section 5.2.3.

Outlook

There are several possibilities to extend the presented experiments. With the help of EMG, the muscle activity could be measured additionally, as it was already performed for the measurements of Vielemeyer et al. (2019) and is presented in Müller et al. (2020). This allows an even more comprehensive analysis of the perturbed gait and its stabilization. Furthermore, other extrinsic perturbations as obstacles, bumps or other irregular surfaces, could be investigated from the point of view of the VPP. Additionally, experiments with other intrinsic perturbations can be performed to examine whether a stable gait can be observed without a VPP. It would also be interesting to study other symmetric gaits such as grounded running and even asymmetric gaits such as skipping or galloping with the focus on the VPP. Moreover, this work could provide a basis for clinical studies. Elderly or patients with a neurological disorder (e.g. cerebral palsy, down syndrome or multiple sclerosis) could be examined, since they have a higher risk of falling (Berg et al., 1997; Menz et al., 2003), and thus it is particularly important to maintain the gait stability. Here, the suitability of the VPP and its R^2 as stability parameter could be investigated. Another aspect is the implementation of the VPP as a control variable in robots. Here, the findings of Drama et al. (2020) can be used to construct robots with smaller actuators, after adopting VPP positions that are leading to lower joint loads. It is planned to implement the VPP concept in the humanoid robot LOLA, since here currently no VPP can be observed (Staufenberg et al., 2019). Finally, while comparing the human experimental data with simulations (e.g. Drama et al., 2020) it can be seen that although the simulations are stable, they could be improved by better adaptations to human gait parameters like swing leg dynamics, collision dynamics, and ankle push-off effects. In addition, the influence of the VPP position on the robustness against perturbations could be investigated to increase the range of perturbations the VPP simulations can successfully negotiate.

List of literature

- Alexander, R. (1976). Mechanics of bipedal locomotion. *Perspectives in experimental biology*, 1:493–504.
- Alexander, R. M. (2004). Bipedal animals, and their differences from humans. *Journal of anatomy*, 204(5):321–330.
- Andrada, E., Nyakatura, J. A., Bergmann, F., and Blickhan, R. (2013). Adjustments of global and local hindlimb properties during terrestrial locomotion of the common quail (*coturnix coturnix*). *Journal of experimental biology*, 216(20):3906–3916.
- Andrada, E., Rode, C., Sutedja, Y., Nyakatura, J. A., and Blickhan, R. (2014). Trunk orientation causes asymmetries in leg function in small bird terrestrial locomotion. *Proceedings of the Royal Society of London B: Biological Sciences*, 281(1797):20141405.
- Barbieri, F. A., Lee, Y.-J., Gobbi, L. T. B., Pijnappels, M., and Van Dieën, J. H. (2013). The effect of muscle fatigue on the last stride before stepping down a curb. *Gait & posture*, 37(4):542–546.
- Berg, W. P., Alessio, H. M., Mills, E. M., and Tong, C. (1997). Circumstances and consequences of falls in independent community-dwelling older adults. *Age and ageing*, 26(4):261–268.
- Blair, S., Lake, M. J., Ding, R., and Sterzing, T. (2018). Magnitude and variability of gait characteristics when walking on an irregular surface at different speeds. *Human movement science*, 59:112–120.
- Blickhan, R. (1989). The spring-mass model for running and hopping. *Journal of biomechanics*, 22(11-12):1217–1227.
- Blickhan, R., Andrada, E., Müller, R., Rode, C., and Ogihara, N. (2015). Positioning the hip with respect to the COM: Consequences for leg operation. *Journal of theoretical biology*, 382:187–197.
- Blum, Y., Rummel, J., and Seyfarth, A. (2007). Advanced swing leg control for stable locomotion. In *Autonome mobile Systeme 2007*, pages 301–307. Springer.
- Bonnefoy, A. and Armand, S. (2015). Normal gait. *Orthopedic management of children with cerebral palsy: a comprehensive approach*, page 567.
- Cappozzo, A., Figura, F., Marchetti, M., and Pedotti, A. (1976). The interplay of muscular and external forces in human ambulation. *Journal of biomechanics*, 9(1):35–43.
- Crowe, A., Schiereck, P., de Boer, R., and Keessen, W. (1993). Characterization of gait of

- young adult females by means of body centre of mass oscillations derived from ground reaction forces. *Gait & posture*, 1(1):61–68.
- Cui, C., Kulkarni, A., Rietdyk, S., Barbieri, F., and Ambike, S. (2020). Synergies in the ground reaction forces and moments during double support in curb negotiation in young and older adults. *Journal of biomechanics*, page 109837.
- Davoodi, A., Mohseni, O., Seyfarth, A., and Sharbafi, M. A. (2019). From template to anchors: transfer of virtual pendulum posture control balance template to adaptive neuromuscular gait model increases walking stability. *Royal Society open science*, 6(3):181911.
- van Dieën, J. H., Spanjaard, M., Konemann, R., Bron, L., and Pijnappels, M. (2007). Balance control in stepping down expected and unexpected level changes. *Journal of biomechanics*, 40(16):3641–3649.
- van Dieën, J. H., Spanjaard, M., Könemann, R., Bron, L., and Pijnappels, M. (2008). Mechanics of toe and heel landing in stepping down in ongoing gait. *Journal of biomechanics*, 41(11):2417–2421.
- Drama, Ö. and Badri-Spröwitz, A. (2019). Trunk pitch oscillations for joint load redistribution in humans and humanoid robots. In *2019 IEEE-RAS 19th International Conference on Humanoid Robots (Humanoids)*, pages 531–536. IEEE.
- Drama, Ö., Vielemeyer, J., Badri-Spröwitz, A., and Müller, R. (2020). Postural stability in human running with step-down perturbations: an experimental and numerical study. *Royal Society open science*, 7:200570.
- Eames, M., Cosgrove, A., and Baker, R. (1999). Comparing methods of estimating the total body centre of mass in three-dimensions in normal and pathological gaits. *Human movement science*, 18(5):637–646.
- Enoka, R. (2008). *Neuromechanics of Human Movement*. Colorado: Human Kinetics.
- Firminger, C. R., Vernillo, G., Savoldelli, A., Stefanyshyn, D. J., Millet, G. Y., and Edwards, W. B. (2018). Joint kinematics and ground reaction forces in overground versus treadmill graded running. *Gait & posture*, 63:109–113.
- Firouzi, V., Seyfarth, A., and Sharbafi, M. A. (2019). Does VPP exist in lateral balancing? In *9th International Symposium on Adaptive Motion of Animals and Machines (AMAM 2019)*.
- Full, R. J. and Koditschek, D. E. (1999). Templates and anchors: neuromechanical hypotheses of legged locomotion on land. *Journal of experimental biology*, 202(23):3325–3332.
- Gard, S. A., Miff, S. C., and Kuo, A. D. (2004). Comparison of kinematic and kinetic methods for computing the vertical motion of the body center of mass during walking. *Human movement science*, 22(6):597–610.

- Gates, D. H., Wilken, J. M., Scott, S. J., Sinitski, E. H., and Dingwell, J. B. (2012). Kinematic strategies for walking across a destabilizing rock surface. *Gait & posture*, 35(1):36–42.
- Geyer, H. and Herr, H. (2010). A muscle-reflex model that encodes principles of legged mechanics produces human walking dynamics and muscle activities. *IEEE Transactions on neural systems and rehabilitation engineering*, 18(3):263–273.
- Geyer, H., Seyfarth, A., and Blickhan, R. (2006). Compliant leg behaviour explains basic dynamics of walking and running. *Proceedings of the Royal Society B: Biological Sciences*, 273(1603):2861–2867.
- Grasso, R., Zago, M., and Lacquaniti, F. (2000). Interactions between posture and locomotion: motor patterns in humans walking with bent posture versus erect posture. *Journal of neurophysiology*, 83(1):288–300.
- Gruben, K. G. and Boehm, W. L. (2012). Force direction pattern stabilizes sagittal plane mechanics of human walking. *Human movement science*, 31(3):649–659.
- Gruben, K. G. and Boehm, W. L. (2014). Ankle torque control that shifts the center of pressure from heel to toe contributes non-zero sagittal plane angular momentum during human walking. *Journal of biomechanics*, 47(6):1389–1394.
- Götz-Neumann, K. (2011). *Gehen verstehen. Ganganalyse in der Physiotherapie*. Stuttgart: Georg Thieme Verlag KG.
- Hak, L., Houdijk, H., Steenbrink, F., Mert, A., van der Wurff, P., Beek, P. J., and van Dieën, J. H. (2012). Speeding up or slowing down?: Gait adaptations to preserve gait stability in response to balance perturbations. *Gait & posture*, 36(2):260–264.
- Herr, H. and Popovic, M. (2008). Angular momentum in human walking. *Journal of experimental biology*, 211(4):467–481.
- Hicks, J. L., Schwartz, M. H., Arnold, A. S., and Delp, S. L. (2008). Crouched postures reduce the capacity of muscles to extend the hip and knee during the single-limb stance phase of gait. *Journal of biomechanics*, 41(5):960–967.
- Hof, A. L. (1996). Scaling gait data to body size. *Gait & posture*, 3(4):222–223.
- Hortobágyi, T. and DeVita, P. (2000). Muscle pre- and coactivity during downward stepping are associated with leg stiffness in aging. *Journal of electromyography and kinesiology*, 10(2):117–126.
- Inman, V., Ralston, H., and Todd, F. (2006). *Human locomotion*. In Rose, J. & Gamble, J.G. (2006). *Human Walking (S. 1-18)*. Philadelphia: Lippincott Williams & Wilkins.
- Jordan, K. and Newell, K. M. (2008). The structure of variability in human walking and running is speed-dependent. *Exercise and sport sciences reviews*, 36(4):200–204.
- Kaufman, K. and Sutherland, D. (2006). *Kinematics of Normal Human Walking*. In

- Rose, J. & Gamble, J.G. (2006). *Human Walking (S. 33-52)*. Philadelphia: Lippincott Williams & Wilkins.
- Keller, T. S., Weisberger, A., Ray, J., Hasan, S., Shiavi, R., and Spengler, D. (1996). Relationship between vertical ground reaction force and speed during walking, slow jogging, and running. *Clinical biomechanics*, 11(5):253–259.
- Kenwright, B., Davison, R., and Morgan, G. (2011). Dynamic balancing and walking for real-time 3D characters. In *International Conference on Motion in Games*, pages 63–73. Springer.
- Kirtley, C., Whittle, M. W., and Jefferson, R. (1985). Influence of walking speed on gait parameters. *Journal of biomedical engineering*, 7(4):282–288.
- Kistler (2008a). Data sheet - Mehrkomponenten Messplattform - Typ 9281B.
- Kistler (2008b). Data sheet - multicomponent measuring force plate for biomechanics and industry - type 9281B.
- Kluitenberg, B., Bredeweg, S. W., Zijlstra, S., Zijlstra, W., and Buist, I. (2012). Comparison of vertical ground reaction forces during overground and treadmill running. A validation study. *BMC musculoskeletal disorders*, 13(1):235.
- Lee, J., Vu, M. N., and Oh, Y. (2017). A control method for bipedal trunk spring loaded inverted pendulum model. In Westphall, CB and Mendonca, M and Vasconcelos, RO, editor, *13th International Conference on Autonomic and Autonomous Systems (ICAS 2017)*, pages 24–29.
- de Leva, P. (1996). Adjustments to Zatsiorsky-Seluyanov’s segment inertia parameters. *Journal of biomechanics*, 29(9):1223–1230.
- van der Linden, M. H., Hendricks, H. T., Bloem, B. R., and Duysens, J. (2009). Hitting a support surface at unexpected height during walking induces loading transients. *Gait & posture*, 29(2):255–260.
- Lu, H.-L., Kuo, M.-Y., Chang, C.-F., Lu, T.-W., and Hong, S.-W. (2017a). Effects of gait speed on the body’s center of mass motion relative to the center of pressure during over-ground walking. *Human movement science*, 54:354–362.
- Lu, H.-L., Lu, T.-W., Lin, H.-C., and Chan, W. P. (2017b). Comparison of body’s center of mass motion relative to center of pressure between treadmill and over-ground walking. *Gait & posture*, 53:248–253.
- Mann, R. A., Moran, G. T., and Dougherty, S. E. (1986). Comparative electromyography of the lower extremity in jogging, running, and sprinting. *The american journal of sports medicine*, 14(6):501–510.
- Marquardt, M. (2012). *Geh- und Laufbewegung*. In Marquardt, M. (2012). *Laufen und Laufanalyse: Medizinische Betreuung von Läufern (S. 63-90)*. Stuttgart: Georg Thieme Verlag KG.

- Maufroy, C., Maus, H. M., and Seyfarth, A. (2011). Simplified control of upright walking by exploring asymmetric gaits induced by leg damping. In *2011 IEEE International Conference on Robotics and Biomimetics*, pages 491–496. IEEE.
- Maus, H.-M. (2013). *Towards understanding human locomotion*. Technische Universität Ilmenau, Germany.
- Maus, H.-M., Lipfert, S., Gross, M., Rummel, J., and Seyfarth, A. (2010). Upright human gait did not provide a major mechanical challenge for our ancestors. *Nature communications*, 1:70.
- Maus, H.-M., Rummel, J., and Seyfarth, A. (2008). Stable upright walking and running using a simple pendulum based control scheme. In *Advances in mobile robotics*, pages 623–629. World Scientific.
- Maus, M. H. (2008). Stabilisierung des Oberkörpers beim Rennen und Gehen. diploma thesis, Friedrich Schiller University Jena.
- Maykranz, D., Grimmer, S., Lipfert, S., and Seyfarth, A. (2009). Foot function in spring mass running. In *Autonome mobile Systeme 2009*, pages 81–88. Springer.
- McMahon, T. A. and Cheng, G. C. (1990). The mechanics of running: how does stiffness couple with speed? *Journal of biomechanics*, 23:65–78.
- Menz, H. B., Lord, S. R., and Fitzpatrick, R. C. (2003). Acceleration patterns of the head and pelvis when walking are associated with risk of falling in community-dwelling older people. *The journals of gerontology series A: biological sciences and medical sciences*, 58(5):M446–M452.
- Mochon, S. and McMahon, T. A. (1980). Ballistic walking. *Journal of biomechanics*, 13(1):49–57.
- Muir, G., Gosline, J., and Steeves, J. (1996). Ontogeny of bipedal locomotion: walking and running in the chick. *The journal of physiology*, 493(2):589–601.
- Müller, R. and Blickhan, R. (2010). Running on uneven ground: leg adjustments to altered ground level. *Human movement science*, 29(4):578–589.
- Müller, R., Ernst, M., and Blickhan, R. (2012). Leg adjustments during running across visible and camouflaged incidental changes in ground level. *Journal of experimental biology*, 215(17):3072–3079.
- Müller, R., Rode, C., Aminiaghdam, S., Vielemeyer, J., and Blickhan, R. (2017). Force direction patterns promote whole body stability even in hip-flexed walking, but not upper body stability in human upright walking. *Proceedings of the Royal Society A*, 473(2207):20170404.
- Müller, R., Tschiesche, K., and Blickhan, R. (2014). Kinetic and kinematic adjustments during perturbed walking across visible and camouflaged drops in ground level. *Journal of biomechanics*, 47(10):2286–2291.

- Müller, R., Vielemeyer, J., and Häufle, D. F. (2020). Negotiating ground level perturbations in walking: visual perception and expectation of curb height modulate muscle activity. *Journal of biomechanics*, page 110121.
- Nigg, B. M., De Boer, R. W., and Fisher, V. (1995). A kinematic comparison of overground and treadmill running. *Medicine and science in sports and exercise*, 27(1):98–105.
- Nilsson, J. and Thorstensson, A. (1989). Ground reaction forces at different speeds of human walking and running. *Acta physiologica scandinavica*, 136(2):217–227.
- O’Connor, C. M., Thorpe, S. K., O’Malley, M. J., and Vaughan, C. L. (2007). Automatic detection of gait events using kinematic data. *Gait & posture*, 25(3):469–474.
- Panizzolo, F. A., Lee, S., Miyatake, T., Rossi, D. M., Siviyy, C., Speeckaert, J., Galiana, I., and Walsh, C. J. (2017). Lower limb biomechanical analysis during an unanticipated step on a bump reveals specific adaptations of walking on uneven terrains. *Journal of experimental biology*, 220(22):4169–4176.
- Peck, A. J. and Turvey, M. (1997). Coordination dynamics of the bipedal galloping pattern. *Journal of motor behavior*, 29(4):311–325.
- Peekema, A. T. (2015). Template-based control of the bipedal robot ATRIAS. Master’s thesis, Oregon State University, Corvallis, USA.
- Peng, J., Fey, N. P., Kuiken, T. A., and Hargrove, L. J. (2016). Anticipatory kinematics and muscle activity preceding transitions from level-ground walking to stair ascent and descent. *Journal of biomechanics*, 49(4):528–536.
- Perry, J. and Burnfield, J. M. (1993). Gait analysis: normal and pathological function. *Developmental medicine and child neurology*, 35:1122–1122.
- Plagenhoef, S., Gaynor, E. F., and Abdelnour, T. (1983). Anatomical data for analyzing human motion. *Research quarterly for exercise and sport*, 54(2):169–178.
- Poulakakis, I. and Grizzle, J. (2007). Formal embedding of the spring loaded inverted pendulum in an asymmetric hopper. In *2007 European Control Conference (ECC)*, pages 3159–3166. IEEE.
- Raibert, M. H. (1986). *Legged robots that balance*. MIT press.
- Rubenson, J., Heliam, D. B., Lloyd, D. G., and Fournier, P. A. (2004). Gait selection in the ostrich: mechanical and metabolic characteristics of walking and running with and without an aerial phase. *Proceedings of the Royal Society of London. Series B: Biological Sciences*, 271(1543):1091–1099.
- Rummel, J. and Seyfarth, A. (2010). Passive stabilization of the trunk in walking. *International Conference on Simulation, Modeling and Programming for Autonomous Robots, Darmstadt, Germany, 2010, Proceedings*, 180(190):200.
- Saha, D., Gard, S., and Fatone, S. (2008). The effect of trunk flexion on able-bodied gait. *Gait & posture*, 27(4):653–660.

- Saranli, U., Buehler, M., and Koditschek, D. E. (2001). Rhex: A simple and highly mobile hexapod robot. *The international journal of robotics research*, 20(7):616–631.
- Seipel, J. and Holmes, P. (2007). A simple model for clock-actuated legged locomotion. *Regular and chaotic dynamics*, 12(5):502–520.
- Seyfarth, A., Grimmer, S., Häufle, D. F., and Kalveram, K.-T. (2012). Can robots help to understand human locomotion? *Automatisierungstechnik*, 60(11):653–661.
- Sharbafi, M. A., Ahmadabadi, M. N., Yazdanpanah, M. J., Nejad, A. M., and Seyfarth, A. (2013a). Compliant hip function simplifies control for hopping and running. In *2013 IEEE/RSJ International Conference on Intelligent Robots and Systems*, pages 5127–5133. IEEE.
- Sharbafi, M. A., Maufroy, C., Ahmadabadi, M. N., Yazdanpanah, M. J., and Seyfarth, A. (2013b). Robust hopping based on virtual pendulum posture control. *Bioinspiration & biomimetics*, 8(3):036002.
- Sharbafi, M. A. and Seyfarth, A. (2014). Stable running by leg force-modulated hip stiffness. In *5th IEEE RAS/EMBS International Conference on Biomedical Robotics and Biomechatronics*, pages 204–210. IEEE.
- Sharbafi, M. A. and Seyfarth, A. (2015). FMCH: a new model for human-like postural control in walking. In *2015 IEEE/RSJ International Conference on Intelligent Robots and Systems (IROS)*, pages 5742–5747. IEEE.
- Shinya, M., Fujii, S., and Oda, S. (2009). Corrective postural responses evoked by completely unexpected loss of ground support during human walking. *Gait & posture*, 29(3):483–487.
- Simonsen, E. B. (2014). *Contributions to the understanding of gait control*. University of Copenhagen.
- Sinclair, J., Richards, J., Taylor, P. J., Edmundson, C. J., Brooks, D., and Hobbs, S. J. (2013). Three-dimensional kinematic comparison of treadmill and overground running. *Sports biomechanics*, 12(3):272–282.
- Staufenberg, N.-S., Vielemeyer, J., Müller, R., Renjewski, D., and Rixen, D. J. (2019). Virtual pivot point analysis of the humanoid robot Lola. In *Dynamic Walking 2019*.
- Thies, S. B., Ashton-Miller, J. A., and Richardson, J. K. (2007). What causes a crossover step when walking on uneven ground?: A study in healthy young women. *Gait & posture*, 26(1):156–160.
- Vielemeyer, J., Grißbach, E., and Müller, R. (2019). Ground reaction forces intersect above the center of mass even when walking down visible and camouflaged curbs. *Journal of experimental biology*, 222(14):jeb204305.
- Vielemeyer, J., Müller, R., Staufenberg, N.-S., Renjewski, D., and Abel, R. (2021).

- Ground reaction forces intersect above the center of mass in single support, but not in double support of human walking. *Journal of biomechanics*, page 110387.
- Vu, M. N., Lee, J., and Oh, Y. (2017). Control strategy for stabilization of the biped trunk-slip walking model. In *2017 14th International Conference on Ubiquitous Robots and Ambient Intelligence (URAI)*, pages 1–6. IEEE.
- White, S. C., Yack, H. J., Tucker, C. A., and Lin, H.-Y. (1998). Comparison of vertical ground reaction forces during overground and treadmill walking. *Medicine and science in sports and exercise*, 30(10):1537–1542.
- Whittington, B. R. and Thelen, D. G. (2009). A simple mass-spring model with roller feet can induce the ground reactions observed in human walking. *Journal of biomechanical engineering*, 131(1).
- Whittle, M. W. (1993). *Gait Analysis: An introduction*. Oxford: Ipswich Book Company.
- Winter, D. A. (1995). Human balance and posture control during standing and walking. *Gait & posture*, 3(4):193–214.
- Winter, D. A. (2009). *Biomechanics and motor control of human movement*. John Wiley & Sons.
- Zhao, G., Sharbafi, M., Vlutters, M., van Asseldonk, E., and Seyfarth, A. (2017). Template model inspired leg force feedback based control can assist human walking. In *2017 International Conference on Rehabilitation Robotics (ICORR)*, pages 473–478. IEEE.

A Appendix: Summary

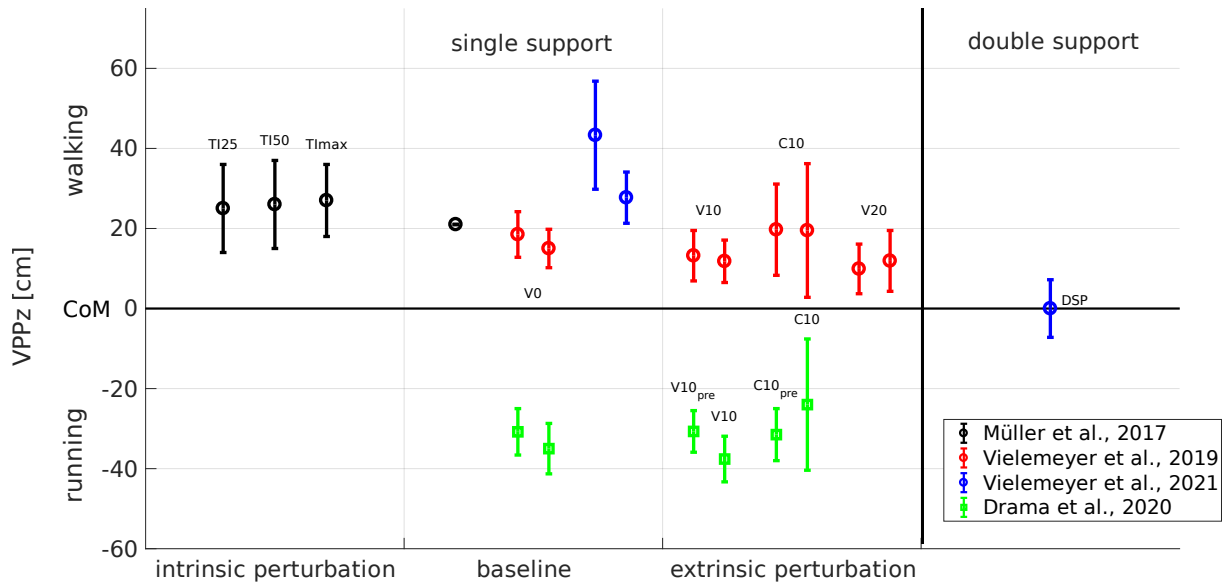


Figure A.1: Vertical (z) position of the virtual pivot point (VPP) above the center of mass (CoM) for all studies, median of all trials (T) and subsequent mean and standard deviation of all subjects (N) are illustrated. For the data of Müller et al. (2017), the grand mean over N and T is shown. The baseline denotes the single support phase of normal level walking or running (visible level - V0). The intrinsic perturbations (black circles) measured by Müller et al. (2017) are different trunk inclinations. Here, TI25 stands for a trunk inclination of $31.9 \pm 5.4^\circ$, TI50 for $47.1 \pm 5.4^\circ$, and TI_{max} for $72.5 \pm 8.1^\circ$ (N=10, T=8 for each TI). Vielemeyer et al. (2019) measured visible and camouflaged curbs of different heights (red circles) as extrinsic perturbation. V10 and V20 stand for the step down of visible curbs (walking)/drops (running) of 10 cm and 20 cm, respectively. C10 describes the perturbed contact of a camouflaged curb (walking)/drop (running) of 10 cm. The left-hand circles of the red pairs of a setting are the results of walking at $1.2 \pm 0.1 \text{ ms}^{-1}$, the right-hand ones at $1.7 \pm 0.1 \text{ ms}^{-1}$ (N=10, T=8 for visible/T=4 for C10). In Vielemeyer et al. (2021), the VPP was calculated for the double support phase of walking (DSP, blue circle). Additionally, the two single support phases surrounding the DSP were analyzed in V0 (N=9, T=10). In Drama et al. (2020), running was analyzed (green squares). The extrinsic perturbations are defined analogously to Vielemeyer et al. (2019). Here, the subscript *pre* denotes the contact previous to the perturbed contact (N=10, T=15 for visible/T=8 for C10).

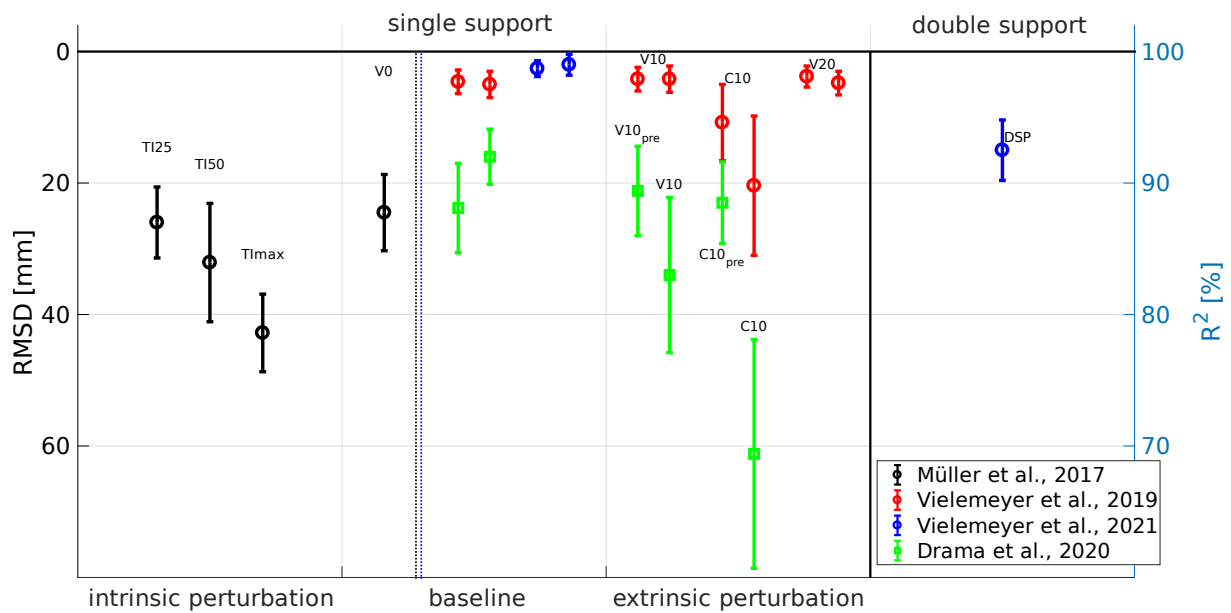


Figure A.2: Blur size of the virtual pivot point (VPP) for all studies, median of all trials (T) and subsequent mean and standard deviation of all subjects (N) are illustrated. For the data of Müller et al. (2017), the grand mean over N and T is shown. The baseline denotes the single support phase of normal level walking or running (visible level - V0). The intrinsic perturbations (black circles) measured by Müller et al. (2017) are different trunk inclinations. Here, TI25 stands for a trunk inclination of $31.9 \pm 5.4^\circ$, TI50 for $47.1 \pm 5.4^\circ$, and TImax for $72.5 \pm 8.1^\circ$ (N=10, T=8 for each TI). Müller et al. (2017) chose the root mean squared distance (RMSD) as blur size parameter (left vertical axis). The other studies took the coefficient of determination, R^2 , as blur size parameter (right vertical axis). Vielemeyer et al. (2019) measured visible and camouflaged curbs of different heights (red circles) as extrinsic perturbation. V10 and V20 stand for the step down of visible curbs (walking)/drops (running) of 10 cm and 20 cm, respectively. C10 describes the perturbed contact of a camouflaged curb (walking)/drop (running) of 10 cm. The left-hand circles of the red pairs of a setting are the results of walking at $1.2 \pm 0.1 \text{ ms}^{-1}$, the right-hand ones at $1.7 \pm 0.1 \text{ ms}^{-1}$ (N=10, T=8 for visible/T=4 for C10). In Vielemeyer et al. (2021), the VPP was calculated for the double support phase of walking (DSP, blue circle). Additionally, the two single support phases surrounding the DSP were analyzed in V0 (N=9, T=10). In Drama et al. (2020), running was analyzed (green squares). The extrinsic perturbations are defined analogously to Vielemeyer et al. (2019). Here, the subscript *pre* denotes the contact previous to the perturbed contact (N=10, T=15 for visible/T=8 for C10).

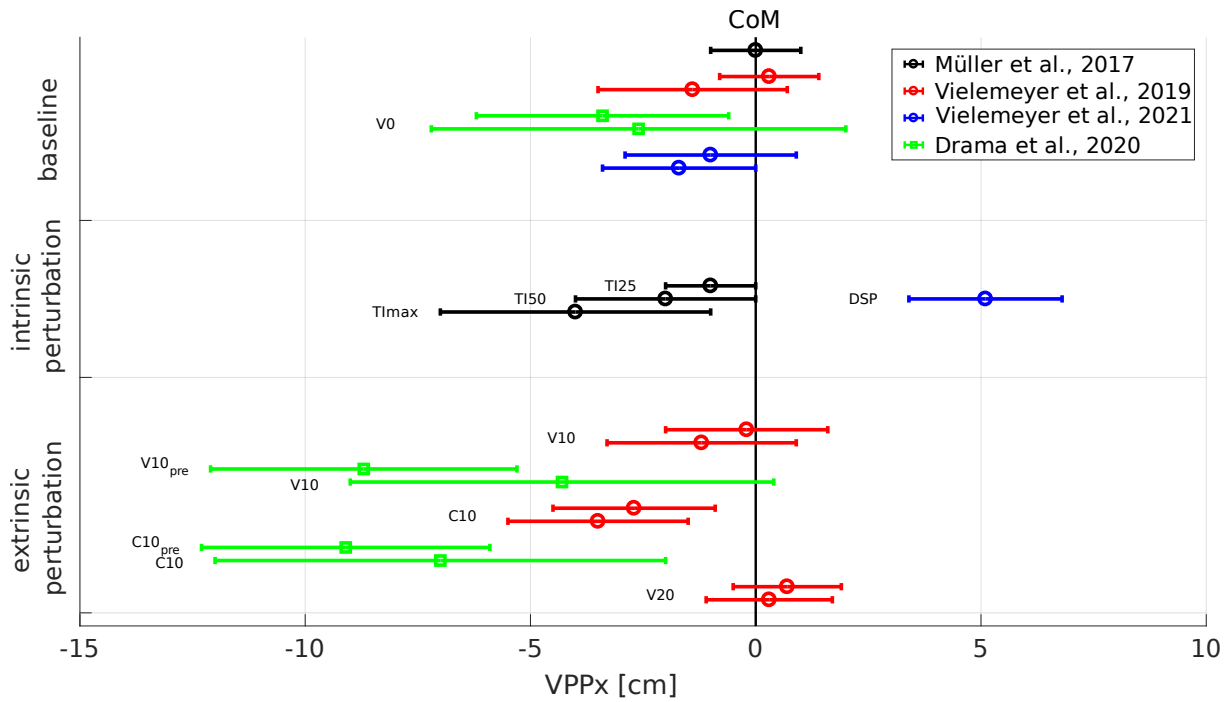


Figure A.3: Horizontal (x) position of the virtual pivot point (VPP) relative to the center of mass (CoM) for all studies, median of all trials (T) and subsequent mean and standard deviation of all subjects (N) are illustrated. For the data of Müller et al. (2017), the grand mean over N and T is shown. The baseline denotes the single support phase of normal level walking or running (visible level - V0). The intrinsic perturbations (black circles) measured by Müller et al. (2017) are different trunk inclinations. Here, TI25 stands for a trunk inclination of $31.9 \pm 5.4^\circ$, TI50 for $47.1 \pm 5.4^\circ$, and TImax for $72.5 \pm 8.1^\circ$ (N=10, T=8 for each TI). Vielemeyer et al. (2019) measured visible and camouflaged curbs of different heights (red circles) as extrinsic perturbation. V10 and V20 stand for the step down of visible curbs (walking)/drops (running) of 10 cm and 20 cm, respectively. C10 describes the perturbed contact of a camouflaged curb (walking)/drop (running) of 10 cm. The upper circles of the red pairs of a setting are the results of walking at $1.2 \pm 0.1 \text{ ms}^{-1}$, the lower ones at $1.7 \pm 0.1 \text{ ms}^{-1}$ (N=10, T=8 for visible/T=4 for C10). In Vielemeyer et al. (2021), the VPP was calculated for the double support phase of walking (DSP, blue circle). Additionally, the two single support phases surrounding the DSP were analyzed in V0 (N=9, T=10). In Drama et al. (2020), running was analyzed (green squares). The extrinsic perturbations are defined analogously to Vielemeyer et al. (2019). Here, the subscript *pre* denotes the contact previous to the perturbed contact (N=10, T=15 for visible/T=8 for C10).

Table A.1: Selected variables of the studies. M17: Müller et al., 2017, M17a: adapted data of Müller et al., 2017, V19: Vielemeyer et al., 2019, D20: Drama et al., 2020, and V21: Vielemeyer et al., 2021. VPP is the horizontal (x) and vertical (z) position of the virtual pivot point. The blur size denotes the root mean squared distance for the data of M17 and the coefficient of determination R^2 for the other studies. V0 (visible, 0 cm) describes the gait over a visible, level ground. V10/V20 are the gait over visible curbs (walking)/drops (running) of 10 cm/20 cm, C10 over a camouflaged curb (walking)/drop (running) of 10 cm. SSP1/SSP2 is the single support phase of the first/second contact and DSP the double support phase. In the running experiment, *step -1* indicates the contact before perturbation and *step 0* the perturbed contact. The intrinsic perturbations were different trunk inclinations (TI), the measured TIs are given in the brackets.

	speed (ms^{-1})	VPPx (cm)	VPPz (cm)	blur size (%/mm*)	
baseline level					
upright ($7.4 \pm 3.1^\circ$)	1.49 ± 0.08	0 ± 1	21 ± 7	24.5 ± 5.8	M17
		-6.5 ± 6.7	31.8 ± 11.9	97.5 ± 1.3	M17a
walking V0	1.17 ± 0.07	0.3 ± 1.1	18.5 ± 5.7	97.7 ± 0.9	V19
walking V0	1.66 ± 0.09	-1.4 ± 2.1	15.0 ± 4.8	97.5 ± 1.0	V19
walking V0 (SSP1)	1.70 ± 0.15	-1.0 ± 1.9	43.3 ± 13.5	98.7 ± 0.6	V21
walking V0 (SSP2)	1.70 ± 0.16	-1.7 ± 1.7	27.7 ± 6.4	99.0 ± 0.8	V21
step -1 running V0	4.9 ± 0.5	-3.4 ± 2.8	-30.8 ± 5.8	88.1 ± 3.4	D20
step 0 running V0	4.9 ± 0.5	-2.6 ± 4.6	-35.0 ± 6.3	92.0 ± 2.1	D20
intrinsic perturbation					
TI25 ($31.9 \pm 5.4^\circ$)	1.59 ± 0.11	-1 ± 1	25 ± 11	26.0 ± 5.4	M17
		-10.9 ± 14.5	31.7 ± 16.1	97.2 ± 1.1	M17a
TI50 ($47.1 \pm 5.4^\circ$)	1.64 ± 0.14	-2 ± 2	26 ± 11	32.1 ± 9.0	M17
		-4.6 ± 6.2	31.4 ± 12.5	95.5 ± 3.1	M17a
TImax ($72.5 \pm 8.1^\circ$)	1.64 ± 0.16	-4 ± 3	27 ± 9	42.8 ± 5.9	M17
		-5.4 ± 3.8	36.9 ± 4.5	90.2 ± 5.3	M17a
extrinsic perturbation					
walking V10	1.21 ± 0.07	-0.2 ± 1.8	13.2 ± 6.3	97.9 ± 0.9	V19
walking V10	1.68 ± 0.13	-1.2 ± 2.1	11.8 ± 5.3	97.9 ± 1.0	V19
step -1 running V10	4.9 ± 0.5	-8.7 ± 3.4	-30.7 ± 5.2	89.4 ± 3.4	D20
step 0 running V10	4.9 ± 0.5	-4.3 ± 4.7	-37.6 ± 5.7	83.0 ± 5.9	D20
walking V20	1.20 ± 0.08	0.7 ± 1.2	9.9 ± 6.2	98.1 ± 0.8	V19
walking V20	1.70 ± 0.08	0.3 ± 1.4	11.9 ± 7.6	97.6 ± 0.9	V19
walking C10	1.28 ± 0.08	-2.7 ± 1.8	19.7 ± 11.4	94.6 ± 2.9	V19
walking C10	1.77 ± 0.15	-3.5 ± 2.0	19.5 ± 16.7	89.8 ± 5.3	V19
step -1 running C10	5.1 ± 0.4	-9.1 ± 3.2	-31.5 ± 6.5	88.5 ± 3.1	D20
step 0 running C10	5.1 ± 0.4	-7.0 ± 5.0	-24.0 ± 16.4	69.4 ± 8.7	D20
double support					
walking V0 (DSP)	1.92 ± 0.18	5.1 ± 1.7	0.0 ± 7.2	92.5 ± 2.3	V21

*for M17 in mm, else in %.

B Appendix: Influence of the input variables between the studies

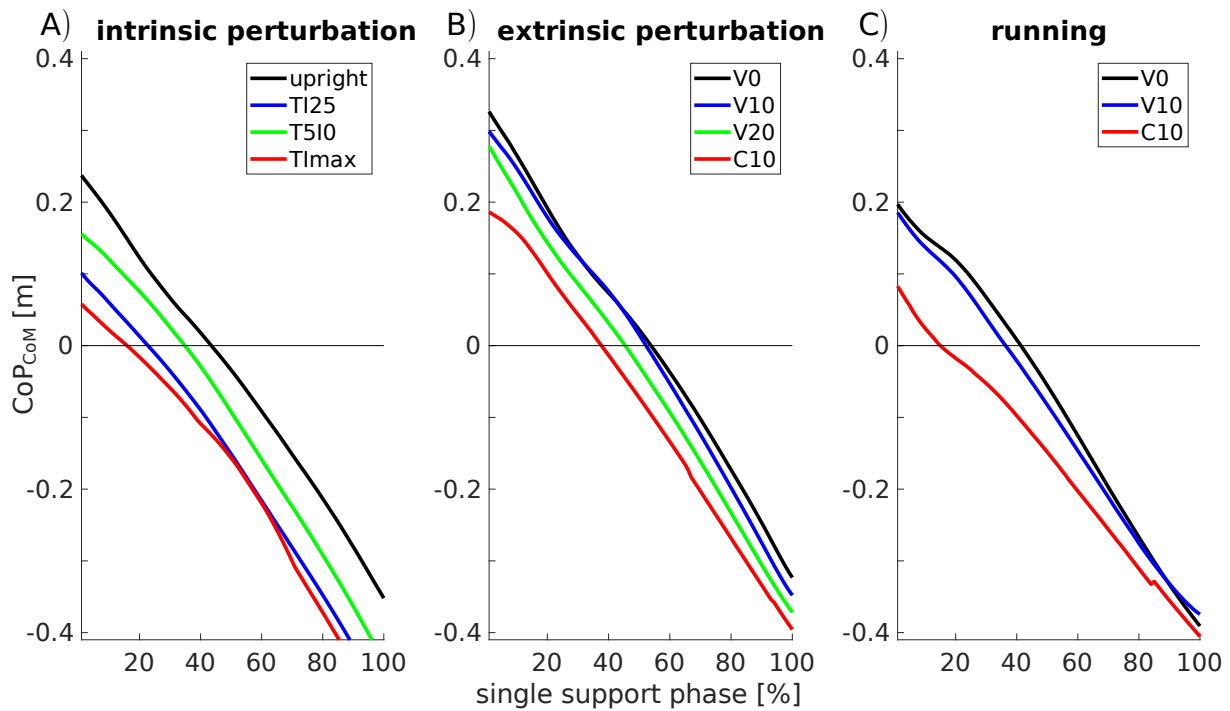


Figure B.1: Horizontal position of the center of pressure (CoP) relative to the center of mass (CoM) for the single support phase, median of all trials and mean of all subjects. The black lines represent the baseline (upright, level) conditions. A) The intrinsic perturbations are different trunk inclinations. TI25 (blue) stands for a trunk inclination of $31.9 \pm 5.4^\circ$, TI50 (green) for $47.1 \pm 5.4^\circ$, and TImax (red) for $72.5 \pm 8.1^\circ$. B) The extrinsic perturbations are visible and camouflaged curbs of different heights (V10/V20: visible curb of 10 cm/20 cm (blue/green), C10: camouflaged curb of 10 cm (red)) for walking at $1.7 \pm 0.1 \text{ ms}^{-1}$. C) The running was perturbed by visible and camouflaged drops (V10/C10: visible/camouflaged drop of 10 cm (blue/red)).

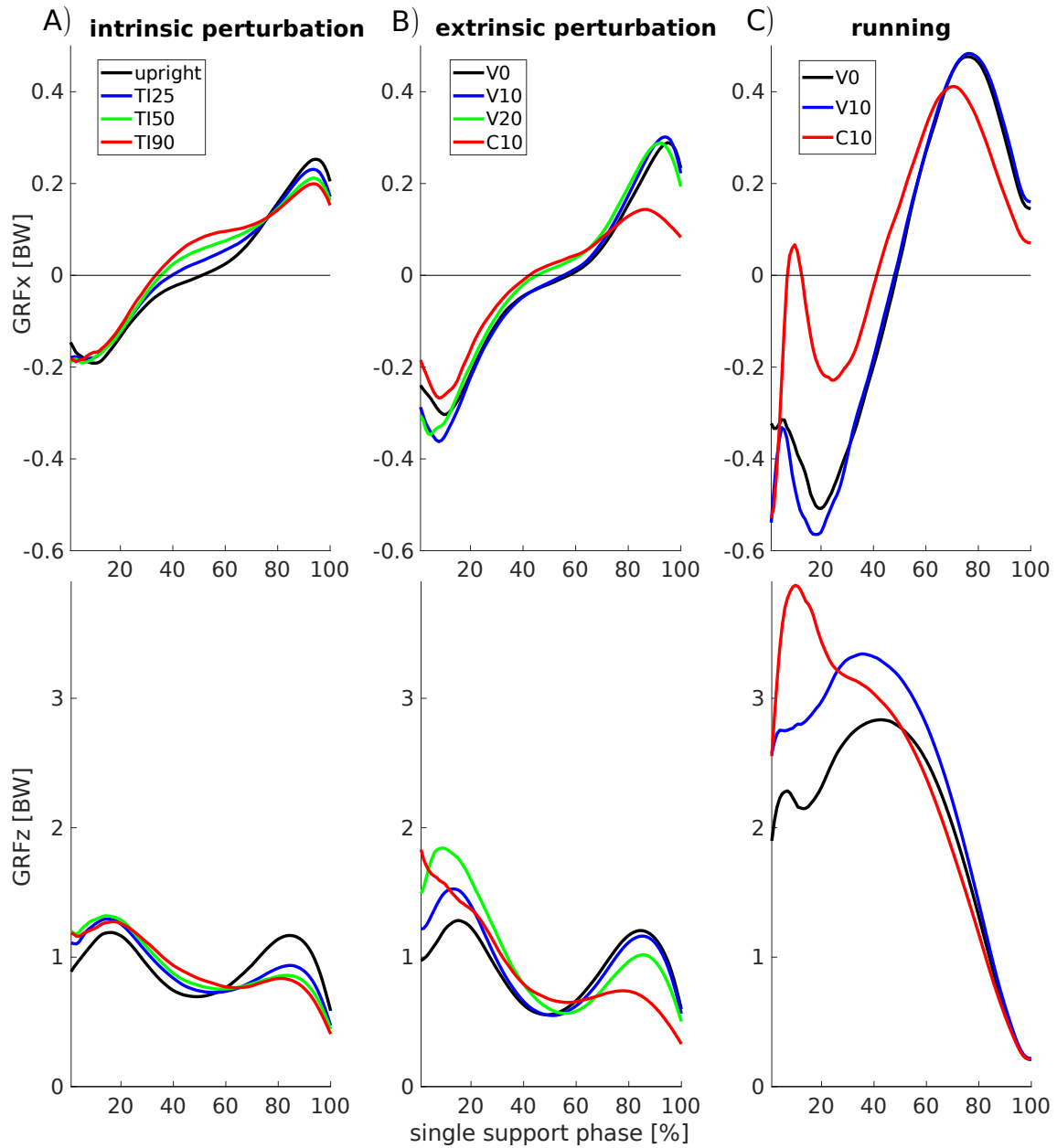


Figure B.2: Horizontal (x, top) and vertical (z, bottom) ground reaction forces (GRF) for the single support phase, median of all trials and mean of all subjects. The black lines represent the baseline (upright, V0 - level) conditions. A) The intrinsic perturbations are different trunk inclinations. TI25 (blue) stands for a trunk inclination of $31.9 \pm 5.4^\circ$, TI50 (green) for $47.1 \pm 5.4^\circ$, and TImax (red) for $72.5 \pm 8.1^\circ$. B) The extrinsic perturbations are visible and camouflaged curbs of different heights (V10/V20: visible curb of 10 cm/20 cm (blue/green), C10: camouflaged curb of 10 cm (red)) for walking at $1.7 \pm 0.1 \text{ ms}^{-1}$. C) Running was perturbed by visible and camouflaged drops (V10/C10: visible/camouflaged drop of 10 cm (blue/red)).

Table B.1: Mean vertical position of the center of mass (CoM) at touch down (mean CoM height - MCH). MCH is also shown relatively to the mean subject height (MSH). The intrinsic perturbations were different trunk inclinations (TI), the measured TIs are given in the brackets. V0 describes the gait over a visible, level ground. V10/V20 are the gait over visible curbs (walking)/drops (running) of 10 cm/20 cm, C10 over a camouflaged curb (walking)/drop (running) of 10 cm. *Slow* describes the walking speed of 1.2 ± 0.1 ms⁻¹, *fast* of 1.7 ± 0.1 ms⁻¹. SSP1/SSP2 is the single support phase of the first/second contact.

	MCH (cm)	MCH/MSH
Müller et al., 2017		
		MSH: 169.5 cm
upright ($7.4\pm 3.1^\circ$)	94.6	0.56
TI25 ($31.9\pm 5.4^\circ$)	92.4	0.55
TI50 ($47.1\pm 5.4^\circ$)	89.5	0.53
TI _{max} ($72.5\pm 8.1^\circ$)	81.8	0.48
Vielemeyer et al., 2019		
		MSH: 178.9 cm
V0 slow/fast	99.5/98.9	0.56/0.55
V10 slow/fast	103.1/102.9	0.58/0.58
V20 slow/fast	107.0/106.7	0.60/0.60
C10 slow/fast	104.2/104.5	0.58/0.58
Drama et al., 2020		
		MSH: 179.9 cm
V0	101.8	0.57
V10	104.7	0.58
C10	105.5	0.59
Vielemeyer et al., 2021		
		MSH: 171.1 cm
SSP1	94.9	0.56
SSP2	95.5	0.56

Table B.2: Relative horizontal impulse for the baseline conditions. V0 denotes the level, unperturbed gait, *slow* stands for $1.2\pm 0.1\text{ ms}^{-1}$ and *fast* for $1.7\pm 0.1\text{ ms}^{-1}$. SSP1/SSP2 is the single support phase of the first/second contact.

	relative horizontal impulse (%)
Müller et al., 2017	
upright	10.88
Vielemeyer et al., 2019	
V0 slow	11.27
V0 fast	13.59
Drama et al., 2020	
V0	22.21
Vielemeyer et al., 2021	
SSP1	9.49
SSP2	10.48

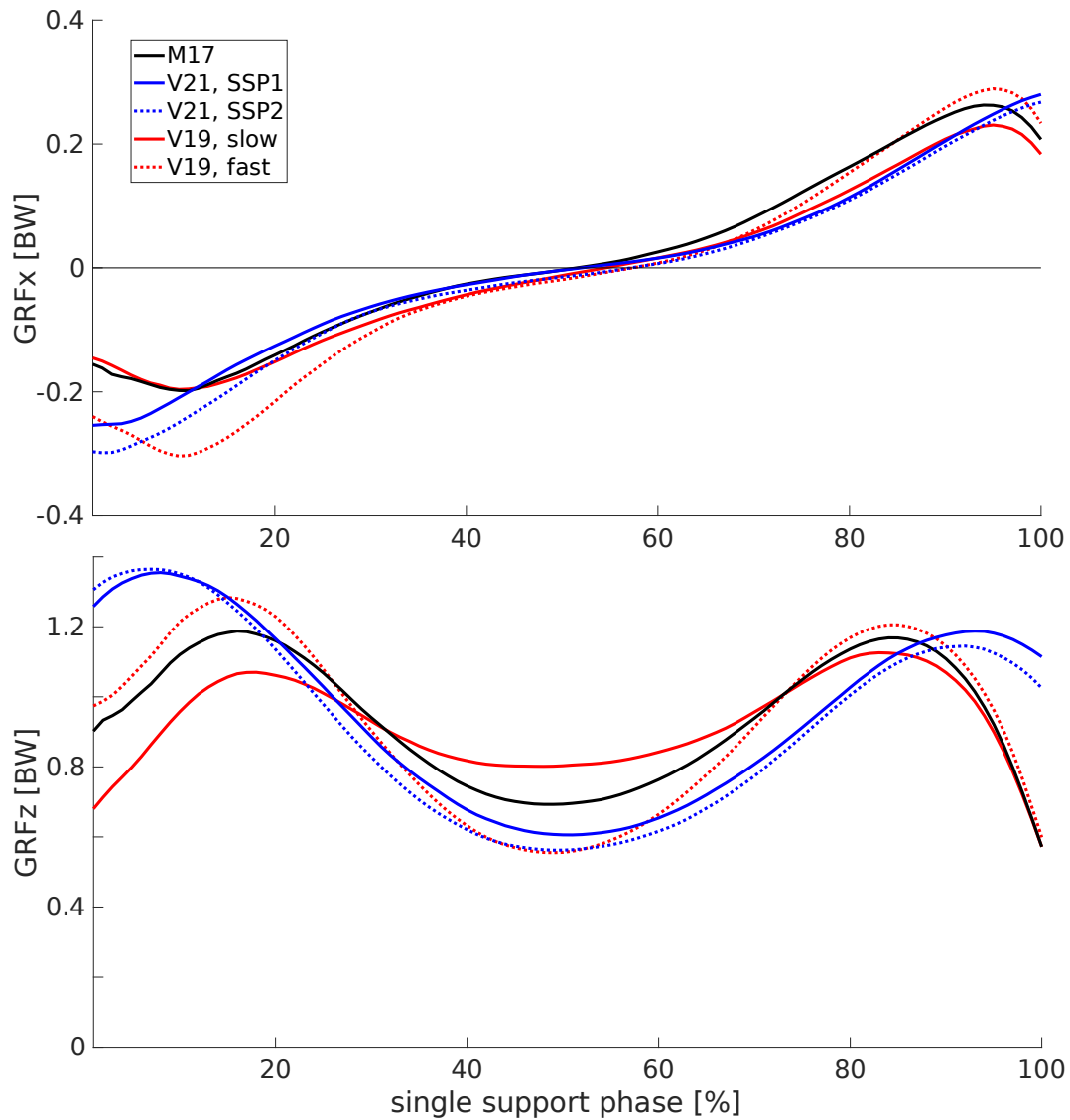


Figure B.3: Horizontal (x, top) and vertical (z, bottom) ground reaction forces (GRF) for the single support phase of walking (level, unperturbed), median of all trials and mean of all subjects. The black line illustrates the data of Müller et al. (2017) - M17. The solid blue line shows the data of the first contact (single support phase - SSP1), the dotted blue line shows the data of the second contact, SSP2, (Vielemeyer et al., 2021) - V21. The red lines represent the data of Vielemeyer et al. (2019) - V19 - with different speeds (solid line: $1.2 \pm 0.1 \text{ ms}^{-1}$, *slow*; dotted line: $1.7 \pm 0.1 \text{ ms}^{-1}$, *fast*).

C Appendix: Influence of the input variables within the studies

Preparatory Work In Müller et al. (2017), no significant differences in the VPP position and R^2 were noticed between the setups. Considering the ratio of GRFx to GRFz (figure C.1A) and the time evolution of the forces (figure B.2), the relative horizontal impulse suggests a higher propulsion impulse for a larger trunk inclination (table C.1). This means that in sum the contribution of the horizontal component increases for a larger trunk inclination, which should shift the VPP downwards, as illustrated in figure 5.3B. However, this could not be observed in the VPP values due to compensating effects of the input variables (see also section 5.2.1). For an increasing trunk inclination, the $CoMz_{TD}$ decreases, which should shift the VPP upwards (see figure 5.3C). The same applies to the range of the CoP_{CoM} (figure B.1A), because a larger range, which could be found for larger trunk inclinations, would shift the intersection point of the force vectors upwards (see figure 5.3A). Thus, it could be that the effects of the input variables compensate each other and therefore no significant differences could be observed between the setups. Additionally, the CoP_{CoM} is shifted posterior for all setups, more so for larger trunk inclinations. This asymmetry may explain the posterior VPPx positions (for TI25 and TI_{max}, the position even differs significantly from zero with $p=0.045$ and $p<0.001$).

Article I In Vielemeyer et al. (2019), there are significant differences in all VPP variables, but only between some setups. Considering the relative horizontal impulse, negative differences are obtained between the visible level and curb conditions (table C.1). This occurs due to a higher influence of the GRFx component in the curb conditions, which can explain the lower VPP position. Between the visible and camouflaged conditions, the opposite is the case. However, there are no significant differences. The $CoMz_{TD}$ height increases as the perturbation grows. This should shift the VPP downwards. Since this effect could only be observed for the visible conditions, it is assumed that in the camouflage setups other variables have a greater influence. For example, a considerable difference between the forces of the visible and camouflaged conditions can be observed and thus, the effect of the ratio of the forces seems to predominate. No major differences are found in the range of the CoP_{CoM} . Here, only the position shifts from balanced in V0 to more posterior in C10. This results in a more posterior position of the VPPx in the camouflaged condition compared to the visible conditions. However, the VPPx shifts in V20 compared to V0 in the anterior direction, which compensates the effect of the

CoP_{CoM}.

Article II In Vielemeyer et al. (2021), analyses of the input variables have already been performed. Here, no major differences could be observed in the CoP_{CoM}, but in the relative horizontal impulses, which could explain the VPP position.

Article III In Drama et al. (2020), there are only significant differences in VPP_x between V0 and C10 and in R² between all setups. In VPP_z, there are no significant differences. The ratio of the forces indicates a slightly lower horizontal component in V10 compared to V0 and a considerably lower horizontal component in C10 compared to the visible conditions (figure C.1C). This should shift the VPP upwards. However, since there are no significant differences and the trend does not fit to the visible conditions, the influence of the other variables seems to outweigh it. The CoM_{zTD} increases with greater perturbation, which, contrary to the ratio of the forces, should shift the VPP downwards. The range of the CoP_{CoM} is smaller in the camouflaged condition compared to the visible ones. This should shift the VPP downwards in the camouflaged condition. The input variables therefore apparently balance each other out. The CoP_{CoM} is more posterior in all setups and even more posterior with increasing perturbation. This could explain the shift in the VPP_x.

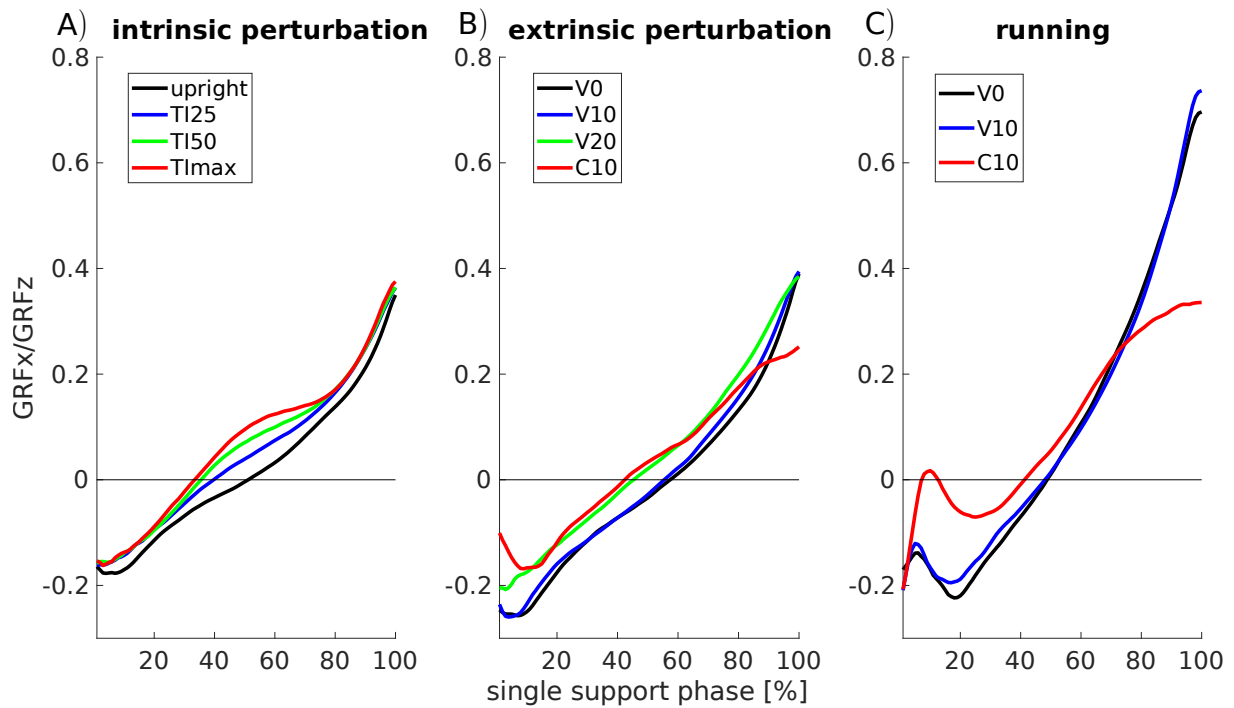


Figure C.1: Ratio of the horizontal (x) and vertical (z) ground reaction forces (GRF) for the single support phase, median of all trials and mean of all subjects. The black lines represent the baseline (upright, level) conditions. A) The intrinsic perturbations are different trunk inclinations. TI25 (blue) stands for a trunk inclination of $31.9 \pm 5.4^\circ$, TI50 (green) for $47.1 \pm 5.4^\circ$, and TImax (red) for $72.5 \pm 8.1^\circ$. B) The extrinsic perturbations are visible and camouflaged curbs of different heights (V10/V20: visible curb of 10 cm/20 cm (blue/green), C10: camouflaged curb of 10 cm (red)) for walking at $1.7 \pm 0.1 \text{ ms}^{-1}$. C) The running was perturbed by visible and camouflaged drops (V10/C10: visible/camouflaged drop of 10 cm (blue/red)).

Table C.1: Differences of the relative horizontal impulses. *Upright* stands for a trunk inclination of $7.4 \pm 3.1^\circ$, *TI25* for $31.9 \pm 5.4^\circ$, *TI50* for $47.1 \pm 5.4^\circ$, and *TImax* for $72.5 \pm 8.1^\circ$. V0 describes the gait over a visible, level ground. V10/V20 are the gait over visible curbs (walking)/drops (running) of 10 cm/20 cm, C10 over a camouflaged curb (walking)/drop (running) of 10 cm. SSP1/SSP2 is the single support phase of the first/second contact, DSP is the double support phase. For Vielemeyer et al., 2019, the walking speed of $1.7 \pm 0.1 \text{ ms}^{-1}$ was considered.

	difference of relative horizontal impulses (%)
Müller et al., 2017	
upright - TI25	-0.66
upright - TI50	-1.53
upright - TImax	-2.22
TI25 - TI50	-0.87
TI25 - TImax	-1.56
TI50 - TImax	-0.69
Vielemeyer et al., 2019	
V0 - V10	-0.55
V0 - V20	-0.07
V0 - C10	2.15
V10 - V20	0.47
V10 - C10	2.70
Drama et al., 2020	
V0 - V10	0.98
V0 - C10	8.25
V10 - C10	7.27
Vielemeyer et al., 2021	
SSP1 - SSP2	-0.98
SSP1 - DSP	-6.47
SSP2 - DSP	-5.49

D Appendix: Error estimation

Table D.1: Accuracy of the Kistler force plates. F are the ground reaction forces in the separate dimensions (x,y: horizontal, z: vertical). The same relative error is assumed for the bending moment M.

type of the force plate :	9281B	9287B
	1st contact	2nd contact
Crosstalk (cross)		
$F_x \leftrightarrow F_y$	$< \pm 1.0\%$	$< \pm 1.5\%$
$F_x, F_y \rightarrow F_z$	$< \pm 2.0\%$	$< \pm 1.5\%$
$F_z \rightarrow F_x, F_y$	$< \pm 1.0\%$	$< \pm 1.0\%$
Accuracy of the amplifier		
(ampl)	$< \pm 1.0\%$	$< \pm 0.5\%$

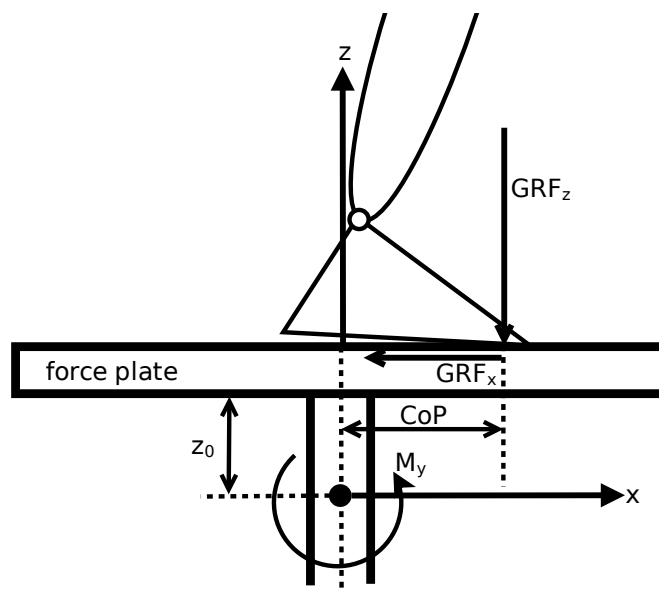


Figure D.1: Force plate (central support type) with the location of the center of pressure (CoP) and the horizontal (x) and vertical (z) ground reaction forces (GRF) and moments (M_y - bending moment with respect to the axis of rotation of support) involved, according to Winter (2009). z_0 is the distance between the support axis and the force plate surface.

Publications in peer-reviewed journals

- AminiAghdam, S., Griefsbach, E., Vielemeyer, J., and Müller, R. (2019). Dynamic postural control during (in) visible curb descent at fast versus comfortable walking velocity. *Gait & posture*, 71:38–43.
- AminiAghdam, S., Vielemeyer, J., Abel, R., and Müller, R. (2019). Reactive gait and postural adjustments following the first exposures to (un) expected stepdown. *Journal of biomechanics*, 94:130–137.
- Drama, Ö., Vielemeyer, J., Badri-Spröwitz, A., and Müller, R. (2020). Postural stability in human running with step-down perturbations: an experimental and numerical study. *Royal Society open science*, 7:200570.
- Müller, R., Rode, C., Aminiaghdam, S., Vielemeyer, J., and Blickhan, R. (2017). Force direction patterns promote whole body stability even in hip-flexed walking, but not upper body stability in human upright walking. *Proceedings of the Royal Society A*, 473(2207):20170404.
- Müller, R., Vielemeyer, J., and Häufle, D. F. (2020). Negotiating ground level perturbations in walking: visual perception and expectation of curb height modulate muscle activity. *Journal of biomechanics*, page 110121.
- Vielemeyer, J., Griefsbach, E., and Müller, R. (2019). Ground reaction forces intersect above the center of mass even when walking down visible and camouflaged curbs. *Journal of experimental biology*, 222(14):jeb204305.
- Vielemeyer, J., Müller, R., Staufenberg, N.-S., Renjewski, D., and Abel, R. (2021). Ground reaction forces intersect above the center of mass in single support, but not in double support of human walking. *Journal of biomechanics*, page 110387.

Conference abstracts

- Staufenberg, N.-S., Vielemeyer, J., Müller, R., Renjewski, D., and Rixen, D. J. (2019). Virtual pivot point analysis of the humanoid robot Lola. In *Dynamic Walking 2019*.
- Vielemeyer, J., Griefsbach, E., AminiAghdam, S., and Müller, R. (2019). Do ground reaction forces intersect above the center of mass during camouflaged curb negotiation? *25th Congress of the European Society of Biomechanics*, Vienna, Austria.

Erklärung

Hiermit versichere ich, dass mir die geltende Promotionsordnung der Fakultät für Sozial- und Verhaltenswissenschaften der Friedrich-Schiller-Universität bekannt ist. Ich habe die Dissertation selbst angefertigt und alle von mir benutzten Hilfsmittel, persönlichen Mitteilungen und Quellen in meiner Arbeit angegeben. Darüber hinaus erkläre ich, dass ich keine Hilfe eines kommerziellen Promotionsvermittlers in Anspruch genommen habe und dass Dritte weder unmittelbar noch mittelbar geldwerte Leistungen von mir für Arbeiten erhalten haben, die im Zusammenhang mit dem Inhalt der vorgelegten Dissertation stehen.

Mit Ausnahme der allgemeinen Einleitung und Schlussfolgerung (Kapitel 1 und 5) sind die Kapitel des vorliegenden Manuskripts in internationalen wissenschaftlichen Zeitschriften publiziert. Die Ideen für die Kapitel 2-4 entstanden in Zusammenarbeit mit Dr. Roy Müller. Von ihm habe ich auch konzeptionelle Unterstützung für die Erstellung der Manuskripte erhalten. Dr. Roy Müller war an der Erhebung der experimentellen Daten von Kapitel 2-4 beteiligt. Die Daten für Kapitel 2 habe ich zusammen mit Eric Griebach erhoben und ausgewertet, und das Manuskript und dessen Überarbeitung anhand der Gutachterkommentare entstand in enger Zusammenarbeit mit ihm. Die experimentellen Daten für Kapitel 3 wurden von Kevin Moll erhoben, die Daten für Kapitel 4 von Martin Götze und Michael Ernst. Als alleinige Hauptautorin von Kapitel 3 habe ich hier die experimentellen Daten ausgewertet, das Manuskript verfasst und die Gutachterkommentare bearbeitet. In Kapitel 3 waren Nora-Sophie Staufenberg und Dr. Daniel Renjewski an der Auswertung der Modelldaten beteiligt, welche jedoch in der finalen Variante des Artikels nicht mehr berücksichtigt wurden. In Kapitel 4 oblag mir das Bearbeiten der experimentellen Daten, während Özge Drama als weitere Erstautorin die Simulationsdaten erhob und auswertete. Das Verfassen des Manuskripts und das Bearbeiten der Gutachterkommentare erfolgte in enger Zusammenarbeit mit Özge Drama. Alexander Badri-Sprowitz war hier an der Konzeptentwicklung des Simulationsteils des Manuskripts beteiligt. Weitere Personen haben mich bei der Erstellung der Manuskripte nicht unterstützt.

Die Dissertation wurde noch nicht als Prüfungsarbeit für eine staatliche oder andere wissenschaftliche Prüfung eingereicht. Es wurde keine gleiche, ähnliche oder eine andere Abhandlung bei einer anderen Hochschule als Dissertation eingereicht. Ich versichere, nach bestem Wissen die reine Wahrheit gesagt und nichts verschwiegen zu haben.

Jena, den

.....

Johanna Vielemeyer